Transactions of the ASME

Journal of Fluids Engineering

Published Quarterly by The American Society of Mechanical Engineers

VOLUME 114 • NUMBER 2 • JUNE 1992

Transactions of the ASME, Journal of Fluids Engineering (ISSN 0098-2202) is published quarterly (Mar., June, Sept., Dec.) for $110.00 per year by The American Society of Mechanical Engineers, 345 East 47th Street, New York, NY 10017. Second class postage paid at New York, NY and additional mailing offices. POSTMASTER: Send address changes to Transactions of the ASME, Journal of Fluids Engineering, c/o THE AMERICAN SOCIETY OF MECHANICAL ENGINEERS, 22 Law Drive, Box 2300, Fairfield, NJ 07007-2300.
CHANGES OF ADDRESS must be received at Society headquarters seven weeks before they are to be effective. Please send old label and new address.
PRICES: To members, $36.00, annually: to nonmembers, $110.00. Add $20.00 for postage to countries outside the United States and Canada.
STATEMENT from By-Laws. The Society shall not be responsible for statements or opinions advanced in papers or . . . printed in its publications (B7.1, Par. 3).

INDEXED by Applied Mechanics Reviews and Engineering Information, Inc.
Canadian Goods & Services Tax Registration #126148048

Journal of Fluids Engineering

Editorial

The Editorial Board of this Journal has been considering for the past few years the broader issues of scope, aims, and goals of archival publishing and in particular publishing in the area of fluids engineering. This has been stimulated by recent changes in the methods of communication between different sectors of the engineering community. We are also experiencing great advances in tools for research which, combined with a rise in the number of researchers, led to an increased number of papers appearing in technical journals. As a result, we are required to emphasize publication selectivity. This process will be strongly influenced by the needs of the readers. Authors are, therefore, encouraged to address themselves to the broader audience of the Journal and not just to the very few researchers who work on topics of their specialties. We understand that not all readers could be expected to follow the details of advanced methodologies. However, most fluids engineers should be able to comprehend the basic findings of a contribution and assess its significance.

The Board believes that the primary purposes of archival publishing are to communicate with readers new, significant, and useful technical information and to document such information for posterity. To serve these purposes, this Journal is seeking to publish articles in fluids engineering, namely articles that do not only make a contribution to the discipline of fluid mechanics but also have a clear relationship to a motivating engineering problem. The specific areas and topics of interest defining the scope of the Journal are listed on the inside of the back cover. This list is continuously updated in response to scientific and engineering developments. The basic criteria of the reviewing process have been outlined in an earlier editorial (March, 1991, Vol. 113, p. 1).

The following type of articles are invited.

Contributed Articles

The mainstream articles published in an archival journal are contributed papers reporting on progress of research. Theoretical contributions should offer the framing and/or solution of a new engineering problem, or provide a significant improvement to the solution of a problem. Contributions based on experimental results should contain significant new information on the flow features of a problem or report on new experimental techniques. Adequate information should be provided for readers to be able to reconstruct and use the proposed experimental devices. Similarly, contributions based on numerical analysis should present numerical results for problems that have not previously been investigated and/or provide information on new or improved numerical techniques. Reporting on the use of a new numerical method, without documenting its superiority and supplying enough information on how to use it, is not a sufficient reason to publish a paper in this Journal.

All experimental papers should provide adequate information on the experimental uncertainty following the guidelines outlined in an earlier editorial (September, 1991, Vol. 113, p. 313). Numerical papers should also provide a thorough report on numerical accuracy. For more information on this issue the authors should refer to an other earlier editorial (March, 1986, Vol. 108, p. 2). The CFD Coordinating Group of the Division is in the process of preparing a new set of guidelines for CFD papers which will appear in one of the following issues of the Journal.

All papers, theoretical, experimental, or numerical should offer a thorough discussion of the physical aspects of the results and their possible significance in fluids engineering.

A very important part of a paper is the section on conclusions. Authors will be required to prepare their conclusions in such a manner that a broad audience comprehends them. Moreover, the conclusions should make clear the significance of the authors' contributions to the permanent literature. Broad and general statements must be avoided. In case authors feel that preparing in detail and in simplified terms the basic elements of their contributions would dilute the scientific impact of their contribution, they may wish to prepare a separate section entitled "Technical Contributions." In such a section they could also include ideas on how their results could be implemented in engineering applications.

Technical Briefs

Technical Briefs are shorter contributions which could be (i) an addendum to previously published results, (ii) material relating to new ideas, (iii) or just results of limited extent. Technical Briefs generally require shorter review times.

Reviews

These papers are reviews of recent contributions in an area of current interest. Reviews appear every three to four years on a particular topic, include all major related references and are usually addressed to the specialists. The scope and topics in such articles are the choice of the author but care should be taken to consult the Journal Editor concerning suitability and timeliness for publication.

Perspectives

A Perspective is a new type of article introduced by this Journal. A perspective article should provide a critical evaluation of work contributed in an area over the past ten or more years. The author of such an article should limit discussion to contributions of major significance and should provide his/her own interpretation of advances in understanding of physical phenomena based on the evidence collected over the years. For perspectives that are focused on methodology, be it experimental or numerical, the author should again provide a clear description of successful methods, supplementing it with his/her own evaluation. A good criterion to determine whether certain material is appropriate for a perspective article is its maturity. A perspective should cover material that has reached the level of completeness and acceptance that would

qualify it to be a chapter in a book. Authors are strongly encouraged to prepare such articles in a way that they could reach a broad audience.

Historical Articles

In such articles we encourage authors to follow the history of thinking, not the history of events. The latter belongs to magazines like *Mechanical Engineer*. Historical articles will be valuable to the readers if they can follow the inception and maturation of significant ideas through decades of development. Discussion and clarification of pioneering earlier contributions and evaluation of how such information has impacted to our present understanding of fluid flow phenomena are strongly encouraged.

Editorials

Editorials are invited on topics of interest to the readership of the Journal. Authors wishing to contribute an editorial should submit their manuscript to the Technical Editor. Directions and guidelines for the authors also appear in the form of editorials.

Special Articles

Occasionally, articles of special character appear in this Journal as, for example, reports on recent panel discussions or workshops, reports on educational issues, reports on the progress of major research efforts, etc.

Discussions

Short discussions of published papers and authors' responses are also published. The readers of this Journal are encouraged to submit their Discussions directly to the Technical Editor.

The Editorial Board

Numerical Simulation of Flows Driven by a Torsionally Oscillating Lid in a Square Cavity

Reima Iwatsu
Research Scientist,
Institute of Computational Fluid Dynamics,
Tokyo 152, Japan

Jae Min Hyun
Professor,
Korea Advanced Institute of Science and Technology,
Cheongryang, Seoul, Korea

Kunio Kuwahara
Associate Professor,
The Institute of Space and Astronautical Science,
Yoshinodai, Sagamihara, Kanagawa, Japan

Numerical studies were made of the flow of a viscous fluid in a two-dimensional square container. The flows are driven by the top sliding wall, which executes sinusoidal oscillations. Numerical solutions were acquired by solving the time-dependent, two-dimensional incompressible Navier-Stokes equations. Results are presented for wide ranges of two principal physical parameters, i.e., Re, the Reynolds number and ω', the nondimensional frequency of the lid oscillation. Comprehensive details of the flow structure are presented. When ω' is small, the flow bears qualitative similarity to the well-documented steady driven-cavity flow. The flow in the bulk of cavity region is affected by the motion of the sliding upper lid. On the contrary, when ω' is large, the fluid motion tends to be confined within a thin layer near the oscillating lid. In this case, the flow displays the characteristic features of a thin-layer flow. When ω' is intermediate, $\omega' \sim O(1)$, the effect of the side walls is pronounced; the flow pattern reveals significant changes between the low-Re and high-Re limits. Streamline plots are constructed for different parameter spaces. Physically informative interpretations are proposed which help gain physical insight into the dynamics. The behavior of the force coefficient C_f has been examined. The magnitude and phase lag of C_f are determined by elaborate post-processings of the numerical data. By utilizing the wealth of the computational results, characterizations of C_f as functions of Re and ω' are attempted. These are in qualitative consistency with the theoretical predictions for the limiting parameter values.

Introduction

Incompressible viscous flow in a closed container constitutes an important subject, from the standpoints of both theoretical analyses and technological applications. Numerous studies have been made on the two-dimensional square cavity flow with its upper lid sliding at a constant speed (Pan and Acrivos, 1967; Bozeman and Dalton, 1973; Ozawa, 1975; Tuann and Olson, 1978; Benjamin and Denny, 1979; Ghia et al., 1982; Schreiber and Keller, 1983; Iwatsu et al., 1989, 1990). The major parameter of this problem is the Reynolds number Re, defined by using the lid speed U_0, the height of the cavity L, the kinematic viscosity of the fluid ν, as $\mathrm{Re} = U_0 L/\nu$. The essential features of the flow, as the Reynolds number is varied, have been rigorously investigated. When Re is very low, i.e., in the Stokes flow limit, the viscous term and the pressure gradient term are the two principal driving forces. In the case of high Reynolds numbers, say, up to $\mathrm{Re} \simeq 10^4$ (Benjamin and Denny, 1979; Ghia et al., 1982; Schreiber and Keller, 1983; Iwatsu et al., 1989, 1990), the advection effect dominates over the viscous and the pressure gradient effects. In the majority of the two-dimensional numerical investigations conducted to date, steady solutions were dealt with. However, the problem of unsteady flows, induced by the unsteady motion of the sliding upper wall, has not received much attention in the literature (Soh and Goodrich, 1988). As observed by Soh and Goodrich (1988), due mainly to the inherent difficulties in constructing reliable numerical models, the numerical efforts to tackle unsteady driven-cavity flows have been scanty.

In this paper, we shall address the unsteady flows in a square cavity driven by the upper surface which is executing a simple harmonic oscillation. This presents an interesting and attractive benchmark flow model. Owing to its simple geometry and regular boundary conditions, much can be learned about the fundamental issues underlying the steady flows in a finite closed enclosure. The sliding motion of the top surface is describable by a sine function, which allows considerable easiness and simplifications in the numerical coding.

The unsteady motion in the infinite expanse of a viscous fluid, of kinematic viscosity ν, generated by an infinite flat plate undergoing a sinusoidal oscillation in its own plane, poses a classical problem. This flow, referred to as the Stokes' second problem, admits a well-known analytical solution (Schlichting, 1979). If the x-component velocity of the motion of the solid plate in the plane $y=0$ is prescribed as $U = U_0 \sin\omega t$, then the fluid motions are given as $u(y,t) = U_0 e^{-ky} \sin(\omega t - ky)$. In the above, y measures the coordinate perpendicular to the sliding plate, U_0 the amplitude of the x-component velocity of the plate, ω the dimensional frequency of the oscillation; and $k \equiv (\omega/2\nu)^{1/2}$, is an important physical parameter to emerge from the analysis (Schlicting, 1979). The dimension of k is length^{-1}. As is obvious, the induced velocities in the fluid decay

Contributed by the Fluids Engineering Division for publication in the JOURNAL OF FLUIDS ENGINEERING. Manuscript received by the Fluids Engineering Division September 24, 1990. Associate Technical Editor: S. H. Ragab.

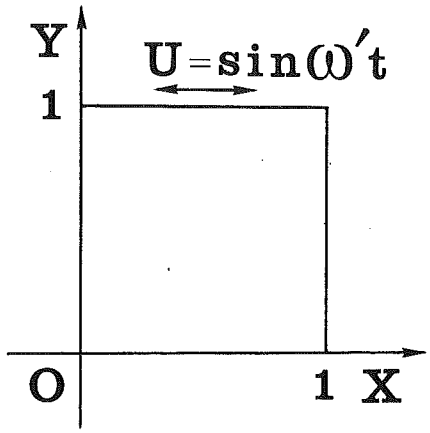

Fig. 1 The cavity configuration with the coordinate system

exponentially as e^{-ky} away from the plate. Also, there is a phase lag of (ky) between the plate and the flow field. The physical meaning of k^{-1} can be stated as a length scale in the y direction over which the direct influence of the solid plate is felt (Schlichting, 1979; Soh and Goodrich, 1988).

In the present paper, we are concerned with the situations in which the oscillating solid plate is finite in size and the viscous fluid is confined inside a closed finite container. This flow portrays an extension of the classical Stokes' second problem to finite geometry. Soh and Goodrich (1988) utilized this flow model as an example to test the validity of a new time-accurate numerical model. Rudimentary and restricted results were illustrated in (Soh and Goodrich, 1988) for only one parameter setting; no comprehensive and in-depth delineations of the salient flow characteristics over a broad range of parameters were attempted by Soh and Goodrich (1988).

As is intuitively clear, since the flow configuration in a finite closed geometry is considered, the overall size of the container L is an externally specified length scale. The penetration depth in the viscous fluid over which the impact of the sliding top wall is felt is scaled by $k^{-1}[\equiv(2\nu/\omega)^{1/2}]$ (see Schlichting, 1979). This is another length scale in the present problem. The effect of the accelerating top surface is measured by $U_0\omega'$. The ratios of these scales produce relevant nondimensional parameters; the prominent flow characteristics are determined by the two principal nondimensional parameters, i.e., the Reynolds number $\mathrm{Re}=U_0L/\nu$, and the frequency parameter $\omega'[\equiv L\omega/U_0]$.

The objective of the present work is to obtain extensive and systematically-organized computational results of the driven-cavity flow with an oscillating lid. Complete flow details have been acquired over wide ranges of two principal parameters, i.e., Re and ω'. The numerical model to solve the Navier-Stokes equations used in the present study has been well established and proven to be highly effective for this kind of flow simulations (Harlow and Welch, 1965).

The emphasis will be placed on illuminating the changes in flow characteristics as Re and ω' encompass broad ranges. Of particular interest are the flow regimes of extreme values of ω'. These limiting situations should recover the much-studied qualitative features of steady driven-cavity flows (when ω' is very small) and of thin-layer flow approximations (when ω' is very large). It will be demonstrated that, by scrutinizing the comprehensive numerical results, when ω' is intermediate, the character of flow displays marked differences between the low-Re and high-Re regimes.

The Model

Consider an incompressible viscous fluid of density ρ, initially at rest, inside a stationary square cavity of width L. At $t=0$, the upper lid at $y=L$ starts sinusoidal oscillation in its own plane, described as $U=U_0\sin\omega t$ (see Fig. 1). The task is to portray the subsequent time-dependent motion of the fluid. In the present paper, the primary aim is to depict the quasi-steady cyclic motion of the fluid; the initial transitory approach to the cyclic state is not of major interest in the present work.

The flow is governed by the equation of continuity and the Navier-Stokes equations. These can be expressed, in nondimensional form, written in the Cartesian coordinate, as

$$\mathrm{div}\mathbf{V}=0 \tag{1}$$

$$\frac{\partial\mathbf{V}}{\partial t}+(\mathbf{V}\cdot\mathrm{grad})\mathbf{V}=-\mathrm{grad}\,p+\mathrm{Re}^{-1}\Delta\mathbf{V} \tag{2}$$

where $\mathbf{V}=(u,v)$ is the velocity, p the pressure,

$$\mathrm{div}\mathbf{V}=\frac{\partial u}{\partial x}+\frac{\partial v}{\partial y},$$

$$\mathrm{grad}=\left(\frac{\partial}{\partial x},\frac{\partial}{\partial y}\right),$$

and

$$\Delta=\mathrm{div}\cdot\mathrm{grad}$$

is the Laplacian operator.

The initial condition is that the fluid is motionless in the whole domain, i.e.,

$$\mathbf{V}=0 \text{ for } 0\le x\le 1, 0\le y\le 1. \tag{3}$$

The associated boundary conditions are

$$\mathbf{V}=(\sin\omega' t,0) \text{ at } y=1, \tag{4}$$

$\mathbf{V}=0$ at the rest of the solid walls: $y=0, 0\le x\le 1$, $x=0, 0\le y\le 1$ and

$$x=1, 0\le y\le 1. \tag{5}$$

In the above system of equations, the reference scales of the length, time, velocity, and pressure were respectively, L, L/U_0, U_0, ρU_0^2. As indicated earlier, the relevant nondimensional parameters in the problem emerge to be Re and ω'.

The finite difference procedure adopted here is based on the MAC method (Harlow and Welch, 1965). For the sake of completeness, the methodology is briefly highlighted below. First, the Poisson equation for the pressure is derived by taking the divergence of the Navier-Stokes equations. The time derivative term, which appears in the source term of the Poisson equation, is treated as a correction term such that the incompressibility of the velocity field is satisfied:

$$\Delta_h p^n=-\mathrm{div}_h((\mathbf{V}^n\cdot\mathrm{grad}_h)\mathbf{V}^n)+\mathrm{div}_h\mathbf{V}^n/\Delta t, \tag{6}$$

where the index n stands for the time step, and subscript h indicates that the differential operator is substituted by the corresponding appropriately defined finite difference operator. In order to improve stability, the Navier-Stokes equations are solved by handling the viscous terms fully implicitly and the advection terms semi-implicitly (Kawamura and Kuwahara, 1984):

$$\frac{\mathbf{V}^{n+1}-\mathbf{V}^n}{\Delta t}+(\mathbf{V}^n\cdot\mathrm{grad}_h)\mathbf{V}^{n+1}=-\mathrm{grad}_h p^n+\mathrm{Re}^{-1}\Delta_h\mathbf{V}^{n+1}. \tag{7}$$

The overall accuracy of the scheme is $O(\Delta t,h^2)$, where Δt is the time stepping interval and h the spatial grid size. An upwind modulated third-order scheme (Kawamura and Kuwahara, 1984) is applied for the nonlinear terms. The rest of the spatial derivatives are approximated by the second-order central difference scheme. The mesh system is designed such that $\mathbf{V}$ and p are defined on the same grid points. To solve the pressure Poisson equation, the boundary conditions for the pressure need to be specified. The pressure value on the boundary is prescribed via the Neumann condition; the normal derivatives

of the pressure are approximated by the first-order one-sided difference scheme applied to the Navier-Stokes equations.

The Poisson equation for the pressure and the Navier-Stokes equations are solved iteratively by using a modified SOR method. The algorithm is completely vectorizable. A uniform grid system is employed. The number of grid points, N^2, is 65^2 for the case of Re = 100 and Re = 400, 129^2 for Re = 1000, respectively. The typical cpu time per one cycle of lid oscillation was 14 s, 43 s on the Fujitsu VP-200 supercomputer (513 MFLOPS) for the case of $N = 65$, 129, respectively.

Extensive numerical solutions were secured for a total of 16 cases. However, a large number of additional runs were performed in order to check the grid and Δt-dependency of the solutions. Calculation was continued from the initial state to the time instant which contained approximately 20 cycles of lid motion. In most cases, the periodic state was reached within the first 3 to 6 cycles.

In order to establish the spatial grid convergence, calculations were repeated using several different spatial resolutions, i.e., $h = 1/64$, $1/128$ for Re = 100 and 400; and $h = 1/128$, $1/256$ for Re = 1000. For these tests, $\Delta t = 2\pi/500\omega'$ for Re = 100 and 400; and $\Delta t = 2\pi/1000\omega'$ for Re = 1000. In a similar manner, the Δt-dependency was examined by employing various values of Δt, i.e., from $\Delta t = 2\pi/500\omega'$ to $\Delta t = 2\pi/4000\omega'$ for Re = 400 and $\omega' = 1.0$. At this particular parameter setting, the illustrative results of Soh and Goodrich (1988) are also available. The outcome of these exercises indicated that the discrepancies in the computed velocity and pressure fields were less than 1 percent.

In summary, the above-stated sensitivity tests clearly demonstrated that the solutions are, to a fair degree of accuracy, independent of the grids and time intervals used in the present study. Consequently, in most of the numerical computations, Δt was chosen either as $\Delta t = 2\pi/500\omega'$ or $2\pi/1000\omega'$, and $h = 1/64$ or $/128$. One of the main impetus of the present work is to bring into focus the qualitative character of flow in the various parameter spaces. The values of Δt and h adopted here are, therefore, believed to be adequate in providing useful data to capture the physically illuminating features of the flow. We shall henceforth concentrate on presenting the computational results and proper discussions.

Results and Discussion

First, we shall consider the flows at a relatively small Reynolds number, Re = 100. The representative velocity profiles of u along the vertical center line $x = 0.5$ are exhibited in Fig. 2 for three values of frequencies, $\omega' = 0.1$, 1.0, and 10.0. In order to emphasize the relevance of the length scale $k^{-1}[\equiv (2\nu/\omega)^{1/2}]$, in Fig. 2, the vertical coordinate nondimensionalized by this scale, $y'' = (1-y)/(2\nu/\omega)^{1/2}$, is also indicated. Obviously, the velocity profiles over the half cycle, $0 \le t \le T/2$ and $T/2 \le t \le T$, are symmetric with respect to the center line, because of the symmetry of the domain and the sinusoidal time variation of the lid speed. Here, T is the period of oscillation, i.e., $T = 2\pi/\omega'$.

The effect of the frequency is clearly discernible in the penetration depth, which may be defined to be the vertical distance over which the motion of the top wall has direct influence in the flow field. In the case of an extremely low value of ω', i.e., $\omega' = 0.1$, (see Fig. 2(a)), the effect of the lid motion penetrates a long depth into much of the whole domain of the cavity. The velocity profiles shown at $t = T/4$, $3T/4$ appear to be very similar to the usual steady solution of the driven-cavity flow. The fluid near the top lid is driven in the same direction as that of the lid-motion, and a counter flow exists in the regions near the bottom wall. These velocity structures clearly imply that a primary vortex fills in much of the cavity.

In the case of an extremely high frequency, i.e., $\omega' = 10.0$ (see Fig. 2(c)), the direct effect of the lid motion penetrates into only a small vertical length of the cavity near the top wall; the bulk of the cavity region remains substantially unaffected. The velocity distribution, scaled by using the factor $(\mathrm{Re}\omega')^{-1/2}$, bears strong resemblance to the standard analytic solution of the Stokes' second problem flow in the semi-infinite fluid. This demonstrates that $(2\nu/\omega)^{1/2}$ gives an appropriate scale for the boundary layer thickness in the high-frequency flow regime.

Between these two extreme cases, i.e., when ω' is moderate, $\omega' \simeq O(1)$, a hybrid nature of the above two flows is evident (see Fig. 2(b)). The fluid motion is generally stronger in the upper portion of the cavity. However, the solution displays considerable differences from the classical Stokes' second

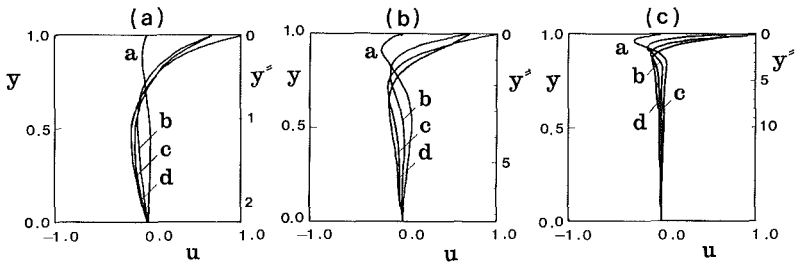

Fig. 2 Profiles of the horizontal velocity u along the vertical center line, $x = 0.5$, during a half cycle of lid-oscillation. Re = 100. $y'' \equiv (1-y)/(2\nu/\omega)^{1/2}$. Times are: a,0; b,$T/8$; c,$T/4$; d,$3T/8$; e,$T/2$, f,$3T/4$, where T is the period of lid-oscillation $T = 2\pi/\omega'$. (a) $\omega' = 0.1$, (b) $\omega' = 1.0$, (c) $\omega' = 10.0$

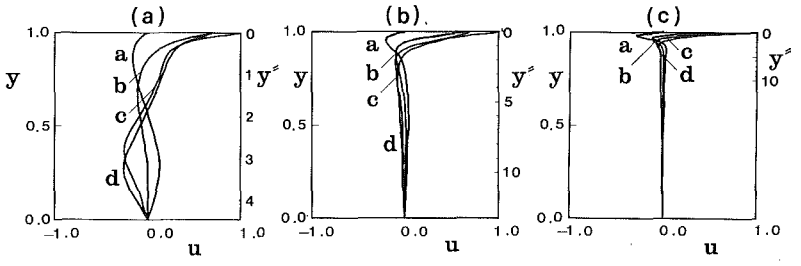

Fig. 3 The same as in Fig. 2 except for Re = 400

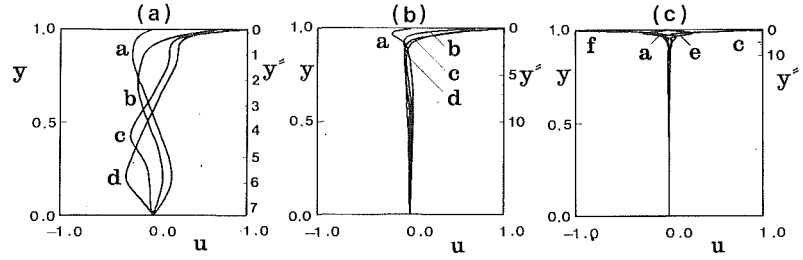

Fig. 4 The same as in Fig. 2 except for Re = 1000

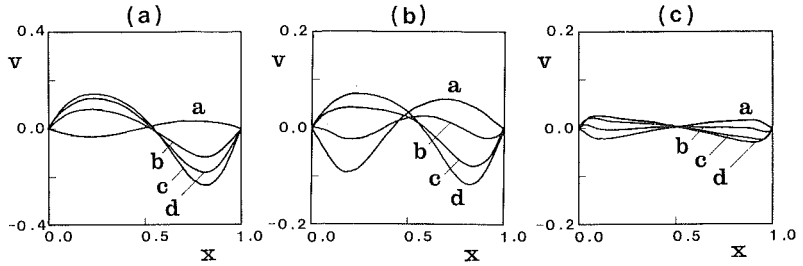

Fig. 5 Profiles of the vertical velocity v along the horizontal mid-height, $y = 0.5$, during a half cycle of lid-oscillation. Re = 100. Note that the difference in the scale of the ordinate between (*a*), (*b*), and (*c*). Times are, *a*,0, *b*,$T/8$, *c*,$T/4$, *d*,$3T/8$, *e*,$T/2$, *f*,$3T/4$, where T is the period of lid-oscillation $T = 2\pi/\omega'$. (*a*) $\omega' = 0.1$, (*b*) $\omega' = 1.0$, (*c*) $\omega' = 10.0$

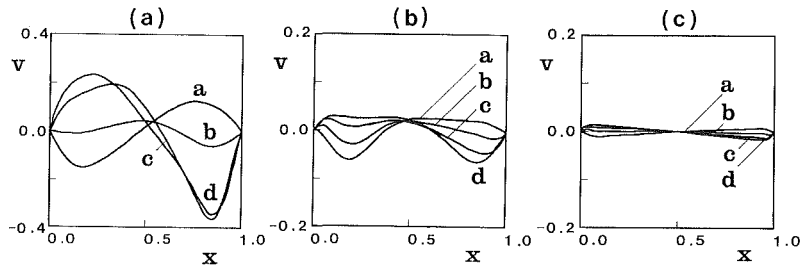

Fig. 6 The same as in Fig. 5 except for Re = 400

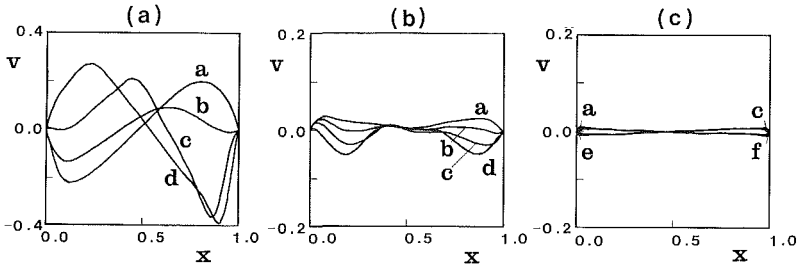

Fig. 7 The same as in Fig. 5 except for Re = 1000

problem. These are attributable to the appreciable advection effects that are apparent in the finite domain.

The overall structure of fluid motion is substantially influenced by another factor, i.e., the Reynolds number. Velocity profiles for a moderate Reynolds number, Re = 400, are shown in Fig. 3. Again, much of the entire flow in the whole cavity is affected by the motion of the lid when ω' is small (see Fig. 3(*a*)). In the low-Re regime, the profiles point to the dominance of the viscous effect (see Fig. 2(*a*)). As the frequency is increased, the effect of the lid-motion prevails over a shallower depth of fluid. In the case of a large frequency, e.g., $\omega' = 10.0$, profiles are qualitatively similar to the case of Re = 100; however, the boundary layer thickness is thinner for Re = 400 than that for Re = 100.

The results for a very high Reynolds number, i.e., Re = 1000, are illustrated in Fig. 4. When the frequency is low, i.e., $\omega' = 0.1$ (see Fig. 4(*a*)), the meandering velocity profile is indicative of complex flow structure due to a significant increase in the nonlinear effects. On the contrary, when the frequency is high, i.e., $\omega' = 10.0$ (see Fig. 4(*c*)), the flow is substantially confined to a thin boundary layer near the top surface. The boundary layer thickness is about 1/3 of that for the case of Re = 100, $\omega' = 10.0$. At a moderate frequency, i.e., $\omega' = 1.0$ (see Fig. 4(*b*)), the effect of the increased advection shows up to produce finer flow structure, which suggests several recirculating vortex regions. In short, for all the Reynolds numbers covered, when ω' is large, the velocity profiles along the vertical center line manifest that the flow is substantially localized to a thin region near the top wall. This point will further be investigated by examining the vertical velocity profiles along the horizontal line, $y = 0.5$.

We shall then proceed to scrutinize the effect of the sidewalls, $x = 0.0$ and $x = 1.0$, on the velocity distribution. The velocity profiles of v along the mid-height, $y = 0.5$, are exhibited in Figs. 5–7, representing the characteristic features at Re = 100, 400, 1000, respectively. As can be seen from Fig. 5(*a*), 6(*a*),

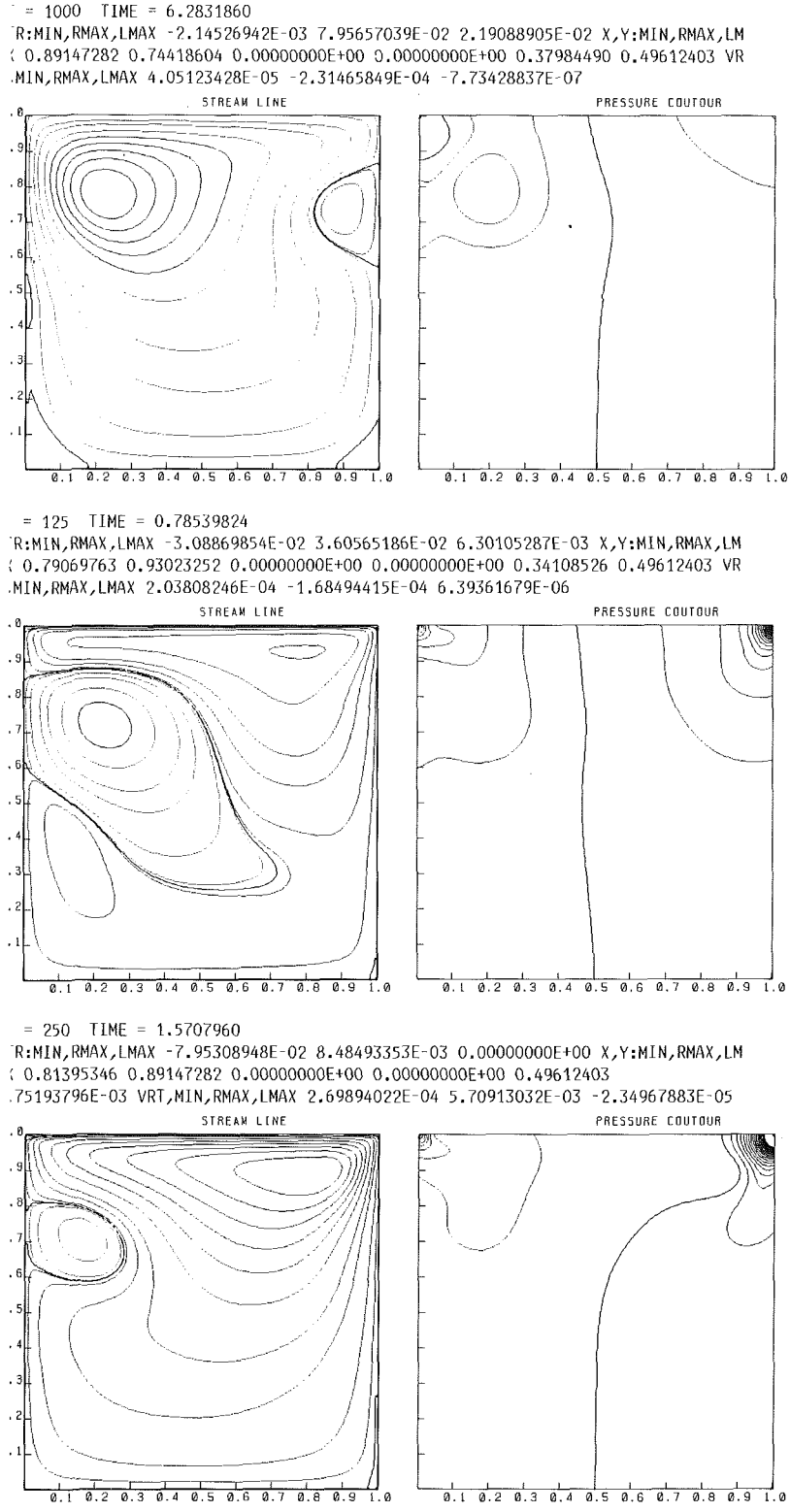

Fig. 8 Representative evolutions of the streamline patterns (on the left column) and pressure contours (on the right column) during a cycle of lid-motion. Re = 400, $\omega' = 1.0$. Times, from top to bottom, are $t = 0$, $T/8$, $T/4$, $3T/8$, $T/2$, $5T/8$, $3T/4$, $7T/8$. The contour values of streamfunction [$\psi \equiv \int\int \omega dy$] are $\psi = 0$, $\pm 1^{-5}$, $\pm 1^{-4}$, $\pm 1^{-3}$, $\pm 1^{-2}$, ± 0.02, ± 0.03, ..., ± 0.12. The contour values of pressure are $p = 0$, $\pm$, 0.0075, ± 0.015, ..., ± 0.3

7(*a*), the magnitude of the maximum v in the low-frequency regime is generally comparable to that of the steady state cavity flow. On the contrary, in the case of a high frequency (see Fig. 5(*c*), 6(*c*), 7(*c*) for $\omega' = 10.0$), the v-velocities are very small. This is in support of the previous assertion that, in the high frequency limit, the flows are predominantly in the x-direction and concentrated only in a narrow strip in the vicinity of the top lid; in the interior core, the fluid is nearly stagnant. Therefore, in the high-frequency limit, the flow resembles the solution of the Stokes' second problem which admits nonzero

= 375 TIME = 2.3561945
R:MIN,RMAX,LMAX -0.10183418 5.94686344E-03 3.09070813E-09 X,Y:MIN,RMAX,LMAX
.79844958 0.83720928 0.00000000E+00 0.00000000E+00 2.32558139E-02
.55038759E-02 VRT,MIN,RMAX,LMAX 2.72115692E-04 3.83273978E-03 -1.29931195E-08

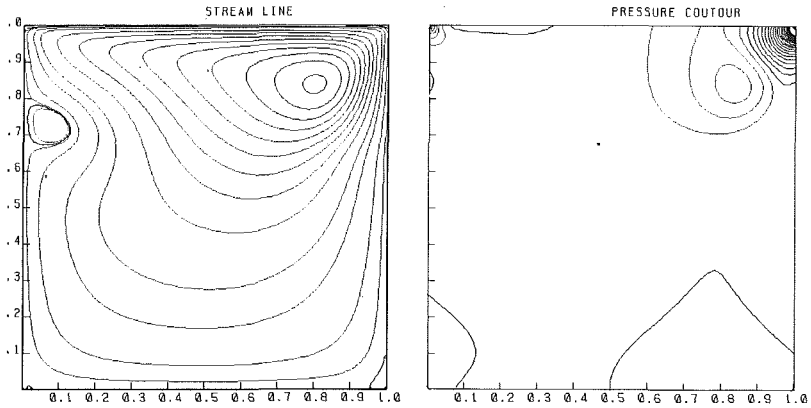

= 500 TIME = 3.1415930
R:MIN,RMAX,LMAX -8.01535249E-02 1.92800397E-03 9.55737596E-06 X,Y:MIN,RMAX,LM
(0.77519375 0.78294569 0.00000000E+00 0.00000000E+00 5.42635657E-02
.20155036E-02 VRT,MIN,RMAX,LMAX 2.32653751E-04 -3.69386544E-05

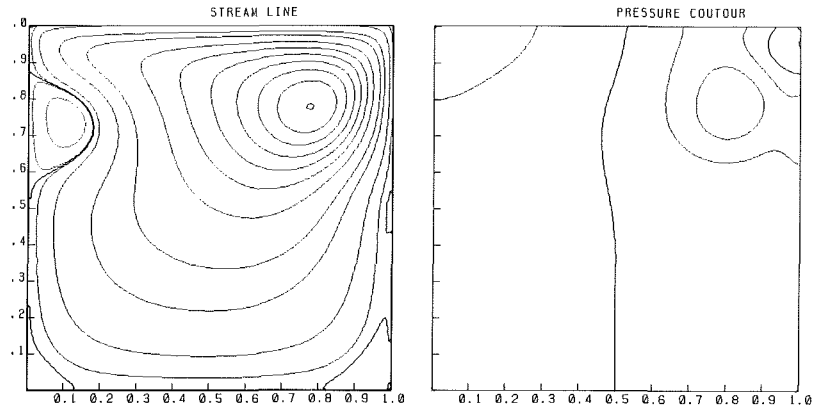

= 625 TIME = 3.9269915
R:MIN,RMAX,LMAX -3.85396779E-02 3.05870287E-02 2.85230298E-03 X,Y:MIN,RMAX,LM
(0.77519375 0.72868216 0.00000000E+00 0.00000000E+00 0.20930231 0.49612403 VR
.MIN,RMAX,LMAX 1.79137103E-04 -1.99351460E-04 3.17771082E-06

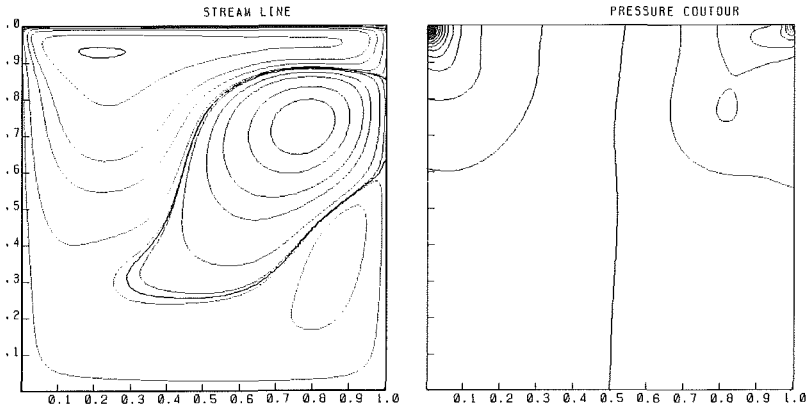

Fig. 8 (cont.)

u and $v=0$. The vanishingly small values of v in the bulk of the flow field lead to the observations that, in this high-frequency limit, the existence of the sidewalls has little effect on the global flow patterns. This fact can be easily understood when we recall that the high-ω' limit implies that the ratio of $(\nu/\omega)^{1/2}$ to L is very small, i.e., $(\nu/\omega)^{1/2}/L \equiv (\omega' \mathrm{Re})^{-1/2} \ll 1$. Alternatively stated, the impact of the oscillating top lid penetrates only a small distance into the fluid.

Between these extreme cases, when $\omega' \simeq O(1)$ (see Fig. 5, 6, 7(b)), the effect of the sidewalls is felt through much of the whole horizontal width of the cavity. These figures also indicate that the whole cavity region is occupied by a single main vortex at times when the lid speed is near its maximum value, i.e., $t \simeq T/4$ (see curves b in these figures).

However, for moderate frequencies, $\omega' \sim O(1)$, the character of flow shows considerable differences as Re varies. When Re is low (see Fig. 5(b) for $\mathrm{Re}=100$), the v–x plots generally indicate that, in the left (right) half of the cavity the flows are

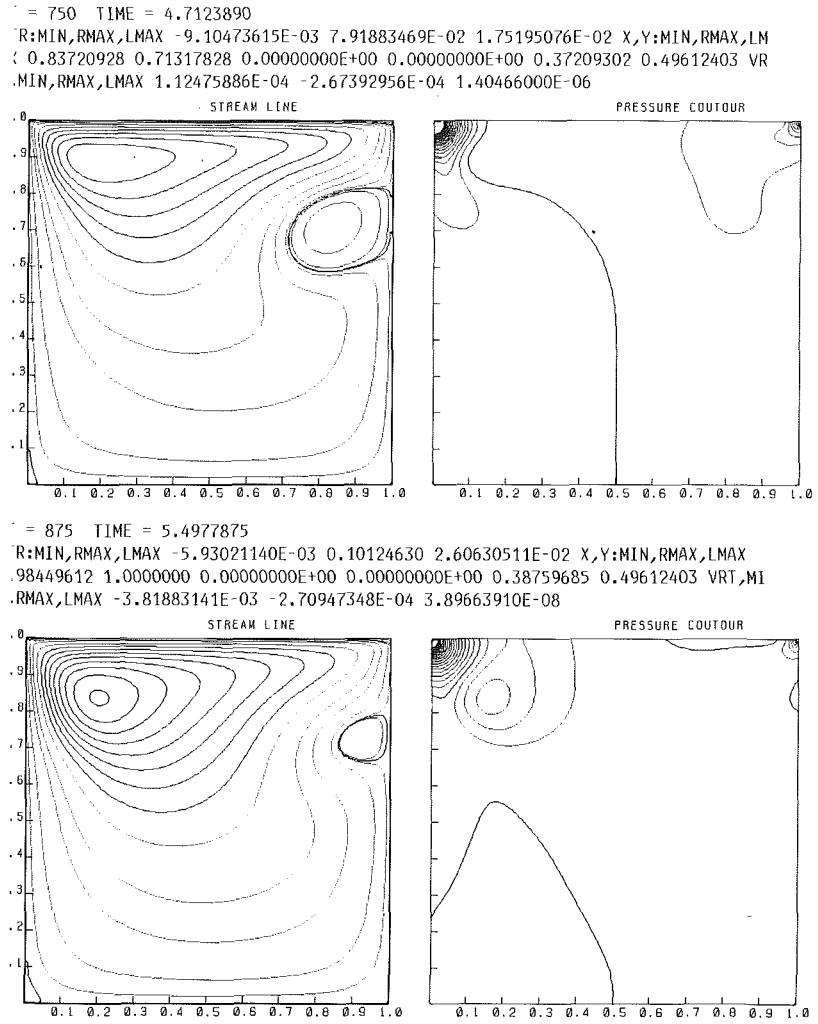

Fig. 8 (cont.)

generally upward (downward). This suggests that, in the bulk of the interior, a single clockwise-rotating cell exists. On the contrary, when Re is large (see Fig. 7(*b*) for Re = 1000), the v–x plots display more complicated shapes. These imply that the flow in the interior can be characterized by a possible multicell structure.

In order to visualize the overall flow patterns, the contour lines of stream function have been constructed, and only a typical picture is shown in Fig. 8 [Re = 400, $\omega' = 1.0$]. In the figures, the frames in the left column denote the time sequences of the stream function plots, and the frames in the right column show the evolution of the pressure field. Careful inspection of these figures clearly points to the following observations. Firstly, as was detectable in the velocity profiles, in the case of low frequencies, $\omega' \ll O(1)$, the whole cavity region is occupied by a primary vortex. This primary vortex quickly shrinks in the late stage toward the first half-cycle, and then is replaced by a counter rotating vortex in the second half-cycle. Secondly, as ω' increases, the differences in the streamline patterns between the low-Re and high-Re flows are noted especially in the motions of fluid relative to the lid-motion. It is evident in the streamlines for Re = 100 that a counter rotating vortex persists for about $T/8$ period after the completion of a half-cycle and then disappears afterward. Corresponding figures for Re = 400 (see Fig. 8) indicate that the counter rotating vortex region survives the next half cycle. The recirculating region that was created during the previous half cycle continues to exist in the vicinity of the top lid and the sidewall; the size

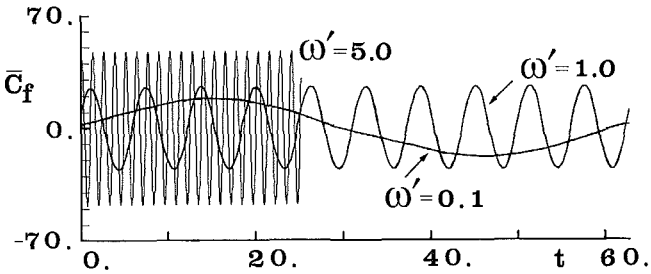

Fig. 9 A representative time history of force coefficient, C_f. Re = 400, $\omega' = 0.1$, 1.0, 5.0 (for the case of $\omega' = 5.0$, only the first 20 cycles are shown)

of this separate cell decreases with time. When the Reynolds number is further increased, the size of the counter rotating region increases, and owing to the decreased viscosity effect, a finer flow structure is observed. For example, for Re = 1000, $\omega' = 1.0$, at $t = T/8$, $5T/8$, the whole cavity domain can be described as a combination of four counter rotating vortices of nearly the same size.

The pressure contour plots are now examined. For all the computed results, the pressure difference is large near the upper sliding wall. The pressure field in the lower portion of the cavity manifests a fair degree of uniformity. The pressure distribution is nearly symmetric with respect to the center line $x = 0.5$ when ω' is large. A considerable build-up of pressure

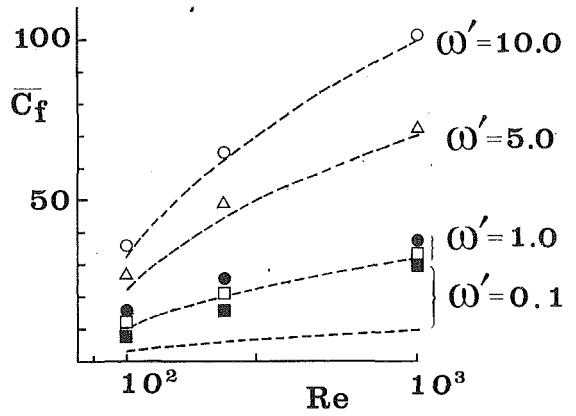

Fig. 10 The amplitude of force coefficient, $\overline{C}_f$ as a function of Re. The dotted lines indicate the solutions based on Stokes's second problem in the infinite domain. The symbols denote the present numerical results. ■,$\omega'=0.1$; □,$\omega'=0.5$; ●,$\omega'=1.0$; △,$\omega'=5.0$; ○,$\omega'=10.0$

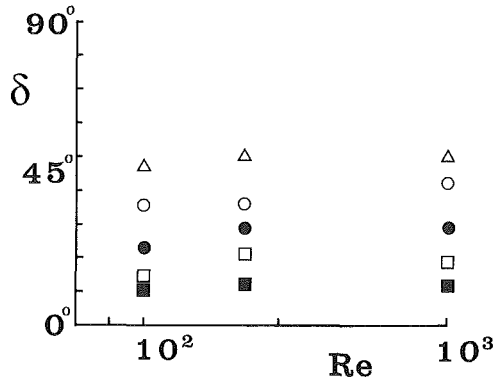

Fig. 11 The calculated phase shift δ as a function of Re. The symbols denote the present numerical results. ■,$\omega'=0.1$; □,$\omega'=0.5$; ●,$\omega'=1.0$; △,$\omega'=5.0$; ○,$\omega'=10.0$

is observed in the downstream corner, where the sliding lid abuts the sidewall.

We shall now consider the behavior of the force which is necessary to maintain the lid motion, and the phase shift between the lid motion and the force coefficient C_f, where C_f is defined as

$$C_f = \int_0^1 \left.\frac{\partial u}{\partial y}\right|_{y=1} dx. \tag{8}$$

Figure 9 is a typical time history of $C_f[\equiv \overline{C}_f \sin(\omega' t - \delta)]$ at three different frequencies, i.e., low, moderate, and high-frequency at Re = 400. As ω' increases, $\overline{C}_f$ increases. It seems that C_f executes sinusoidal oscillation for moderate to high frequencies, i.e., $\omega' \gg 1$; however, a small deviation of the C_f curve from a pure sine-wave is noted for low-frequency flows, i.e., $\omega' = 0.1$. The solid lines of Fig. 10 depict the computational results of the amplitude of force coefficient, $\overline{C}_f$, for the finite and closed cavity as a function of Re. In Fig. 10, the results of the analytical solution of the Stokes' second problem in the finite domain are plotted as dotted lines. As can be anticipated, for high-frequency flows, the calculated values of $\overline{C}_f$ for finite geometry are in close qualitative agreement with the analytic solutions of infinite domain. For moderate and low-frequency flows, i.e., $\omega' = 1.0 \sim 0.1$, $\overline{C}_f$ for the finite square cavity is greater than that of Stokes' second problem, due principally to the pronounced effects stemming from the constraints of finite and closed geometry. It is noteworthy that, for low ω', the discrepancy between the computed $\overline{C}_f$ and the analytical prediction of the infinite plate is substantial. This reinforces the argument that, for the motions in closed geometry, the flow characteristics are qualitatively dissimilar to the flow about an infinite plate when ω' is very small. This underscores the limitations of the applicability of the model of the classical Stokes' second problem to more realistic cavity-flow situations.

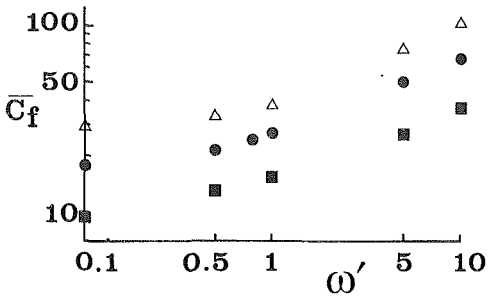

Fig. 12(*a*) Variation of $\overline{C}_f$ with ω'. The symbols denote the present numerical results. ■,Re = 100; ●,Re = 400; △,Re = 1000

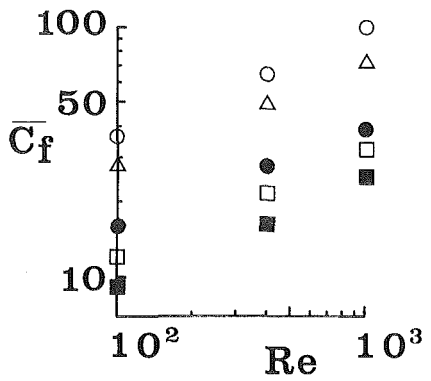

Fig. 12(*b*) Variation of $\overline{C}_f$ with Re. The symbols denote the present numerical results. ■,$\omega'=0.1$; □,$\omega'=0.5$; ●,$\omega'=1.0$; △,$\omega'=5.0$; ○,$\omega'=10.0$

Figure 11 displays the variations of the calculated phase shift δ with Re. The phase lag for high-frequency flows approaches 45 deg, which is the limiting value of the Stokes' solution. In the high-frequency regime, the approach of δ to the limiting value of 45 deg is oscillatory with ω'. On the contrary, for cases with $\omega' \leq O(1)$, the phase shift increases monotonically as ω' increases. As is discernible in Fig. 11, the dependency of δ on Re is very weak for all the ranges of ω' considered.

In order to gain an improved understanding of the behavior of C_f, Fig. 12 demonstrates the separate effects of Re and ω' on $\overline{C}_f$. The well-known Stokes' second problem gives the relationship, $\overline{C}_f = \sqrt{2}U_0 k/(U_0/L) = L(\omega/\nu)^{1/2} = (\mathrm{Re}\omega')^{1/2}$, and $\delta = 45$ deg. The numerical results shown in Fig. 12(*a*) are supportive of the validity of the above relationships, $\overline{C}_f \propto (\omega')^{1/2}$, $\delta \simeq 45$ deg in the high-frequency regime, i.e., $\omega' \geq 5.0$. In the low-frequency range, however, i.e., $\omega' \leq 5.0$, the increase of $\overline{C}_f$ with ω' is milder than for the high-frequency regime. The rate of increase of $\overline{C}_f$ with ω', as manifested in the slopes of the curves in Fig. 12(*a*), appears to be insensitive to Re. The computed results of $\overline{C}_f$, plotted against Re, are shown in Fig. 12(*b*). Inspection of these data leads to an approximate relation between $\overline{C}_f$ and Re as $\overline{C}_f \propto \mathrm{Re}^{1/2}$ for all the values of ω'.

It is recalled that, in Fig. 11, δ is fairly constant with Re, for a given value of ω'. Therefore, summarizing the results of Figs. 11 and 12(*b*), the force coefficient C_f may be characterized as follows: the amplitude $\overline{C}_f$ is proportional to $\mathrm{Re}^{1/2}$, and the phase lag δ is nearly constant with Re, for a given value of ω'.

Summary

Fluid motion within a square cavity with an oscillating upper lid has been examined. It is found that the flow bears similarity

to the Stokes' second problem when the frequency of lid-motion is large, i.e., $\omega' \geq 5.0$, for the range of the Reynolds numbers considered, $10^2 \leq \mathrm{Re} \leq 10^3$. Accordingly, the amplitude of the force that is necessary to maintain the lid-motion is well approximated by $\overline{C}_f \sim (\mathrm{Re}\omega')^{1/2}$ when $\omega' \gg O(1)$.

When the frequency is small, the entire cavity is affected by the lid motion. Between these two extreme cases, i.e., when $\omega' \sim O(1)$, owing to the presence of the sidewalls, several vortices are observed as the Reynolds number is increased. The phase lag δ of the force relative to the lid motion does not vary much as Re changes.

The scope of the present study has been confined to the motion of a viscous incompressible fluid driven by a mechanical means. As an expanded, parallel problem, the flows driven by both mechanical and thermal means within a closed container shall provide a useful flow model. The flow driven by the oscillating upper lid with a stable temperature stratification within the cavity will be addressed in the subsequent papers.

References

Benjamin, A. S., and Denny, V. E., 1979, "On the Convergence of Numerical Solutions for Two-Dimensional Flows in a Cavity at Large Re," *Journal of Computational Physics*, Vol. 33, pp. 340–358.

Bozeman, J. D., and Dalton, C., 1973, "Numerical Study of Viscous Flow in a Cavity," *Journal of Computational Physics*, Vol. 12, pp. 348–363.

Ghia, U., Ghia, K. N., and Shin, C. T., 1982, "High-Re Solutions for Incompressible Flow Using the Navier-Stokes Equations and a Multigrid Method," *Journal of Computational Physics*, Vol. 48, pp. 387–411.

Harlow, F. H., and Welch, J. E., 1965, "Numerical Calculation of Time-Dependent Viscous Incompressible Flow of Fluid With Free Surface," *Physics of Fluids*, Vol. 8, pp. 2182–2187.

Iwatsu, R., Ishii, K., Kawamura, T., Kuwahara, K., and Hyun, J. M., 1989, "Numerical Simulation of Three-Dimensional Flow Structure in a Driven-Cavity," *Fluid Dynamics Research*, Vol. 5, pp. 173–189.

Iwatsu, R., Hyun, J. M., and Kuwahara, K., 1990, "Analyses of Three-Dimensional Flow Calculations in a Driven Cavity," *Fluid Dynamics Research*, Vol. 6, pp. 91–102.

Kawamura, K., and Kuwahara, K., 1984, "Computation of High Reynolds Number Flow Around a Circular Cylinder With Surface Roughness," AIAA Paper 84-0340 (unpublished).

Ozawa, S., 1975, "Numerical Studies of Steady Flow in a Two-Dimensional Square Cavity at High Reynolds Numbers," *Journal of Physical Society of Japan*, Vol. 38, pp. 889–895.

Pan, F., and Acrivos, A., 1967, "Steady Flows in Rectangular Cavities," *Journal of Fluid Mechanics*, Vol. 28, pp. 643–655.

Schlichting, H., 1979, *Boundary-Layer Theory*, Seventh English Edition, Translated by Kestin, J., MacGraw-Hill, New York, pp. 93–94.

Schreiber, R., and Keller, H. B., 1983, "Driven Cavity Flow by Efficient Numerical Technique," *Journal of Computational Physics*, Vol. 49, pp. 310–333.

Soh, W. H., and Goodrich, J. W., 1988, "Unsteady Solution of Incompressible Navier-Stokes Equations," *Journal of Computational Physics*, Vol. 79, pp. 113–134.

Tuann, S. Y., and Olson, M. D., 1978, "Review of Computing Methods for Recirculating Flows," *Journal of Computational Physics*, Vol. 29, pp. 1–19.

L. C. Thomas
Knoxville, TN 37929

S. M. F. Hasani
Graduate Student,
The University of Akron,
Akron, Ohio

Equilibrium Boundary Layers—A New Wall/Outer Variable Perspective

Introduction

The existence of turbulent boundary layers with approximate outer region similarity was discovered in the context of non-transpired incompressible flows by Clauser (1954), and has been substantiated for a wide range of adverse and favorable pressure gradients by Townsend (1961), Mellor and Gibson (1966), Bradshaw (1966), Ludwieg and Tillmann (1950), Herring and Norbury (1967), and others. The occurence of equilibrium boundary layers has also been convincingly demonstrated in the experimental work by Andersen et al. (1972).

Equilibrium boundary layers are associated with constant values of the pressure gradient parameter β,

$$\beta = \frac{\delta_1}{\bar{\tau}_0}\frac{d\bar{P}}{dx} \tag{1}$$

and blowing parameter B_M,

$$B_M = \frac{\rho \bar{v}_0 U_\infty}{\bar{\tau}_0} \tag{2}$$

and with distributions in free-stream velocity U_∞ and transpiration rates $\bar{v}_0$ of the form

$$U_\infty = U_{\infty_1}\left(\frac{x-X_0}{x_1-X_0}\right)^m \quad \text{and} \quad F = F_1\left(\frac{x-X_0}{x_1-X_0}\right)^{m_0} \tag{3,4}$$

where $F(=\bar{v}_0/U_\infty)$, m, U_{∞_1}, m_0, F_1, x_1, X_0, are all independent of x. In this connection, the Clauser shape factor G,

$$G = \frac{U_\infty^+(H-1)}{H} = \frac{\int_0^\infty (u^+ - U_\infty^+)^2 d\xi}{\int_0^\infty (u^+ - U_\infty^+) d\xi} \tag{5}$$

has been reported to be essentially independent of x and a unique function of $\beta + B_M$ for equilibrium flows; ξ represents the dimensionless distance y/δ.

Equilibrium boundary layers are also characterized by velocity defect profiles $(u^+ - U_\infty^+)$ that are essentially independent of x within the outer region when expressed in terms of x, ξ coordinates; that is,

$$\frac{\partial}{\partial x}(u^+ - U_\infty^+) = 0 \tag{6}$$

where $u^+ = \bar{u}/U^*$, $U_\infty^+ = U_\infty/U^*$ and $U^* = \sqrt{\bar{\tau}_0/\rho}$.

Contributed by the Fluids Engineering Division for publication in the JOURNAL OF FLUIDS ENGINEERING. Manuscript received by the Fluids Engineering Division February 14, 1991. Associate Technical Editor: D. M. Bushnell

The purpose of this paper is to establish an additional useful characteristic of equilibrium turbulent boundary layers.

New Wall/Outer Variable Perspective

The integral momentum equation provides a basis for characterizing the behavior of equilibrium boundary layers in terms of the parameters β and B_M. The form of the integral momentum equation that contains these parameters is given for uniform density by [after Kays and Crawford (1966)]

$$\frac{d}{dx}(U_\infty^2 \delta_2) = \frac{\bar{\tau}_0}{\rho}(1 + \beta + B_M) \tag{7}$$

With β and B_M constant, this equation indicates that the ratio of axial gradient in momentum flux deficit within the boundary layers to wall shear stress is constant. This equilibrium condition is also known to give rise to similiar laminar boundary layers.

In addition to providing an indication of the significance of constant values of β and B_M, Eq. (7) provides the basis for establishing a new wall/outer variable shear velocity U^{**} of the form

$$U^{**} = U^*(1 + \beta + B_M)^{1/2} \tag{8a}$$

or

$$U^{**} = \left[\frac{\bar{\tau}_0}{\rho} + \frac{\delta_1}{\rho}\frac{d\bar{P}}{dx} + \bar{v}_0 U_\infty\right]^{1/2} \tag{8b}$$

This defining equation for U^{**} represents a generalization of the pressure velocity $u_P = [\delta_1(dP/dx)/\rho]^{1/2}$ which was introduced by Mellor and Gibson (1966). Whereas u_P was found to be useful for equilibrium flows at or near separation, U^{**} proves to be capable of characterizing equilibrium boundary layers for a wide range of conditions, with the only restriction being $\beta + B_M > -1$. Because $\beta + B_M$ are independent of x for equilibrium boundary layers, the velocity defect can also be characterized by

$$\frac{\partial}{\partial x}(u^{++} - U_\infty^{++}) = 0 \tag{9}$$

where the wall/outer variable dimensionless velocities are defined by

$$u^{++} = \frac{\bar{u}}{U^{**}} \quad \text{and} \quad U_\infty^{++} = \frac{U_\infty}{U^{**}} \tag{10a,b}$$

Standard velocity defect profiles associated with the equilibrium flows reported by Andersen et al. (1972) are shown in Figs. 1(*a*) and 2(*a*). These figures clearly indicate that the

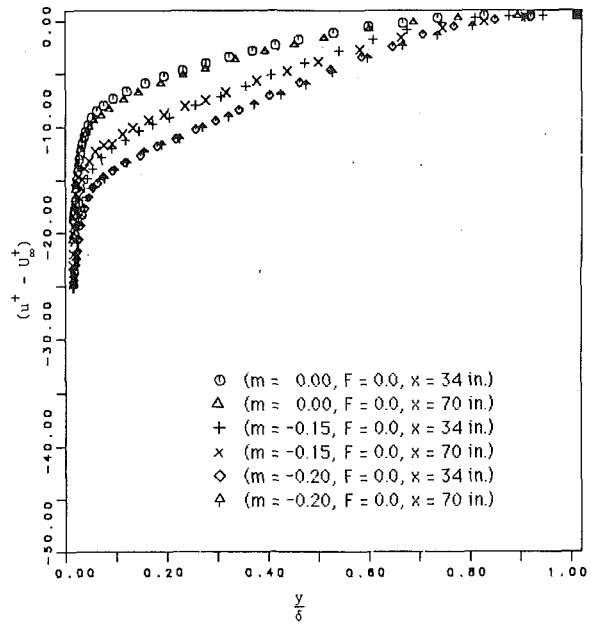

Fig. 1(*a*) Standard velocity defect profiles for nontranspired equilibrium boundary layers of Andersen et al. (1972)

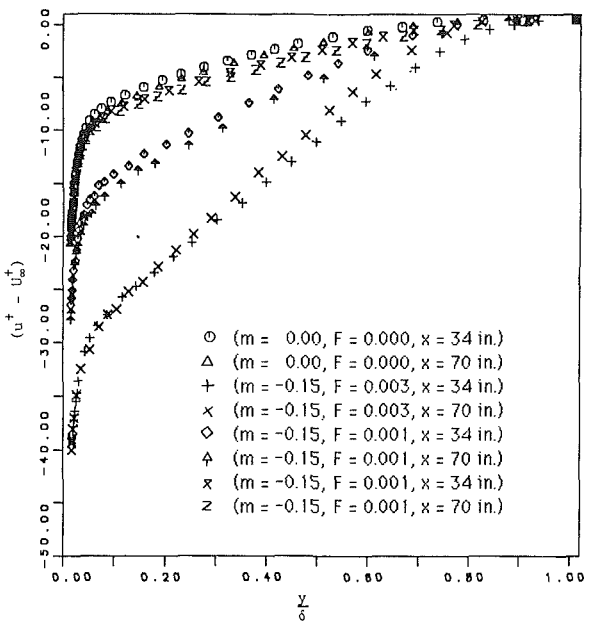

Fig. 2(*a*) Standard velocity defect profiles for transpired equilibrium boundary layers of Andersen et al. (1972)

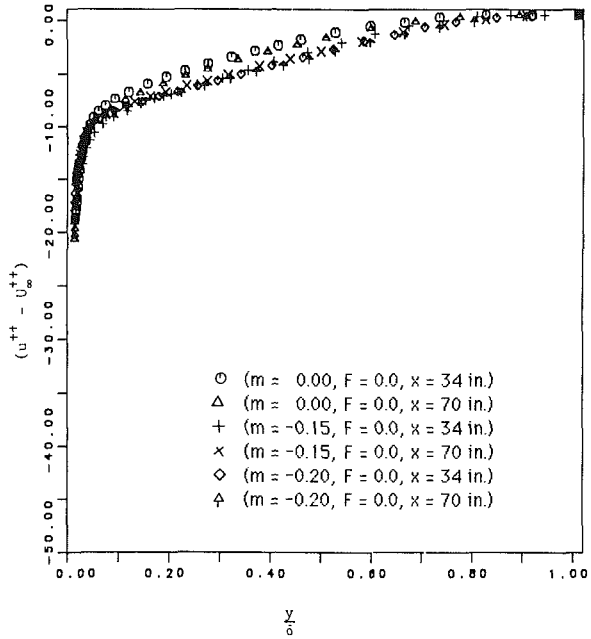

Fig. 1(*b*) Wall/outer variable velocity defect profiles for nontranspired equilibrium boundary layers of Andersen et al. (1972)

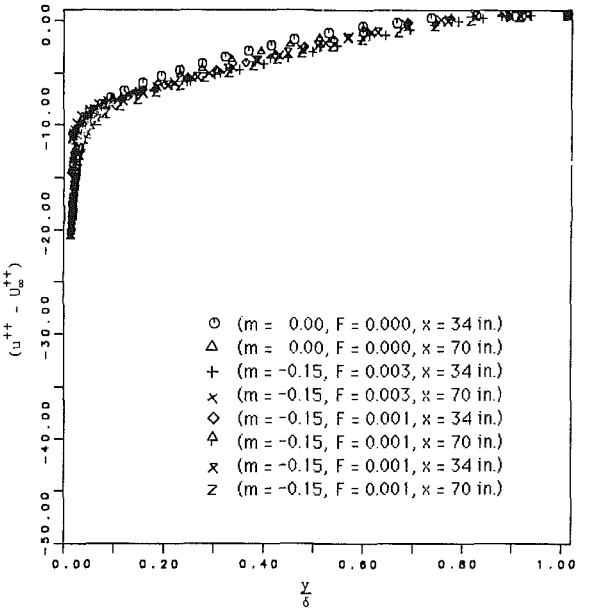

Fig. 2(*b*) Wall/outer variable velocity defect profiles for transpired equilibrium boundary layers of Andersen et al. (1972)

Nomenclature

B_M = $\rho\overline{v}_0 U_\infty/\overline{\tau}_0$, blowing parameter
F = $\overline{v}_0/U_\infty$, blowing fraction
G = Clauser shape factor
H = δ_1/δ_2, shape factor
m = exponent in Eq. (3)
m_0 = exponent in Eq. (4)
$\overline{u}$ = mean velocity in x-direction
U_∞ = free-stream velocity
U^* = $\sqrt{\overline{\tau}_0/\rho}$, friction velocity
U^{**} = $\sqrt{(\overline{\tau}_0/\rho)(1+\beta+B_M)}$, wall/outer variable shear velocity
u^+ = $\overline{u}/U^*$
U_∞^+ = U_∞/U^*
u^{++} = $\overline{u}/U^{**}$
U_∞^{++} = U_∞/U^{**}
$\overline{v}_0$ = mean transpiration velocity
x = streamwise coordinate
x_1 = reference location in Eqs. (3) and (4)
X_0 = virtual origin of turbulent boundary layer
y = vertical coordinate
y^+ = yU^*/ν
$d\overline{P}/dx$ = pressure gradient
β = $\delta_1(d\overline{P}/dx)/\overline{\tau}_0$, pressure gradient parameter
δ = boundary layer thickness
δ_1 = displacement thickness
δ_2 = momentum thickness
ξ = y/δ
$\overline{\tau}_0$ = mean shear stress at wall
ρ = density

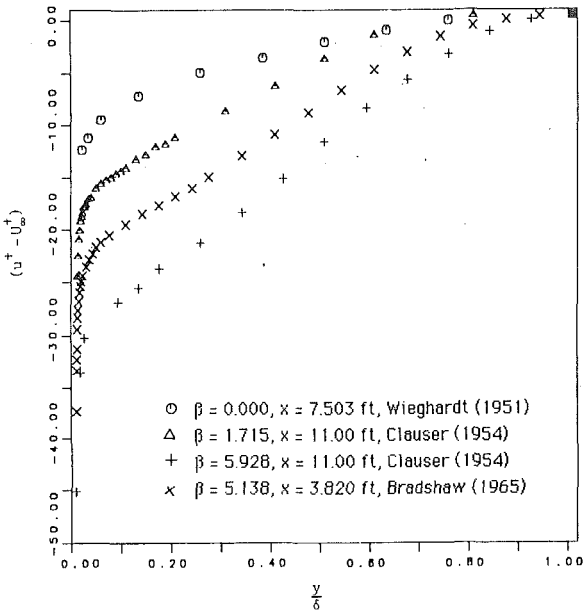

Fig. 3(*a*) Standard velocity defect profiles for nontranspired boundary layers from 1968 Stanford Conference

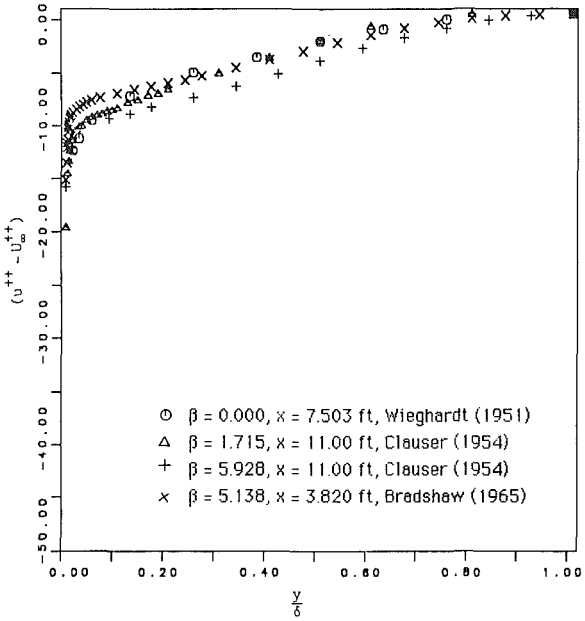

Fig. 3(*b*) Wall/outer variable velocity defect profiles for nontranspired boundary layers from 1968 Stanford Conference

distributions in velocity defect $(u^+ - U_\infty^+)$ within the outer region are independent of x. These data are also shown in Figs. 1(b) and 2(b) in the context of the alternate velocity defect $(u^{++} - U_\infty^{++})$ format. Notice that the use of the wall/outer variable shear velocity U^{**} results in equilibrium velocity defect profiles that are essentially congruent throughout the outer region.

Figure 3 presents the data for some of the earlier classic nontranspired flows selected from the AFOSR-IFP-Stanford Conference Proceedings (1968) in the standard velocity defect and wall/outer variable velocity defect formats. As in the case of the more recent data shown in Figs. 1 and 2, it is observed that the wall/outer variable velocity defect curves fall along a very narrow band.

Conclusion

To conclude, this paper demonstrates that the equilibrium boundary layers can be effectively characterized in terms of the wall/outer variable shear velocity U^{**}. The use of this wall/outer variable perspective results in velocity defect profiles [i.e., $(u^{++} - U_\infty^{++})$ versus (y/δ)] that are essentially independent of β and B_M as well as x for equilibrium boundary layers. It follows that this dimensionless representation of turbulent velocity distributions may provide a convenient indication of the degree of departure from equilibrium and be useful in estimating the rate of return to equilibrium. Finally, because $y^{++} = yU^{**}/\nu$ is finite as $\bar{\tau}_0$ approaches zero, this dimensionless wall/outer variable may prove to be more useful than the standard wall variable $y^+ = yU^*/\nu$ in the analysis of near separating boundary layers.

Acknowledgment

The authors wish to acknowledge the support provided for this study by King Fahd University of Petroleum and Minerals.

References

Andersen, P. S., Kays, W. M., and Moffat, R. J., 1972, "The Turbulent Boundary Layer on a Porous Plate: An Experimental Study of the Fluid Mechanics for Adverse Free-Stream Pressure Gradients," Department of Mechanical Engineering, Stanford University, Stanford, Calif.

Andersen, P. S., Kays, W. M., and Moffat, R. J., 1975, "Experimental Results for the Transpired Turbulent Boundary Layer in an Adverse Pressure Gradient," *Journal of Fluid Mechanics*, Vol. 69, pp. 353-375.

Bradshaw, P., and Ferriss, D., 1965, "The Response of a Retarded Equilibrium Turbulent Boundary Layer to the Sudden Removal of Pressure Gradient," NPL Aero Report 1145.

Bradshaw, P., 1966, "The Turbulence Structure of Equilibrium Boundary Layers," NPL Aero Report 1184.

Clauser, F., 1954, "Turbulent Boundary Layers in Adverse Pressure Gradients," *Journal of Aeronautical Sciences*, Vol. 21, pp. 91-108.

Coles, D. E., and Hirst, E. A., 1968, "Computation of Turbulent Boundary Layers," AFOSR-IFP-Stanford Conference Proc., Vol. II, Department of Mechanical Engineering, Stanford University, Stanford, Calif.

Herring, H., and Norbury, J., 1967, "Some Experiments on Equilibrium Turbulent Boundary Layers in Favorable Pressure Gradients," *Journal of Fluid Mechanics*, Vol. 27, pp. 541-549.

Ludwieg, H., and Tillmann, W., 1950, "Investigations of the Wall Shearing Stress in Turbulent Boundary Layers," NACA 1285; Translated from *Ing. Arch.*, Vol. 17, 1949, pp. 288-299.

Mellor, G. L., and Gibson, D. M., 1966, "Equilibrium Turbulent Boundary Layers," *Journal of Fluid Mechanics*, Vol. 24, pp. 225-253.

Townsend, A. A., 1961, "Equilibrium Layers and Wall Turbulence," *Journal of Fluid Mechanics*, Vol. 11, pp. 97-120.

Wieghardt, K., and Tillmann, W., 1951, "On the Turbulent Friction Layer for Rising Pressure," NACA TM 1314; Translated from U & M Report 6617, 1944.

Kays, W. M., and M. E. Crawford, *Convective Heat and Mass Transfer*, 2nd ed., McGraw-Hill, New York, 1980.

Decay of Temperature Variance in the Presence of Nonhomogeneous Strain

H. R. Rahai
Mechanical Engineering Department,
California State University, Long Beach
Long Beach, CA 90840

J. C. LaRue
Department of Mechanical Engineering,
University of California, Irvine,
Irvine, CA 92717

The effect of nonhomogeneous strain caused by two-dimensional objects on single point statistical properties of the turbulent velocity and turbulent scalar (temperature) and their cross moments are investigated experimentally. The heated turbulent flow is produced by means of a biplane array of round rods and a biplane array of heated, thin wires placed downstream of the turbulence producing grid. The experiments are performed for three different ratios of the integral scale, L_0, to the object dimension, D, of 0.38, 1.90 and 3.1. Measurements of time resolved temperature and longitudinal and transverse velocity components are obtained using a triple wire probe consisting of a cold wire and two hot wires. Results indicate that, for $L_0/D = 1.9$ and 3.1, the decay rate of temperature variance is nearly the same in the region of maximum shear stress (mss) and near the centerline. However, the decay rate in these regions is less than the decay rate of the temperature variance outside the cylinder wake. For $L_0/D = 0.38$, the decay rates of temperature variance are the same in the regions of mss, near the centerline and outside the wake. Transverse growth of the wake is found to be either increased or nearly unchanged depending on, respectively, whether the free stream integral scale is larger or less than that of the wake.

1 Introduction

Mixing and dispersion of a turbulent passive scalar downstream of an object are of both fundamental and applied interest. For example, understanding of this type of flow is critical to the safe operation of fuel rods in nuclear reactors.

There have been numerous experimental and theoretical studies on mixing of temperature variance in the wake of a heated cylinder or unheated cylinder in a passively stratified field. Examples are, Durbin et al. (1982), Freymuth and Uberoi (1971), Alexopoulos and Keffer (1977), LaRue and Libby (1974), and Lumley (1975). However, in these studies, the effect of free-stream turbulence intensity or integral length scale on the mixing of the passive scalar has not been determined. The object of the present experimental study is to examine the simple case of mixing of a turbulent scalar in the wake of an unheated cylinder placed in a nearly homogeneous, isotropic and heated turbulent flow for different external turbulence intensities and integral scales.

2 Background

Symes and Fink (1977) study the effects of constant free-stream turbulence intensity of 3.5 percent with different axial integral length scales, on the unheated flow past cylinders. They use two different turbulence producing grids with mesh spacing of, respectively, 1.53 and 10 cm with grid Reynolds number of, respectively, 10^4 and 6.6×10^4. Cylinder Reynolds numbers are 0.67×10^4 and 1.35×10^4. Their results show that when the length scale of the external turbulence is larger than the diameter of the cylinder, the external turbulence causes a decrease in the mean defect velocity and axial (the term axial refers to the streamwise direction) integral length scales, an increase in the axial normal stress and wake half width and the moving equilibrium is reached at smaller axial distances than those of the conventional wake. However, when the length scale of the external turbulence is nearly the same as the diameter of the cylinder, the external turbulence has negligible effect on the wake flow.

Seely et al. (1975) study the effects of free stream turbulence of 7 and 10 percent on spheres by using the flash photolysis technique at Reynolds numbers based on sphere diameter of 700 and 3200. In their experiments, the level of background intensity is changed by changing the spacing between a turbulence producing grid and the sphere. Their results show that the size of the wake is progressively reduced with increasing free stream intensity. However, neither the position of the separation point, nor the attached boundary layer are affected by the background intensity. They conclude that free stream intensity causes enhancement of momentum transfer in the wake which results in smaller drag.

Zukauskas and Ziugzda (1985) study the effect of background intensity on the separation point of cylinders. Their results show that at the subcritical Reynolds number of 5.12×10^4, turbulence intensity of 0.5 percent does not change the

Contributed by the Fluids Engineering Division for publication in the JOURNAL OF FLUIDS ENGINEERING. Manuscript received by the Fluids Engineering Division October 30, 1990. Associate Technical Editor: D. M.Bushnell.

location of the separation point which is found to be at 84 degrees. However, if the turbulence intensity is increased to 7 percent, separation moves slightly downstream to approximately 90 degrees.

At the near critical Reynolds number of 9.74×10^4, the shift in separation point is more pronounced where turbulence intensity of respectively 1.2, 3.5, and 9.9 percent causes the separation point to move to respectively 90, 100, and 120 degrees.

For the present study, the maximum Reynolds number is 18435 and the maximum intensity is 4.4 percent. Based on the results of Zukauskas and Ziugzda (1985), the separation point should be unaffected by changes in the free-stream intensity and any change in the transverse wake width and decay of turbulent temperature fluctuations will be due to the interaction of the free-stream and wake turbulence.

Alexopoulos and Keffer (1977) study the turbulent wake in a passively stratified field for different L_0/D ratios. They change the ratio, by changing the cylinder diameter. Thus the intensity at the cylinder remains a constant. Their results show that as the wake spreads laterally, the maximum temperature defect increases in the streamwise direction. There is also an increase in temperature variance in the downstream direction which they conclude is due to the presence of the mean temperature gradient. In their study no discussion is presented of the effect of different ratios of the free stream to wake integral scales on the decay of temperature variance.

Elghobashi and LaRue (1983) study the effect of mechanical strain on the dissipation of temperature variance and time scale ratio, r. Their study is limited to only one ratio of L_0/D with the main focus of the paper being the comparison of numerical predictions and experimental results of the dissipation and time scale ratio.

Additional related studies of the effect of strain on a turbulent scalar field include those of Mills and Corrsin (1959) and Warhaft (1980). Mills and Corrsin (1959) present results of an experimental study of the effect of a contraction with a 4:1 area ratio on temperature fluctuations which are generated by heating a turbulence producing grid, placed upstream of the contraction. In their study the root mean squared, rms, temperature fluctuations in the strained flow are compared to those obtained in the unstrained flow. The results show that contraction accelerates the decay of temperature fluctuations.

Warhaft (1980) also uses a symmetrical contraction with an area ratio of 4:1 to study the effect of a contraction on a passive scalar. Rather than using the turbulence producing grid to heat the flow, another grid (mandoline) made of fine, parallel horizontal wires is electrically heated to produce the temperature fluctuations. By heating different sets of wires in the mandoline, the initial scale size of the thermal fluctuations and hence the mechanical to thermal time scale ratio, r, can be varied. His results show that when r is greater than one, the contraction accelerates the thermal fluctuation decay rate, which does not approach a constant value. However, when r is less than one, the thermal fluctuation decay rate does not change. When $r \sim 1$, the thermal length scale increases by an amount equal to the contraction ratio.

3 Experimental Arrangement

The measurements discussed herein are carried out in the UCI low speed, closed circuit wind tunnel which has a cross section of 60 × 90 cm and a background intensity of about 0.06 percent. Figure 1 shows the arrangement of the flow field and the axial development of turbulence intensity and integral length scale of the external flow. Here, X_0 is measured from the turbulence producing grid.

The turbulent velocity fluctuations are produced by one of two square mesh, biplane grids consisting of either 0.476 or 0.95 cm polished, round aluminum rods with mesh spacing, M_u, respectively, of 2.54 or 5.08 cm. The solidity for both grids, which are placed 97.80 cm downstream of the contraction, is 0.34. The nominal mean velocity is 9 m/s which corresponds to grid Reynolds numbers of about 14,750 and 29,500.

Heat is introduced into the flow by means of a biplane grid of chromel-p heater wires of 0.254 mm dia with a mesh spacing of 1.27 cm which is placed 46 cm downstream of the turbulence-

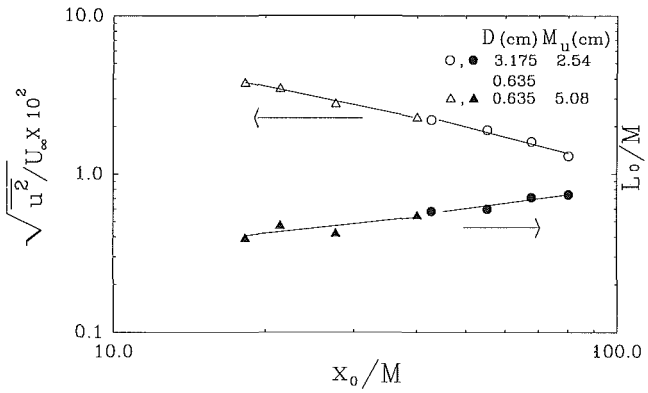

Fig. 1 Flow configuration and streamwise development of turbulence intensity and integral length scale of the external flows. (Uncertainty in $\sqrt{u^2} \times 10^2/U_\infty = \pm 0.02$, in $X_0/M = \pm 0.1$, and in $L_0/M = \pm 0.05$ at 20:1 odds.)

Table 1

D (cm)	Re_D	M_u (cm)	$L_0^{1,2}/D$	$\overline{u}^{21/2,2}/U_\infty$
0.635	3687	2.54	3.1	0.027
0.635	3687	5.08	1.9	0.044
3.175	18435	5.08	0.38	0.044

1. The integral scale is obtained using the variance of the time derivative and the axial turbulent velocity, Taylor's hypothesis and the assumption of local isotropy as $L_0 = \overline{u}^{23/2}/\epsilon_u$ where $\epsilon_u = 15\nu(\partial u/\partial x)^2$ (cf. Tennekes and Lumley (1972)).
2. Evaluated in the free stream at the downstream location of the cylinder.

Nomenclature

L_0 = integral length scale (cm)
M_u = mesh spacing (cm)
$\overline{q^2}$ = twice the turbulent kinetic energy (m^2/s^2)
Re = Reynolds number, $\rho U_\infty D/\nu$, $\rho U_\infty M_u/\nu$
r = time scale ratio
U_∞ = free-stream velocity (m/s)
U_{dmax} = maximum defect velocity m/s
$\overline{u}^{21/2}$ = streamwise turbulent velocity m/s
S = spreading parameter
X_0 = distance from turbulence producing grid (cm)
$Y_{1/2}$ = half width (cm)
ϵ_u = dissipation rate of kinetic energy (m^2/s^3)
ϵ_θ = dissipation rate of temperature variance (C^2/s)
Θ = momentum thickness (cm)
$\overline{\theta^2}$ = temperature variance (C^2)
ν = kinematic viscosity (m^2/s)
ρ = density (kg/m^3)
ΔT = mean temperature difference, 0.55 C

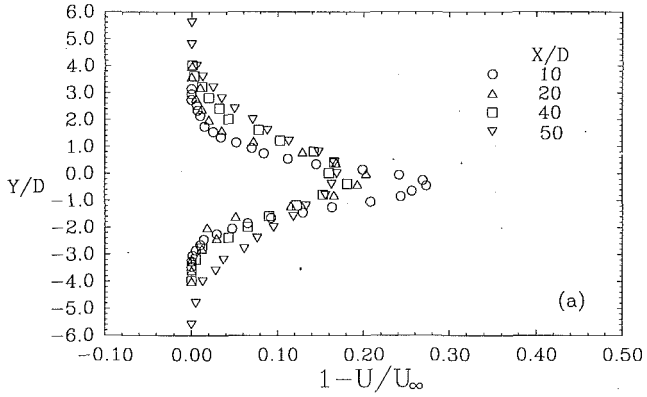

Fig. 2(*a*)

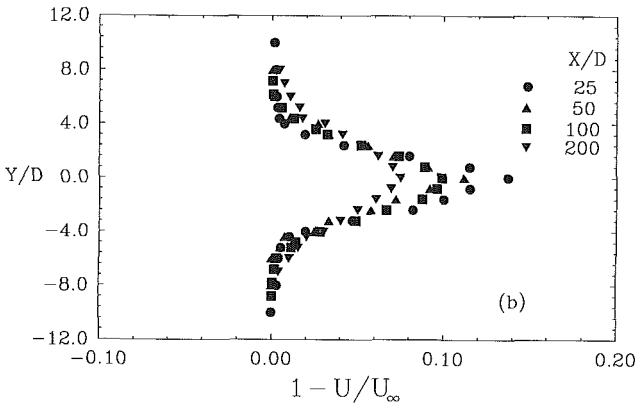

Fig. 2(*b*)

Fig. 2 Transverse variation of the mean defect velocity for experiments with (*a*) L_0/D = 0.38, and (*b*) L_0/D = 3.1. (Uncertainty in L_0/D = ±0.05, in Y/D = ±0.01, and in U/U_∞ = ±0.005 at 20:1 odds.)

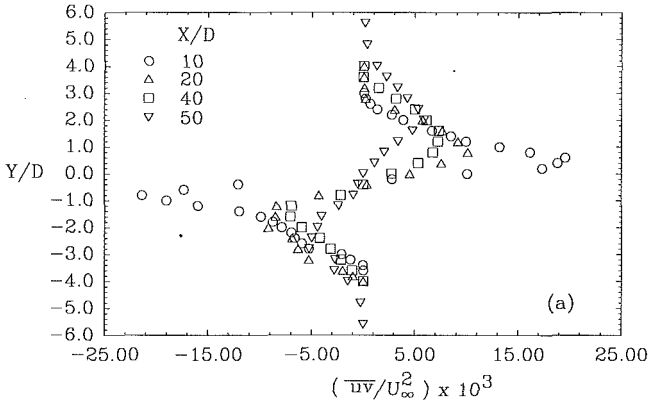

Fig. 3(*a*)

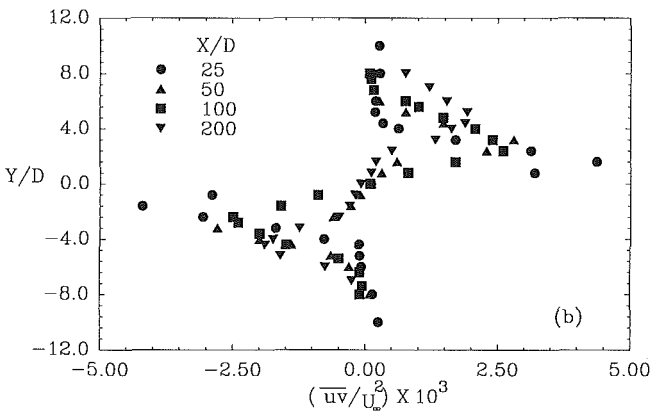

Fig. 3(*b*)

Fig. 3 Transverse variation of the turbulent shear stress for experiments with (*a*) L_0/D = 0.38, and (*b*) L_0/D = 3.1. (Uncertainty in $\overline{uv} \times 10^3/U_\infty^2$ = ±0.25 at 20:1 odds.)

producing grid (all wires are heated during the experiment). The solidity of the grid is 0.04. The grid is electrically heated and a power dissipation of 2.7 kW leads to a 0.55°C rise in the mean temperature across the grid. The corresponding mean temperature is uniform and constant both upstream and downstream of the cylinder.

The two dimensional wake flow is produced using polished aluminum cylinders which are placed 31 cm downstream of the heater wires and at the center plane of the tunnel. The dimensions of the cylinders and corresponding grids and flow characteristics are presented in Table 1.

Simultaneous time-resolved measurements of the streamwise and transverse velocities (u, v) and temperature (θ) are obtained using a triple-wire probe consisting of two hot wires in the "x" configuration and a cold wire mounted normal to the plane of the hot wires and 0.75 mm upstream of their projected intersection. The hot wires are platinum-plated tungsten which are 5 μm in diameter and 1.2 mm in length. The overheat ratios are 1.7. The cold wire is platinum with a diameter of 0.625 μm and a length of 0.75 mm.

The hot wires and the cold wire are operated respectively by two TSI Model 1050 constant temperature anemometers and a fast-response a.c. temperature bridge. The cold wire is supplied with a constant current of 180 μA which makes it's sensitivity to velocity insignificant (cf. LaRue et al. (1975)). The probe is directly calibrated for velocity and temperature and flow direction in the ranges of respectively, 3 to 9 m/s, 17 to 23 C and ±20 degrees. The frequency response of the hot wires determined using the square wave technique is 16 kHz and that of the cold wire is estimated to be about 4 kHz (cf. LaRue et al. (1975)).

Voltages and voltage derivatives from the constant temperature anemometers and the a.c. bridge are recorded by means of an FM tape recorder on analog magnetic tape at a tape speed of 38.1 cm/s, which correspond to a maximum frequency response of 5 kHz. Signals are then low-pass filtered at 3 kHz and digitized at the AMES department of the University of California, San Diego by means of a Phoenix Analog to Digital converter with 16-bit resolution at a rate of 6000 samples/sec-channel. At each probe position 90 records consisting of 4096 samples/channel which correspond to 31.7 sec of data and more than one hundred thousands data sextets are digitized. Digitized data are analyzed using a DEC LSI-11/73 micro computer and standard software.

4 Results and Discussions

Figures 2 to 4 show transverse variations of the mean defect velocity, shear stress and temperature variance at different downstream locations for experiments with L_0/D = 0.38 and 3.1. On the centerline at X/D = 50, the normalized mean defect velocities for L_0/D = 0.38 and 3.1 are 0.16 and 0.11 respectively. The free-stream intensities at this location is approximately 1.5 and 3.5 percent, respectively. Clearly, the momentum transport from the free stream into the wake is increased when the integral scale in the free stream is larger than that in the wake. Application of a simple eddy viscosity model would suggest that the shear stress would be reduced for the flow with L_0/D = 3.1 as compared to that for L_0/D = 0.38. This is consistent with the results shown on Figs. 3(a) and 3(b). There it can be seen that the maximum normalized

turbulent shear stress is reduced at $X/D = 50$, from about 6×10^{-3} for $L_0/D = 0.38$ to about 2.75×10^{-3} for $L_0/D = 3.1$.

The temperature variance profiles decrease in the wake similar to the mean velocity profiles and reach a minimum at the center line. The decrease in temperature fluctuation is at least in part due to heat transfer between the fluid and the cylinder. The cylinder temperature is equal to the mean temperature of the flow. Thus, the temperature difference of fluid which passes near the cylinder and the mean temperature will be reduced. This leads to a reduction in temperature variance on the centerline of the wake. The temperature difference of fluid which passes closer to the cylinder surface is reduced more than the temperature difference of fluid particles which pass further away from the cylinder surface. It seems reasonable to assume that fluid which pass close to the cylinder surface will have a higher probability of arriving near the wake centerplane than those fluids which pass further away from the cylinder surface. Consequently the temperature variances will be reduced more on the centerplane than at other positions in the wake.

Figure 5(*a–d*) show axial variations of the maximum mean defect velocity, $U_{d\max}$, momentum thickness, Θ, wake half-

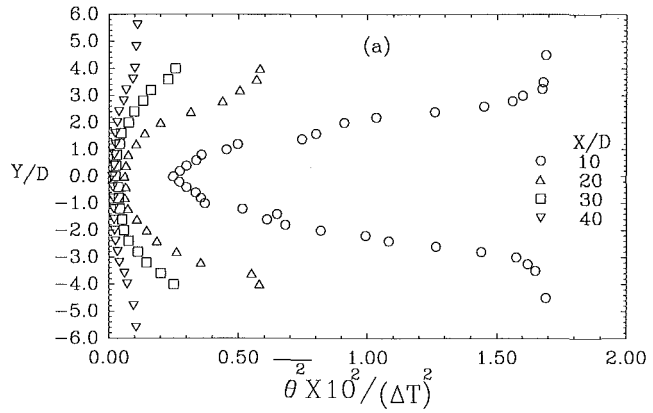

Fig. 4(*a*)

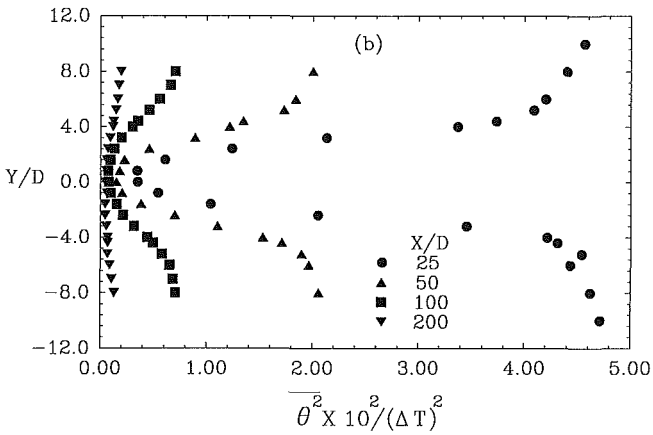

Fig. 4(*b*)

Fig. 4 Transverse variation of the temperature variance for experiments with (*a*) $L_0/D = 0.38$, and (*b*) $L_0/D = 3.1$. (Uncertainty in $\overline{\theta^2} \times 10^2/(\Delta T)^2 = \pm 0.075$ at 20:1 odds.)

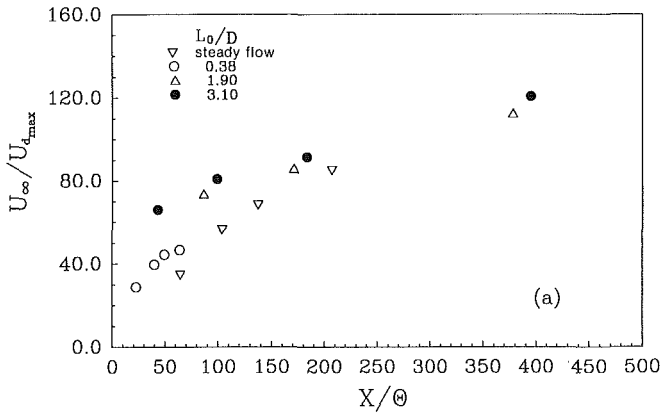

Fig. 5(*a*)

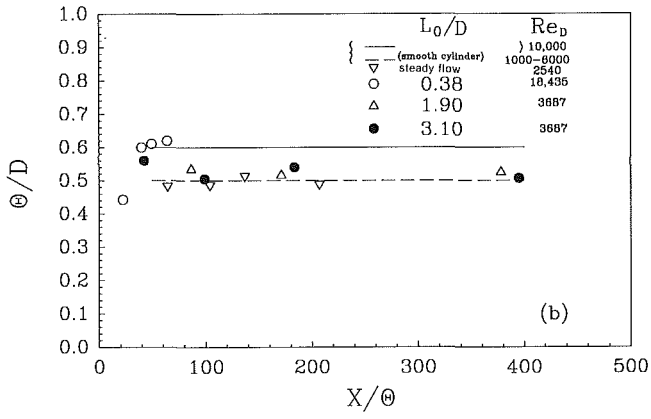

Fig. 5(*b*)

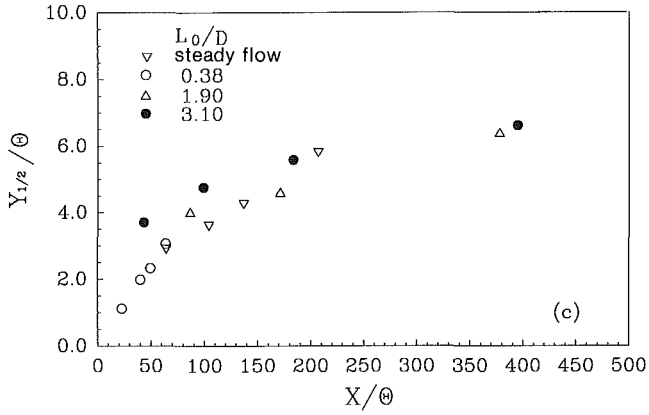

Fig. 5(*c*)

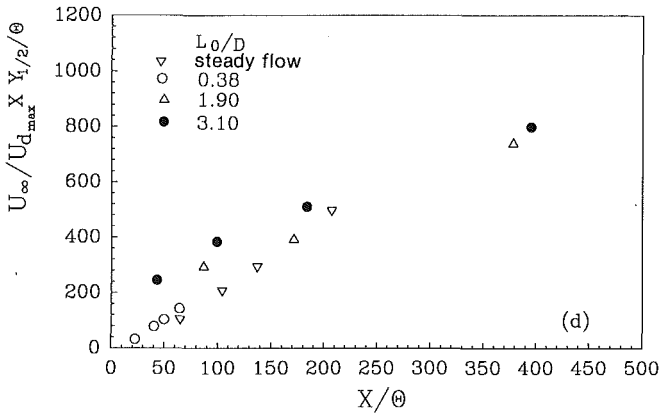

Fig. 5(*d*)

Fig. 5 Streamwise development of (*a*) mean defect-velocity scale, (*b*) wake momentum thickness, (*c*) wake half-width, and (*d*) spreading parameter. (Uncertainty in $U_\infty/U_{d\max} = \pm 0.005$, in $\Theta/D = \pm 0.03$, in $Y_{1/2}/\Theta = \pm 0.05$, in $X/\Theta = \pm 5$ at 20:1 odds.)

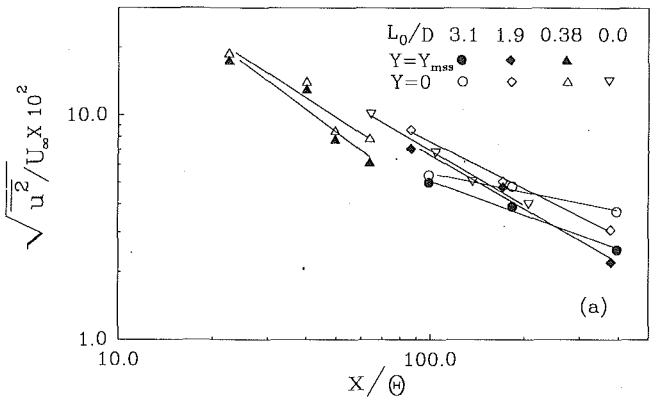

Fig. 6(*a*)

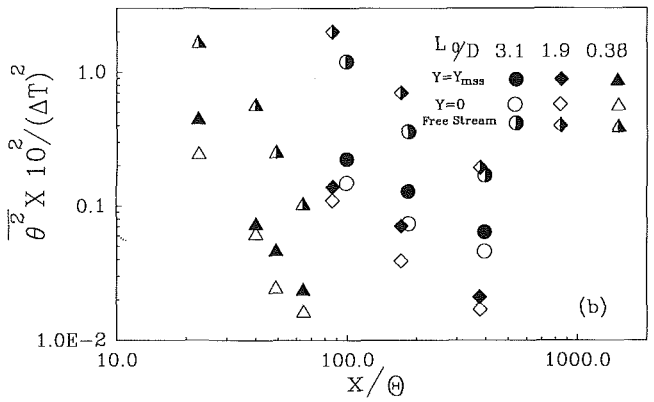

Fig. 6(*b*)

Fig. 6 Streamwise development of (*a*) turbulence intensity, and (*b*) temperature variance

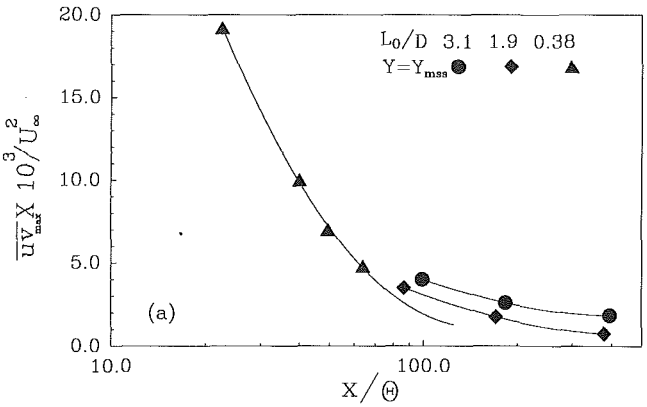

Fig. 7(*a*)

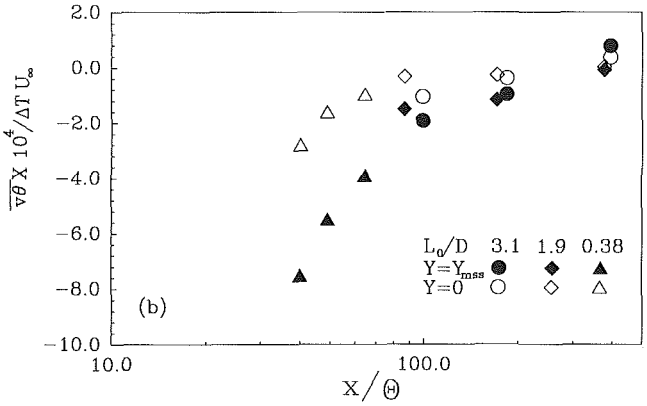

Fig. 7(*b*)

Fig. 7 Streamwise development of (*a*) maximum shear stress, and (*b*) transverse heat flux

width, $Y_{1/2}$, and spreading parameter, S, for experiments with different L_0/D ratios. The momentum thickness is obtained by integrating the wake profiles. The half-width is the transverse distance where the mean defect velocity is half of its maximum value, and the spreading parameter is given by Townsend (1976) as:

$$\frac{S}{\Theta}=\frac{1}{2}\frac{d}{dX}\left(\frac{U_\infty}{U_{d\max}}\times\frac{Y_{1/2}}{\Theta}\right) \tag{1}$$

For experiments with $L_0/D = 0.38$ and for $X/\Theta \leq 40$, where there exist an axial pressure gradient due to the presence of the cylinder, the momentum thickness increases in the downstream direction. However, for $X/\Theta > 40$, the momentum thickness is relatively constant and any variation is due to experimental uncertainty. Figure 5(*b*) also shows the variation of momentum thickness for a smooth cylinder, placed in a uniform flow for different Reynolds number regimes, obtained from Schlichting (1979) and from results obtained as part of the present study. The experimental results with different L_0/D ratios agree with the corresponding results for cylinders in uniform flow. This indicates that the free-stream turbulence does not change the location of the separation point. Thus, any enhancement in the mixing of turbulence is due to the interaction of the large scale structures.

The interaction can be characterized by the ratio of the free stream integral scale to the corresponding integral scale in the wake. The integral scale in the wake is approximately equal to the mixing length (cf. Tennekes and Lumley (1972)) which has an average value of $0.4Y_{1/2}$ (cf. Hinze (1959)). At $x/d = 50$, the ratios of free-stream integral scale to the corresponding average integral scale in the wake are, respectively, 0.61 and 3.58 for $L_0/D = 0.38$ and 3.10. For $L_0/D = 0.38$, the half wake width, velocity defect and spreading parameter are unaffected by the free stream turbulence. In contrast for $L_0/D = 3.10$, where the free-stream integral scale is about twice that of the wake, the half wake width is increased, the velocity defect is decreased and the spreading rate is increased.

Figure 6(*a*) shows the axial decay of turbulence intensity in the wake, in the regions of mss and near the centerline along with the corresponding results for a smooth cylinder placed in a uniform flow. For all L_0/D ratios, the turbulence intensity decays faster in the region of mss than near the center line. For $L_0/D = 0.38$, near the center line, the decay rate is nearly the same as the corresponding value for the smooth cylinder in a uniform flow. In addition, when $L_0/D = 0.38$, the decay rate is higher in both regions than when $L_0/D = 1.9$ and 3.1. Symes and Fink (1977) show that when $L_0/D > 1$, the external turbulence causes an increase in the wake turbulence intensity. In their study as for the present study when $L_0/D = 0.38$ and 1.9, the free stream intensity is maintained constant. Comparisons of the decay rate in both regions of mss and near the center line for these two conditions, consistent with Symes and Fink (1977), show that the turbulence intensity increases with increasing values of L_0/D.

Figure 6(*b*) shows the axial decay of temperature variance. The decay rates are estimated using the method of least squares, to determine the values of A and n in the expression $\overline{\theta^2}/(\Delta T)^2 = AX^{-n}$. For experiments with $L_0/D = 3.1$ and 1.9, the decay rates are nearly the same in the region of mss and near the center line. However, these decay rates are less than the corresponding value outside the wake.

The decay rate of temperature variance increases with decreasing values of L_0/D, and for $L_0/D = 0.38$, the decay rate

of temperature variance is the same in regions of mss, near the centerline and outside the wake. This increase in the decay rate with decreasing L_0/D ratio corresponds to higher shear stress that exists for flows with small values of L_0/D.

Figure 7(a) shows downstream variation of the maximum shear stress for experiments with different L_0/D ratio. The values are taken from the regions of positive shear stress. Results show that the maximum shear stress increases with increasing values of L_0/D.

Figure 7(b) shows downstream variation of the transverse heat flux in the regions of mss and near the center line. The values for the transverse heat flux correspond to the regions of positive shear stress. The heat flux is negative in all regions except far downstream where they approach small positive values. For all L_0/D ratios, the heat flux is higher in magnitude in the region of mss than near the center line. In addition, in both regions of mss and near the center line, the heat flux is not significantly affected by the different values of L_0/D.

5 Conclusion

The effects of different background intensities with different integral length scales on the decay rate of the temperature variance and wake velocity statistics are experimentally investigated. Results show that when $L_0/D > 1$, the maximum mean defect velocity decreases and the wake half-width increases with increasing L_0/D.

The decay rates of turbulence intensity and temperature variance for experiments with $L_0/D < 1$ are larger than the corresponding values for experiments with $L_0/D > 1$.

For experiments with $L_0/D > 1$, the decay rate of turbulence intensity and temperature variance are higher in the region of mss than near the centerline. In addition, in both regions, the decay rates are less than the corresponding values outside the wake. However, when $L_0/D < 1$, the decay rate of temperature variance is the same in regions of mss, near the centerline and outside the wake.

References

Alexopolous, C. C., and Keffer, J. F., 1977, "Turbulent Wake in a Passively Stratified Field," *Phys. of Fluids*, Vol. 14, No. 2, pp. 216–224.

Durbin, P. A., Hunt, J. C., and Firth, D., 1982, "Mixing by a Turbulent Wake of a Uniform Temperature Gradient in the Approach Flow," *Phys. of Fluids*, Vol. 25, No. 4, pp. 588–591.

Elghobashi, S., and LaRue, J. C., 1983, "The Effect of Mechanical Strain on the Dissipation Rate of Scalar Variance," *Fourth Symposium of Turbulent Shear Flow*, Karlsruhe, Germany.

Freymuth, P., and Uberoi, M., 1971, "Structure of Temperature Fluctuations in the Turbulent Wake Behind a Heated Cylinder," *Phys. of Fluids*, Vol. 14, No. 2, pp. 2574–2580.

Hinze, J. L., 1959, *Turbulence*, McGraw-Hill, New York, p. 507.

LaRue, J. C., Deaton, T., and Gibson, C. H., 1975, "Measurement of High-Frequency Turbulent Temperature," *Rev. Sci. Instrum.*, Vol. 46, No. 6, pp. 757–764.

LaRue, J. C., and Libby, P. A., 1974, "Temperature Fluctuations in a Plane Turbulent Wake," *Phys. of Fluids*, Vol. 17, No. 11, pp. 1956–1967.

Lumley, J. L., 1975, "Modeling Turbulent Flux of Passive Scalar Quantities in Inhomogeneous Flows," *Phys. of Fluids*, Vol. 18, No. 6, pp. 619–622.

Mills, R. R., and Corrsin, S., 1959, "Effect of Contraction on Turbulence and Temperature Fluctuations Behind a Heated Grid," NACA Memo 5-5-59W.

Schlichting, H., 1979, *Boundary Layer Theory*, 7th ed., McGraw-Hill, New York.

Seely, L. E., Hummel, R. L., and Smith, J. W., 1975, "Some Observations of the Wake Behavior in Laminar and Turbulent Free Stream Flow," *4th Symposium on Turbulence in Liquids*, University of Missouri, Rolla, pp. 289–301.

Symes, C. R., and Fink, L. E., 1977, "Effects of External Turbulence Upon the Flow Past Cylinders," *Proceeding of the Symposium on Structure and Mechanisms of Turbulence*, Technische Universitat Berlin, pp. 86–101.

Tennekes, H., and Lumley, J. L., 1972, *A First Course in Turbulence*, MIT Press, Boston, Mass., p. 45.

Townsend, A. A., 1976, *The Structure of Turbulent Shear Flow*, Cambridge University Press, 2nd edition.

Warhaft, Z., 1980, "An Experimental Study of the Effect of Uniform Strain on Thermal Fluctuations in Grid-Generated Turbulence," *J. Fluid Mech.*, Vol. 99, pp. 545–573.

Zukaskas, A., and Ziugzda, J., 1985, *Heat Transfer of a Cylinder in Cross Flow*, Hemisphere Publishing Corporation.

Viscous Simulation Method for Unsteady Flows Past Multicomponent Configurations

Kamran Fouladi

Oktay Baysal

Mechanical Engineering and Mechanics Department,
Old Dominion University,
Norfolk, VA 23529

An algorithm is developed to obtain numerical simulations of flows about complex configurations composed of multiple and nonsimilar components with arbitrary geometries. The algorithm uses a hybridization of the domain decomposition techniques for grid generation and to reduce the computer memory requirement. Three-dimensional Reynolds-averaged, unsteady, compressible, and full Navier-Stokes equations are solved on each of the subdomains by a fully vectorized, finite-volume, upwind-biased, approximately factored, and multigrid method. The effect of Reynolds stresses is incorporated through an algebraic turbulence model with several modifications for interference flows. The algorithm is applied to simulate supersonic flows past an ogive-nose-cylinder near or inside a cavity. The cylinder is attached to an offset L-shaped sting when placed above the cavity opening. The unsteady nature of these flowfields and the interaction of the cavity shear layer with the cylinder are simulated. These cases illustrate two significantly different and important interference characteristics for an internally carried store separating from its parent body. Unsteadiness of the cavity flow has a more pronounced effect on the normal forces acting on the cylinder when the cylinder is placed inside the cavity. The time averaged surface pressures compare favorably with the wind tunnel data, despite the averaging time period for the computations being three orders of magnitude smaller than that of the experimental measurements.

Introduction

In recent years, computational fluid dynamics (CFD) has taken a more dominant role in solving complex flow problems. This is primarily due to the recent advancement of high speed supercomputers with large memories as well as the relative high cost of wind-tunnel tests and model fabrication. The efforts in solving these problems have often been hampered by the difficulties encountered in discretizing the physical domain around a complex configuration. This problem is more evident in the case of a configuration which has multiple bodies with nonsimilar, joint or disjoint, components. Various approaches, such as, domain decomposition, grid adaptation, unstructured grids, or some hybridization of these techniques are being used by researchers to ease the grid generation efforts.

A domain decomposition technique (DDT) subdivides the flow domain into simpler subdomains which accept easily constructed grids. These methods vary in constructing the grid interfaces and establishing the communication among the subdomain grids. Popular DDT's are the overlapped grids, the zonal grids, and the multiblock grids. The multiblock grids allow any number of blocks to be employed to fill an arbitrary three dimensional region without any holes or overlaps. The lines normal to the grid interfaces need to be contiguous, hence no interpolation is needed at these interfaces. The zonal grids are patched together along common boundaries without the need for the lines normal to the grid interfaces to be contiguous. The zonal method is shown to be conservative except across surfaces with high curvature. Ensuring conservation across these surfaces is not theoretically impossible, but it is rather difficult to obtain. In contrast to the other two, the grid overlapping method does not require common boundaries among its subdomains and matching the solution across the boundaries is provided by a common or overlapped region (Benek et al., 1983; Baysal et al., 1991).

There are two other reasons to utilize the DDT's besides easing the grid generation for complex geometries. Since no more than one subdomain has to reside on the computer memory at one given instant of the computation, the computer memory requirement is limited only by the subdomain with the largest number of grid points. This virtually removes the limit on the total number of grid points which can be used in a given problem. The other advantage of the DDT's is related to the computer processing. One of the most natural ways of mapping a CFD problem to a computer with multiple processors is decomposing the domain and assigning each processor to the work of a different subdomain. The only extra programming effort for such parallel processing is the exchange of intergrid boundary data.

Hybridization techniques, such as the adaptive unstructured

Contributed by the Fluids Engineering Division and presented (in a different version) at the Symposium on Recent Advances and Applications in Computational Fluid Dynamics, Winter Annual Meeting November 25-30, 1990 Dallas, Texas of THE AMERICAN SOCIETY OF MECHANICAL ENGINEERS. Manuscript received by the Fluids Engineering Division September 25, 1990. Associate Technical Editor: C. J. Freitas.

grid technique, are also shown to be useful for complex configurations. Use of grid adapting is beneficial in showing the changes in the strength and the location of shocks and the grid for the complicated geometry is obtained in an unstructured manner. Two major drawbacks of the unstructured grids are their often prohibitive need for the computer memory and the difficulties encountered in generating the highly stretched grids to solve the Navier-Stokes equations. In an effort to overcome this deficiency, a hybrid method made up of the finite-difference (FDM) and the finite-element method (FEM) has been developed by Nakahashi and Obayashi (1987). The FDM and the FEM are combined using the zonal technique where the FDM is applied only to the viscous region near the body surface.

The first objective of the current investigation is to utilize the advantages of the DDT's with an efficient Navier-Stokes solution algorithm. In this attempt, the aforementioned DDT's are judiciously used in a hybrid manner to retain the advantages of each technique. The Navier-Stokes equations are then solved by an implicit, approximately factored, finite volume, upwind scheme (Thomas et al., 1987; Baysal et al., 1989). Baysal et al. (1991) have combined the advantages of this efficient, geometrically conservative, only minimally and automatically dissipative solution algorithm with the advantages and the flexibility of the overlapped grids. The efficiency of the algorithm is enhanced by employing the approximate diagonalization of the coefficient matrices and the multigrid convergence acceleration on the overlapped grids.

The second objective is to solve the unsteady, complete Navier-Stokes equations to simulate the flow past an ogive-nose-cylinder with an offset sting positioned in the proximity of a cavity. Empty cavity flows have recently been computationally investigated by several researchers. Among them are the three dimensional calculations of Rizzeta (1988), Suhs (1987), Baysal et al. (1988a, 1990), Srinivasan and Baysal (1991), and the two-dimensional calculations of Baysal and Stallings (1988b) and Om (1988). The present paper is an extension of such efforts, where the cavity is no longer considered to be empty, to study the interference effects of an object in or near the cavity. Another application of this computational algorithm, where a blunt-nose-cylinder with four fins and a circular offset sting is placed inside a cavity, has previously been reported by Baysal et al. (1992).

Governing Equations and Their Solution

A rectangular cavity consists of walls in all three directions. Consequently, diffusion effects of the viscous fluxes are not negligible, and their gradients are approximately of the same order of magnitude in all three directions. This requires the solution of the full Navier-Stokes equations. Their reduced forms, such as, the thin layer approximation or the Euler equations produce nonphysical results for the flows being considered. The conservative form of the nondimensional, unsteady, compressible, Reynolds-averaged, full Navier-Stokes equations are used in the generalized curvilinear coordinates (Baysal and Yen, 1990),

$$\frac{\partial \overline{Q}}{\partial t}+\frac{\partial}{\partial \xi^m}(\overline{E}-\overline{E}_v)_m=0 \tag{1}$$

where the dummy index is $m = 1, 2, 3$ for the three-dimensional equations. The coordinate transformation is,

$$\xi^m=\xi^m(x_1,x_2,x_3) \tag{2}$$

$\overline{E}$ and $\overline{E}_v$ are the column vectors of the inviscid and viscous fluxes, respectively. The ideal gas law is used for closure, and the Sutherland formula is used to determine the molecular viscosity. The coefficient of bulk viscosity is determined through the Stokes hypothesis.

The effect of Reynolds stresses is incorporated through the Baldwin-Lomax (1987) algebraic turbulence model with modifications. Several modifications have been done to the model for all the points in the cavity in order to determine the proper length and velocity scales in the highly vortical regions of massive separation, near three-dimensional corners and near the shear layer. Details of these modifications are given by Baysal et al. (1990) and Srinivasan and Baysal (1991).

Finite volume differencing is formulated by integrating the conservation equations (Eq. (1)) over a stationary control volume (computational domain),

$$\frac{\partial}{\partial t}\int\int\int \overline{Q}d\Omega+\int\int \overline{E}\cdot\overline{n}dS=0 \tag{3}$$

where $\overline{n}$ is the unit normal vector pointing outward from the surface S bounding the volume Ω.

Equation (3) is solved using the second-order accurate method described by Thomas et al. (1987), Baysal et al. (1989), and Van Leer et al. (1987). Either Van Leer's flux vector splitting (FVS) or Roe's flux-difference splitting (FDS) are used to construct the upwind-biased differences for the convective and pressure terms. A consequence of the FDS type upwinding is when an eigenvalue of a flux Jacobian vanishes, the corresponding eigenvalue of the dissipation matrix also vanishes. This leads to a crisp resolution of the regions with high flow gradients, such as in capturing shocks. The dissipative nature of upwind methods have made them a prevailing alternative to central difference schemes where artificial terms are generally needed to overcome oscillations or instabilities arising in regions of high gradients. Spatial derivatives are written conservatively as flux balances across a cell. The diffusion terms are centrally differenced.

Spatial approximate factorization, and Euler backward integration after linearization in time, results in the solution through 5 × 5 block-tridiagonal matrix inversions in three directions. The delta form of Eq. (1) obtained in this manner is given below.

$$\left[\frac{I}{J\Delta t}+\Delta_{\xi^1}(\partial_Q\hat{E}_1)-\Delta^2_{\xi^1}(\partial_Q\hat{E}_{v1}\right]$$

$$*\left[\frac{I}{J\Delta t}+\Delta_{\xi^2}(\partial_Q\hat{E}_2)-\Delta^2_{\xi^2}(\partial_Q\hat{E}_{v2})\right]$$

$$*\left[\frac{I}{J\Delta t}+\Delta_{\xi^3}(\partial_Q\hat{E}_3)-\Delta^2_{\xi^3}(\partial_Q\hat{E}_{v3})\right]$$

$$*\Delta Q=-\mathrm{Res}(\overline{Q}^n) \tag{4}$$

Nomenclature

C_A = axial force coefficient
C_N = normal force coefficient
D = cavity depth
d = diameter
DDT = domain decomposition technique
F = floor
FF = front face
FP1 = front flat plate
FP2 = rear flat plate
J = transformation Jacobian
L = cavity length
M = Mach number
ms = milliseconds
Q = conserved variables
q = primitive variables
RF = rear face
Re = Reynolds number
SFP = side flat plate
SW = side wall
t = time
x_1, x_2, x_3 = Cartesian coordinates
X, Y, Z = Cartesian coordinates
W = cavity width
α = angle of attack in degrees
ξ^1, ξ^2, ξ^3 = curvilinear coordinates

where

$$\text{Res} = [\Delta_\xi{}^m \hat{E}_m - \Delta_\xi^2{}^m (\hat{E}_v + \hat{E}_{vc})_m] \qquad \text{(sum over } m\text{)} \qquad (5)$$

Δ, Δ^2 denote upwind-biased and central differences, respectively. $\hat{E}_m$, $(\hat{E}_v)_m$, $(\hat{E}_{vc})_m$ represent the inviscid fluxes, viscous fluxes, and the fluxes of viscous cross-derivatives terms, respectively. (I) is the unit diagonal matrix and (n) denotes a time level.

Numerical oscillations, such as overshoots and undershoots, are expected to appear in the presence of large flow gradients when an upwind-biased approximation scheme is used. A flux limiter can be used to reduce an upwind-biased difference to a fully one-sided upwind scheme in these regions. This in turn ensures a monotonic interpolation and eliminates the overshoots and the undershoots. In an upwind scheme, the conserved state variables on a cell interface, for example at $(i + 1/2)$, are obtained as

$$(q_R^L)_{i+1/2} = q_{i+1}^i \pm \left\{ \frac{1}{4}[(1 \pm \kappa)\Delta + (1 \mp \kappa)\nabla] \right\}_{i+1}^{i} \qquad (6)$$

where

$$\Delta = (q_{i+1} - q_i); \quad \nabla(q_i - q_{i-1}) \qquad (7)$$

and $\kappa = -1$ and $1/3$ correspond to fully upwind and upwind-biased differences, respectively.

Three flux limiters have been chosen for this study. First limiter considered is called the minimum-modulus (min-mod) limiter (Chakravarthy and Osher, 1983). The min-mod limiter is implemented by interpreting Δ and ∇ in the Eq. (6) as follows,

$$\overline{\Delta} = \max[0, \min(\Delta \ \text{sgn} \nabla, \beta \nabla \text{sgn} \Delta)] \text{sgn} \Delta \qquad (8a)$$

$$\overline{\nabla} = \max[0, \min(\nabla \text{sgn} \Delta, \beta \Delta \ \text{sgn} \nabla)] \text{sgn} \nabla \qquad (8b)$$

$$\beta = \frac{(3 - \kappa)}{(1 - \kappa)} \qquad (8c)$$

The min-mod limiter is activated only in the regions of high flow gradients and it has shown to cause a limit cycle in the residual on the fine grids.

The second limiter acts in a continuously differentiable fashion, and it has the advantage to overcome the convergence problem encountered with the first limiter. This limiter, known as Van Albada (1982) limiter, is implemented by rewritting the Eq. (6) as

$$(q_R^L)_{i+1/2} = q_{i+1}^i \pm \left\{ \frac{S}{4}[(1 \mp \kappa S)\nabla + (1 \pm \kappa S)\Delta] \right\}_{i+1}^{i} \qquad (9)$$

where

$$S = \frac{2\nabla\Delta + \epsilon}{\Delta^2 + \nabla^2 + \epsilon} \qquad (10)$$

and ϵ is a small number ($\sim 10^{-6}$) to prevent the division by zero in the regions of zero gradient. The quantity S is the limiter control function. Its value reaches unity at the regions of small gradients, thus using no limiter for these regions. However, its value goes to zero for very large gradients regions, hence reducing to first order interpolation.

The third limiter, which is due to Spekreijse (1987), invokes the monotonicity at the interpolation stage by rewriting the Eq. (6) as

$$(q^L)_{i+1/2} = \left[q + \frac{1}{2} \ \varphi(R) \ \phi(R) \ \nabla \right]_i \qquad (11)$$

$$(q^R)_{i+1/2} = \left[q - \frac{1}{2} \varphi\left(\frac{1}{R}\right) \ \phi\left(\frac{1}{R}\right) \ \Delta \right]_{i+1} \qquad (12)$$

where

$$\varphi(R) = \frac{1}{3} + \frac{2}{3} R; \quad \phi(R) = \frac{3R}{2R^2 - R + 2}; \quad R = \frac{\Delta q}{\nabla q} \qquad (13)$$

Algorithm for Domain Decomposition

The solution algorithm described in the previous section is for a single subdomain. However, the flow domain considered here is comprised of multiple domains, and their union is called a *composite* grid. The method to generate such a composite grid is briefly described in this section. The standard block or scalar tridiagonal inversions of Eq. (4) can easily be extended for zonal and multiblock grids. However, due to the existence of overlap regions and the holes in the overlapped grids, modification to the baseline algorithm is necessary. These modifications are summarized in the next subsection.

In deciding on the type of DDT or a hybridization of DDT's for a given configuration, two major concerns are the geometry of the configuration and a priori knowledge of the expected flowfield. A combination of the DDT's should provide a mechanism that simplifies the selection process of the subdomains. Each subdomain is chosen to ease the grid generation task, and to create a suitable mesh for the region of that particular subdomain, where the boundary conditions can easily be implemented. A proper choice of DDT can, for example, eliminate the need for a common boundary between subdomains by using overlapped grids, or eliminate the need for interpolation at the grid interfaces by using multiblock grids, or eliminate the need for contiguous grid lines normal to the interface by using zonal grids.

An order of hierarchial form between the grids allows the interaction of the appropriate grids and simplifies the development of the data structure required for the interaction. It also limits the search to locate points for the purpose of interpolation in the case of overlapped grids. Grids which are on level (L) of the hierarchy, G_L, are partially or completely embedded in grids of level $(L - 1)$ and may contain grids of level $(L + 1)$, which are partially or completely embedded in them. At the same time, G_L may overlap other grids at level (L). This is also true for grids which are interfaced through zonal or multiblock techniques, where the overlap region reduces to zero.

As subdomains are moved to their overlapped positions, some cells of one grid may be found to coincide with a solid boundary contained within another grid. Also, a significant number of cells must be interpolated, if every cell common to more than one subdomain grid is to be updated. This becomes computationally expensive and it could have an adverse effect on the global accuracy when mesh sizes are not compatible on different subdomain grids. This problem can be avoided by updating only the boundary of the common region between subdomains, and excluding the other cells inside this region from the calculation. This process introduces an artificial boundary or a hole inside the overset subdomain. Hence, a search method is used to create and locate these holes. This search procedure is detailed by Benek et al. (1983) and Baysal et al. (1991a). A cell which lies inside the hole is defined as a *hole* cell in G_L. A hole cell is flagged for grid G_L by setting an array IFLAG = 0. A cell of G_L which is not in the hole is flagged by setting IFLAG = 1.

The G_L cells which are immediate neighbors of the hole cells are called the *fringe* cells, and the intergrid communication of the conserved variables from G_{L+1} grid is performed to these cells. A fringe cell is also flagged as IFLAG = 0. A cell in G_{L+1} with the smallest distance to a fringe cell in G_L is located and called a *target* cell. Then a search is conducted to find seven cells of G_{L+1} near the target cell. The objective is to form a hexahedron which has these seven cell centers and the target point as the vertices, and this hexahedron has to include the fringe point of G_L. (The words cell center and point are used interchangeably herein.)

The information transfer from the eight cells of G_{L+1} grid to the fringe cell of G_L is done through trilinear interpolations coupled with the characteristic intergrid boundary conditions. This process is called *updating* herein. The interpolated values of Q vector can be calculated as,

$$Q = \sum_{i=1}^{8} \alpha_i a_i \tag{14}$$

The values for the eight free variables, a_i, are determined from the known values of Q_i at the eight vertices of the information hexahedron. The coefficient, α_i, is a function of coordinates of the fringe cell which is being updated relative to its target cell. Since Eq. (14) assigns the interpolation weights without any consideration to the volumes of the cells, the error introduced by interpolation is minimized by choosing the cells of the overlap regions of comparable sizes. The error is largest when interpolating from much smaller cells to a coarser cell. However, this may be corrrected by incorporating the cell volumes into the weighting. The interpolation procedure is repeated in an opposite manner at the outer boundary of the overlap region, where the information is transferrred from the grid G_L to the grid G_{L+1}.

There are efforts currently being undertaken by researchers to improve the intergrid communication between overlapped grids. One such approach is the conservative method of matching proposed by Berger (1987). This method is used for maintaining conservation at the intergrid boundaries. In this method, a consistent approximation to the intergral of conserved variables determines a matching equation, which gives a weak solution to the partial differential equation being solved, if this approximation converges as the limit of h (spatial step size) goes to zero. If this matching is linear, the interpolation of fluxes, as needed for conservation, is equivalent to interpolation for the solution itself. The differencing stencil required for this scheme, based upon the concept of weak solution to the differential equation, is rather irregular even for two-dimensional curvilinear grids.

Modified Solution Algorithm. The fringe cells along with the cells located inside the holes or outside the outer boundary, which are flagged as IFLAG = 0, are treated by the following modification to the implicit algorithm: (*a*) set the elements of the off-diagonal 5 × 5 blocks in the coefficient matrix to zero, (*b*) for the diagonal blocks, set the diagonal elements to unity and the off-diagonal elements to zero, (*c*) set the residuals to zero. This results in the computed value of ΔQ for these cells to be zero. Thus, the updated or specified boundary conditions for these cells are automatically preserved. For example, let one of the spatial factors of Eq. (4) be written as a system of algebraic equations in block tridiagonal form represented as

$$a_{ij} \times \phi_i = R_i \tag{15}$$

where a_{ij} are the 5 × 5 blocks of the coefficients tridiagonal matrix. ϕ_i are the unknown vectors which represent ΔQ of Eq. (4). The right-hand side residual is represented by R_i which are the known vectors. Then,

$$R_i \leftarrow R_i \times \text{IFLAG}_i \tag{16}$$

$$a_{ij} \leftarrow a_{ij} \times \text{IFLAG}_i, \qquad i \neq j \tag{17}$$

$$a_{ij} \leftarrow (a_{ij} \times \text{IFLAG}_i) + (1 - \text{IFLAG}_i), \quad i = j \tag{18}$$

where (←) indicates that its left hand is to be replaced by its right-hand side. It should be noted that all the elements of the block a_{ij}, $i \neq j$, must become zero for the hole cells. However, only the diagonal elements must be set to unity for the diagonal blocks a_{ii}.

Composite Grids. Two computational examples are considered in this study. In both cases, a sharp ogive-nose-cylinder is positioned near a cavity with a length-to-depth ratio of 6.73 (Fig. 1). The cavity is 29.363 in. long, 4.363 in. deep, and

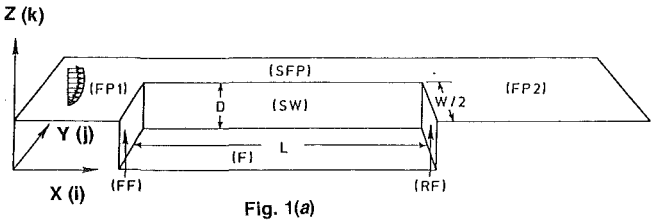

Fig. 1(*a*)

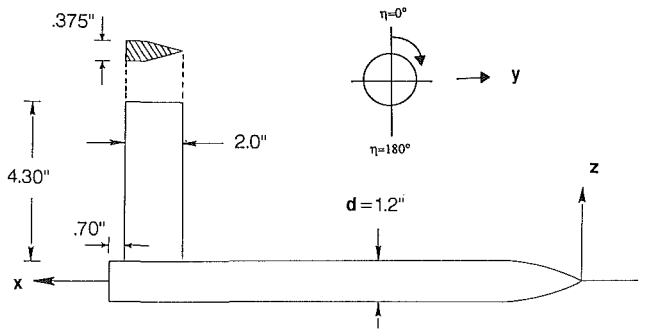

z/d = (9.58**2-(x/d-3.06)**2)-2.56 0<x/d<3.06

z/d = .500 3.06<x/d<22.69

Fig. 1(*b*)

Fig. 1 Schematics of (*a*) rectangular cavity with *L/D* = 6.73, (*b*) ogive-nose-cylinder

Table 1 Dimensions of the subdomain grids for Cases 1 and 2

Grid	Description	$i \times j \times k$
1	upper Cartesian grid	$103 \times 28 \times 57$
2	lower Cartesian grid	$81 \times 23 \times 43$
3	H-O grid for cylinder	$121 \times 29 \times 33$
4	O-H grid for offset sting	$21 \times 25 \times 57$
Total number of grid points		390,219

5.768 in. wide. The base diameter and the length of the cylinder are 1.2 in. and 24.028 in., respectively. The cylinder is mounted to an L-shaped offset sting, which has a 3.2 in. axial section. The cylinder is placed 6.0 in. above the cavity opening for Case 1, and it is positioned 2.0 in. below the cavity opening for Case 2.

The computational domain is divided into four subdomains. The stretched Cartesian grid for the cavity has a lower block inside the cavity and an upper block above the cavity subdomain. The conservation across the grid interface is extremely important since the cavity flow is driven by the shear layer. To ensure the conservation, the grid lines are contiguous normal to the interface of these two blocks where the solutions are matched. A boundary fitted H-O grid is wrapped around the cylinder and the sting is contained in an O-H grid. Both grids are embedded in the Cartesian grids. The end surface of the O-H grid containing the sting root is coincident with the cylinder surface. These component grids are used to form the composite grids for both cases. In fact, this is one of the advantages of the current algorithm in which the component grids are reusable. The composite grids of both cases are shown in Fig. 2. Portions of the overlapped regions are marked by the solid circular dots. Dimensions of the subdomain grids for both cases are given in Table 1.

The flow is assumed symmetric with respect to the center plane of the cavity and the cylinders. Therefore, the computations are performed only for the half bodies, resulting in substantial savings in computer time and memory. Based on their experimental results, Stallings and Wilcox (1987) have

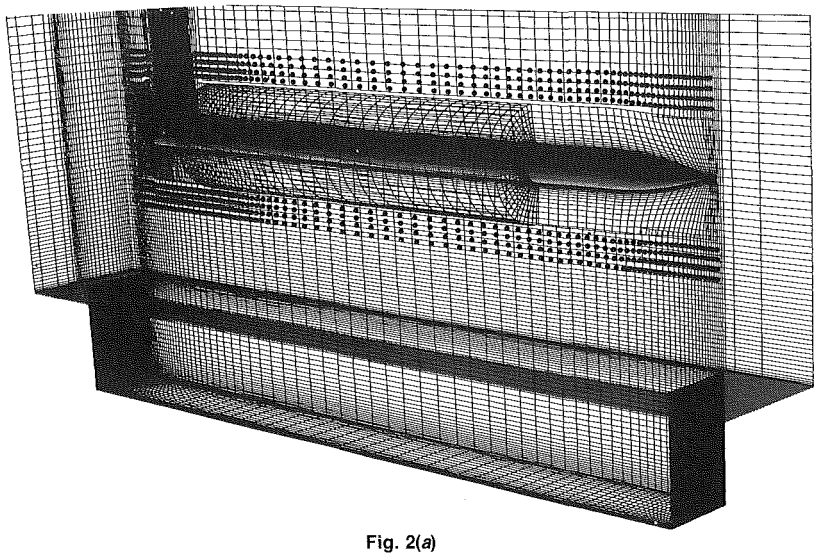

Fig. 2(*a*)

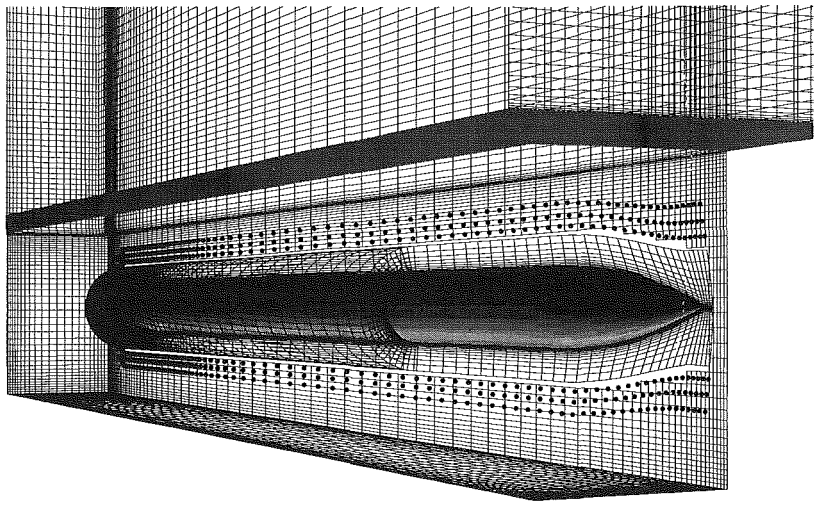

Fig. 2(*b*)

Fig. 2 Composite grid of (*a*) ogive-nose-cylinder with sting near the cavity (Case 1), (*b*) ogive-nose-cylinder inside the cavity (Case 2)

concluded that the flowfield inside a three-dimensional cavity is predominantly symmetric with respect to the center plane ($Y = 0$ plane), when the approaching flow is at zero angle of yaw (i.e., in the X-direction), and the three-dimensional effects are mainly confined to either side of this plane. Therefore, almost all the computational simulations of the cavity flows (Rizzeta, 1988; Suhs, 1987; Om, 1988; Baysal et al., 1988b, 1990; Srinivasan and Baysal, 1991) have used this assumption in order to reduce the computational effort, and their results compared favorably with the pertinent experimental data. This assumption is further discussed and favored by Stallings et al. (1990), where a cylinder is placed in or near a cavity.

It is rather difficult to perform a grid refinement study for a complex, three-dimensional flow, particularly, when the flow is unsteady. Based on the previous experiences with cavity flow simulations (Baysal et al., 1988a, 1988b, 1990, 1992; Srinivasan and Baysal, 1991), it is believed that a minimum step size of 10^{-4} of the characteristic length, followed by an adequate grid stretching, results in an appropriate grid resolution. In the present case, the cavity depth is used as the characteristic length.

Initial and Boundary Conditions. Since the flow is two-dimensional on the flat plate ahead of the cavity, a two-dimensional, turbulent boundary layer profile is generated to match the experimentally determined thickness (0.4 in.) at upstream of the cavity lip. Using this profile as an upstream boundary condition allows the computational domain to start 22.1 in. downstream of the flat plate leading edge, thus significant computational time and memory savings are obtained. The conventional viscous flow boundary conditions, that is, no-slip, impermeability, and adiabatic-wall conditions are imposed on all solid surfaces. First order extrapolation of the primitive variables are used at the downstream boundary. One-dimensional characteristic boundary conditions are imposed at the outer boundary and the lateral outboard boundary. The symmetry of the flow at the plane, where symmetry is assumed, is ensured by setting the contravariant velocity normal to this plane equal to zero and extrapolating the other primitive variables. The boundary conditions for the intergrid boundaries between the subdomain grids are given in detail by Baysal et al. (1991). The dependent variables (conserved variables) of Eq. (1) are also initialized using the advanced *initialization* procedure proposed by Baysal et al. (1992).

The code developed for this class of flows is run on the Cray-2 computer of NASA Langley Research Center. The com-

puter memory required by the solver of the flow equations is 136 megabytes for Case 1 and 120 megabytes for Case 2.

Two characteristic times are defined for two different reasons. The first characteristic time is defined as the maximum of all the times obtained as the ratio of a cavity dimension, l (length or width) to the corresponding component of the freestream velocity, $t_{c1} = \max(l/u)$. It is used as a time scale for this unsteady flow. The numerical transients due to the nonphysical initialization of the clean cavity computational domain are assumed to be removed after running the solution algorithm for $(4t_{c1})$. The second characteristic time is defined as the ratio of the minimum length of the discretization stencil used by the solution algorithm to the freestream value of the speed of sound, $t_{c2} = \min(5.\Delta x_m)/a_\infty$. Note that this second-order algorithm uses five-point stencils in each direction. The characteristic time, t_{c2}, is used to determine the physical limitation set on the time step size of the solution algorithm which is advanced time accurately. To collect computational data a rate faster than the wave propagation speed, the computational time step should be an order of magnitude less than t_{c2}. This practice ensures capturing numerically the pressure fluctuations of the cavity flow. The values of t_{c1} and t_{c2} for the present cavity are 1.56 and 0.073 milliseconds, respectively.

The clean cavity solution is obtained after $15t_{c1}$, which requires about 17.5 hours of computer time. The steady-state solution for cylinder-sting in freestream is obtained by using one hour of computer time. The computer time to advance the interference flow for one t_{c1} is about 20 hours. This is mainly due to the minimum step size on the cylinder-sting grid being an order of magnitude smaller than the minimum step size of the cavity grid. Consequently, the global time step being used is at least an order of magnitude smaller, which results in an order of magnitude more computational time.

In the present study, the interference flow between the components of the configuration is observed in less than one t_{c1}, after the advanced initialization. However, the solution is advanced for nearly 2 t_{c1}. The reason for this extended calculation is to mimic the experimental procedure for code validation purposes. In the experiment (Stallings et al., 1990), a steady flow measurement technique is being used to measure these unsteady flows.

Results and Discussion

Two test cases are chosen to demonstrate the applicability and the performance of the current algorithm. In both cases, the flow is turbulent at $M = 1.65$, Re/ft $= 2 \times 10^6$, $\alpha = 0°$, $P_t = 1092$ lb/ft^2, and $T_t = 584°$ R, where P_t and T_t denote the freestream total pressure and temperature, respectively.

The rationale behind these cases are three fold: (i) To demonstrate the versatility of the current algorithm, since the configuration considered here consists of multiple, geometrically nonsimilar components. (ii) Availability of the experimental data for comparison (Stallings et al., 1990). (iii) To study the interference effect of the cylinder on the unsteady cavity flowfield as the cylinder is positioned inside and outside the cavity. Inclusion of the sting in Case 1 further demonstrates the ability of the present algorithm for a complicated configuration, such as a cylinder-sting assembly in which solid surfaces meet. The main reason, however, is to simulate the complete experimental configuration designed for the validation of the computer code developed with this algorithm. The interference patterns are known to be significantly different when the cylinder is placed inside a cavity (Stallings et al., 1990). Hence, Case 2 is devoted to this type of flow. The configuration for Case 2 does not contain the sting in an attempt to obtain a better understanding of flow between the cylinder base and the cavity rear face. Besides, such a sting certainly does not exist in an application environment, such as an internally carried store separating from its parent body during the flight.

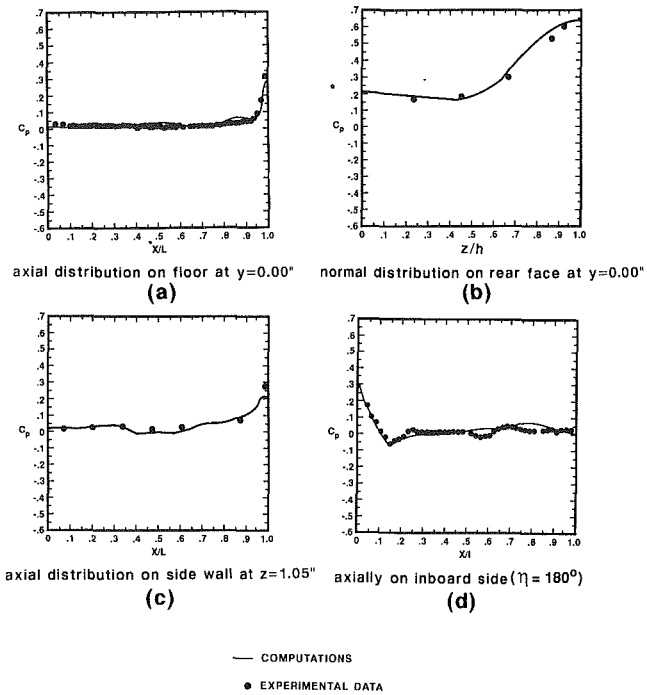

Fig. 3 Time averaged surface pressure coefficient distributions for Case 1

Roe's flux-difference splitting along with the min-mod limiter (Eq. (8)) is used for flowfield initialization of both the cavity and the cylinder. However, this method fails for the subdomain of the sting. The sharp leading edge and the blunt trailing edge of the sting, and its upright position perpendicular to the freestream velocity are believed to contribute to a rather difficult test for the solution algorithm. Subsequently, both upwind methods (FVS and FDS) along with each one of the three limiters (Eqs. (8)–(13)) are tested. The solution of the supersonic flow about the sting is obtained only when the FVS method along with the Spekreijse (1987) limiter is employed.

The computed values of the averaged pressure coefficient (C_p) distributions on the cavity surface and the cylinder for Case 1 are presented in Fig. 3 in comparison with the experimental data. In Figs. 3(a–b), C_p distributions are plotted along the horizontal centerline of the floor (F) and the vertical centerline of the rear face (RF). The pressures are near the freestream value on most of the F, but they increase near and along the RF. The same trend is observed in Fig. 3(c) for the side wall (SW). The longitudinal C_p distribution on the inboard surface of the cylinder ($\eta = 180$ deg) shows the sharp increase owing to the nose shock followed by the expansion around the forebody (Fig. 3(d)). In comparison with the results of clean cavity (Baysal and Yen, 1990), these results show that the cylinder has very small effect on pressure distributions on the centerline of the cavity. In any event, the computed C_p values compare very well with the experimental data at all locations. It should be noted that these values vary with time for this unsteady flow and the only basis for comparison is through time averaging and agreement becomes better with longer elapsed times of averaging. However, the initial time and the elapsed time of the averaging process are different for the computations and the measurements. Also, a true characteristic time for averaging is not evident since the flow fluctuations are nonperiodic at supersonic speeds (Baysal et al., 1988a, 1988b, 1990). The measured surface pressure data are averaged values of over 100 measurements obtained within a time span of 2 to 3 seconds. The surface pressure distributions in this study are averaged over a period of approximately 3 ms. The averaging is done over 11,000 computed values.

The instantaneous streamwise Mach number contours at the

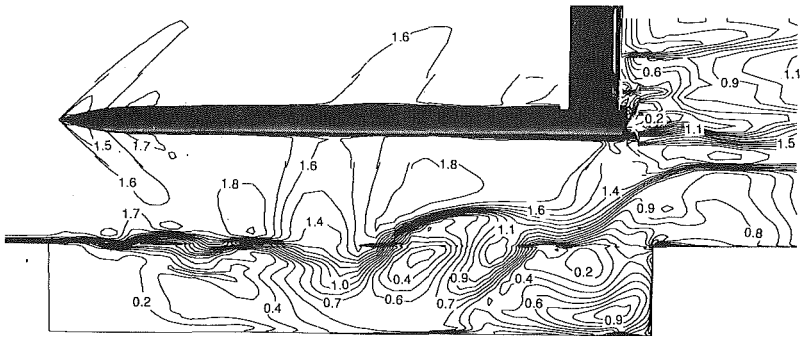

Fig. 4 Instantaneous Mach contours on the symmetry plane of Case 1

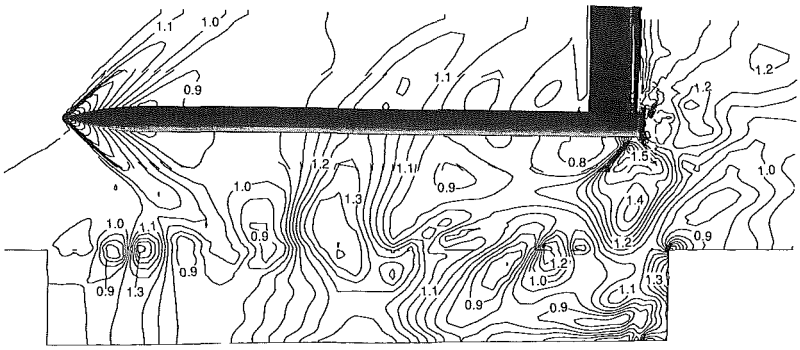

Fig. 5 Instantaneous Mach contours on the symmetry plane of Case 1

plane of symmetry ($Y = 0.0$) for Case 1 are displayed in Fig. 4. Evident in this figure is the undulation of the free shear layer which is formed between the high speed external flow and the slower internal flow. For a clean cavity (no interference) with $L/D \approx 6.0$, the shear layer is known to be inherently unstable and continuously pulled into and pushed out of the cavity as a result of the pressure oscillations inside the cavity (Baysal et al. 1988a; Srinivasan and Baysal, 1991). The shear layer is deflected down when the pressure inside the cavity is below the freestream pressure. At this instant, air is pumped into the cavity. This air mass is then slowed down by various dissipative processes within the cavity and this in turn increases the cavity pressure above the freestream value. The shear layer is then deflected out of the cavity by the excess pressure and the mass is pumped out of the cavity. However, this cycle is changed when a cylinder is placed near the cavity. The pressure of the flow between the shear layer and the inboard side of the cylinder is increased due to the nose shock of the cylinder and its reflection off of the shear layer. The rise in the pressure value then causes the shear layer to deflect downward deep inside the cavity. The formation of the wake flow at the base of the cylinder and the blunt trailing edge of the sting and its interference with the shear layer are also shown in Fig. 4.

The vortical nature of the shear layer is depicted in Fig. 5. This figure also shows the expansion at the sharp corner of the front face and the compression at the rear face of the cavity. Also shown is the nose shock on the cylinder and impingement of this shock on the shear layer. The flow over a cylinder at $\alpha = 0°$ is typically a steady flow, i.e., computed force and momentum coefficients remain virtually constant after reaching convergence. The unsteady nature of the cylinder-near-cavity flow is captured computationally and are presented in Fig. 6. The oscillation of the normal force coefficient, C_N, due to this unsteadiness is observed over a period of 1.59 ms. The computed mean value of the axial force coefficient C_A and C_N of the cylinder over this period are (0.3532) and (0.0056), respectively. The experimentally measured values of C_A and C_N are (0.3756) and (-0.0258), respectively.

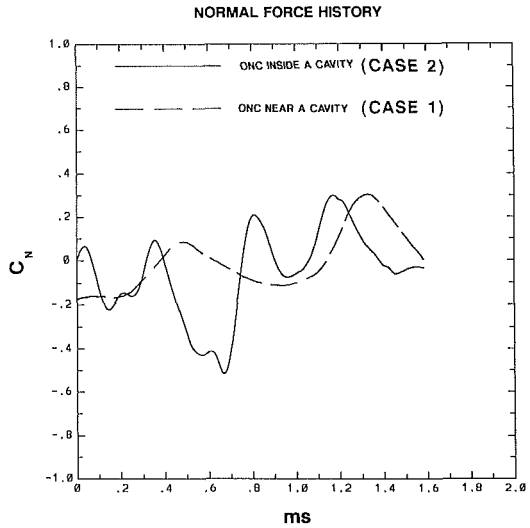

Fig. 6 Variation of C_N with time over a period of 1.59 ms for Case 1 and Case 2

The instantaneous total pressure contours of the symmetry plane show the complicated flow structure of Case 2 (Fig. 7). The shear layer separates the supersonic external flow and the low speed flow inside the cavity. The nose shock on the cylinder apparent in Case 1 does not occur here due to this low speed flow. The pressure difference between the external and the internal flows just downstream of the forebody junction causes the inward deflection of the shear layer and its impingement on the outboard surface ($\eta = 0$ deg) of the cylinder. The wavy motion of the shear layer causes it to impinge on the cylinder again and then deflect out of the cavity due to higher pressure near the RF. At this instant, some air is pumped into the cavity from behind the base of the cylinder. As the flow streams into the cavity through the opening between the base and RF, it is slowed down by dissipative processes inside the cavity and it separates near the floor. This clockwise rotating vortex is il-

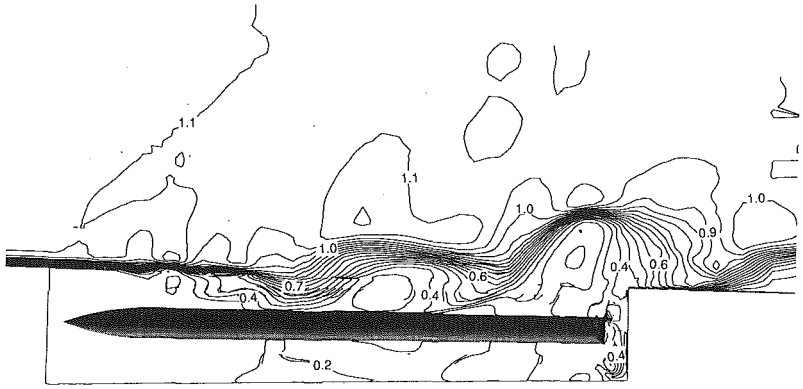

Fig. 7 Instantaneous normalized total pressure contours on the symmetry plane of Case 2

Fig. 8 Instantaneous streamlines on the symmetry plane of cavity for Case 2

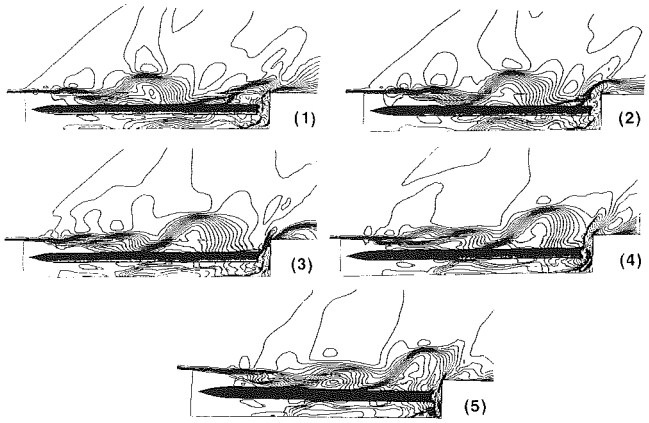

Fig. 9 Instantaneous Mach contours on symmetry plane of Case 2. Frame interval = 1/4 ms.

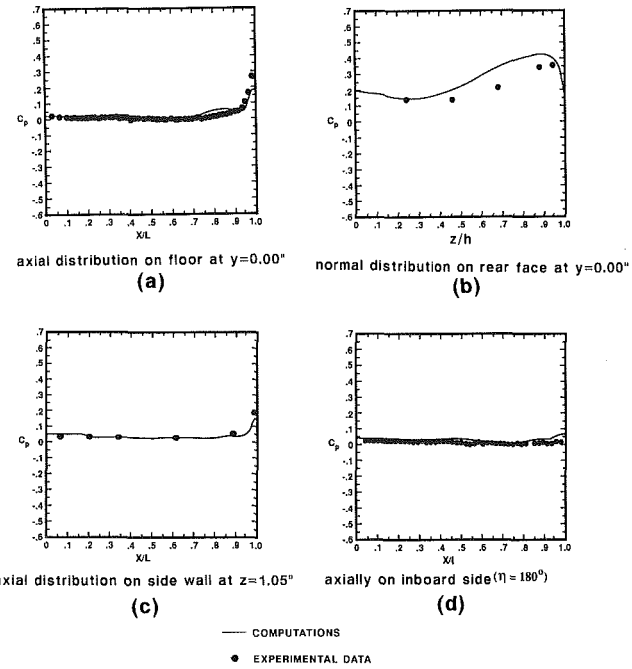

Fig. 10 Time averaged surface pressure coefficient distributions for Case 2

lustrated through the instantaneous streamlines of the symmetry plane (Fig. 8). Shown in this figure are a relatively weak vortex structure near the FF and a counter clockwise rotating vortex near the floor downstream of the forebody junction. The flow is shown to separate on the outboard side of the cylinder (η = 0 deg) just prior to the first impingement and immediately after the second impingement.

The unsteady nature of the flowfield and the interaction of the shear layer with the cylinder are illustrated in Fig. 9, where Mach number contours of symmetry plane at five consecutive instants over a period of 1 ms are shown. The shape of the shear layer and in turn its points of contact with the cylinder constantly change with time. This motion of the shear layer and its interaction with the rear lip of the cavity was shown to generate shedding of vortices (Baysal and Yen, 1990).

Time averaged pressure coefficients on various surfaces of the cavity and the cylinder are presented in Fig. 10. The trend of computed C_p distribution on most surfaces agree very well with the data of Stallings et al. (1990). The discrepancy in the distribution of RF is attributed to the sting, which exists in the experimental model but not in the computational model. The computed C_p at the vertical centerline of RF is slightly higher than the experimental data. This effect is also evident on the surfaces of the cylinder. The mean value of C_A and C_N for the cylinder over a period of 1.59 ms are (0.0580) and (-0.0551), respectively. The experimental values (Stallings et al., 1990) for C_A is (0.0283) and for C_N is (-0.0611). The variation of C_N over this period is illustrated in Fig. 6. The difference between a high and a low instantaneous values of C_N, which may be interpreted as the amplitude, is much larger for Case 2 than it is for Case 1. This is expected since the unsteadiness is much more pronounced inside the cavity.

Conclusions

An algorithm is developed to obtain solutions for flows about arbitrary complex configurations with multiple and nonsimilar components. The algorithm uses a hybrid domain decomposition technique and solves the time-dependent, Reynolds-averaged, compressible, full Navier-Stokes equations on each subdomain.

The algorithm is applied to solve the supersonic flow over an ogive-nose-cylinder near a cavity. The cylinder is attached to an offset L-shaped sting to simulate the complete experimental configuration designed for the validation of the computer code developed with this algorithm. Generally, good agreement between the computational results and the experi-

mental data is obtained. A similar configuration without the offset sting is considered for further validation of the current algorithm. The component grids of the previous configuration are reused to form the composite grid for this configuration. In this case the cylinder is placed inside the cavity. The unsteady nature of this flowfield and the interaction of the shear layer with the cylinder are simulated. Computationally obtained pressure coefficient distributions on most surfaces agree very well with the experimentally measured data. However, some discrepancies are observed due to the elimination of the offset sting from the computational configuration.

In the case of an internally carried store separating from its bay at supersonic speeds, various types of interference are encountered. The results presented in this study demonstrate two of the most important types of interference. The results of the present computation should contribute to the much needed database for the internal store carriage and separation. Future investigations should include the rigid body dynamics into the algorithm to study effects of the induced flow generated by the moving bodies.

Due to the generality of the present computational method, it can be used for other applications, such as, propulsion integration simulation and studies of ground effects. Other steps should also be taken to capitalize on the advantages of the domain decomposition as it relates to parallel processing. Each processor can be assigned to a separate subdomain. The only extra programming effort for such concurrent processing is the exchange of intergrid boundary data.

Acknowledgment

This work is supported by NASA Langley Research Center under the grant NAG-1-664. The technical monitor is D. S. Miller. Composite grids are generated with the help of V. R. Lessard.

References

Baldwin, B. S., and Lomax, H., 1978, "Thin-Layer Approximation and Algebraic Model for Separated Turbulent Flows," AIAA Paper 78-257.

Baysal, O., Srinivasan, S., and Stallings, R. L., Jr., 1988a, "Unsteady Viscous Calculations of Supersonic Flows Past Deep and Shallow 3-D Cavities," AIAA Paper 88-0101.

Baysal, O., and Stallings, R. L., Jr., 1988b, "Computational and Experimental Investigations of Cavity Flowfields," *AIAA Journal*, Vol. 26, No. 1, pp. 6–8.

Baysal, O., Fouladi, K., and Miller, D. S., 1989, "Computations of Supersonic Flows Over a Body at High Angles of Attack," *AIAA Journal*, Vol. 27, No. 4, pp. 427–437.

Baysal, O., and Yen, G.-W., 1990, "Implicit and Explicit Computations of Flows Past Cavities With and Without Yaw," AIAA Paper No. 90-0049.

Baysal, O., Fouladi, K., and Lessard, V. R., 1991, "Multigrid and Upwind Viscous Flow Solver on 3-D Overlapped and Embedded Grids," *AIAA Journal*, Vol. 29, No. 6, pp. 903–910.

Baysal, O., Fouladi, K., Leung, R. W., and Sheftic, J. S., 1992, "Interference Flows Past Cylinder-Fin-Sting-Cavity Assemblies," *Journal of Aircraft*, Vol. 29, No. 2, pp. 194–202.

Benek, J. A., Steger, J. L., and Dougherty, F. C., 1983, "A Flexible Grid Embedding Technique with Application," AIAA Paper No. 83-1944.

Berger, M. J., 1987, "On Conservation at Grid Interfaces," *SIAM Journal of Numerical Analysis*, Vol. 24, No. 5, pp. 986–983.

Chakravarthy, S. R., and Osher, S., 1983, "Computing with High Resolution Upwind Scheme for Hyperbolic Equations," AMS-SIAM Summer Seminar on Large Scale Computational in Fluid Dynamics, La Jolla, CA, June–July.

Nakahashi, K., and Obayashi, S., 1987, "Viscous Computations Using a Composite Grid," AIAA Paper No. 87-1128.

Om, D., 1988, "Navier-Stokes Simulation for Flow Past an Open Cavity," *Journal of Aircraft*, Vol. 25, No. 9, pp. 842–848.

Rizzeta, D. P., 1988, "Numerical Simulation of Supersonic Flow Over a Three-Dimensional Cavity," *AIAA Journal*, Vol. 26, No. 7, pp. 799–807.

Spekreijse, S. P., 1987, *Multigrid Solution of the Steady Euler Equations*, Ph.D. dissertation, Centrum voor Wiskunde en Informatica, Amsterdam, The Netherlands.

Srinivasan, S., and Baysal, O., 1991, "Navier-Stokes Calculations of Transonic Flows Past Cavities," *Advances and Applications in Computational Fluid Dynamics*, Ed, O. Baysal, ASME-FED-Vol. 66, Nov. 1988, pp. 121–133. Also ASME JOURNAL OF FLUIDS ENGINEERING, Vol. 113, No. 3, pp. 368–376.

Stallings, R. L., Jr., Wilcox, F. J., Jr., 1987, "Experimental Cavity Pressure Distributions at Supersonic Speeds," NASA-TP-2683.

Stallings, R. L., Jr., Wilcox, F. J., Jr., and Forrest, D. K., 1990, "Measurements of Pressures, Forces and Moments on a Generic Store Separating From a Box Cavity at Supersonic Speeds," NASA-TP-3110.

Suhs, N. E., 1987, "Computations of 3-D Cavity Flow at Subsonic and Supersonic Mach Number," AIAA Paper No. 87-1208.

Thomas, J. L., Taylor, S. L., and Anderson, W. K., 1987, "Navier-Stokes Computations of Vortical Flows Over Low Aspect Ratio Wings," AIAA Paper No. 87-0207.

Van Albada, G. D., Van Leer, B., and Roberts, W. W., 1982, "A Comparative Study of Computational Methods in Cosmis Gas Dynamics," *Astronomy and Astrophysics*, Vol. 108, pp. 76–84.

Van Leer, B., Thomas, J. L., Roe, P. L., and Newsome, R. W., 1987, "A Comparison of Numerical Flux Formulas for the Euler and Navier-Stokes Equations," AIAA 87-1104.

Y. C. Leung
Environmental Engineer,
Hong Kong Electric Co., Ltd.,
Hong Kong

N. W. M. Ko
Professor.
Mem. ASME

K. M. Tang
Undergraduate Student.

Department of Mechanical Engineering,
University of Hong Kong,
Hong Kong

Flow Past Circular Cylinder With Different Surface Configurations

Measurements of the mean pressure distributions and Strouhal numbers on partially grooved cylinders with different groove subtend angles were made over a Reynolds number range of 2.0×10^4 to 1.3×10^5 which was within the subcritical regime of smooth cylinder. The Strouhal number, pressure distributions, and their respective coefficients were found to be a function of the groove subtend angles. In general, a progressive shift of the flow regime to lower Reynolds number was observed with higher subtend angle and a subtend angle of 75 deg was found for optimum drag reduction. With the configuration of asymmetrical groove surface, lower drag, and higher lift coefficients were obtained within the same Reynolds number range. Wake traverse and boundary layer results of the asymmetric grooved cylinder indicated that the flows at the smooth and groove surfaces lied within different flow regimes and a downward shift of the wake.

Introduction

For flow over circular cylinder, surface roughness has been found to affect the vortex shedding, drag, and heat-transfer characteristics (Achenbach, 1971; Guven et al., 1980; Achenbach and Heinecke, 1981; Nakamura and Tomonari, 1982; and Buresti, 1983). The effects of surface roughness were found to promote boundary-layer transition and significantly affected the subsequent flow development at Reynolds numbers higher than the subcritical regime. Generally, the drag coefficient and Strouhal number of rough cylinders varied with Reynolds number in a way similar to those of a smooth cylinder, an increase in surface roughness moving the curves towards lower Reynolds numbers. This shift provided a means in producing effective high Reynolds number flow at relatively low Reynolds number. The surface roughness was produced by using commercial sandpaper (Guven et al., 1980), polystyrene particles (Nakamura and Tomonari, 1982) and pyramidal surface roughness produced by knurling process (Achenbach and Heinecke, 1981). Except in the pyramidal surface roughness, the other were of random nature.

In the earlier parts of the present investigation the flow over circular cylinder with streamwise grooves covering the whole cylinder within the subcritical Reynolds number regime of a smooth cylinder was studied (Ko et al., 1987; Leung and Ko, 1987; and Leung and Ko, 1991). Different groove configurations, such as V-groove, square groove and trapezoidal groove, were adopted. Based on the division of the flow regimes of Achenbach (1971), it was found that transition from subcritical to critical and from critical to supercritical flow regimes occurred at lower Reynolds number for the grooved cylinder than for the smooth cylinder. In the subcritical regime laminar separation and in the critical regime laminar separation, turbulent reattachment (separation bubble) and turbulent separation were observed. Based on an equivalent diameter, taking into account of the increase in surface area due to the grooves, the Reynolds number trends were nearly the same for the grooved and smooth cylinders.

Since the earlier parts only concerned cylinder with streamwise grooves covering the whole cylinder, this part of the investigation concerned flow over cylinder with symmetrical and asymmetrical covering of grooves over only part of the cylinder. It was hoped to study the effect of lesser groove surface on the flow characteristics such as lift and drag. It is anticipated that this investigation offers a means in the manipulation of the lift and drag not only of circular cylinder but of bluff body and aerofoil.

Experimental Arrangement

The experiments were carried out in a wind tunnel with a test section measuring 56 × 56 cm. The freestream turbulence intensity was about 0.4 percent at 22 m/s. The diameter of the cylinder tested was 88.5 mm. The blockage ratio for the cylinder was 16 percent. The effect of blockage ratio was corrected by applying the formulae of Allen and Vincenti (1930). End plates were used to eliminate the effect of the tunnel boundary layers. The aspect ratio ℓ/d for the cylinder was 4.3. The range of Reynolds number was from about 2.0×10^4 to 1.3×10^5 and was within the subcritical Reynolds number regime of smooth cylinder. The adoption of the diameter of the cylinder was for optimum boundary layer measurements. The present aspect ratio of 4.3 was within the range of 3.12 to 6.14 of past workers (Achenbach, 1968; Achenbach, 1971; Guven et al., 1980; Achenbach and Heinecke, 1981; Nakamura and Tomonari, 1982; Celik and Patel, 1982 and Farell and Blessmann, 1983). The present blockage ratio of 16 percent was also within the range of 12 percent to 18 percent of above workers. The

Contributed by the Fluids Engineering Division for publication in the JOURNAL OF FLUIDS ENGINEERING. Manuscript received by the Fluids Engineering Division September 20, 1990. Associate Technical Editor: Chih-Ming Ho.

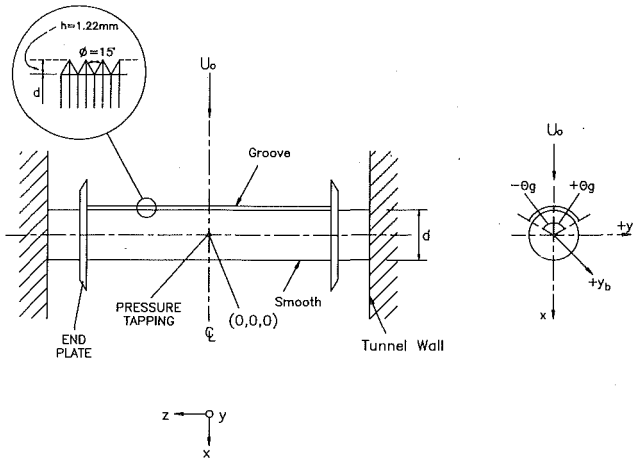

Fig. 1 Schematic diagram of V-groove circular cylinder

turbulence intensities 0.12 percent to 0.7 percent of the wind tunnels of above workers were of the same order of magnitude as that of the present investigation. Further, the effect of aspect ratio on the mean static pressure coefficients and drag coefficient of the present set-up was investigated (Leung and Ko, 1991). It was found that except at the critical Reynolds number two-dimensionality was found at aspect ratio greater than 2.0.

The surface configurations studied are shown in Fig. 1. V-groove of height of 1.22 mm and angle ϕ of 15°, giving h/d of 13.8×10^{-3}, was adopted. The adoption of this V-groove configuration was due to its near lowest drag coefficient (Leung and Ko, 1991) and the shift to lower Reynolds number such that flow characteristics in higher flow regime could be studied. The subtend angle θ_g of the grooves from the front stagnation point on the cylinder surface varied from ± 30 to ± 165 deg. There were two other cylinders of $\theta g = {}^{+180\text{ deg}}_{-0\text{ deg}}$ and ${}^{+75\text{ deg}}_{-0\text{ deg}}$, that is, grooves from 0 to 180 deg and 0 to 75 deg, respectively but smooth on the other half. The diameter of the bottom of the groove was the same as that of the smooth portion downstream of the groove. These two cylinders were used to study the interaction of the flow over the groove and smooth surfaces of the cylinder. Because of the small dimensions involved, it was difficult to obtain identical configurations of the V-grooves across the span of the cylinder. The dimensions were the averaged results of a few samples of the V-groove. Circumferential pressure taps at 7.5 deg interval were located at the midsection. The pressure taps had an inner diameter of 0.6 mm and were centered in the V-groove. However, because of the small dimensions of the V-grooves, each pressure tap covered more than one groove.

In order to study the spanwise uniformity of flow under the conditions of symmetrical and asymmetrical mean static pressure distributions within the subcritical and critical flow regimes, three single hot wires, each separated by a lateral spacing of 2 mm and located at $x/d = 0.75$ and $y/d = 0.5$ downstream of the cylinder, were used.

From the mean static pressure distribution, the base pressure coefficient C_{pb}, the minimum pressure coefficient C_{pm} and the approximate location θ_w of the beginning of the wake region were also determined (Guven et al., 1980 and Niemann, 1971). As discussed by Guven et al. (1980), θ_w indicates the approximate position at which the boundary layer separates. The drag coefficient C_d was calculated from the integration of the pressure distribution around the whole cylinder. For the asymmetrical grooved cylinder, due to the uneven pressure distributions on the two halves, both lift and drag coefficients were obtained.

For the measurements of mean and fluctuating velocities downstream of the cylinder, cross-wire probe was used. All the wire had a diameter of 5×10^{-6} m and a working length of 2 mm. Velocity traverses at several planes were carried out and the signals were acquired and digitally analyzed by a Digital Minicomputer VAX 11/750. The Strouhal number of the vortex wake thus obtained was not corrected for blockage.

Boundary layer of the cylinder was studied by means of a single hot-wire which was mounted on a computer controlled table and was translated radially or normally to the cylinder surface, that is, in the y_b direction from outside toward the top of the grooves or surface of the cylinder.

The experimental uncertainty of the data was as follows: the mean velocity ± 3 percent, fluctuating velocity ± 5 percent and linear dimensions ± 0.1 mm; the uncertainty of the nondimensional groups such as distance ratio ± 1 percent and pressure coefficient ± 0.1.

Results and Discussion

Cylinder With Symmetrical Groove. Figures 2(*a*) to (*e*) show the respective static pressure distributions measured on the cylinder of $\theta_g = \pm 45$, ± 60, ± 75, ± 90 and ± 135 deg at the Reynolds number range 2.2×10^4 to 1.3×10^5, which is within the subcritical regime of smooth cylinder. As will be shown later, the results at $\theta_g > \pm 135$ deg are similar to those at $\theta_g = \pm 135$ deg. Thus, they are not presented. At $\theta_g < \pm 75$ deg the slight increase in the static pressure at $\theta = \theta_g$ is due to the expansion of the flow from the groove smooth surfaces. This slight increase in the static pressure at the junction is not obvious in the distributions of $\theta_g \geq \pm 75$ deg when the grooves extended into region where adverse pressure gradient occurs. However, as indicated later this small change in static pressure results in drastic change in the boundary layer characteristics.

Asymmetry of the pressure distribution is found for all the

Nomenclature

C_d = drag coefficient
C_{dm} = minimum drag coefficient
C_l = lift coefficient
C_p = pressure coefficient $(p-p_o)/\frac{1}{2}\rho U_o^2$
C_{pb} = base pressure coefficient
C_{pm} = minimum pressure coefficient
d = diameter of cylinder
h = depth of V-groove
ℓ = length of cylinder
p = static pressure
p_o = freestream static pressure
Re = Reynolds number, $U_o d/\nu$
$\mathrm{Re_{cr}}$ = critical Reynolds number
Re_i = approximate Reynolds number when inflexion point still found
St = Strouhal number, fd/U_o
U_E = edge mean velocity at boundary layer
U_o = freestream mean velocity
U_T = vortex transport velocity
u = streamwise velocity fluctuations
u_R, v_R = recovered streamwise and lateral velocities
x, y, z = streamwise, lateral, and spanwise coordinates, respectively
y_b = distance normal to surface of cylinder from bottom of grooves
δ = boundary layer thickness
δ_1 = displacement thickness
δ_2 = momentum thickness
ν = kinematic viscosity
ϕ = angle of V-groove
θ_g = V-groove subtend angle
θ_i = angle of inflexion point of pressure distribution
θ_w = angle at the beginning of wake region

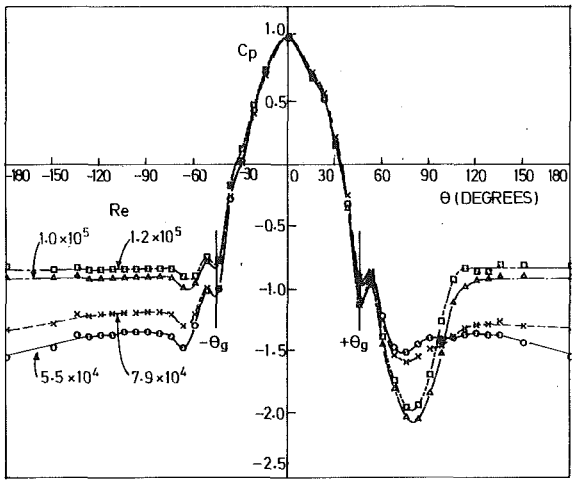

Fig. 2(*a*) $\theta_g = \pm 45$ deg

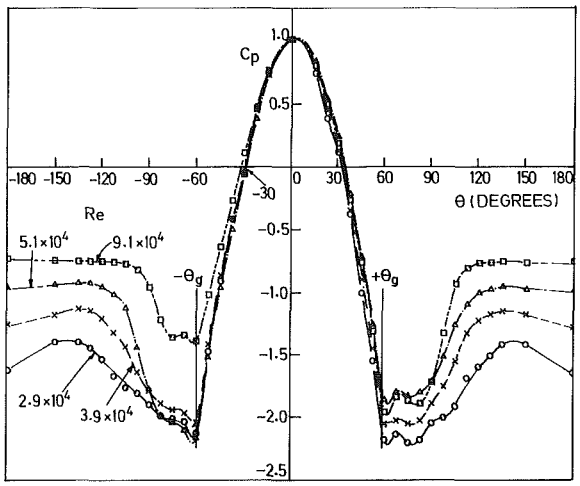

Fig. 2(*b*) $\theta_g = \pm 60$ deg

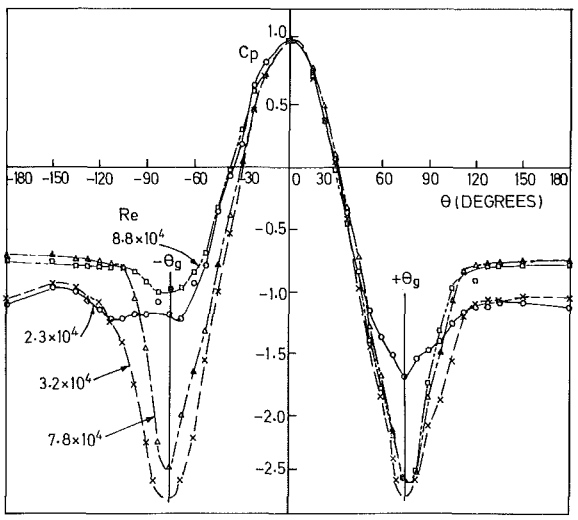

Fig. 2(*c*) $\theta_g = \pm 75$ deg

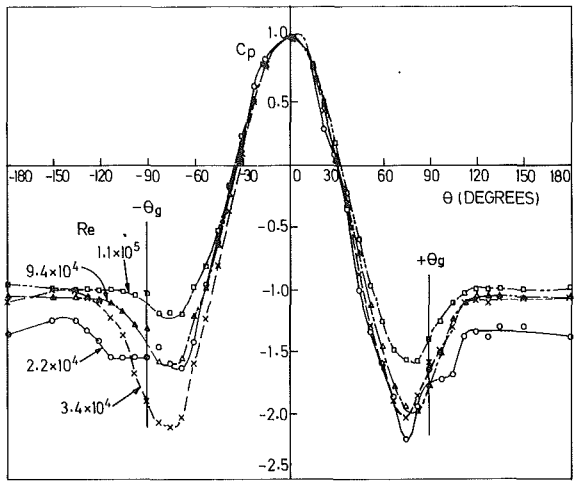

Fig. 2(*d*) $\theta_g = \pm 90$ deg

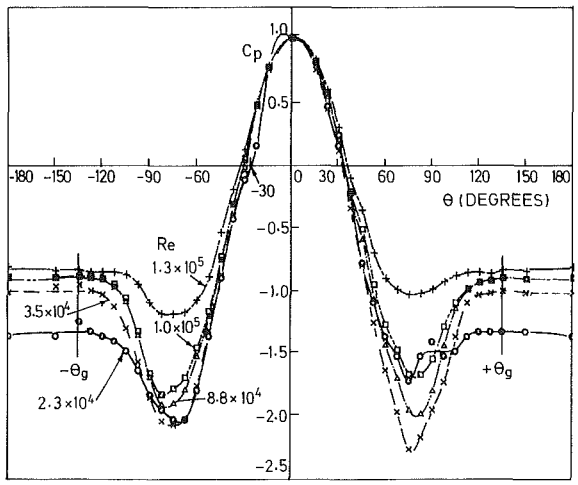

Fig. 2(*e*) $\theta_g = \pm 135$ deg

Fig. 2 Pressure distributions on cylinder at different groove subtend angles

groove configuration tested. The approximate lowest Reynolds number, where asymmetry still occurs, is found to be function of the groove subtend angle θ_g and is tabulated in Table 1. There is a progressive shift from Re = 9.0×10^4 at $\theta_g = \pm 30$ deg to Re = 2.0×10^4 at $\theta_g = \pm 75$ deg. At $\theta_g > \pm 75$ deg it is independent of Reynolds number. As had been observed before by Ko et al. (1987), this Reynolds number is lower than that of smooth cylinder of about Re = 3.0×10^5 (Farell and Blessmann, 1983).

The spanwise variations of the flow at different Reynolds numbers were investigated. Typical examples for the cylinder with $\theta_g = \pm 45$ deg are shown in Fig. 3. Spanwise uniformity is observed for Re = 5.5×10^4 (Fig. 3(*a*)) but not for Re = 7.9×10^4, where asymmetric pressure distribution is found (Fig. 3(*b*)). This asymmetry in the pressure distribution, together with the spanwise non-uniformity, marks the beginning of the critical regime.

The static pressure distributions of $\theta_g = \pm 75$ deg have the lowest minimum pressure coefficient and highest base pressure coefficient within the critical regime (Fig. 2(*c*)). Within the same Reynolds number range the static pressure distributions at $\theta_g \geq \pm 90$ deg are different from those at $\theta_g = \pm 75$ deg with higher minimum pressure coefficient and lower base pressure coefficient (Figs. 2(*d*) and 2(*e*)). The distributions of $\theta_g > \pm 135$ deg at the same Reynolds number are basically the same and they are not presented.

The inflexion point, defined as the flat plateau in the static pressure profile, indicates the presence of the separation bubble due to the laminar separation and turbulent reattachment (Farell and Blessmann, 1983). The approximate Reynolds number Re_i and angle θ_i, where inflexion point is still found, are also tabulated in Table 1. Those of smooth cylinder of Achenbach (1968), Farell and Blessmann (1983), Fage and Falkner (1931),

Table 1 Different Reynolds numbers, minimum coefficients, and inflexion points of V-groove cylinders

θ_g (deg)	Re [a]	Re_{cr}	C_{dm}	Re_i [b]	θ_i (deg)	θ_w-θ_i (deg)	
	3.7×10^5	3.8×10^5	0.25	2.3×10^5	81	22	Farell and Blessmann (1983)
				3.3×10^5	84	23	
				3.4×10^5	80	29	
				2.1×10^5	91	26	Fage and Falkner (1931)
				6.7×10^5	100	22	Flachsbart (1932)
				8.5×10^5	105	31	Achenbach (1968)
				9.2×10^5	97	27	James et al. (1980)
				1.3×10^6	99	28	
				4.8×10^5	103	27	Van Nunen (1972)
±30	9.0×10^4	-	-	1.0×10^5	82	26	
±45	6.0×10^4	-	-	7.9×10^4	90	23	
±60	2.5×10^4	8.0×10^4	0.64	2.9×10^4	90	28	
±75	2.0×10^4	4.0×10^4	0.52	2.3×10^4	86	29	
±90	2.0×10^4	3.0×10^4	0.82	2.2×10^4	90	24	
±105	2.0×10^4	2.8×10^4	0.94	2.4×10^4	90	24	
±120	2.0×10^4	3.2×10^4	0.80	2.4×10^4	90	23	
±135	2.0×10^4	3.5×10^4	0.78	2.3×10^4	90	24	
±165	2.0×10^4	4.2×10^4	0.77	2.3×10^4	90	25	
±180	2.2×10^4	1.0×10^5	0.77				
±180	7.2×10^4			7.2×10^4	80	32	Ko et al. (1987)
	6.3×10^4			6.0×10^4	80	32	

[a] Approximate lowest Reynolds number when asymmetry in static pressure distribution was found.

[b] Approximate Reynolds number when inflexion point was still found.

Flachsbart (1932), James et al. (1980), and Van Nunen (1972) are also tabulated. As the case of asymmetry of the static pressure distribution, there is a progressive shift to lower Reynolds number Re_i from $\theta_g = 0$ to ± 75 deg. This indicates that increase in the groove subtend angle causes earlier formation of the separation bubble and hence reduces the Reynolds number Re_i. At $\theta_g \geq \pm 75$ deg the Reynolds number Re_i is nearly the same. In compared with smooth cylinder the Reynolds number Re_i is lower. The corresponding angle for smooth cylinder varies from 80 to 105 deg. Within the single-bubble regime which is denoted by the asymmetry of the pressure profile, large increase in $|C_{pm}|$ and much smaller spectral peak of vortex shedding (Farell and Blessmann, 1983), the inflexion angle lies between 80 to 91 deg while it is slightly higher within the twin-bubble regime which is denoted by sharp change in drag coefficient, $|C_{pm}|$ and $|C_{pb}|$. For the present V-groove cylinders and those of previous investigation, the inflexion angle also lies between 80 to 90 deg which coincide with those of smooth cylinders (Table 1).

Asymmetry at higher Reynolds number range than that of the critical regime is also found in the static pressure distribution. For $\theta_g = \pm 75$ deg the asymmetry at $7.8 \times 10^4 \leq Re \leq 8.8 \times 10^4$ and symmetry again at $Re = 1.0 \times 10^5$ (which is not shown here) suggest the flow is within the supercritical regime.

Based on the above static pressure distributions and those not shown here, the drag coefficients C_d, the pressure rise to separation ($C_{pb} - C_{pm}$) and the approximate location of the beginning of wake region θ_w are shown in Figs. 4 to 6, respectively. The uncorrected Strouhal numbers St are shown in Fig. 7. The corresponding results of smooth cylinder of the present investigation are also included in these figures. For simpler presentation the following sections will mainly discuss the results based on drag coefficient even though other coefficients have also been taken into consideration.

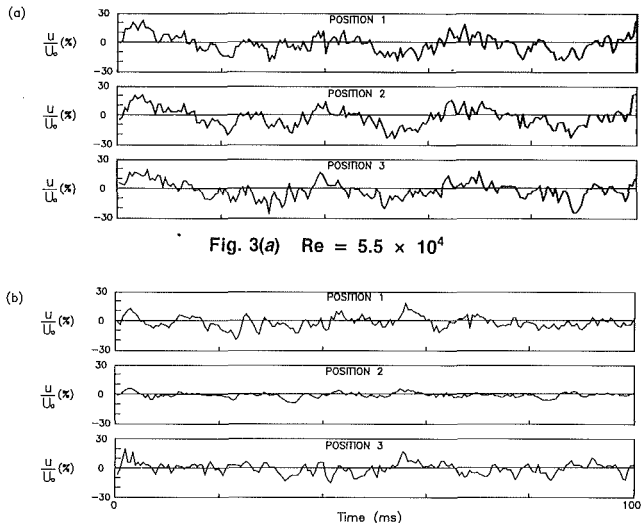

Fig. 3(*a*) Re = 5.5×10^4

Fig. 3(*b*) Re = 7.9×10^4

Fig. 3 Spanwise velocity fluctuations for $\theta_g = \pm 45$ deg

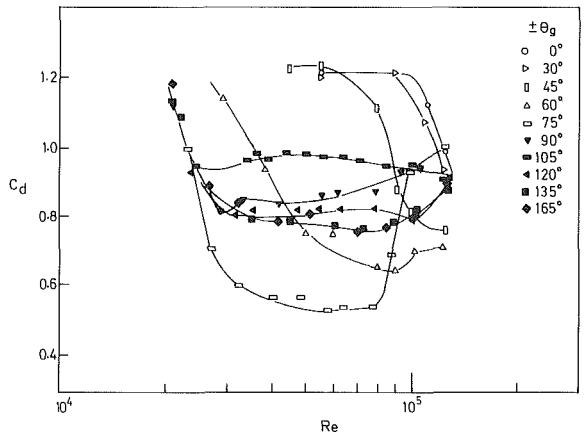

Fig. 4 Drag coefficients at different groove subtend angles

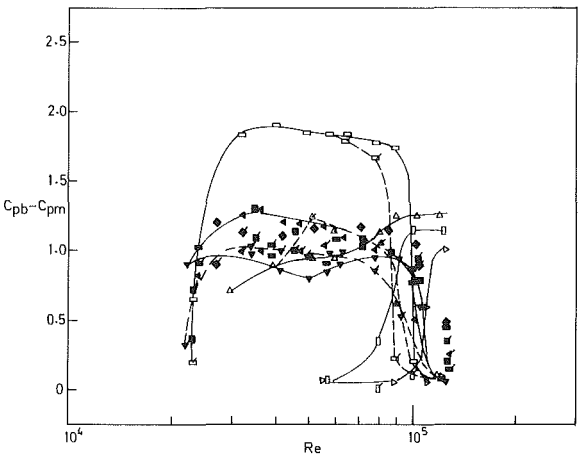

Fig. 5 $C_{pb} - C_{pm}$ at different θ_g. No Flag: 0-180 deg; Flagged: 180-360 deg (other symbols as in Fig. 4)

There is a progressive shift of the drag coefficient curves to lower Reynolds number till $\theta_g = \pm 75$ deg. The shift results in the transition from subcritical regime of St = 0.21 to critical regime of progressively higher Strouhal number. At $\theta_g > \pm 75$ deg the shift is constant and at the beginning of the critical regime the drag coefficients fall on one curve up to Reynolds number of about 2.3×10^4. This Reynolds number of $2.3 \times$

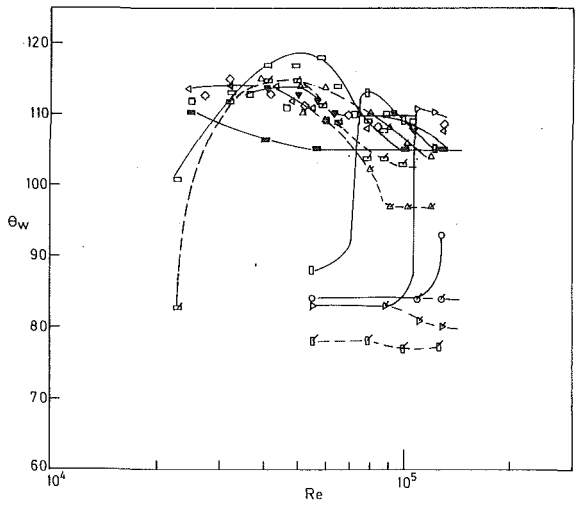

Fig. 6 Wake angle at different θ_g (symbols as in Figs. 4 and 5)

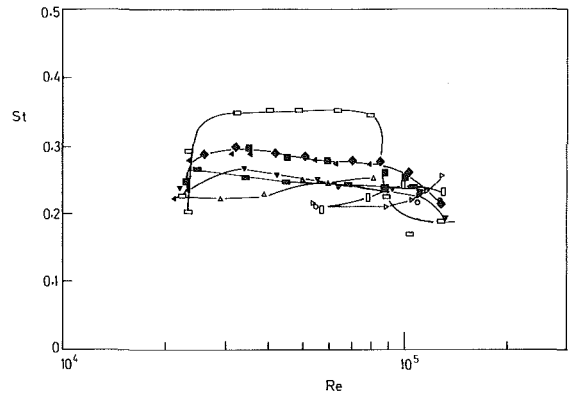

Fig. 7 Strouhal number (uncorrected) at different θ_g (symbols as in Fig. 4)

10^4 is nearly the same as the approximate Reynolds number when inflexion point was still found at $\theta_g \geq \pm 75$ deg (Table 1). This means that at $\theta_g \geq \pm 75$ deg the inflexion point and the critical Reynolds number are independent of the groove subtend angle θ_g. This phenomenon is expected because of nearly the same inflexion point θ_i, be it of smooth or V-groove cylinders and the laminar boundary layer requires the same distance for its separation. The presence of the V-grooves and the associated change in skin friction only change the effect of Reynolds number, resulting in separation at lower Reynolds number. For this case of $\theta_g > \pm 75$ deg, the groove subtend angle is very close to or greater than the inflexion point θ_i of about 90 deg. This may impose the same effect on the laminar boundary layer, which results in the observed phenomenon.

It is interesting to note that despite the slight variations in θ_i between the single and twin-bubble regimes, the angle between the wake angle and inflexion angle $(\theta_w - \theta_i)$ as tabulated in Table 1, is nearly the same for the grooved and smooth cylinders. The former θ_w indicates the approximate location of separation of the turbulent boundary layer and the latter θ_i of separation of the laminar boundary layer. Since the present results only represent those within the single-bubble regime, it is not sure whether the above is also true for the twin-bubble regime. Most probably, as for the case of smooth cylinder, the formation of twin-bubble affects the inflexion point but not the difference in the angle $(\theta_w - \theta_i)$. Thus, it suggests that the distance from the formation of the separation bubble to the separation of the reattached turbulent boundary layer is constant and is independent of surface configuration. This means that the reattached turbulent boundary layer is not significantly affected by the surface condition of the cylinder.

Beyond the similarity there is a big variation in the drag coefficients with groove subtend angle θ_g, suggesting big variation in the flow within the critical regime. The minimum drag coefficients and critical Reynolds numbers $\mathrm{Re_{cr}}$, as tabulated in Table 1, have the lowest C_{dm} of 0.52 at $\theta_g = \pm 75$ deg and highest of 0.94 at $\theta_g = \pm 105$ deg. $\mathrm{Re_{cr}}$ is defined as the Reynolds number at which minimum drag coefficient C_{dm} occurs. However, due to the difficulty in determining C_{dm}, such as the distributions of $\theta_g \geq \pm 75$ deg, the $\mathrm{Re_{cr}}$ thus determined is only an indication of the critical regime. For $\theta_g = \pm 75$ deg the lowest C_{dm} is associated with the abrupt increase in the Strouhal number from the value of the subcritical regime to that of critical regime and with the highest Strouhal number of 0.34. It is also at this groove subtend angle $\theta_g = \pm 75$ deg that the pressure rise to separation $(C_{pb} - C_{pm})$ within the critical regime is the highest at 1.9 and the wake angle θ_w is also highest at about 118 deg.

It is interesting to note that at the subtend groove angles ± 60 deg $\leq \theta_g \leq \pm 75$ deg, θ_g matches with the angle of minimum pressure (Fig. 2(*b*) and 2(*c*)). However, it is at $\theta_g = \pm 75$ deg that minimum drag coefficient is observed. As reported by Leung and Ko (1991), the presence of grooves induces instability in the boundary layer, causing premature boundary layer transition. The present study further indicates that this effect is the most effective at and near the position of minimum pressure at which maximum local mean velocity is found. Instability induced by the grooves together with the disturbances caused by the expansion of the flow from groove to smooth surfaces are the probable causes. However, at $\theta_g = \pm 45$ deg although the induced instability and the change of flow from the groove to smooth surfaces result in the "local" minimum and maximum pressure, the favourable pressure gradient suppresses the disturbances and allows the flow to continuously develop to the condition of minimum pressure.

For ± 75 deg $< \theta_g < \pm 120$ deg there is an increase in the drag coefficient from $\theta_g = \pm 75$ deg to ± 105 deg. The highest drag coefficient at $\theta_g = \pm 105$ deg is associated with the lowest Strouhal number of 0.26, the lowest $(C_{pb} - C_{pm})$ of about 0.9 and the smallest wake angle θ_w of about 105 deg. The coincidence of θ_w and θ_g of 105 deg indicates that the boundary layer separates at or near the end of the groove surface. This further suggests that the flow expansion at the junction of the groove and smooth surfaces affect the development of the boundary layer. Under the influence of adverse pressure gradient, the boundary layer may separate earlier, resulting in higher drag coefficient. For $\theta_g \geq \pm 120$ deg, no flow expansion occurs because $\theta_w < \theta_g$, that is, separation occurs at the groove surface. Hence, the drag coefficients and other coefficients are nearly the same and are nearly independent of Reynolds number.

In the critical regime of smooth cylinder two subregimes are identified (Farell and Blessmann, 1983). The first subregime is characterized by asymmetric pressure distributions, intense vortex shedding and gradual and significant variations in characteristic parameters as the Reynolds number increases and the second subregion by intense flow oscillations associated with formation and bursting of single laminar separation bubbles on one or both sides of the cylinder. The results of the present grooved cylinder indicate that for $\theta_g < \pm 60$ deg both the first and second subregimes are found. For $\theta_g \geq \pm 75$ deg the second subregimes is found even at the lowest Reynolds number of 2×10^4 of the present study and the immediate jump to higher Strouhal number at slightly higher Reynolds number signifies the transition into the twin-bubble regime, indicating the beginning of the supercritical regime. However, the Strouhal numbers of the V-grooved cylinder is lower, even with the highest of St = 0.34 of $\theta_g = \pm 75$ deg, than that of the smooth cylinder of 0.42 to 0.43 (Farell and Blessmann, 1983) and of 0.46 (Bearman, 1969).

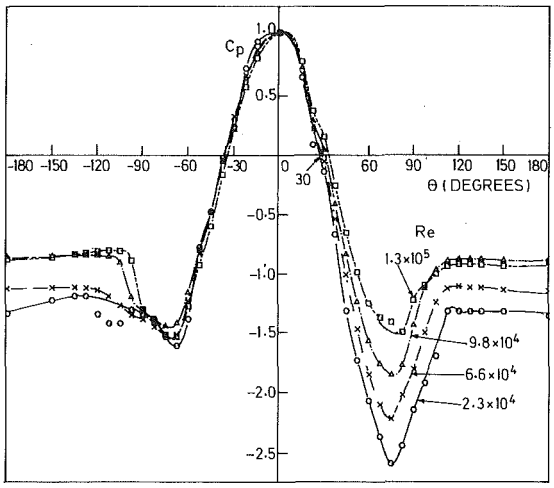

Fig. 8 Pressure distributions on cylinder with $\theta_g = +180$ deg

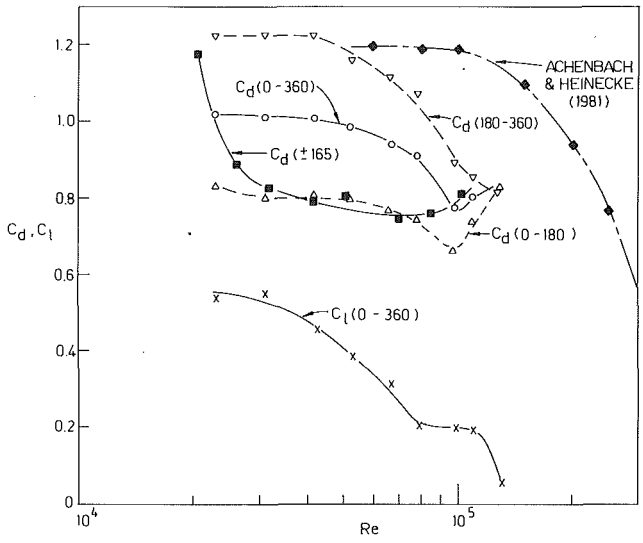

Fig. 9 Drag and lift coefficients of cylinder with $\theta_g = +180$ deg

The limited drag coefficients and Strouhal numbers at Re $\approx 2 \times 10^4$ for $\theta_g \geq \pm 75$ deg seem to indicate that the first subregime of "gradual" variation in the characteristic parameters is insignificant and is dominated by the second subregime of "sharp" variation and of single laminar separation bubble. For smooth cylinder it is within this first subregime that the fragmentary breakdown of the double shear layer interaction instability due to the increasing three dimensionality of the flow and partial reattachment of the separated shear layers occurs (Farell and Blessmann, 1983 and Morkovin, 1964). Further, the secondary vortices due to single layer instability supply the necessary lateral momentum transfer for reattachment. Thus, for the present V-grooved cylinder of $\theta_g \geq \pm 75$ deg the increase in skin friction and the disturbances associated with the V-grooves and with the change from groove to smooth surfaces induce definite reattachment instead of partial one and thus earlier formation of the laminar separation bubble at 86 deg $< \theta_i <$ 90 deg and the earlier transition to the second subregime.

Transition into supercritical regime of the grooved cylinder seems to be more complex. The increase in the Strouhal number and in $(C_{pb} - C_{pm})$ the low drag coefficient and the reoccurrence of asymmetry of the static pressure distribution after the end of the second subregime are found over quite a wide range of Reynolds number up to about 8×10^4. As suggested by Farell and Blessmann (1983), this is the twin bubble regime which indicates the beginning of the supercritical regime. For the present grooved cylinder the Strouhal number is only increased to about 0.34 for $\theta_g = \pm 75$ deg, about 0.26 for ± 105 deg $\geq \theta_g \geq \pm 90$ deg and 0.3 for $\theta_g \geq \pm 120$ deg. This suggests that the shedding frequency of the present V-grooved cylinder does not attain the value of approximately twice that of the subcritical regime as the case of smooth cylinder. However, in the study of smooth cylinder it was observed that near the end of the second subregime of single bubble and in the beginning of the twin bubble regime, the Strouhal number is about 0.32, comparing with about 0.19 in the first subregime and with about 0.45 in the twin bubble regime (Bearman, 1969). The presence of the peak of this Stouhal number of 0.32 was not observed by Farell and Blessmann (1983) and the argument proposed was to be the absence of preference of the bubble to form on either side of the cylinder.

The above phenomenon observed on the grooved cylinder seems to suggest that because of the grooves the transition from the single bubble to twin bubble regimes occurs within very narrow Reynolds number range due to the additional skin friction and disturbances introduced. Somehow, the twin bubble regime and its doubling vortex shedding frequency may not be reached but may possibly be maintained at the "intermediate" stage between the two regimes, such as that of $\theta_g = \pm 75$ deg. The cause of this is not yet known.

The increased drag coefficient, decreased $(C_{pb} - C_{pm})$ and Strouhal number and the reoccurrence of asymmetry of the static pressure distribution at higher Reynolds number indicate the supercritical regime. It is within this regime that direct transition from laminar boundary layer to turbulent boundary layer occurs. The transition from the twin bubble to this region of the supercritical regime also depends on θ_g. Because of the grooves, the wake angle θ_w in this region is smaller, indicating earlier turbulent separation. The rapid rise in the drag coefficient at $\theta_g = \pm 75$ deg and the more gradual rise at $\theta_g > \pm 120$ deg indicate the difference in the streamwise extent of the grooves. The lower pressure rise to separation $(C_{pb} - C_{pm})$ and slightly lower wake angle θ_w for $\theta_g = \pm 75$ deg than those for $\theta_g > \pm 120$ deg indicate that for these two cases the smooth surface between θ of 75 to 120 deg and the expansion at the groove and smooth surface junction for the former result in earlier separation of the turbulent boundary layer and the formation of the wake.

Due to the behavior of the symmetrical grooved cylinders, further investigation of different combination of asymmetrical grooved surfaces was carried out. The static pressure distributions of the cylinder with half-groove surface of $\theta_g = +180$ deg are shown in Fig. 8. In this case there are significant differences in the distributions on the two surfaces and much bigger variation on the groove surface with Reynolds numbers. This is due to the shift to different flow regimes at the groove and smooth surfaces.

The lift and drag coefficients are shown in Fig. 9. There is significant reduction in the lift coefficient C_ℓ with the increase in Reynolds number. Nevertheless, the presence of lift at a wide range of Reynolds number of this half-grooved cylinder is different from the zero lift of smooth circular cylinder and of symmetrical grooved cylinder. The flow asymmetry and the lift observed are due to the difference in the boundary layer characteristics at the groove and smooth surfaces. In general, it can be observed that the flow at the upper groove surface is at higher flow regime than the smooth surface. Further discussions in this aspect will be found in the next section.

The drag coefficients $C_{d(0\text{-}360)}$ over the whole cylinder are shown in Fig. 9. The drag coefficients $C_{d(0\text{-}180)}$ was obtained by assuming the same pressure distribution of the groove half for the other smooth half. Similarly, the drag coefficients $C_{d(180\text{-}360)}$ was obtained by assuming the same pressure distribution of the smooth half for the other groove half. The drag coefficients of $\theta_g = \pm 165$ deg, which is similar to the wholly

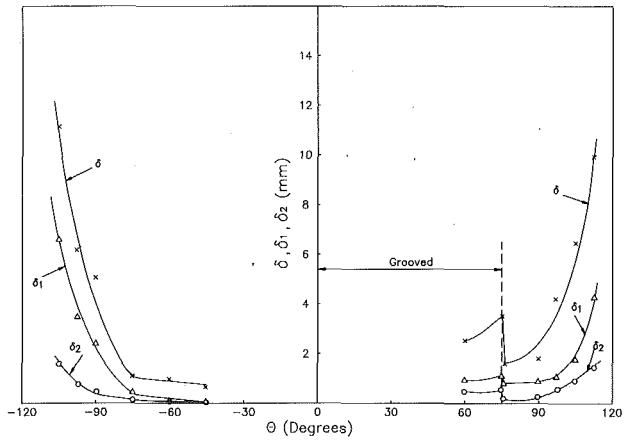

Fig. 10 Boundary layer characteristics for $\theta_g = +75$ deg at Re = 9.4 × 10^4

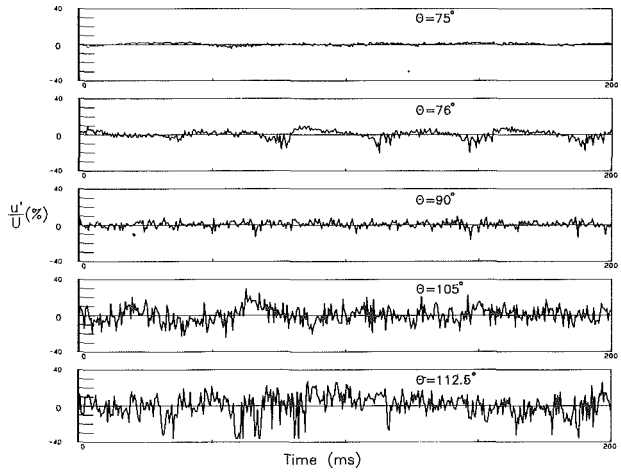

Fig. 11 Time records of maximum boundary layer velocity fluctuations at different circumferential angles

grooved cylinder, and of smooth cylinder [3] are also shown. Although the drag coefficients $C_{d(0\text{-}360)}$ seem to suggest division into different regimes, due to the difference in the surface configuration the respective drag coefficient curves on each surface are best to be considered. The drag coefficients of $C_{d(0\text{-}360)}$ are significantly lower than those of $C_{d(180\text{-}360)}$ and of smooth cylinder, but higher than those of $C_{d(0\text{-}180)}$. For $C_{d(180\text{-}360)}$ agreement with the drag coefficients of $\theta_g = \pm 165$ deg is mainly found within the twin-bubble regime. For $C_{d(180\text{-}360)}$ agreement with those of smooth cylinder is found in the subcritical regime. Because of the presence of the V-grooves on $\theta = 0$ to 180 deg, there is a shift of the drag coefficient on this smooth surface to lower Reynolds number. This means that the flow on the two halves are interacting and the flow on the V-groove surface has an effect on that of the smooth surface. This is also indicated by the occurrence of single narrow-band vortex shedding, as shown in Fig. 7. However, at Re = 1.3 × 10^5, near the end of the supercritical regime, near symmetrical static pressure distributions at the two halves, the same drag coefficients and near zero lift coefficient suggest that mainly the same flow characteristics are found on the groove and smooth surfaces and the flow is independent of the surface configuration.

Boundary Layer Measurements. *In order to obtain more* information on the interaction of the groove and smooth surfaces, detailed boundary layer measurements have been carried out for the cylinder with only the groove surface of $\theta_g = +75$ deg at Re = 9.4 × 10^4, at which the characteristics at the groove and smooth surfaces differ significantly.

Figure 10 shows the boundary layer integral parameters of the cylinder. The boundary layer thickness δ is defined as the distance from the bottom of the groove to the location where $U = 0.995\ U_E$. U_E is the mean velocity at the edge of boundary layer. Within the grooves extrapolation of the local mean velocity at the top of the grooves to zero velocity at the groove bottom was assumed in the estimation of the displacement and momentum thicknesses. For the smooth half of 0 deg > θ > − 180 deg, the abrupt increases in the boundary layer thickness, displacement thickness and momentum thickness indicate that boundary layer separation occurs at −75 deg > θ > −90 deg, which further indicates that the flow lies within the subcritical regime.

For the groove half of 0 deg < $\theta \leq$ 180 deg, however, abrupt decreases in the boundary layer thickness, displacement thickness and momentum thickness occur at $\theta \approx 75$ deg, that is, the junction of the groove and smooth surfaces. From continuity there should be a decrease in the flow velocity near the wall when the flow changes over from the groove to smooth surfaces as suggested by the local drop in pressure (Fig. 2). This change in the boundary layer velocity probably affects the stability of the boundary layer by perturbing it as indicated in the time history of its velocity fluctuations (Fig. 11). From the time records shown in Fig. 11 and others are not shown here, it can be observed that the boundary layer is laminar for $\theta \leq 75$ deg, becomes intermittent (indicated by the occurrence of large fluctuations) at $\theta = 76$ deg and becomes turbulent at about $\theta = 90$ deg. The large velocity fluctuations at $\theta = 112.5$ deg together with the sharp increase in the boundary layer integral parameters (Fig. 10) signify that boundary layer separation occurs at this angle.

The difference in the boundary layer characteristic at the smooth and groove halves also affects the flow in the wake in the vortex shedding mechanism. Figure 12 shows the streamwise velocity profiles of the wake of the cylinder. Different from the symmetric profile of smooth cylinder, unsymmetrical velocity profiles are found, indicating that the mean flow streamline is highly distorted. Generally, higher freestream velocity at the smooth half than the groove half of the cylinder is obtained and the abrupt change in the streamwise velocity at $y/d = -0.2$ to -0.3 is believed to be in the centre of the wake. However, the effect of blockage ratio on the increase in the freestream velocity is not known and will be subjected to further investigation.

The mean velocity vectors of the streamwise and lateral velocity components are shown in Fig. 13. The velocity vectors on the groove half direct more inwardly towards the centre than those on the smooth side. Due to the flow distortion, it is difficult to determine the centre of the wake which is usually identified as the region where lateral and streamwise velocities are minimum. From Fig. 13 and from the lateral velocity profiles not shown here, the approximate location of the wake centre is estimated. Downward shift from $y/d = 0$ for smooth cylinder to $y/d \approx 0.25$ in the present case is observed.

Conclusions

The present study is aimed at providing an understanding of the effect of lesser groove surface on the flow over circular cylinder. The experimental results for cylinders of different groove subtend angles within the Reynolds number range of $2.0 \times 10^4 \leq$ Re $\leq 1.3 \times 10^5$ have shown substantial changes in the flow characteristics of the cylinders. Within the range of 0 deg $\leq \theta_g \leq \pm 75$ deg there is a progressive shift of the flow regimes to lower Reynolds number with increasing groove subtend angle. At larger angles, no further shift of the flow regime is observed but the change in the flow behavior including the drag coefficient and Strouhal number, still persists

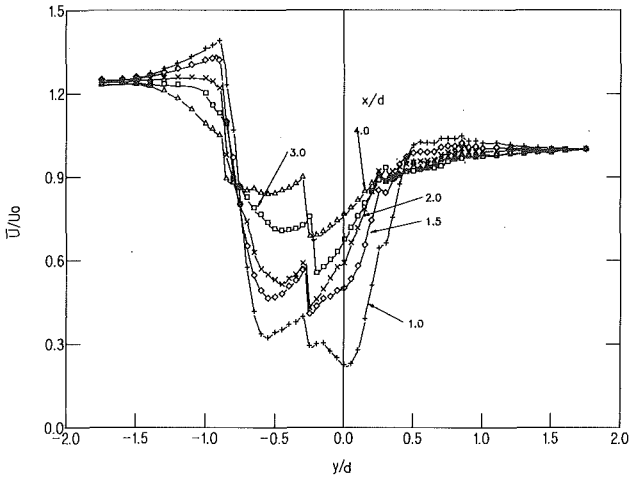

Fig. 12 Mean streamwise velocity profiles

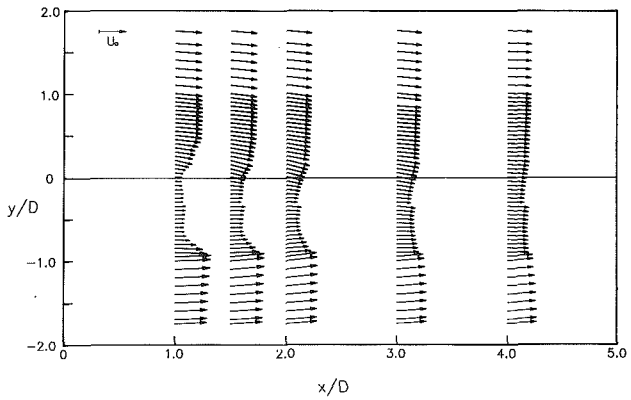

Fig. 13 Velocity vectors in the wake of the cylinder

until $\theta_g \geq \pm 120$ deg. For drag reduction the optimum groove subtend angle is found to be $\theta_g = \pm 75$ deg. Despite the difference in the flow characteristics, the occurrence of the separation bubble within the critical regime is the same and with nearly constant angle $(\theta_w - \theta_i)$ for both the V-grooved and smooth cylinders. By making use of the difference in the flow characteristics on the smooth and groove surfaces of an asymmetrical grooved cylinder ($\theta_g = +75$ deg), higher lift coefficient and lower drag coefficient are obtained within the subcritical regime of smooth cylinder. The increase in the lift coefficient is found to be associated with the different boundary layers developed at the smooth and groove halves, causing a downward shift of the wake and higher freestream mean velocity on the smooth half side. Of the two vortex sheets the one sheds from the smooth half is much more dominant.

Acknowledgments

The first author, Y. C. Leung, wishes to thank the Croucher Foundation for its support through the award of a Croucher Foundation Fellowship.

The research is partly supported by a research grant from the Committee of Conference and Research Grant, University of Hong Kong.

References

Achenbach, E., 1968, "Distribution of Local Pressure and Skin Friction Around a Circular Cylinder in Cross-flow up to Re = 5×10^6," *Journal of Fluid Mechanics*, Vol. 34, pp. 625–639.

Achenbach, E., 1971, "Influence of Surface Roughness on the Cross-Flow Around a Circular Cylinder," *Journal of Fluid Mechanics*, Vol. 46, pp. 321–335.

Achenbach, E., and Heinecke, E., 1981, "On Vortex Shedding from Smooth and Rough Cylinders in the Range of Reynolds Number 6×10^3 to 5×10^6," *Journal of Fluid Mechanics*, Vol. 109, pp. 239–251.

Allen, H. J., and Vincenti, W. G., 1930, "Wall Interference in a Two-Dimensional-flow Wind Tunnel with Consideration of the Effect of Compressibility," NACA Rept. 782.

Bearman, P. W., 1969, "On Vortex Shedding from a Circular Cylinder in the Critical Reynolds Number Regime," *Journal of Fluid Mechanics*, Vol. 37, pp. 577–585.

Buresti, G., 1983, "Appraisal of Universal Wake Numbers from Data for Roughened Circular Cylinders," ASME JOURNAL OF FLUIDS ENGINEERING, Vol. 105, pp. 464–468.

Celik, I., and Patel, V. C., 1982, "Boundary Layer Development on Circular Cylinders," *Boundary Layer Meteorology*, Vol. 24, pp. 281–293.

Fage, A., and Falkner, V. M., 1931, "Further Experiments on the Flow Around a Circular Cylinder," ARC R & M No. 1369.

Farell, C., and Blessmann, J., 1983, "On Critical Flow Around Smooth Circular Cylinders," *Journal of Fluid Mechanics*, Vol. 136, pp. 375–391.

Flachsbart, O., 1932, "Windruck auf Gasbehalter," *Reports of the Aerodyn. Versuchsanstalt*, IVth Series, Gottingen, FRG, pp. 134–138.

Guven, O., Farell, C., and Patel, V. C., 1980, "Surface-roughness Effects on the Mean Flow Past Circular Cylinders," *Journal of Fluid Mechanics*, Vol. 98, pp. 673–701.

James, W. D., Paris, S. W., and Malcolm, G. N., 1980, "Study of Viscous Crossflow Effects on Circular Cylinders at High Reynolds Numbers," *AIAA Journal*, Vol. 18, pp. 1066–1072.

Ko, N. W. M., Leung, Y. C., and Chen, J. J. J., 1987, "Flow Past V-Groove Circular Cylinders," *AIAA Journal*, Vol. 25, pp. 806–811.

Leung, Y. C., and Ko, N. W. M., 1987, "Investigation of Flow Over Grooved Circular Cylinder," *Proceedings of International Conference on Fluid Mechanics, Beijing*, pp. 578–583.

Leung, Y. C., and Ko, N. W. M., 1991, "Near Wall Characteristics of Flow Over Grooved Circular Cylinder," *Experiments in Fluids*, Vol. 10, pp. 322–332.

Morkovin, M. V., 1964, "Flow Around a Circular Cylinder—a Kaleidoscope of Challenging Fluid Phenomena," *Proceedings of ASME Symposium on Fully Separated Flows*, pp. 102–118.

Nakamura, Y., and Tomonari, Y., 1982, "The Effects of Surface Roughness on the Flow Past Circular Cylinders at High Reynolds Numbers," *Journal of Fluid Mechanics*, Vol. 123, pp. 363–378.

Niemann, H. J., 1971, "On the Stationary Wind Loading of Axisymmetric Structure in the Transcritical Reynolds Number Region," *Institut Konstruktiven Ingenieurban*, Ruhr University, Bochum, FRG, Rept. 71–2.

Van Nunen, J. W. G., 1972, "Pressure and Forces on a Circular Cylinder in a Cross-Flow at High Reynolds Number," *Proceedings of Symposium on Fluid Induced Structure Vibration*, Germany, pp. 748–754.

Simulation of Three-Dimensional Shear Flow Around a Nozzle-Afterbody at High Speeds

Oktay Baysal
Associate Professor.
Mem. ASME

Wendy B. Hoffman
Former Graduate
Research Assistant,
Mechanical Engineering and
Mechanics Department.

Old Dominion University,
Norfolk, VA 23529

Turbulent shear flows at supersonic and hypersonic speeds around a nozzle-afterbody are simulated. The three-dimensional, Reynolds-averaged Navier-Stokes equations are solved by a finite-volume and implicit method. The convective and the pressure terms are differenced by an upwind-biased algorithm. The effect of turbulence is incorporated by a modified Baldwin-Lomax eddy viscosity model. The success of the standard Baldwin-Lomax model for this flow type is shown by comparing it to a laminar case. These modifications made to the model are also shown to improve flow prediction when compared to the standard Baldwin-Lomax model. These modifications to the model reflect the effects of high compressibility, multiple walls, vortices near walls, and turbulent memory effects in the shear layer. This numerically simulated complex flowfield includes a supersonic duct flow, a hypersonic flow over an external double corner, a flow through a non-axisymmetric, internal-external nozzle, and a three-dimensional shear layer. The specific application is for the flow around the nozzle-afterbody of a generic hypersonic vehicle powered by a scramjet engine. The computed pressure distributions compared favorably with the experimentally obtained surface and off-surface flow surveys.

Introduction

Propulsion-airframe integration for hypersonic airbreathing vehicles is an important feature for the design of a national aero-space plane configuration. The lower afterbody expands the supersonic exhaust gases from the scramjet engine; therefore, it becomes a part of the nozzle. This strong coupling between the engine and the airframe necessitates a combined analysis of internal and external flows. The hypersonic free-stream and the supersonic exhaust flow mix through a shear layer, where mass, momentum, and energy transfers occur. The interference of the exhaust on the control surfaces of the aircraft can have adverse effects on the stability of the aircraft. Therefore, some method of simulating this type of flow is required to properly design the nozzle and the afterbody region.

A simplified configuration (Fig. 1) is assumed to model the single-module scramjet nozzle-afterbody. A rectangular duct precedes the internal nozzle, which has a 12 deg upper surface and a 20 deg lower surface. The external part of the nozzle is bounded by a 20 deg ramp and side ramp and a vertical reflection plate. The external hypersonic flow is initially over a double-corner formed by the reflection plate, the top surface of the nozzle, the exterior of the nozzle sidewall, and a side flat plate. The viscous effects become dominant in all the corner regions. Both of the flows expand over the 20 deg ramp and side ramp. The supersonic jet expands in the axial, the normal, and the spanwise directions as it clears the nozzle exit plane. A three-dimensional shear layer structure forms between these coflowing turbulent streams which are at different speeds.

Accurate simulation of the non-axisymmetric nozzle-afterbody flow is not an easy task, and it is further complicated by turbulence modeling concerns. The algebraic eddy viscosity model is used in this study, because it is simple to implement and requires little additional computational time and memory. A model which requires the solution of partial differential equations for its length and velocity scales would most likely be prohibitive for the present three-dimensional application, which contains over 0.8 million grid points. The standard Baldwin-Lomax model was developed assuming local equilibrium and for two-dimensional flows over simple surfaces. Hence, deficiencies exist when it is applied to three-dimensional shear and corner flows. The model may not accurately determine the proper length and velocity scales in regions of massive separation. Also, the model does not account for flow history effects, i.e., it does not have any "turbulent memory." The limitations of the Baldwin-Lomax turbulence model and eddy viscosity models in general have been revealed and analyzed in various investigations. For example, Davis et al. (1986) showed that the Baldwin-Lomax model is unable to predict turbulent secondary flow in a rectangular duct. However, Harloff et al. (1990) and Brown (1986) obtained good experimental comparisons when numerically simulating nozzle-afterbody flow using the Baldwin-Lomax model.

In order to circumvent some of the aforementioned concerns, the Baldwin-Lomax model is modified in the present study. These modifications, which are briefly explained later in this paper, demonstrate the capability of the numerical

Contributed by the Fluids Engineering Division of THE AMERICAN SOCIETY OF MECHANICAL ENGINEERS and presented at the Symposium on Advances in Numerical Simulation of Turbulent Flows, Joint Meeting of ASME and JSME, Portland, Oregon, June 23–26, 1991. Manuscript received by the Fluids Engineering Division March 4, 1991. Associate Technical Editor: R. K. Agarwal.

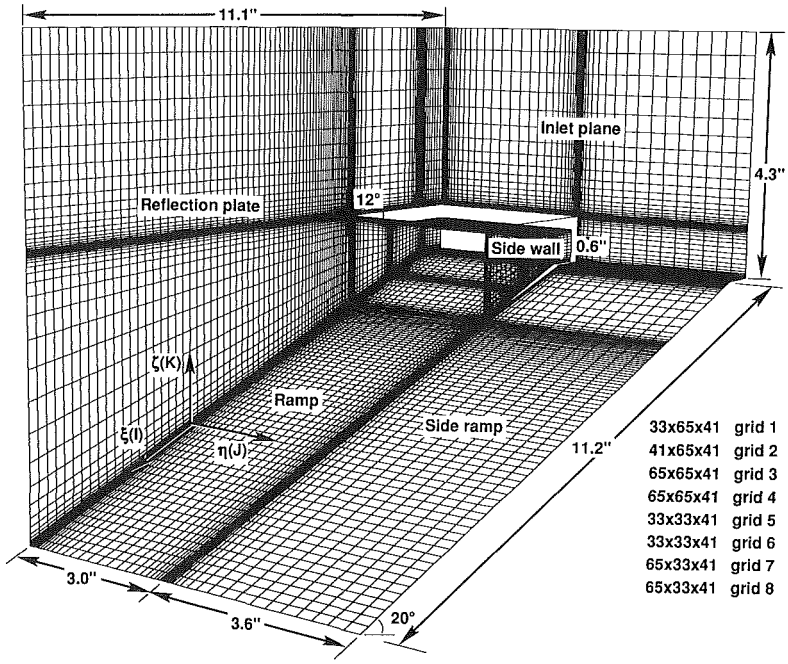

Fig. 1 Three-dimensional fixed grid for the internal-external nozzle-afterbody

scheme in modeling the flow around a complex three-dimensional configuration.

Experimental investigations of this flowfield were reported by Cubbage and Monta (1991) and Monta (1992). Two-dimensional analyses, assessing the effects of flow-adaptive grids on shear layer calculations, were reported by Hsu (1989) and Baysal et al. (1989a). Ray et al. (1988), Ruffin et al. (1989), and Hsu (1989) used air as the exhaust gas. The first multispecies computations on this type of flowfield was given by Baysal et al. (1988, 1989a, 1989b, 1992). In these studies, the variation of the thermodynamic properties of the actual exhaust gases, which were at temperatures exceeding 1500°F, were simulated by the cold gases via matching the ratio of specific heats. Computational investigations of three-dimensional nozzle-afterbody configurations are rather sparse. A three-dimensional inviscid analysis, which employs a space-marching solution was given by Ray et al. (1988). Three-dimensional laminar computations were reported by Ruffin et al. (1989) and Harloff et al. (1990).

The present paper extends the realms of the above-mentioned investigations in several directions. A combined analysis is performed for the internal and external turbulent flows, where the plume structure is allowed to expand and shear in all three directions. In an attempt to understand the viscous effects, a thorough analysis is performed on the internal and external regions where the turbulent effects are modeled. Experimental off-surface and surface pressure data enable a detailed analysis of the flowfield. The validity of the numerical scheme is assessed when comparisons with the experimental data are made.

Governing Equations and Their Solution

The indicial form of the equations are written below in generalized curvilinear coordinates,

$$\xi^m = \xi^m(x_1, x_2, x_3) \tag{1}$$

The conservative form of the nondimensional, unsteady, compressible, Reynolds-averaged, complete Navier-Stokes equations are as follows,

$$\frac{\partial \overline{Q}}{\partial t} + \frac{\partial}{\partial \xi^m}(\overline{E} - \overline{E}_v)_m = 0; \quad m = 1,2,3 \tag{2}$$

where

$$\overline{Q} = [\rho, \rho u_1, \rho u_2, \rho u_3, \rho e]^T / J \tag{3}$$

The symbols t, ρ, u_i, e denote the time, the density, the Cartesian velocity component, and the total energy, respectively. Expressions for the heat flux ($\dot{q}$) and the shear stress (τ) are stated in the references by Baysal et al. (1989a,b). The state equations are written assuming air to be a perfect gas. Molecular viscosity is calculated using the Sutherland's law and the Stoke's hypothesis.

Finite volume differencing is formulated by integrating the conservation equations (Eq. (2)) over a stationary control volume,

$$\frac{\partial}{\partial t}\iiint \overline{Q} d\Omega + \iint \overline{E} \cdot \overline{n} dS = 0 \tag{4}$$

where $\overline{n}$ is the unit normal vector pointing outward from the surface S bounding the volume Ω. This second-order accurate method is described by Baysal et al. (1991). The flux-difference splitting is used to construct the upwind differences for the convective and pressure terms. Spatial derivatives are written conservatively as flux balances across the cell. The Roe-averaged cell interface values of fluxes are evaluated after a state variable interpolation where the primitive variables are used. The diffusion terms are centrally differenced. Spatial approximate factorization, and Euler backward integration after linearization in time, results in the solution through 5×5 block-tridiagonal matrix inversions in three directions.

Turbulence Model. The Reynolds stresses and heat fluxes arising from mass averaging are assumed proportional to the laminar stress tensor with the coefficient of proportionality defined as the eddy viscosity coefficient, μ_t. A two-layer algebraic model proposed by Baldwin and Lomax (1978) is chosen for the current study to calculate the local values of the eddy viscosity. The mixing-length model employed in this model divides the shear layer into an inner and outer region, and is patterned after a method developed for attached boundary layers by Cebeci and Smith (1974). The eddy viscosity coefficient, μ_t, is given by

$$\mu_t = \begin{cases} (\mu_t)_{\text{inner}} & y \le y_{\text{crossover}} \\ (\mu_t)_{\text{outer}} & y > y_{\text{crossover}} \\ (\mu_t)_{\text{wall}} = 0 \end{cases} \tag{5}$$

where y is the normal distance from the wall, and $y_{\text{crossover}}$ is the smallest value of y at which the values from the inner and outer formulas are equal.

From the Prandtl-Van Driest mixing length formulation, the eddy viscosity for the inner region is given as:

$$(\mu_t)_{\text{inner}} = \rho\, l^2 |\omega| \tag{6}$$

where $|\omega|$ is the magnitude of the local three-dimensional vorticity vector,

$$|\omega| = \left[\left(\frac{\partial u}{\partial y} - \frac{\partial v}{\partial x}\right)^2 + \left(\frac{\partial v}{\partial z} - \frac{\partial w}{\partial y}\right)^2 + \left(\frac{\partial w}{\partial x} - \frac{\partial u}{\partial z}\right)^2 \right]^{1/2}, \tag{7}$$

and

$$l = ky[1 - \exp(y^+/A^+)] \tag{8}$$

where,

$$y^+ = \frac{y\sqrt{\rho_w \tau_w}}{\mu_w} \tag{9}$$

The eddy viscosity for the outer region is given as,

$$(\mu_t)_{\text{outer}} = KC_{cp}\rho F_{\text{wake}} F_{\text{kleb}}(y) \tag{10}$$

with

$$F_{\text{wake}} = \text{minimum} \begin{Bmatrix} y_{\max} F_{\max} \\ C_{wk} y_{\max} u_{\text{diff}}^2 / F_{\max} \end{Bmatrix} \tag{11}$$

where $F_{\max}$ is the maximum value of the function $F(y)$ defined as,

$$F(y) = y|\omega|[1 - \exp(-y^+/A^+)] \tag{12}$$

and $y_{\max}$ is the value of y at which $F_{\max}$ occurs. The function $F_{\text{kleb}}(y)$ is the Klebanoff intermittency factor and is defined as,

$$F_{\text{kleb}}(y) = \left[1 + 5.5 \left(\frac{C_{\text{kleb}}}{y_{\max}}\right)^6 \right]^{-1} \tag{13}$$

where u_{diff} is the difference between the maximum and minimum total velocity at a fixed station,

$$u_{\text{diff}} = \left(\sqrt{u^2 + v^2 + w^2}\right)_{\max} - \left(\sqrt{u^2 + v^2 + w^2}\right)_{\min} \tag{14}$$

The second term in u_{diff} is set to zero except in the shear layer region. The constants which appear in Eqs. (15)–(19) are given the following values,

$$A^+ = 26;\ C_{cp} = 2.0;\ C_{\text{kleb}} = 0.35;$$
$$k = 0.4;\ K = 0.0168;\ C_{wk} = 0.25$$

where the values of C_{cp} and C_{kleb} are slightly higher than the values suggested by Baldwin and Lomax (1978) to account for the increased compressibility (Baysal et al., 1989a, 1992). One major advantage of this model lies in the fact that the location of the boundary layer edge does not need to be computed, since the length scales are based on the distribution of vorticity. Some improvements to this model are suggested by Granville (1990).

The Baldwin-Lomax model faces difficulty in determining the proper length and velocity scales in regions of crossflow separation and near three-dimensional corners. An overlying vortical structure outside the attached layer may exhibit a greater $F(y)$ value than the local peak inside the boundary layer. Choosing such a greater value as $F_{\max}$ certainly would result in a $(\mu_t)_{\text{outer}}$ value that is too high. To eliminate this shortcoming, the implementation of Baldwin-Lomax model is modified as proposed by Degani and Schiff (1986). At each station, a search is conducted outward, sweeping from wall to freestream, in order to find the first peak in $F(y)$. The search is stopped when the peak is reached. A peak is considered to have been found when the value of $F(y)$ drops to 90 percent of the local maximum value. This ensures the exclusion of an erroneous peak which might be caused by a nonsmooth behavior in $F(y)$.

Another modification made to the standard Baldwin-Lomax model is the inclusion of multiple wall effects inside the nozzle. In this case, the eddy viscosity, μ_t is first computed from each wall, and then an effective viscosity is computed. The purpose of this inverse averaging is to ensure that the wall with the lowest (y^+) value has the greatest influence on the resulting viscosity at that computational point. Therefore, the eddy viscosity is determined in the nozzle by the following equation with top, bottom, right, and left walls denoted by the subscripts, *tw*, *bw*, *rw*, *lw*, respectively.

$$\mu_t = \frac{\left(\frac{\mu_t}{y^+}\right)_{tw} + \left(\frac{\mu_t}{y^+}\right)_{bw} + \left(\frac{\mu_t}{y^+}\right)_{rw} + \left(\frac{\mu_t}{y^+}\right)_{lw}}{\sqrt{(y^+)_{tw}^{-2} + (y^+)_{bw}^{-2} + (y^+)_{rw}^{-2} + (y^+)_{lw}^{-2}}} \tag{15}$$

The final modification to the turbulence model addresses the turbulence in a mixing shear layer or wake. This modification employs the empirical concept of relaxation eddy viscosity (Waskiewicz et al., 1980). The eddy viscosity in the shear layer is:

$$\mu_t = (\mu_t)_c + [(\mu_t)_e - (\mu_t)_c][1 - \exp(-X_c/\beta\delta_c)] \tag{16}$$

where $(\mu_t)_c$ is the calculated eddy viscosity at the top of the cowl, and $(\mu_t)_e$ is the calculated outer eddy viscosity based on local equilibrium in the wake. The distance between these two stations is denoted by X_c, and β is the relaxation length scale with values between 10 and 50. (δ_c) denotes the boundary layer thickness at the tip of the top cowl surface. Since the Waskiewicz model is two-dimensional, it is applied in both the normal and spanwise directions to effect the three-dimensionality of the shear layer.

A distinguishing flow feature of the shear layer is its high pitot pressure (P_p) values. Therefore wake relaxation is applied to the shear layer when $(P_p)_{\text{local}} > 0.75(P_p)_{\max}$, where (P_p) can be calculated using the local Mach number (M) and the local total pressure (P_t),

$$P_p = P_t \left[\frac{6M^2}{M^2 + 5}\right]^{7/2} \left[\frac{6}{7M^2 - 1}\right]^{5/2} \tag{17}$$

Grids and Boundary Conditions

The computational domain consists of the region above the cowl and to the right of the side wall where the flow is hypersonic, and another region bounded by the lower surface of the cowl and the ramp, where the supersonic internal nozzle flow expands (Fig. 1). The cowl and ramp angles are 12 and 20 deg, respectively. An algebraic grid generation algorithm is used, because it can easily define the physical surfaces of the present configuration. The global grid, which consists of 808,848 cells, is block-structured with eight subdomains in order to ease the grid generation. The grid lines are contiguous across the block interfaces, where the solutions are matched with flux conservation. This multiblock approach of domain decomposition helps better implementing the boundary conditions and reduces the computer core memory requirement, since the largest block (173,225 cells) is about 21 percent of the global grid.

The initial spacings normal to the walls vary in the range of 10^{-5} to 10^{-4} with respect to the throat height. The same grid point distributions are used for all eight blocks in the η-direction. The grid is also longitudinally clustered around the corners inside the nozzle, where the expansions occur. The grid spacings for the shear layer vary from 10^{-4} to 10^{-3} with respect to the ramp length in the ζ-direction.

The computational domain is selected to be 11.1 in. by 8.1 in. by 6.6 in. The upstream boundaries for the external and internal regions require specifying a viscous, double-corner flow profile and a viscous, duct profile, respectively. Generating such profiles requires solving the three-dimensional compressible Navier-Stokes equations. The duct flow solution is started with the two-dimensional boundary layers in the normal direction, and with the inviscid conditions on the sidewalls. The boundary layers on all four walls and in the corner regions grow in the streamwise direction as expected. The boundary layer thickness of the final cross-plane profile, which is used as the upstream boundary condition for the nozzle, is approximately 0.072 in. on all four walls.

The double-corner flow solution is also started with two-dimensional boundary layers in the normal direction and as an inviscid flow in the spanwise direction. In addition to the boundary layer growth on the walls and in the corner regions, the interaction of the two co-flowing hypersonic flows are computationally captured. Details of the viscous duct flow and the viscous double-corner flow are given by the authors in another report (Baysal and Hoffman, 1990). Similar solutions were obtained by Hung and Barth (1990). The final cross-plane of the double-corner flow is used as the upstream boundary conditions for the blocks above the cowl and outside the sidewall.

No slip, impermeability, adiabatic, and zero-normal-gradient of pressure conditions are imposed on all solid surfaces. First-order extrapolation for the conserved variables are used at the downstream boundary. The outer boundary conditions are specified after checking the sign of the normal contravariant velocity (extrapolation is used if the flow is outward and freestream values are used if the flow is inward).

The solution is obtained on two coarser level grids, and finally the finest level grid (Fig. 1), in an attempt to overcome the initial numerical transients. This approach is commonly known as the mesh sequencing. The residual and the normal force histories are used to determine the solution convergence. The convergence is deemed to be achieved when the residual is decreased by four orders of magnitude. An examination of the normal force coefficient, C_N, reveals an asymptotic approach to a constant value after 1500 work units. A work unit corresponds to the amount of iterations on any combination of coarse or fine grids, which requires the same amount of computer time necessary to perform one iteration on the finest grid (Baysal et al., 1991). The solution is terminated at approximately 2300 work units, in which 300 work units are performed on coarser levels. This amounts to roughly 30 hours on the CRAY-2 of NASA Langley Research Center. A grid refinement study was not conducted for the present three-dimensional problem since it would require prohibitively large amount of computational effort. However, previous two-dimensional studies performed by Baysal et al. (1989a,b, 1992) used the same nozzle-afterbody configuration and similar grid spacing strategies; the solution convergence was obtained for the two-dimensional flow on flow adapted grids. Since adapting the grid to the flow gradients decreased the computational error, the flow field was better resolved in the previous studies than the present three-dimensional study.

Results and Discussion

The upstream flow conditions for the external and the internal flows are:

External: $M_e = 6.000$, $\mathrm{Re} = 3.3 \times 10^5$, $T_t = 885°\mathrm{R}$

$P_t = 361$ psia

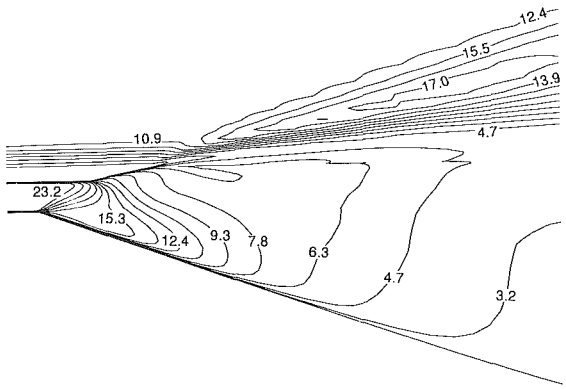

Fig. 2 Pitot pressure contours in the internal nozzle and ramp region for an η-constant plane

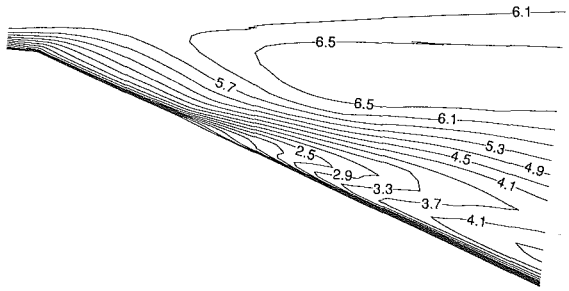

Fig. 3(*a*)

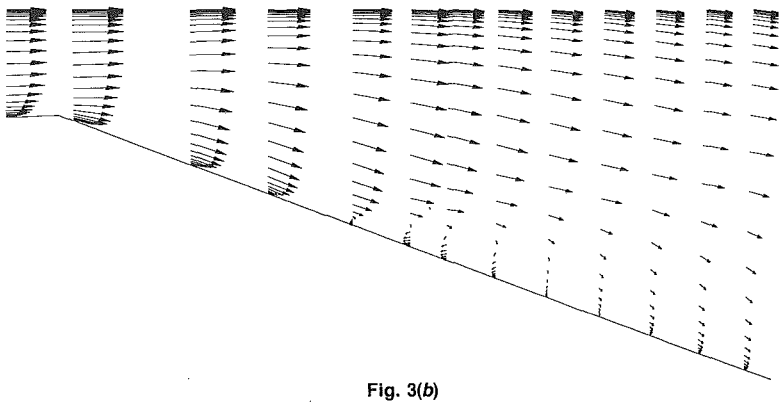

Fig. 3(*b*)

Fig. 3 (*a*) Mach contours, (*b*) velocity vectors, of the external flow along the side ramp for an η-constant plane

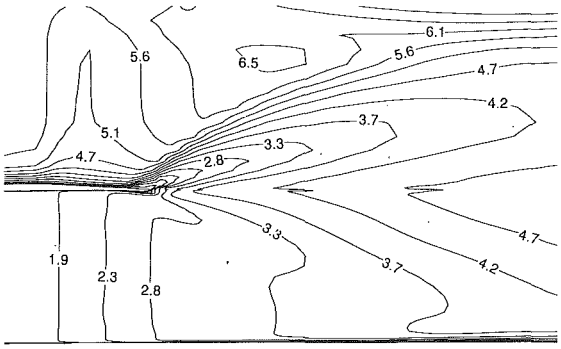

Fig. 4 Mach contours for a ζ-constant plane of the nozzle-afterbody

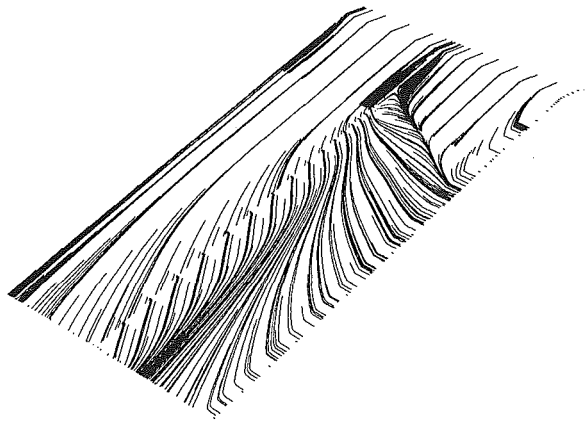

Fig. 5 Limiting streamlines on the floor of the afterbody ($\zeta = 0$)

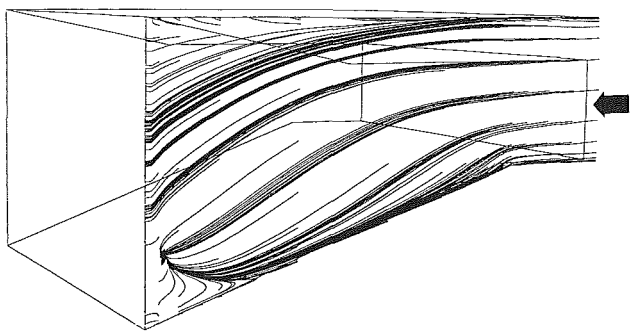

Fig. 6 Limiting streamlines on the nozzle side wall

Internal: $M_i = 1.665$, $\mathrm{Re} = 3.4 \times 10^5$, $T_t = 610°\mathrm{R}$

$P_t = 27.5$ psia

where T_t and P_t are the total temperature and the total pressure. The Reynolds number is based on the 0.6 in. throat height of the internal nozzle. The static pressure ratio for this nozzle is 25.5.

The three-dimensional results obtained for the afterbody configuration are shown in Figs. 2 through 12. The pitot pressure contours for an η-constant plane, located at 1.5 in. from the reflection plate, are shown in Fig. 2. Just upstream of the cowl tip, a 0.53 in. thick boundary layer is formed for the external flow. The supersonic-hypersonic mixing of air forms a shear layer downstream of the cowl tip. This shear layer behaves like an extension of the cowl and the flow continues to expand between the ramp and the shear layer. Two centered expansion fans develop around the corners inside the nozzle. As expected, pitot pressure values are highest in the nozzle (7.8 to 24.0 psia) and the shear layer (13.9 to 17.0 psia). A small compression shock, caused by the high-pressure expanding jet interacting with the low pressure external flow, forms at the cowl tip and deflects downward at about -10 deg.

The Mach contours on an η-constant plane located at 5.5 in. from the reflection plate are shown in Fig. 3(*a*). The external hypersonic air expands in the streamwise and normal directions. The crossflow jet expansion from the nozzle results in a 6.5 Mach number flow. Due to the nozzle aspect ratio, the lateral expansion exceeds the expansion in the normal direction. A streamwise separation is predicted along the ramp floor. The separation starts at approximately 40 percent ramp length (from the corner) and extends to about 70 percent ramp length. This is more clearly depicted in Fig. 3(*b*), where a two-dimensional projection of this separation is shown using the velocity vectors.

Shown in Fig. 4 are the Mach contours for a ζ-constant plane (approximately parallel to the ramp at 0.3 in.) of the afterbody configuration, where the nozzle, the ramp, and the side ramp are seen. The jet expands downstream of the nozzle forming a highly expanded lateral plume. A much thicker boundary layer develops at the side wall in comparison to the one seen in the normal direction. The higher-pressure jet causes the external hypersonic flow, approaching the nozzle exit plane, to experience a plume shock. As a result of the spanwise expansion of the jet and this plume shock, a flow separation is started, and it propagates spanwise along the side ramp.

Limiting streamlines on the nozzle floor, ramp, and side ramp are shown in Fig. 5. The separation lines can be recognized by the convergence of the limiting streamlines in the lateral direction. Limiting streamlines on the nozzle side wall are shown in Fig. 6. Another separation is predicted on the lower portion of the wall, again as evidenced by the converging streamline pattern.

A more comprehensive view of the afterbody flowfield is shown through crossflow Mach contours in Fig. 7. Expansion is seen in normal, spanwise, and streamwise directions. The growths of turbulent boundary layers on the reflection plate, ramp, and side ramp are evident. The exiting jet transforms from a rectangular shape at the nozzle exit plane to an enlarged elliptical plume as the flow propagates downstream. Obviously, this affects the shape of the resulting three-dimensional shear layer.

Skin friction, C_f, distributions for the nozzle-afterbody floor are shown in Fig. 8, where (xs) is the tangential distance along the ramp (or side ramp) plus the 0.6 in. before the ramp corner (Fig. 1). It should be noted here that C_f values were not measured in any of the wind tunnel tests (Cubbage and Monta, 1991; Monta, 1992) of this configuration. Therefore, although it would be desirable, skin friction comparisons are not made in this study. The C_f distributions for the nozzle floor and ramp (Fig. 8(*a*)) are qualitatively similar for the three η-stations. A sharp decrease in C_f is seen at $xs = 0.6$ in., which is the ramp corner and it marks the beginning of the centered expansion. The C_f values then increase, showing a marked increase at $xs = 2.8$ in., which is the location of the cowl tip and where the two flows first interact. Continued expansion of the flow down the ramp results in a gradual decline of the C_f values.

The C_f distributions for the side ramp are shown in Fig. 8(*b*). Unlike Fig. 8(*a*), each η-station exhibits different C_f trends. The first low peak values represent crossflow separation and substantiate the diverging streamline pattern of Fig. 5. It is clear that at station η_4 separation occurs at $xs \simeq 2.4$ in., while at stations η_5 and η_6, separation occurs at $xs \simeq 3.0$ in. and $xs \simeq 3.6$ in., respectively. Flow reattachment after separation is evident for stations η_4 and η_5, followed by gradual C_f decline. Station η_6 also predicts flow reattachment. However, the C_f distribution indicates another possible separation at $xs \simeq 5.4$ in. This possibility is further substantiated in Fig. 3(*b*), where a projected separation is shown to occur at an η-station of 5.5 in. from the reflection plate.

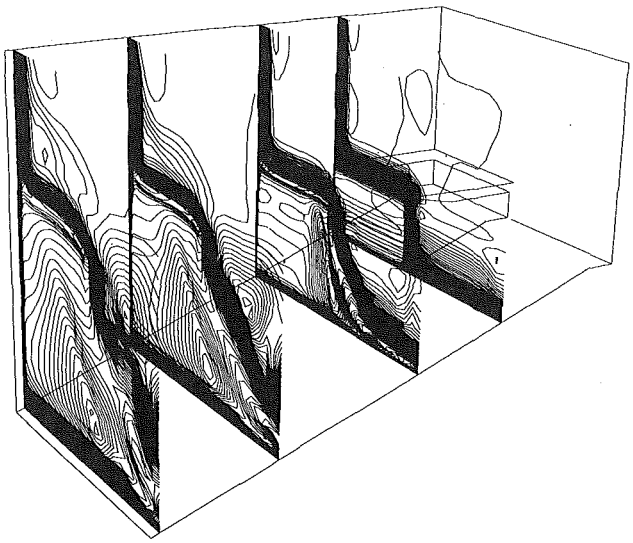

Fig. 7 Mach contours depicting various crossflow (ξ-constant) planes of the nozzle-afterbody

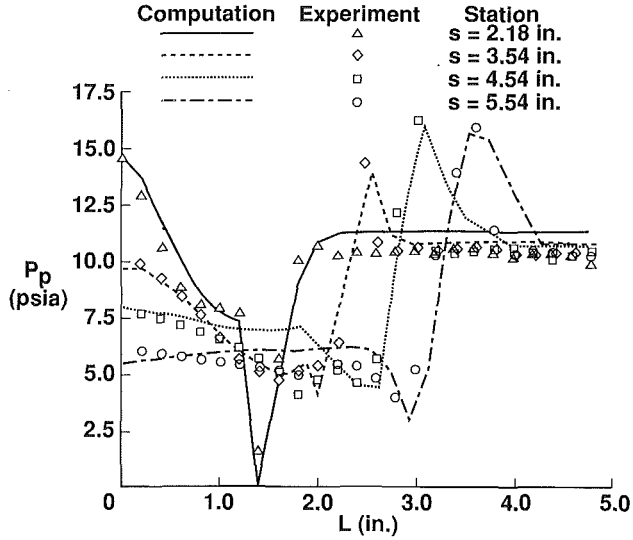

Fig. 9 Comparisons of computational and experimental off-surface pitot pressures

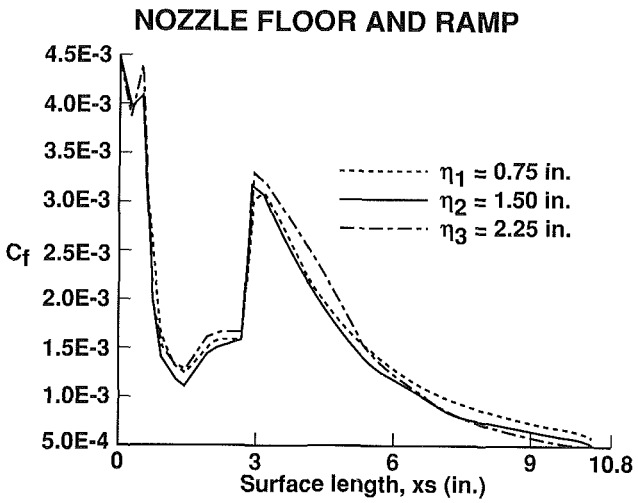

Fig. 8(*a*)

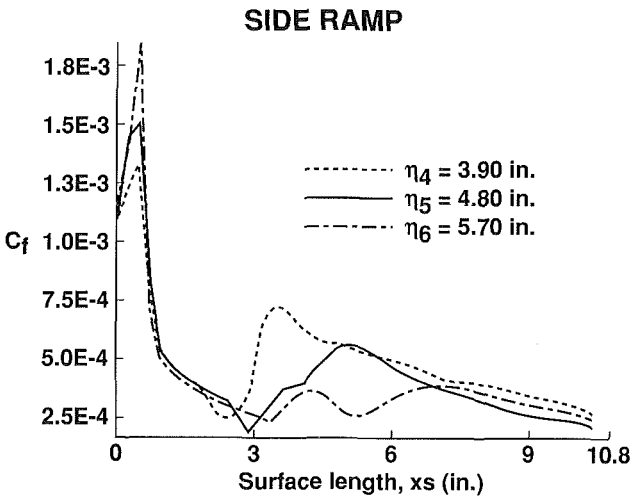

Fig. 8(*b*)

Fig. 8 Surface skin friction distributions for various η-stations ($\zeta = 0$): (*a*) nozzle floor and ramp, (*b*) side ramp

Computational off-surface pitot pressure, P_p, values are compared to the experimental results (Monta, 1992) in Fig. 9. Four separate rake stations (Station 1 is located at the nozzle exit plane), each containing 25 pitot tubes, are placed midspan on the ramp. Here, (L) denotes the length of the rake measured approximately normal from the ramp surface, and (s) denotes the tangential distance along the ramp surface, measured from the 20 deg ramp corner. The pitot pressure calculated for this comparison is the total pressure behind the shock, P_{t2}, and not the total pressure, P_t (see Eq. (17)). All shocks are assumed to be normal to each pitot tube, and possible shock interference between pitot tubes is not considered in Eq. (17). The numerical simulation of the shear layer is accomplished with some deviations seen in the high peak values of Stations 2, 3, and 4 located at $s = 3.54$ in., 4.54 in., and 5.54 in., respectively. According to the experimental results, a compression wave forms at the cowl tip and extends to the third rake station at approximately -10 deg. The effect of this shock is seen both experimentally and computationally in the low peak values. Computational results follow the experimental trend for the shock with some deviation in location and strength. Station 3 reveals the largest discrepancy.

The discrepancies between the experimental data and the calculations in the shock and the shear layer regions may be reduced if the grid were refined further in these regions. A two-dimensional grid adaptation study performed by Baysal et al. (1989a,b, 1992) shows that adapting the grid to the flow improves the solution quality; that is, the shock and the shear layer regions reveal better flow resolution and less smearing. This approach, however, would not be as efficiently possible in the present three-dimensional calculations. More accurate turbulence predictions may also be obtained by varying C_{cp} and C_{kleb} as functions of Mach number and skin friction, as Visbal and Knight (1984) suggest, or by using the relationships for blending of inner and outer eddy viscosities provided by Granville (1990).

Comparisons of the computational and experimental (Cubbage and Monta, 1991) surface pressure coefficients on the ramp and side ramp are shown in Fig. 10. Pressure values are plotted at five spanwise locations. The first three stations (located on the ramp), which are downstream of the nozzle exit plane, exhibit high initial C_p values before gradually declining as the flow continues to expand down the ramp. The C_p distributions on the side ramp ($\eta = 3.50$ in. and $\eta = 4.25$ in.) are relatively constant and predict slightly lower C_p values than the final C_p value attained on the ramp. This is due to the greater spanwise expansion on the side ramp. All of the computed C_p values compare very well with their experimental values.

In order to assess the effectiveness of introducing the present

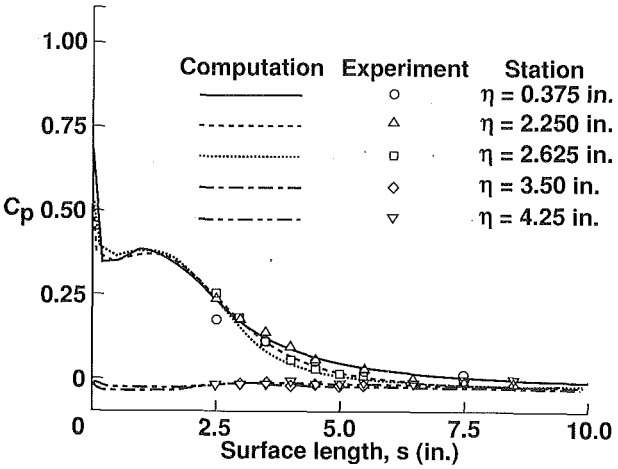

Fig. 10 Comparisons of computational and experimental surface pressure coefficients

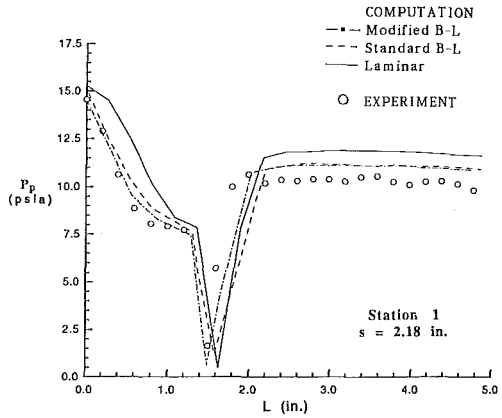

Fig. 11(*a*)

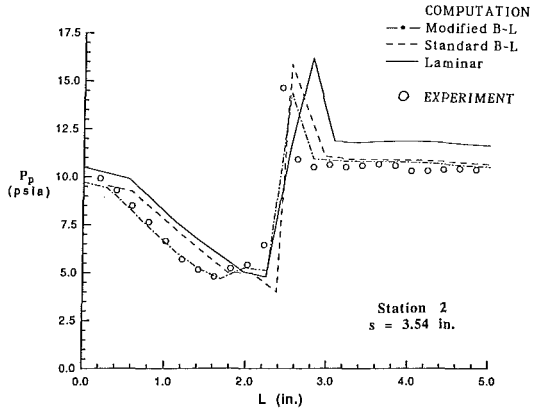

Fig. 11(*b*)

Fig. 11 Comparisons of computational and experimental off-surface data for the standard B-L model, the modified B-L model and the laminar case: (*a*) Station 1 (*b*) Station 2

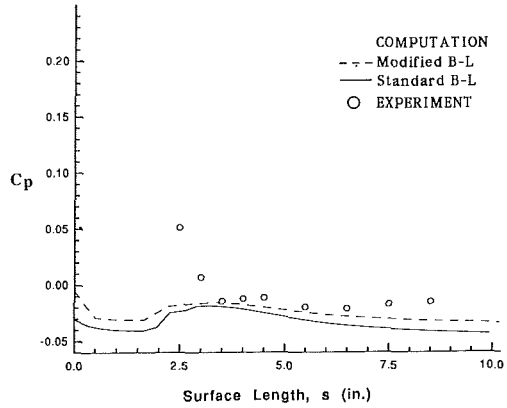

Fig. 12(*a*)

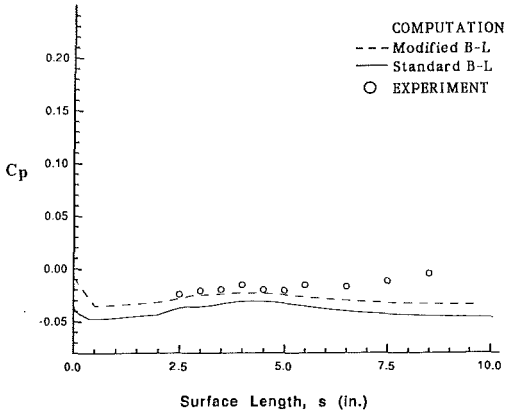

Fig. 12(*b*)

Fig. 12 Comparisons of computational and experimental surface pressure data for the standard B-L model and the modified B-L model: (*a*) $\eta = 3.25$ in., (*b*) $\eta = 4.25$ in.

modifications to the Baldwin-Lomax (B-L) model, three different computations are performed: (i) Modified B-L, (ii) Standard B-L model, and (iii) Laminar flow. The flow prediction of each method is shown in Fig. 11 and is compared to the experimental off-surface pressure data at two different stations. The plot of Station 1 (Fig. 11(*a*)), which is just downstream of the nozzle exit plane, shows that the modified B-L model yields the most accurate prediction. Here the effects of incorporating the multiple-wall calculation in the nozzle can be assessed. The net effect of using the multiple-wall concept is to shift the shock location (represented by the low peak region). This is an improvement over the standard B-L model. As expected, the laminar case yields the worst results. The modified model again provides the best off-surface pressure prediction at Station 2 (Fig. 11(*b*)). The wake relaxation is applied in the shear layer and it reduces the high-pressure peak of the shear layer. Higher peak values are noted for the other two cases.

The variation of C_p with surface length for the standard B-L model and the modified B-L model are shown in Fig. 12. The effect of introducing the multiple-wall calculation (modified B-L model) inside the nozzle is clearly evident. The two models predict similar surface pressure distributions along the ramp. However, notable C_p differences are seen along the side ramp (outboard of the nozzle side wall). A comparison of these two models for $\eta = 3.25$ in. (Fig. 12(*a*)) and $\eta = 4.25$ in. (Fig. 12(*b*)) shows that the modified model improves the C_p distribution when compared to the standard model.

Discrepancies between the computational and the experimental results can be attributed mainly to the grid, the turbulence model, and the uncertainties associated with the wind tunnel data. Also, the boundary layer thickness used at the upstream of the internal nozzle flow (0.072 in.) is only assumed to be approximating the experiment, since boundary layer thicknesses were not measured during the wind tunnel tests. It is believed that some improvement is possible by using a more refined initial grid followed by adapting the grid to the flow solution as it develops. Finally, further modifications to the Baldwin-Lomax are necessary. Both of these issues are recommended as future studies.

Conclusions

Three-dimensional viscous calculations are performed on a nozzle-afterbody configuration. The computational results indicate a flowfield characterized by three-dimensional expansions, mixing and shear layers, plume flow, shocks, and three-dimensional separations. A more extensive jet expansion is noted in the spanwise direction as opposed to the normal direction. This is mainly due to the nozzle aspect ratio. Computational results are compared with available wind tunnel data and they show the suitability of the solution method to this type of flow. Computational values compare very well with the experimental results for surface pressures. Off-surface comparisons show good general prediction; however, the present numerical model shows some deviation in predicting the shear layer and cowl shock. The formation of the cowl shock and shear layer is highly dependent on the turbulence modeling. The modified Baldwin-Lomax model improves surface and off-surface pressure predictions when compared to the standard Baldwin-Lomax model and to laminar flow. The modified Baldwin-Lomax model provides adequate prediction of this complex turbulent flow; however, improvements are still necessary to obtain more accurate off-surface results, especially in the shock and the shear layer regions. Incorporation of multispecies mixing to simulate combustor exhaust, flow adaptive gridding, complete hypersonic vehicle analysis for more suitable upstream conditions, and further turbulence model modifications are suggested for future work on this subject.

Acknowledgment

This work was supported by NASA Langley Research Center under Grant No. NAG-1-811. The technical monitor was David S. Miller.

References

Baldwin, B. S., and Lomax, H., 1978, "Thin Layer Approximation and Algebraic Model for Separated Turbulent Flows," AIAA Paper No. 78-257.

Baysal, O., Engelund, W. C., and Tatum, K. E., 1988, "Navier-Stokes Calculations of Scramjet-Afterbody Flowfields," *Symposium on Advances and Applications in Computational Fluid Dynamics*, Ed., O. Baysal, FED-Vol. 66, ASME, New York, pp. 49–60.

Baysal, O., Engelund, W. C., Eleshaky, M. E., and Pittman, J. L., 1989a, "Adaptive Computations of Multispecies Mixing Between Scramjet Nozzle Flows and Hypersonic Freestream," AIAA Paper No. 89-0009.

Baysal, O., Eleshaky, M. E., and Engelund, W. C., 1989b, "2-D and 3-D Mixing Flow Analyses of a Scramjet-Afterbody Configuration," *Proceedings of International Conference on Hypersonic Aerodynamics*, Paper No. 14, The Royal Aeronautical Society, London.

Baysal, O., and Hoffman, W. B., 1990, "Computation of Hypersonic/Supersonic Flow Through a Single-Module Scramjet Nozzle," *Proceedings of First International Conference on Computational Physics*, IMACS, University of Colorado, pp. 52–59.

Baysal, O., Fouladi, K., and Lessard, V. R., 1991, "A Multigrid and Upwind Viscous Flow Solver on 3-D Overlapped and Embedded Grids," *AIAA Journal*, Vol. 29, No. 6, pp. 903–910.

Baysal, O., Eleshaky, M. E., and Engelund, W. C., 1992, "Computations of Multispecies Mixing Between Scramjet Nozzle-Afterbody Flows and Hypersonic Freestream," *Journal of Propulsion and Power*, Vol. 8, No. 2, pp. 500–506.

Brown, J. J., 1986, "Navier-Stokes Nozzle Analysis Techniques," AIAA Paper No. 86-1613.

Cebeci, T., and Smith, A. M. O., 1974, *Analysis of Turbulent Boundary Layers*, Academic Press, pp. 72–103.

Cubbage, J. M., and Monta, W. J., 1991, "Parametric Experimental Investigation of a Scramjet Nozzle at Mach 6 With Freon and Argon or Air Used for Exhaust Simulation," NASA-TP-3048.

Davis, D. O., Gessner, F. B., and Kerlick, G. D., 1986, "Experimental and Numerical Investigation of Supersonic Turbulent Flow Through a Square Duct," *AIAA Journal*, Vol. 24, No. 9, pp. 1508–1515.

Degani, D., and Schiff, L. B., 1986, "Computation of Turbulent Supersonic Flows Around Pointed Bodies Having Crossflow Separation," *Journal of Computational Physics*, Vol. 66, pp. 173–196.

Granville, P. S., 1990, "A Near-Wall Eddy Viscosity Formula for Turbulent Boundary Layers in Pressure Gradients Suitable for Momentum, Heat, or Mass Transfer," ASME JOURNAL OF FLUIDS ENGINEERING, Vol. 112, pp. 240–243.

Harloff, G. J., Reddy, D. R., and Lai, H. T., 1990, "Viscous Three-Dimensional Analyses for Nozzles for Hypersonic Propulsion," NASA-CR-185197, Lewis Research Center, Cleveland, OH.

Hsu, A. T., 1989, "The Effect of Adaptive Grid on Hypersonic Nozzle Flow Calculations," AIAA Paper No. 89-0006.

Hung, C. M., and Barth, T. J., 1990, "Computation of Hypersonic Flow Through a Narrow Expansion Slot," *AIAA Journal*, Vol. 28, No. 2, pp. 229–235.

Monta, W. J., 1992, "Pitot Survey of Exhaust Flow Field of a 2-D Scramjet Nozzle With Air or Argon and Freon Used for Exhaust Simulation at Mach 6," NASA-TM-4361.

Ray, R., Niggemeir, C., and Erdos, J., 1988, "CFD Analysis of 3-D Effects in Scramjet Exhaust Flowfields," AIAA Paper No. 88-3262.

Ruffin, S. M., Venkatapathy, E., Keener, E. R., and Nagaraj, N., 1989, "Computational Design Aspects of a NASP Nozzle/Afterbody Experiment," AIAA Paper No. 89-0446.

Visbal, M., and Knight, D., 1984, "Evaluation of the Baldwin-Lomax Turbulence Model for Two-Dimensional Shock Wave Boundary Layer Interactions," *AIAA Journal*, Vol. 22, No. 7, pp. 921–928.

Waskiewicz, J. D., Shang, J. S., and Hankey, W. L., 1980, "Numerical Simulation of Near Wakes Utilizing a Relaxation Turbulence Model," *AIAA Journal*, Vol. 18, No. 12, pp. 1440–1445.

J. Katz
Professor.
Department of Aerospace Engineering
and Engineering Mechanics,
San Diego State University,
San Diego, CA 92182-0183

L. Dykstra
President.
Special Chassis Inc.,
Indianapolis, IN 46268

Effect of Passenger Car's Rear Deck Geometry on Its Aerodynamic Coefficients

The effects of aerodynamic modifications near the rear deck of a passenger-car based race car were investigated experimentally. The modifications were evaluated on a quarter-scale wind tunnel model and included a rear spoiler and a wing. The experimental results indicate that these devices alter the flow field on the vehicle's body resulting in considerable negative lift coefficients. Also, this aerodynamic interaction is sensitive to rear wing location and when properly placed the total lift owing to the rear wing, combined with its effect on the vehicle's body, can amount to twice the lift of the isolated wing.

Introduction

Economic considerations leading toward improved fuel economy focused road vehicle's aerodynamic research mainly toward reducing the aerodynamic drag. Other components of the aerodynamic loads such as the lift were considered to be less crucial to passenger car performance and in fact most current passenger cars will have a positive aerodynamic lift (such information can be found in some recent books on this topic, e.g., Howard, 1986 or Hucho, 1987). Race cars based upon production automobiles (e.g., the GTO class sanctioned under the International Motor Sport Association), however, need negative aerodynamic lift (downforce) to improve their tires' adhesion and thus achieve faster turning speeds. Since these cars must closely resemble their passenger car counterpart the allowed aerodynamic modifications are minor and limited to devices which can be used on the actual passenger car. This need for downforce created a variety of spoilers and winglets attached to the vehicle and examples demonstrating their performance are documented in references such as Howard (1986) or Hucho (1987, mainly in Chapter 7).

In this study an effort is made to show that negative values of the aerodynamic lift can be obtained by minor modifications near the vehicle rear stagnation point area where devices such as spoilers and winglets are highly effective. Furthermore, a large portion of the downforce is created by the vehicle's body owing to the flow field altered by these devices and therefore the aerodynamic performance is very sensitive to small changes in their location or geometry. The objective of this report is to demonstrate the magnitude of this interaction and highlight some of the more dominant parameters (relevant to passenger car shapes) that affect this aerodynamic interaction.

Wind Tunnel and Model

The wind tunnel used for the present tests is a closed return type with test section dimensions as shown in Fig. 1. Free-stream speed of up to 80 m/s (180 miles/hr) can be selected and turbulence levels in the test section are less than 1 percent. The model was mounted on an elevated ground plane, as shown in Fig. 1, and the boundary layer thickness (measured on the flat surface without the model) toward the test section end was about 5 mm high (at $\mathrm{Re}=3.5\times10^6$). To correct for this effect the model was raised by this amount to allow more airflow under the vehicle for a better simulation of actual road conditions. Surface pressure distribution on the model, ground plane and wind tunnel walls was measured by static ports connected by 1 mm diameter plastic tubing to an electronic scanner (48 port Scanivalve, Model No. 48J9GM-1). The resulting pressure coefficients were calculated by the data acquisition system with an uncertainty of less than ±0.03. The six-component balance, located under the test section, had an accuracy of ±0.5 lb (±0.23 kg) for the lift and ±0.1 lb (±0.05 kg) for drag (which translates to uncertainty in the aerodynamic coefficients of up to $\Delta C_L=\pm7$ percent, and $\Delta C_D=\pm0.5$ percent). To improve the repeatability of the results (primarily of the lift) the aerodynamic loads were measured at three speeds ($V_\infty=90$, 100, and 110 mph, or about 40, 45, and 50 m/s, respectively) and at each of these speeds the loads were measured (by averaging 1200 individual readings). The aerodynamic data presented in this report is then obtained by fitting a parabola to the experimental data, using the least-square method (see Fig. 2). This is based on the assumption that the lift and drag are proportional to V_∞^2 and for example the lift L versus speed will have the form

$$L=kV_\infty^2 \tag{1}$$

where k is a constant. Now if the lift L_i is measured at N different speeds $V_{\infty i}$ as shown in Fig. 2 (where $N=3$) then the constant k can be calculated by the least square method as:

$$k=\frac{\sum_{i=1}^{N} L_i V_{\infty i}^2}{\sum_{i=1}^{N} V_{\infty i}^4} \tag{2}$$

Contributed by the Fluids Engineering Division for publication in the JOURNAL OF FLUIDS ENGINEERING. Manuscript received by the Fluids Engineering Division March 8, 1991. Associate Technical Editor: Chih-Ming Ho.

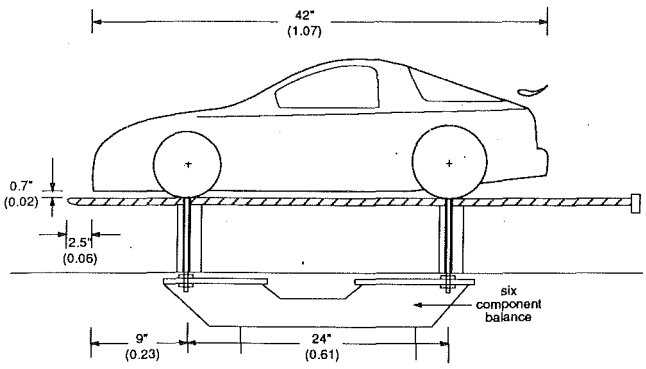

Fig. 1(*a*)

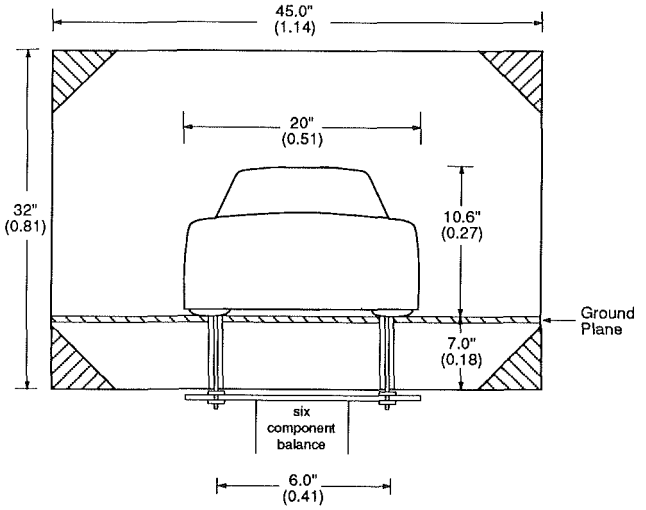

Fig. 1(*b*)

Fig. 1 Description and dimensions of the model as mounted in the wind-tunnel, dimensions in inches (in meters within parentheses)

Using this constant k and Eq. (1) the parabola shown in the figure can be fitted to the experimental points. The lift coefficient which is described by this parabola is then

$$C_L \equiv \frac{L}{\frac{1}{2}\rho V_\infty^2 A} = \frac{k}{\frac{1}{2}\rho A} \tag{3}$$

Since the flow over such vehicle configurations is detached in certain regions (e.g., near the rear section) time-dependent fluctuations are present in the pressure, aerodynamic loads and especially in the wake velocity components. In this type of testing, however, interest is focused on the time-averaged information only and therefore the data presented in this manuscript represents time-average values.

The major dimensions of the one-quarter scale automobile model are depicted in Fig. 1. The model had details such as cooling air ducting and window openings but its wheels did not rotate during the test. The geometry of the rear spoiler and of the winglet, as mounted, are shown in Fig. 3. The regulations for this particular race car category (at the time of the tests) allow a rear spoiler no taller than 2 inches (in quarter-scale) above the rear deck, the trailing edge of which may not be further back than the rear bumper line (see Fig. 3). The spoiler may span the width of the vehicle at the rear deck-line, which was 17.5 in. (in quarter-scale). An alternative to the spoiler allowed by the body governing this class of race cars is a small wing with a maximum chord of 2.6 in. (66 mm), but the span was limited to 15 in. (381 mm) only. The immediate objective of this study, therefore, was to find which device and at what setting to use on the actual race car (again, all dimensions are given for the quarter-scale model).

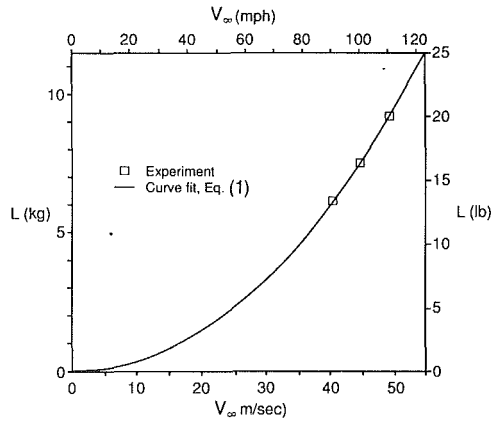

Fig. 2 Parabolic curve fit for the measured aerodynamic lift ($Re_l = 3.5 \times 10^6$, uncertainty in lift ± 0.5 lb, in $V = \pm 3$ percent)

The shape of the airfoil and the spoiler chordline have significant influence on the effectiveness of these devices, and the geometries shown in Fig. 3 were selected based on comparable development efforts for each of those two modifications. Also, the highly cambered airfoil shape was especially developed for this vehicle by using computational methods such as those presented by Katz (1989), since most air-plane type airfoils (e.g., the NACA series) do not have sufficient camber for this application.

The quarter-scale wind tunnel model is a commonly used size for early vehicle shape developments but when this model was mounted in the San Diego State University wind tunnel it created a frontal area blockage on the order of 16.5 percent (including mounting-strut fairings and ground plane). This blockage is more than twice the ratio (of 7.5 percent mentioned by Rae and Pope, 1984) under which wall effects can be considered to be small. Consequently, the dynamic pressure ($1/2\ \rho V_\infty^2$) and the resulting lift and drag coefficients were corrected by using the method of Katz (1989) (by about 20 percent).

As mentioned in the Introduction, the primary objective of this study was to investigate changes in the aerodynamic performance of a road vehicle due to modifications such as the rear spoiler and the rear wing. However a secondary objective evolved as the need to investigate whether reasonable engineering data can be collected by the available testing method, especially in view of the large solid blockage. To clarify this point some comparisons were made with on-track performance data of the actual race car. For example, the drag increment (which was obtained by measuring maximum speed) between the vehicle with the wing and with the spoiler was 0.1 percent,

Nomenclature

A = model (cross section) reference area (202.5 in^2)
c = wing chord
C_D = drag coefficient (drag/$0.5\rho V_\infty^2 A$)
C_L = lift coefficient (lift/$0.5\rho V_\infty^2 A$)
C_p = pressure coefficient (p-p_∞/$0.5\rho V_\infty^2$)
D = drag
h = wing vertical position
L = lift
l = vehicle's length
p = pressure
Re_l = Reynolds No., based on l
V_∞ = free-stream velocity
x = coordinate along the model
α_w = wing angle of attack
ρ = air density

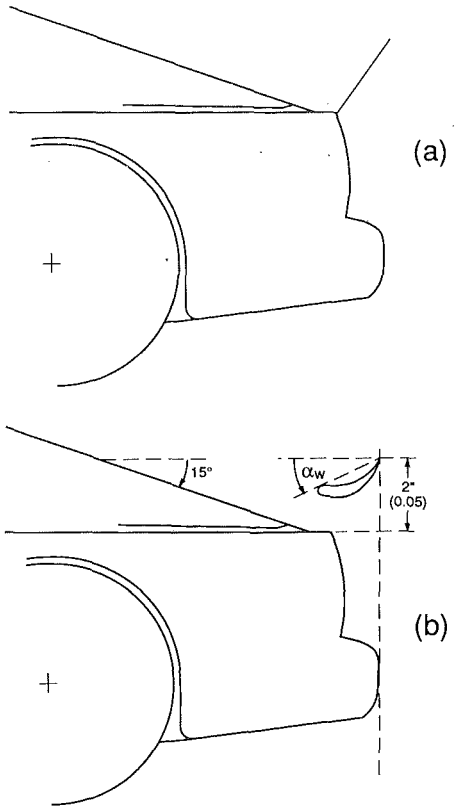

Fig. 3 Geometry of the spoiler (*a*) and the wing (*b*) as mounted on vehicle's rear deck

close to the 1/4 scale test results. This example and other such comparisons clearly indicate that the present testing technique and data reduction is capable of estimating the effect of incremental changes on the vehicle's aerodynamics.

Experimental Results

Following the objective outlined in the introduction the effect of the spoiler and the rear wing on the aerodynamic coefficients was studied first. The trailing edges of the spoiler and the wing were positioned at the same point (which is aligned with the rear bumper and two inches above the rear deck), as shown in Fig. 3. The wing angle of attack was set at $\alpha_W = 17$ deg which seemed to be the highest angle at which fully attached flow over the wing was attained (observed by flow visualization with tufts). Also, note that the wing angle of attack is varied in this test by pitching the wing about its trailing edge. Summary of the experimental data for this comparison, including the baseline car along with the data for the car with the rear spoiler and with the rear wing is presented in the following table:

Table 1 Summary of aerodynamic data for three generic vehicle configurations

Configuration	C_L	C_D	L/D
Baseline	0.04	0.42	0.10
Baseline + spoiler	−0.44	0.51	−0.87
Baseline + wing ($\alpha_W = 17$ deg)	−0.44	0.48	−0.91

The baseline vehicle was derived from a generic two-seater passenger car and owing to the added cooling intakes and exits and open side window (as required by the regulations) its drag coefficient increased to a value of about 0.42. This value is somewhat higher than the range of $C_D = 0.36 - 0.39$ reported by Hucho (1987)[1] for an earlier model of this automobile. The

[1]See eighth vehicle in the "sports cars" list on page 158 of this reference.

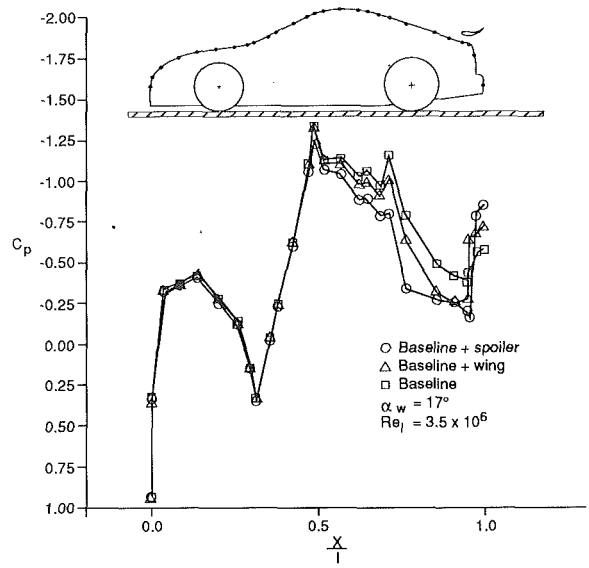

Fig. 4 Effect of rear wing ($\alpha_W = 17$ deg, $h/c = 0.75$) and spoiler on the pressure coefficient distribution along vehicle's upper surface centerline (uncertainty in $C_p = \pm 0.03$, in $x/l = \pm 0.005$)

lift coefficient for the basic shape was marginally small and positive and the addition of the rear spoiler clearly increased the aerodynamic downforce. The wing had a similar effect and usually the downforce was obtained with somewhat less drag than with the spoiler (recall that because of the regulations the spoiler span was much wider than the wing span—but when both had the same span the wing advantage becomes more obvious).

The effect of mounting the rear spoiler or the wing on the upper surface pressure distribution (along the centerline) is shown in Fig. 4. The pressure distribution at the front of the vehicle is only marginally affected by these modifications but their effect becomes more visible in the region behind the rear window. The flow over the rear window of the baseline vehicle was attached and it became detached (separated) when the rear spoiler was added—thereby reducing the lift contribution from this area. The observation that the flow on the baseline vehicle's rear window was attached is documented by Hashiguchi et al. (1986) and by Kawaguchi et al. (1989), and the three-dimensional pressure distribution data presented by Hashiguchi et al. (1986) resembles the data in Fig. 4 (for the baseline shape).

The last two points (near $x/l = 1.0$) indicate that the base pressure with the spoiler decreases which is the cause for the higher drag with the spoiler (note that with smaller spoilers a drag reduction is possible—as reported by Hucho (1987), in p. 123 or p. 174). The rear wing in general followed the same pattern and somewhat reduced the suction force near the rear window area (but the flow was not separated) and the base drag was also less than for the configuration with the spoiler.

This trend is visible, too, on the vehicle's lower surface pressure distribution which is presented in Fig. 5. Here it seems as if the base pressure influences the underbody flow such that the larger negative base pressure will result in the lowest pressure coefficients there (e.g., in the case of the spoiler). Also the effect of these rear deck mounted aerodynamic devices becomes more noticeable toward the aft-section and the large suction peak at the front is affected only marginally. The small suction peak at about $x/l \approx 0.6$ corresponds to the sharp upward turn in the lower panel surface. Such upswept underbody panels are widely used on other types of race cars and sample results for their aerodynamic effects are presented by George (1981) and later by Katz and Largman (1989).

The pressure distribution at the center of the groundplane for the above three vehicle configurations is presented in Fig.

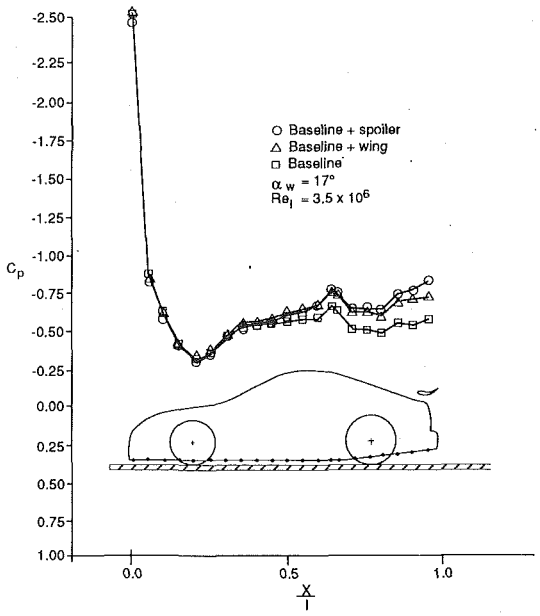

Fig. 5 Effect of rear wing ($\alpha_W = 17$ deg, $h/c = 0.75$) and spoiler on the pressure coefficient distribution along vehicle's lower surface centerline (uncertainty in $C_p = \pm 0.03$, in $x/l = \pm 0.005$)

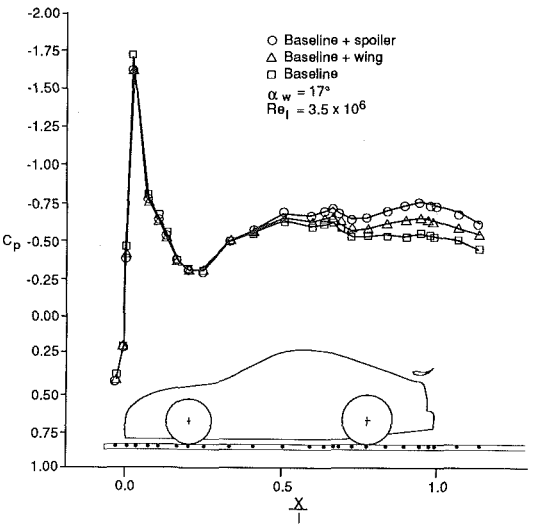

Fig. 6 Effect of rear wing ($\alpha_W = 17$ deg, $h/c = 0.75$) and spoiler on the pressure coefficient distribution along ground plane centerline beneath the model (uncertainty in $C_p = \pm 0.03$, in $x/l = \pm 0.005$)

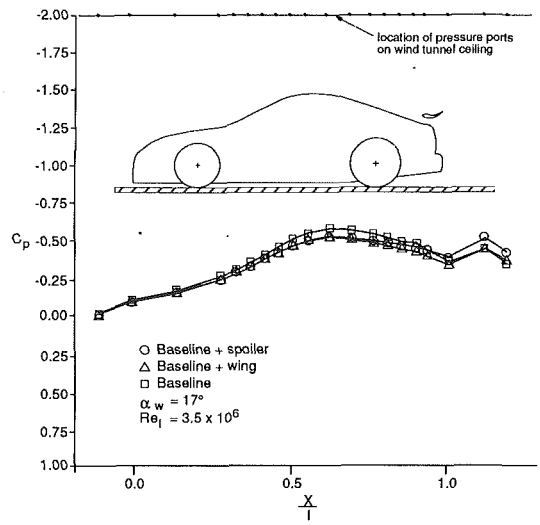

Fig. 7 Effect of rear wing ($\alpha_W = 17$ deg, $h/c = 0.75$) and spoiler on the pressure coefficient distribution along wind tunnel ceiling centerline (uncertainty in $C_p = \pm 0.03$, in $x/l = \pm 0.005$)

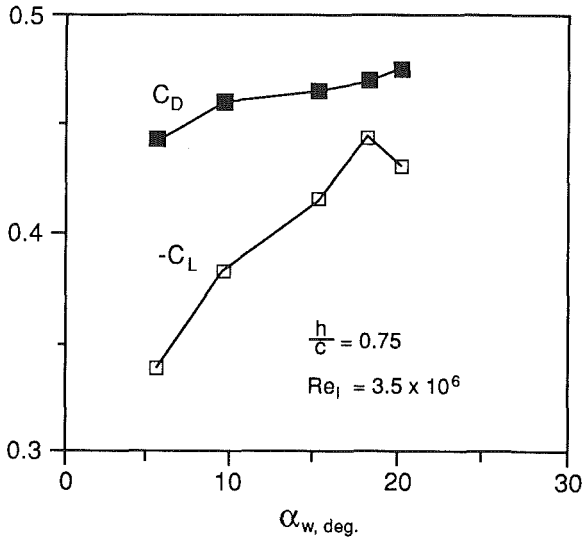

Fig. 8 Effect of rear wing angle of attack α_W on vehicle's downforce and drag coefficients (maximum uncertainty in $C_L = \pm 0.03$, in $C_D = \pm 0.01$, in $\alpha_W = \pm$ 0.2 deg)

6. This pressure distribution resembles the results of Fig. 5 except that near the front stagnation point ahead of the vehicle and in front of the large suction peak (at $x < 0.0$) the pressure coefficient becomes positive.

For completeness, the pressure coefficient distribution at the wind-tunnel ceiling centerline is presented in Fig. 7. This information is used for the solid blockage estimation (using the method of Katz, 1989) and the effect of the spoiler or rear wing is detectable in the figure. Also the static pressure loss behind the vehicle can serve as an indicator for the drag which based on this figure seems to be the largest for the case with the rear spoiler.

The experimental data presented so far indicated that the rear wing did not have a considerable aerodynamic advantage over the much simpler rear spoiler (due to the regulations). However, the lift of the vehicle (especially the aerodynamic load on the rear axle) could be trimmed more accurately with the wing, as indicated by the data presented in Fig. 8. In this case the wing angle of attack α_W was pitched about its trailing edge which was located at the highest allowed point (see Fig. 3) aligned vertically with the rear bumper line (dashed line in Fig. 3). This figure indicates that the lift could be changed in a linear fashion (closely) within the angle of attack range of $5 \text{ deg} < \alpha_W < 18$ deg and that the wing stalled at about $\alpha_W = 18$ deg.

A closer examination of this data revealed that the effect of the wing is much larger than the lift contribution of an isolated wing (for which $C_{L\max} \approx 0.2$, based on vehicle's reference area). Favorable interaction between a wing and purpose built race car shapes has been known for some time (see, for example, Beccio et al., 1987, or Katz and Largman, 1989) but the large magnitude of this effect on passenger car based race cars is more surprising. Consequently, the need to estimate the magnitude of this interaction led to the experiment, results of which are presented in Fig. 9. Here the wing angle of attack was set to $\alpha_W = 15$ deg (so that the wing will not be near stall) and its height was gradually increased. Note that the vertical distance h is measured at the wing trailing edge as shown in the inset to Fig. 9. These data clearly indicate that the lift of the combined vehicle/wing configuration is nearly twice the lift of the isolated wing (which is close to the lift coefficient shown in Fig. 9, for $h/c > 5$). The increase in the negative lift is generated

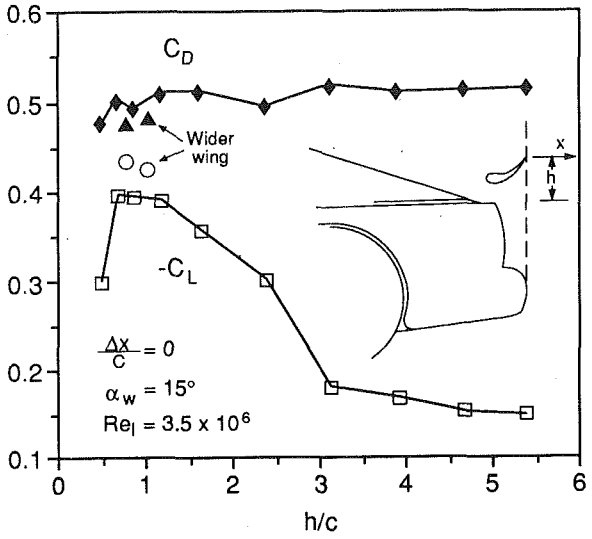

Fig. 9 Effect of wing height above rear deck on the aerodynamic coefficients of the complete vehicle (maximum uncertainty in $C_L = \pm 0.03$, in $C_D = \pm 0.01$, in $h/c = \pm 0.1$)

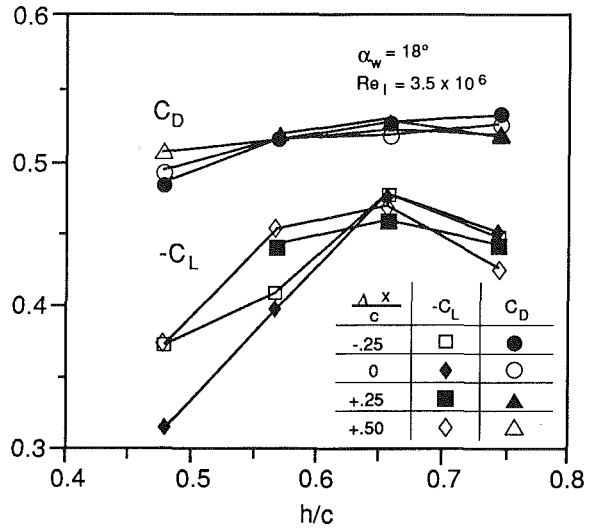

Fig. 10 Effect of rear wing horizontal placing on vehicle's total aerodynamic coefficients (maximum uncertainty in $C_L = \pm 0.03$, in $C_D = \pm 0.01$, in $h/c = \pm 0.1$)

by the vehicle's body due to the proximity of the wing, and the documentation of this favorable interaction for passenger car based race cars is probably the most important result of this study.

The interaction shown in Fig. 9 was later examined with different wing shapes and was found to follow similar trends. For example, the two additional data points in Fig. 9 (solid triangles for C_D, and open circles for C_L) represent results obtained with a wider rear wing with a width similar to the span of the spoiler (17.5 in.). The airfoil shape of this wing was unchanged but its chord was shortened so that wing area was kept the same (thus wing aspect ratio increased from 5.7 to 7.9). The above data points clearly indicate that lift/drag ratio improved slightly, as expected, with increased wing aspect ratio.

To further investigate this wing/body interaction the wing was moved forward (negative Δx) and backward (positive Δx) and the x coordinate is shown by the inset in Fig. 9. Note that positive x is measured backward from the rear bumper line and therefore positive x values are not allowed by the regulations governing these race cars. However, even if such experimental data is not directly applicable to this particular race car, when combined with the pressure distribution information presented in Figs. 4–7 it can be valuable for the validation of computational models. The effect of this horizontal positioning of the wing on the lift and drag coefficients is presented in Fig. 10. It seems that the wing accelerates the fluid beneath it and adds momentum to the two merging flows originating from the vehicle's upper and lower surfaces; this increases the velocity under the car and results in more downforce. Therefore, the resulting wing/body interaction is expected to increase as the wing height is reduced (until the wing reaches the upper surface boundary layer) but seems to be less affected by a horizontal shift to the wing. The data in Fig. 10 clearly reinforce this observation and the vertical distance parameter h/c is more dominant than the horizontal translation parameter $\Delta x/c$.

Conclusions

The interaction between the vehicle body and a rear deck mounted spoiler or wing is large and must be included in the aerodynamic considerations shaping a new design.

This aerodynamic interaction (in the case of the rear wing) is highly sensitive to wing location and when properly placed the total lift owing to the rear wing, combined with its effect on the vehicle's body, can amount to twice the lift of the isolated wing.

From the fabrication point of view spoilers are much simpler, however, wings are much more predictable (and better) for trimming. Also, since the current data indicated similar aerodynamic performance with the wing which had a smaller span than the spoiler, it is safe to assume that a wing with wider span (e.g., equal to that of the spoiler) will outperform the spoiler.

Acknowledgments

The authors wish to thank Mr. Jacob Gill for his assistance in modifying and operating the wind-tunnel data acquisition system for this test.

References

Beccio, S., Lombardi, C., Garrone, A., and Berta, C., 1987, "Endurance Group C1 Lancia Racing Car-Definition of Rear Wing Aerodynamic Contour," SAE Paper No. 870727.

George, A. R., 1981, "Aerodynamic Effects of Shape, Camber, Pitch, and Ground Proximity on Idealized Ground-Vehicle Bodies," ASME JOURNAL OF FLUIDS ENGINEERING, Vol. 103, pp. 631–638.

Hashiguchi, M., Ohta, T., and Kuwahara, K., 1986, "Computational Study of Aerodynamic Behavior of a Car Configuration," AIAA Paper No. 87-1386.

Howard, G., 1986, *Automobile Aerodynamics*, Osprey Publishing Limited, London.

Hucho, W. H., 1987, *Aerodynamics of Road Vehicles*, Butterworth and Co. Publishing, Boston.

Katz, J., 1989, "Integration of Computational Methods into Automotive Wind Tunnel Testing," SAE Paper No. 890601.

Katz, J., and Largman, R., 1989, "Experimental Study of the Aerodynamic Interaction between an Enclosed-Wheel Racing-Car and its Rear Wing," ASME JOURNAL OF FLUIDS ENGINEERING, Vol. 111, No. 2, pp. 154–159.

Kawaguchi, K., Hashiguchi, M., Yamasaki, R., and Kuwahara, K., 1989, "Computational Study of the Aerodynamic Behavior of a Three-Dimensional Car Configuration," SEA Paper No. 890598.

Rae, W. H., Jr., and Pope, A., 1984, *Low-Speed Wind Tunnel Testing*, Wiley, p. 371.

R. K. Sullerey
Professor.
Aerospace Engineering,
Indian Institute of Technology,
Kanpur, India

V. Ashok
Scientist.

K. V. Shantharam
Scientist.

Vikram Sarabhai Space Center,
Trivandrum, India

Effect of Inlet Flow Distortion on Performance of Vortex Controlled Diffusers

The present experimental investigations are concerned with diffusers employing the concept of vortex control to achieve high pressure recovery in a short length. Two types of two-dimensional diffusers have been studied, namely, vortex controlled and hybrid diffusers. Investigations have been carried out on such short diffusers with symmetrically and asymmetrically distorted inlet velocity profiles for area ratios 2.0 and 2.5 and divergence angle of 30 and 45 deg at a Reynolds number of 10^5. For each of the above configurations, experiments have been carried out for a range of fence subtended angles and bleed rates. The results indicate improvement in diffuser effectiveness up to a particular bleed off for both types of diffusers. It was observed that the nature of exit velocity profiles could be controlled by differential bleed.

Introduction

In a gas turbine, the diffuser is placed between the compressor and the combustor that has the primary function of reducing air velocity to ensure efficient combustion at a low pressure loss. In addition, the inlet flow distribution should be optimum for the particular engine operating condition. Variable geometry diffusers could provide the correct air flow distribution at each engine operating condition; however, with considerable increase in mechanical complexity. Alternately by providing diffuser with a wall bleed capability, the inlet air flow distribution could be controlled and the bleed air can be used for turbine blade cooling.

Adkins (1975) carried out a series of experiments on short annular diffusers with sudden area change. It was observed that suction stabilized vortex, established in the wall region, can provide better pressure recovery for such diffusers. The investigations concentrated mainly on the effect of bleed rates on pressure recovery of diffusers of various area ratios. In a subsequent investigation, Adkins et al. (1981) proposed a hybrid diffuser wherein vortex controlled step accounted for part of the area increase while a wide angle conventional diffuser was added immediately behind the vortex diffuser for the remaining area increase. On the basis of concepts first proposed by Ringleb (1964), Adkins et al. (1981) have explained the flow mechanism of vortex controlled hybrid diffusers.

The velocity profile at the exit of a multistage axial compressor is usually nonuniform and under certain operating conditions may be hub biased (Lang, 1970). Adenubi (1976) has carried out experimental investigations on the performance of straight core annular diffusers operating downstream of a compressor and found large effect of relative turbulence intensities.

The present investigations aim to evaluate experimentally the effect of various vortex controlled diffuser geometrical parameters, suction rates and diffuser inlet velocity profile on the diffuser exit flow distribution and pressure recovery. For simplicity, the experimental investigation have been carried out for two-dimensional diffusers. Dolan and Runstadler (1973) have compared the performance of square duct two-dimensional diffusers and conical diffusers and observed only a slight fall off in performance of square duct diffusers. As such two-dimensional diffuser performance can be considered a conservative estimate for the performance of conical/annular diffusers of identical geometrical and flow parameters.

The experimental measurements have been made for two area ratios, namely, 2 and 2.5. Hybrid diffuser with angle of divergence of 30 and 45 degrees were tested for each of the above area ratios and for various fence subtended angles. The suction rate was varied from 1 to 7 percent of the main flow for vortex controlled diffuser and 1 to 4 percent for hybrid diffusers. All measurements were made at Reynolds number of 10^5. Reynolds number is based on the side length of the primary duct. The effect of inlet velocity profile has been investigated for three different profiles including two grid generated velocity profiles. Results have also been obtained with a tail pipe after the diffuser.

Apparatus and Instrumentation

The apparatus consists of a small tunnel mounted on an adjustable traverse table. Figure 1 gives the layout of the tunnel used. The layout consists of a flexible air supply pipe line, a settling chamber, contraction, primary duct, vortex chamber and secondary duct. The air is supplied to the tunnel from compressed air bottles of 85 m^3 volumetric capacity at a maximum pressure of 18.7 bar. The flow rate is regulated through a set of pressure reducing valves and a pneumatically controlled butterfly valve.

The diffuser primary duct was made of perspex with a cross section of 71.5 mm × 71.5 mm and a length of 560 mm.

Contributed by the Fluids Engineering Division for publication in the JOURNAL OF FLUIDS ENGINEERING. Manuscript received by the Fluids Engineering Division February 1, 1990. Associate Technical Editor: U. S. Rohatgi

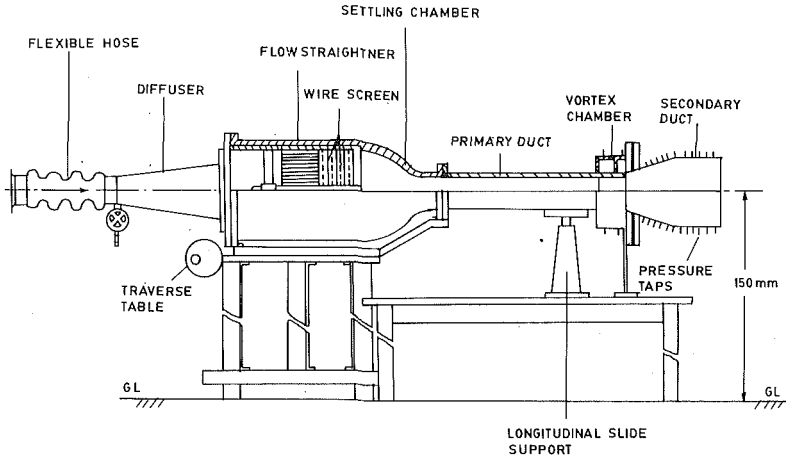

Fig. 1 Layout of the tunnel

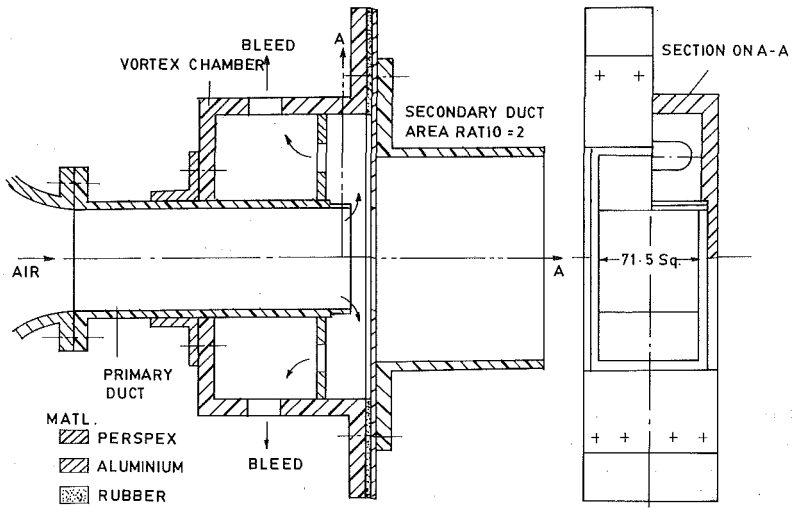

Fig. 2 Schematic of vortex flow controlled diffuser

Diffusers were designed with two area ratios namely 2.0 and 2.5 and corresponding secondary duct dimensions were 71.5 mm × 143 mm and 71.5 mm × 178.7 mm, respectively. The details of vortex chamber are given in Fig. 2.

Figure 3 presents the geometrical parameters for vortex controlled and hybrid diffusers. For hybrid diffusers, vortex control step ratio of 1.2:1 was chosen with same vortex chamber as in Fig. 2. A tail pipe of length 130 mm was used after the divergent portion.

The vortex chamber is an important component of vortex controlled diffuser. A small fraction of main air flow is sucked into the vortex chamber using the suction system shown in Fig. 4. The air entry to the vortex chamber (Fig. 2) is governed by the vortex fence parameters "x" and "y" (Fig. 3). The adjustment of the gap y was made by adjusting the locations of the fence between the flanges thereby varying the fence subtended angle ϕ.

Equal suction was ensured from both top and bottom suction chambers. Suction flow rate was measured using an orifice meter designed according to ASME standards. The flow rate was controlled using a butterfly valve. Fence subtended angle was varied in the range of 0 to 30 deg.

In order to generate typical compressor exit velocity profiles, grids were designed following the method of Wen and Jienkiwicz (1957) and Livesley and Turner (1964). The first grid generated a nonuniform flow at the diffuser inlet with boundary layers extending to 16 percent of duct height from top and bottom walls with a maximum to average velocity ratio of 1.16.

The second grid generated an asymmetric velocity profile about the primary duct center line. The grid consisted of stainless steel tubes of 1 mm diameter.

The pressure difference across the orifice was measured using a multitube manometer with an accuracy of 1 mm of water. However, an electronic digital manometer with a sensor of accuracy of 0.025 mm of water was used for wall pressure, dynamic pressure and vortex chamber depression measurements.

Nomenclature

AR = diffuser area ratio
B = bleed-flow fraction of total mass-flow rate
n = the number of traverse points having equal area weighting
$\dot{m}$ = mass-flow rate
u = local velocity
u_{av} = average velocity at an axial station
u_{max} = maximum velocity
V_c = coefficient of vortex chamber depression
x = axial gap between primary duct and fence
y = gap normal to axis between primary duct and fence
ϕ = fence subtended angle ($\tan^{-1} y/x$)
α = kinetic energy flux parameter
η = diffuser effectiveness
$\theta/2$ = diffuser semidivergence angle

To measure the velocity distribution in primary and secondary ducts, 1 mm diameter total head tube was used with a three-dimensional traverse mechanism. The least count of traverse in the vertical and horizontal directions was 0.05 mm and 0.6 mm, respectively. DISA 55-31 constant temperature hot wire anemometer was used to measure the turbulence distribution at the diffuser inlet.

The reference pressure at the diffuser inlet was measured using pressure taps located on either side at 71.5 mm upstream from the primary duct exit. A large number of pressure taps were used to monitor the wall pressure of secondary duct.

Testing Technique

Velocity traverses have been carried out at the diffuser exit both along the vertical and horizontal directions at three locations each corresponding to quarter span, half span and three fourth span locations.

If steady, one-dimensional ideal flow is assumed, the continuity equation can be written between inlet station 1 and exit station 2 as

$$\dot{m}_1 - \dot{m}_b - \dot{m}_2 = 0 \tag{1}$$

where $\dot{m}_1$ and $\dot{m}_2$ represent the inlet and exit mass flow rates and $\dot{m}_b$ the bleed (in present case suction) flow rates. Defining

$$B = \frac{\dot{m}_b}{\dot{m}_1} \tag{2}$$

Flow distortion was accounted for by Adkins (1975) by the use of kinetic energy flux parameter, defined on the basis of mass-averaged dynamic head as follows

$$\alpha = \frac{n^2 \sum_1^n (\sqrt{h})^3}{\left(\sum_1^n \sqrt{h}\right)^3}$$

(a) VORTEX CONTROLLED DIFFUSER

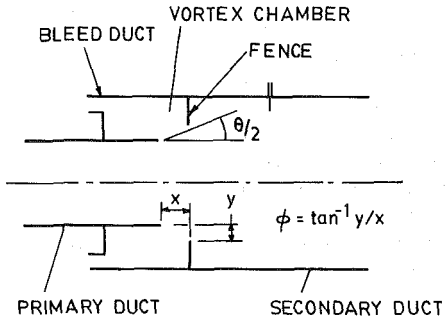

(b) HYBRID CHAMBER

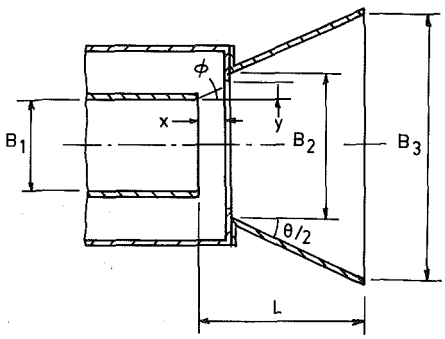

Fig. 3 Geometric parameters

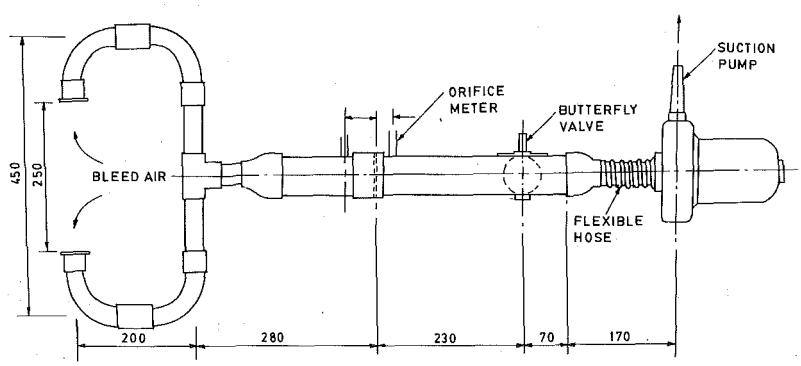

Fig. 4 Suction system

where h is the measured dynamic head and "n" is the number of traverse points which in the present case were more than 20.

The diffuser effectiveness is defined as the ratio of measured to ideal static pressure rise as given below

$$\eta = \frac{(p_2 - p_1)\text{measured}}{1/2\ \rho u_{av1}\left[\alpha_1 - \dfrac{(1-B)^2}{(AR)^2}\right]} \tag{3}$$

where u_{av1} is the inlet average velocity and AR is the diffuser area ratio.

The pressure loss by the bleed air has been expressed as the non-dimensional vortex chamber depression, v_c, where

$$v_c = \frac{p_1 - p_c}{1/2\ \alpha_1 \rho u_{av1}^2}$$

vortex chamber pressure, p_c, is monitored from both top and bottom suction chambers. It was ensured that this pressure is same for both the chambers as would be required for equal suction from both the sides. In case of minor variations, an average of the two readings was taken.

The measurement error in the inlet velocity and mass flow rate ($\dot{m}$) is expected to be less than ± 1 percent. The bleed rate ($\dot{m}_b$) has been measured to an accuracy of ± 2 percent. The effect of these errors on diffuser effectiveness is likely to be ± 2 percent, which would also be an estimate of error for vortex chamber depression, v_c. The mean velocity measurements in diffuser exit flow are not corrected for the effect of streamwise turbulence intensity. In certain regions this effect is estimated to be up to 4 percent of measured velocity, the true mean velocity being lower than the measured value. However, all the results have been presented in the form of ratio of local to maximum velocity. This ratio would not be in error of more than 2 percent.

Pressure measurements have been carried out by wall tappings on the diffuser. Because turbulent fluctuations fall to zero at the surface, the only error which could be caused in pressure measurements by the fluctuations in the flow would be the result of fluctuating inflow and outflow through the holes due to the compressibility of the flow field. To a first approximation, this error is estimated to be less than half a percent of free-stream dynamic head. Therefore, the error in pressure measurements is expected to affect the diffuser effectiveness values by half a percent.

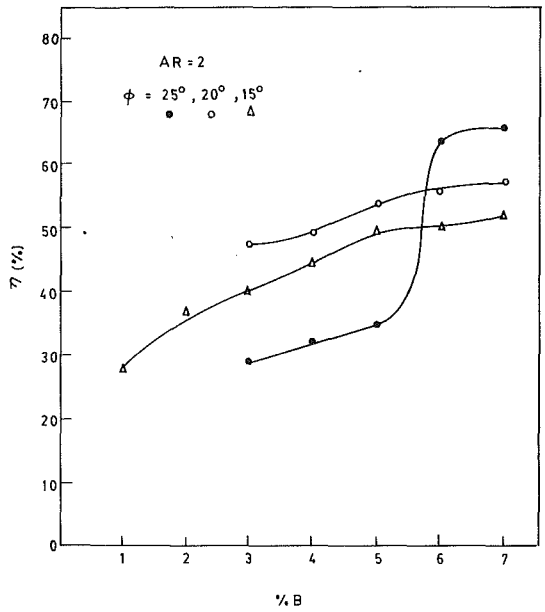

Fig. 5(*a*) Vortex controlled diffuser performance for different bleed-offs

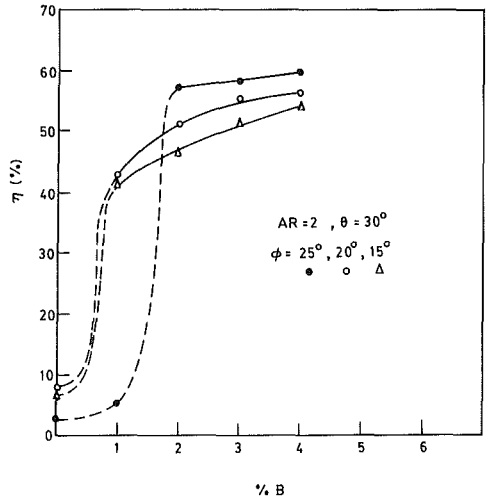

Fig. 5(*b*) Performance characteristics of hybrid diffuser with bleed-off

Results and Discussions

Performance of vortex controlled and hybrid diffusers have been presented in terms of diffuser effectiveness and outlet velocity profiles. Diffuser effectiveness as a function of bleed off rate for vortex controlled diffuser is presented in Fig. 5(*a*). It is observed that the best performance is obtained for fence subtended angle of 25 deg and the maximum effectiveness is about 68 percent. For fence subtended angles of less than 15 deg, the pressure recovery was poor and the results are not presented here. Diffuser effectiveness values are lower than the values obtained by Adkins (1975) for annular diffusers. Figure 5(*b*) shows the performance curves with varying bleed rates for a hybrid diffuser of same included angle and the same area ratio. The diffuser effectiveness shows a steep increase with bleed rates between 1 to 2 percent for all fence subtended angles. Adkins et al. (1981) has obtained even higher values of diffuser effectiveness for conical diffusers as compared to the two dimensional diffusers of the present investigations. Comparing results of Fig. 5(*a*) and 5(*b*) it is seen that the hybrid diffusers require appreciably lower bleed rates to achieve high performance. Fence subtended angle of 25 deg was observed to be optimum for both cases. An explanation of the working of vortex controlled diffuser has been proposed by Adkins (1975). According to the proposed model, due to the external suction, the static pressure inside the vortex chamber is below that in the mainstream. As a result, the stream drawn into the vortex experiences considerable acceleration, while the adjacent stream flowing down the diffuser is flowing to a region of higher pressure and therefore decelerates. A shearing action, produced by the velocity differential between the streams, creates an extremely turbulent layer which inhibits flow separation. This mechanism is found to operate optimally at a certain combination of fence subtended angle and bleed rates. This is a possible explanation of sudden increase in diffuser effectiveness at fence subtended angle of 25 deg in Fig. 5(*a*). Vortex chamber depression increases with bleed rates and fence subtended angle as seen in Fig. 6. The maximum value of v_c for hybrid diffuser is 0.5 for fence subtended angle of 25 deg compared to a value of $v_c = 0.7$ for vortex controlled diffuser.

Diffuser outlet velocity profiles were symmetrically distorted for both cases. The level of flow distortion as indicated by the maximum to average velocity ratio was 1.62 for vortex controlled diffuser and 1.25 for the hybrid diffuser. These measurements were carried out for 6 percent bleed rate for vortex controlled diffuser and 2 percent bleed rates for the hybrid diffuser. Thus it can be concluded that the hybrid diffuser performs better than the vortex controlled diffuser in all three

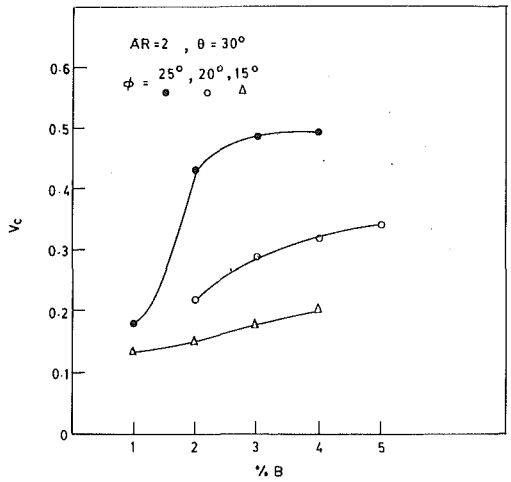

Fig. 6 Vortex chamber depression for different bleed-offs in hybrid diffuser

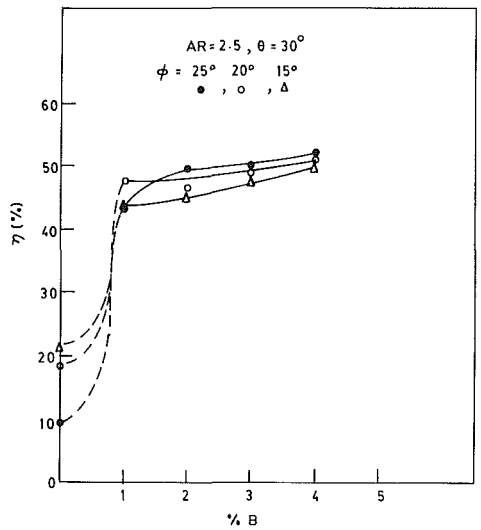

Fig. 7 Performance characteristics of hybrid diffuser with bleed-off

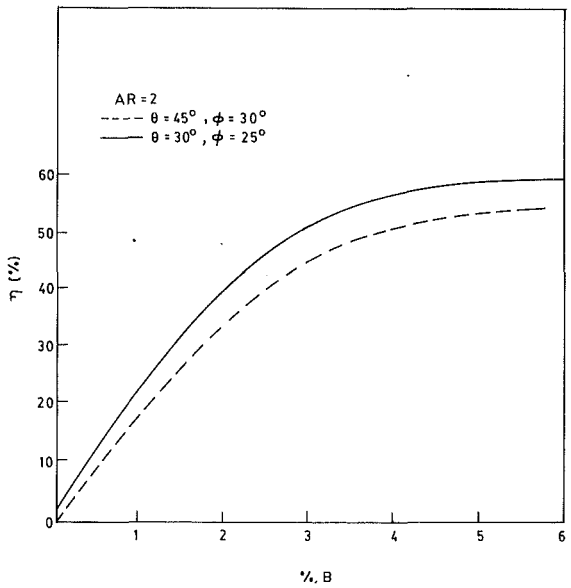

Fig. 8 Comparison of diffuser effectiveness for two divergence angles

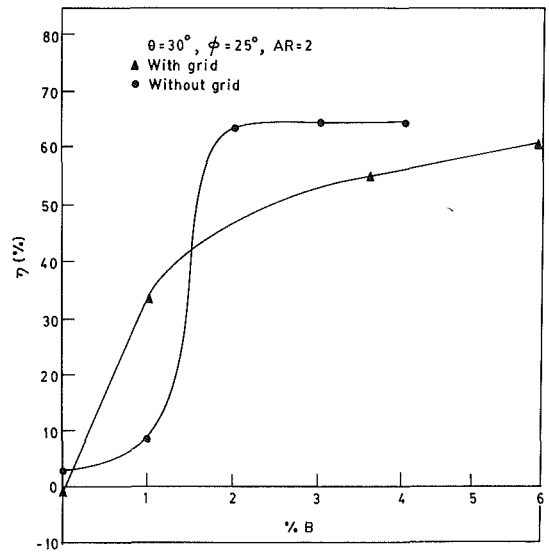

Fig. 9 Comparison of diffuser effectiveness with uniform and nonuniform inlet velocity profiles

respects, namely, lower bleed rate requirements, lower value of coefficient of vortex chamber depression, and more uniform diffuser outlet velocity profile.

For the case of hybrid diffuser of area ratio of 2.5, the variation of diffuser effectiveness with bleed rate is given in Fig. 7. Bleed rates required to substantially improve the diffuser effectiveness are within 1 to 2 percent. However, diffuser effectiveness is lower than for the case of area ratio of 2.0. The coefficient of vortex chamber depression is about 0.4 for the optimum fence subtended angle of 25 deg. Maximum to average velocity ratio at diffuser outlet is 1.46 compared to a value of 1.25 for an area ratio of 2.0. Figure 8 compares the performance of hybrid diffusers with divergence angles of 30 and 45 deg. Pressure recovery for 45 deg diffuser is negative at $B=0$. Results are presented only where the diffuser effectiveness has a positive value.

Although higher divergence angle leads to lower effectiveness (about 10 percent), a 45 deg divergence diffuser would also have a shorter length. As an additional feature, hybrid diffuser performance was also investigated by including a tail pipe at the diffuser exit. The axial length of the tail pipe was equal to the axial length of the diffuser. There was an improvement in pressure recovery to the extent of 10 to 15 percent for various cases. Flow nonuniformity decreased along the length of the tail pipe.

Inlet Flow Distortion. A set of results have been obtained by distorting the inlet flow as it entered the diffuser. For this purpose, as mentioned earlier a velocity profile generating grid was designed using the method of Wen and Jienkiewicz (1975) and Livesly and Turner (1964). Compressor exit flow is seldom uniform in gas turbines. Typically the boundary layer is about 16 percent of the blade height and the maximum to average velocity ratio between 1.10 to 1.20 (Lang, 1970). As such, the grid generated velocity profile in the present case had a maximum to average velocity ratio of 1.16 at the diffuser inlet. The boundary layer region extended to 16 percent of the duct height on either side. The measurements of rms streamwise turbulence indicated that the maxima of streamwise turbulence intensity at the diffuser inlet, was below 3–4 percent with the grid.

A comparison of diffuser effectiveness with uniform and nonuniform inlet flow is presented in Fig. 9. This result is for the case of hybrid diffuser of area ratio 2.0. It is observed that there is only a gradual improvement in performance with bleed rate with distorted inlet flow. Same level of effectiveness values

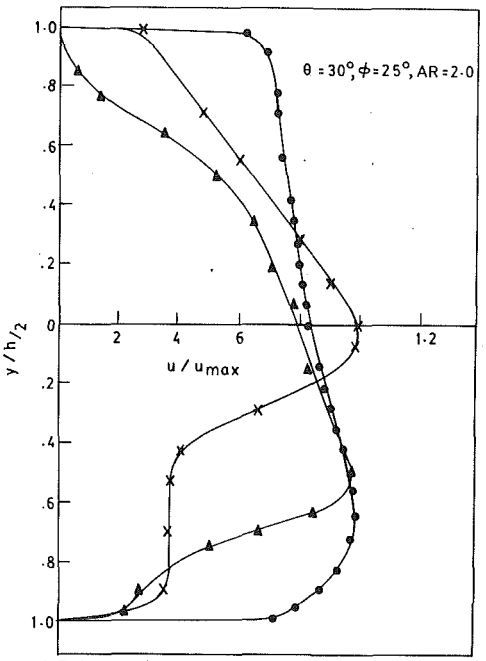

▲ Exit velocity profile with suction from both sides (B = 4 %) ; ● Inlet velocity profile ; X Exit velocity profile with suction from top wall (B = 3·2 %)

Fig. 10 Diffuser inlet and outlet velocity profiles with suction

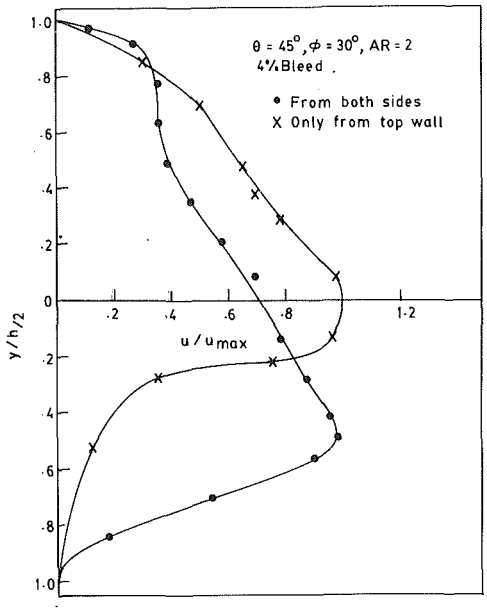

Fig. 11 Diffuser exit velocity profile with suction

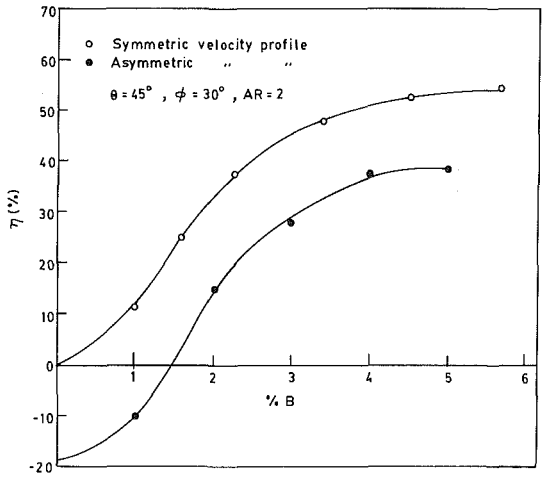

Fig. 12 Effect of assymetry of velocity profile on pressure recovery

are now obtained at bleed rates of about 6 percent as compared to bleed rates of 2 percent for uniform inlet profile case. Measured velocity profiles indicated that the maximum to average velocity ratio is 1.6 and 1.92, respectively, for hybrid diffuser area ratios of 2.0 and 2.5. Further, a scanning of velocity profiles at different heights indicated flow distortion in the diffuser in the crosswise direction where maximum to average velocity ratio was 1.26 for the area ratio of 2.0. Addition of a tail pipe again improved the pressure recovery by 10–15 percent and also reduced the level of flow distortion in the exit flow.

In many cases of off-design operations of compressors, the exit profile is usually hub biased (Lang, 1970). To study the effect of this bias on diffuser performance, the grid was modified to generate a skewed velocity distribution as shown in Fig. 10. The peak velocity is obtained towards the bottom wall and the peak to the average velocity ratio is 1.17. The measurements were repeated at three different stations to ensure that the velocity distribution is same at different sections of the inlet duct. Also shown in Fig. 10 are the diffuser exit velocity profiles for 30 deg angle hybrid diffuser. It is observed that the velocity peak continues to have a similar bias as the inlet flow for equal suction from both top and bottom walls. Next, in order to make the diffuser exit profiles symmetric, suction was applied only on the top wall. The diffuser exit profile now is modified to a center peaked velocity profile as shown in Fig. 10 with a maximum to average velocity ratio of 1.68. A similar change in diffuser outlet velocity profile can be achieved for 45 deg diffuser with a 4 percent bleed rate from the top wall as seen in Fig. 11. The effect of bleed rates on diffuser effectiveness is shown in Fig. 12 for symmetrical and asymmetrical distortions of inlet velocity profile. Diffuser effectiveness of 50 percent is attainable with bleed rates of around 4 percent, for the symmetrical inlet profile. It is seen that increased distortion of inlet flow leads to a loss in pressure recovery. There is further loss in pressure recovery if suction is applied only to one wall. However, differential suction can shift the peak in outlet velocity profile to the diffuser centerline.

Attempts were made to study the nature of the vortex formed with the help of flow visualization techniques. Both kerosene vapor and titanium-tetrachloride were used. However, the pictures obtained were hazy due to high levels of turbulence near the vortex chamber.

Conclusion

Performance of vortex controlled and hybrid diffusers have been evaluated in terms of diffuser effectiveness and outlet velocity profiles. Initial measurements with uniform diffuser inlet velocity profile indicated better performance of hybrid diffusers over vortex controlled diffusers. With a center peaked but distorted diffuser inlet velocity profile, bleed rates required for hybrid diffusers to achieve diffuser effectiveness of 50 percent were about 4 percent as compared to less than 2 percent required for flat uniform inlet velocity profile. The distortion of diffuser outlet velocity profile increases with the distortion of inlet flow. When the diffuser inlet velocity profiles was biased towards the bottom wall, the diffuser exit velocity profile also exhibited similar nature with increased distortion. However, it as possible to achieve a center peaked exit flow velocity profile by differential suction. Increase in diffuser divergence angle from 30 to 45 deg leads to about 10 percent lower pressure recovery.

Acknowledgment

The work reported herein was funded by Aeronautical development Agency, Bangalore. The support and encouragement of ADA, Bangalore is hereby acknowledged with gratitude.

References

Adenubi, S. G., 1976, "Performance and Flow Regime of Annular Diffusers with Axial Turbomachine Discharge Inlet Conditions," ASME JOURNAL OF FLUIDS ENGINEERING, Vol. 48, pp. 236–243.

Adkins, R. C., 1975, "A Short Diffuser with Low Pressure Loss," ASME JOURNAL OF FLUIDS ENGINEERING, Vol. 93, pp. 297–302.

Adkins, R. C., Matharu, D. S., and Yost, J. O., 1981, "The Hybrid Diffuser," ASME *Journal of Engineering for Power*, Vol. 103, pp. 229–236.

Dolan, F., and Runstadler, P. W., 1973, "Pressure Recovery Performance of Conical Diffusers at High Subsonic Mach Numbers," NASA CR-2299.

Lang, S., 1970, "Casing Boundary Layer in Multistage Axial Flow Compressors," *Proceedings of the Symposium on Flow Research on Blading*, Dzung, ed., Elsevier Publishing Co., pp. 275–298.

Livesley, J. L., and Turner, J. T., 1964, "The Generation of Symmetrical Duct Velocity Profiles of High Uniform Shear," *Journal of Fluid Mechanics*, Vol. 20, pp. 201–208.

Ringleb, F. O., 1964, "Discussion of Problems Associated with Standing Vortices," *Proceedings of Symposium on Fully Separated Flows*, ASME Fluids Engineering Division.

Wen, P. R., and Jienkiewicz, H. K., 1957, "The Production of Shear Flow in a Wind Tunnel," *Journal of Fluid Mechanics*, Vol. 2, pp. 521–531.

H. S. Pordal

P. K. Khosla

S. G. Rubin

Department of Aerospace Engineering
and Engineering Mechanics,
University of Cincinnati,
Cincinnati, OH 45221

A Flux-Split Solution Procedure for Unsteady Inlet Flow Calculations

The solution of the reduced Navier Stokes (RNS) equations is considered using a flux-split procedure. Unsteady flow in a two dimensional engine inlet is computed. The problems of unstart and restart are investigated. A sparse matrix direct solver combined with a domain decomposition strategy is used to compute the unsteady flow field. Strong shock-boundary layer interaction, time varying shocks, and time varying recirculation regions are efficiently captured.

1 Introduction

The design of advanced supersonic aircraft configurations require accurate estimates of the flight characteristics and performance of the aircraft propulsion system. An important part of this evaluation centers around the nature and location of the terminal shock in the engine inlet/diffuser. The orientation of the shock and its location is critical to the performance and stability of the inlet flow. For certain flight conditions and diffuser design, a shock can move ahead of the cowling so that inlet unstart occurs. This causes a sharp reduction in mass flow and pressure recovery and an associated large increase in drag. The shock can be swallowed (restart) by increasing the mach number, by increasing the throat area or by decreasing the back pressure; improved performance of the inlet is then recovered. Hsieh et al. (1987), Telcot and Kumar (1984), and Chyu et al. (1989) have investigated flow behavior in diffusers with terminal shocks. Rettle and Lewis (1968) have examined the effect of boundary layer bleed on flow separation and inlet performance. Reymner and Hickox (1972) have investigated steady flow fields in supersonic inlets, using a combined viscous-inviscid analysis. This procedure does not model the shock-boundary layer interaction correctly. Algorithms developed for the numerical solution of the unsteady full Navier-Stokes equations have been applied to predict steady and oscillatory flows in supersonic inlets (Knight, 1981). Investigation of steady or oscillatory flow in inlets with terminal shocks has been carried out by several authors; however, there is limited work (Varner et al., 1984) concerning the problems of unstart and restart.

The present study deals with the computation of two dimensional aircraft engine inlet flow. The problems of unstart and restart are investigated. The first part of the present study was concerned with the computation of two dimensional inviscid flow. The results of this investigation are available in an earlier work by Pordal et al. (1989, 1991). The second part of the study is concerned with the computation of unsteady viscous flow fields and the associated phenomena of inlet unstart and restart. Such flow fields involve strong shock-boundary layer interaction, time varying shocks and time varying regions of separated flow. These phenomena can be investigated using the unsteady full Navier Stokes (NS) equations. In the present study a reduced form of the Navier Stokes equations is applied. The method considered herein combines the asymptotic treatment of interacting boundary-layer theory and the accurate interaction simulation of the full NS methods. The unsteady reduced Navier Stokes (RNS) equations applied herein contain all of the essential physics of the flow and allow for a novel discretization that improves computational efficiency and results in simplified boundary conditions.

The governing equations are written in general non-orthogonal curvilinear co-ordinates and discretized using a form of flux vector splitting that is imbedded in a global pressure relaxation technique. This procedure has been formulated by Rubin and Reddy (1986) and Khosla and Lai (1983). The solution procedure remains the same for viscous and inviscid, incompressible, subsonic, transonic and supersonic flows, see Rubin (1982), Rubin and Reddy (1983), Khosla and Lai (1987) and Ramakrishnan and Rubin (1984). This procedure has been extended for three dimensional (Himansu et al., 1989), as well as unsteady flow (Remakrishnan and Rubin, 1987, 1988) computations. Significant features of this procedure are that it is independent of the Mach number and Reynolds number; moreover, it does not require the addition of artificial viscosity, other than that associated with the accuracy of the discretization. This numerical viscosity can be minimized on fine grids, see Rubin and Himansu (1989).

For unsteady flow computations, in lieu of the global iteration procedure, the complete flow field is computed at each time increment. For this purpose a direct sparse matrix solver (Bender, 1988 and Eisenstadt et al., 1977) is applied. The direct solver provides for stability, robustness, accuracy and time consistency. For steady computations, the solution technique permits large time increments and has strong convergence properties; whereas, for transient flows, time consistency plays a major role. Implicit consistent iterative procedures, such as the one outlined by Khosla and Rubin (1987), usually do not have these strong convergence properties and may require added transient or steady state artificial viscosity. The direct solver retains the simplicity and robustness of the time marching procedure moreover, added artifical viscosity is not required. For time dependent computations the time step limitation for the direct solver is less severe than that for iterative procedures. Section 2 of this paper describes the governing equations. The

Contributed by the Fluids Engineering Division for publication in the JOURNAL OF FLUIDS ENGINEERING. Manuscript received by the Fluids Engineering Division October 30, 1990. Associate Technical Editor: S. A. Ragab.

boundary conditions and discretization are described in Sections 3 and 4, respectively. Section 5 deals with the solution procedure, and the results are discussed in Section 6.

2 Governing Equations

The RNS equations are obtained by neglecting the viscous diffusion terms in an appropriate streamwise direction, as well as, all viscous diffusion terms in the normal momentum and energy balances. The RNS equations applied here are a composite of the Euler and higher order boundary layer systems. Asymptotic analysis of NS equations at large Reynolds numbers shows that axial diffusion and the viscous terms in the normal (η) momentum equations are of higher order and can be neglected in appropriate streamwise coordinates. The inclusion of the normal momentum equation and the unknown streamwise pressure gradient term provides an internal mechanism for viscous-inviscid interaction. This removes any singularities associated with strong interaction separated flows. A comparison of the RNS solution with full NS solution for unsteady flow over an airfoil is described by Ramakrishnan and Rubin (1988). The validity of applying the RNS equations for unsteady flows with large separation is demonstrated.

The conservation form of the RNS equations are written in general non-orthogonal curvilinear co-ordinates (ξ, η), so that an arbitrary grid generation technique can be considered. The metrics and Jacobians are computed using second-order central differencing. The detailed equations are described by Pordal et al. (1990).

The coefficient of viscosity (μ) is computed using a power law approximation i.e., $\mu \simeq T^{\alpha}$ ($\alpha = 0.72$). The coefficient of thermal conductivity (k) is expressed as $\mu Cp/\mathrm{Pr}$.

3 Initial and Boundary Conditions

Initial conditions depend upon the geometry and the procedure for starting the flow. Uniform flow conditions are generally used as initial conditions for inviscid computations; for most viscous flow computations the inviscid flow solution is used as the initial guess. A sketch of the boundary conditions depicting the physical domain is given in Fig. 1(a). Boundary conditions are such that, at the inflow U, V, ρ, and P are prescribed. At the outflow, for boundaries outside of the inlet and far from regions of reversed flow, the negative eigenvalue fluxes are neglected. For supersonic regions, these terms are identically zero. This is non-reflecting, non-interactive boundary condition for subsonic regions. For internal flow boundaries and subsonic outflow, the back pressure is specified. In this case the fluxes are not neglected. This is consistent with the operational or experimental conditions of the inlet. Far from the surface, uniform flow conditions are imposed. At the surface, for inviscid flow calculations, zero normal velocity or injection is specified. For viscous flow computations, additional no slip conditions and the wall temperature are required. A wall pressure condition is not required. The surface pressure is computed as part of the solution. For external outer boundaries, the free stream pressure is specified. More details

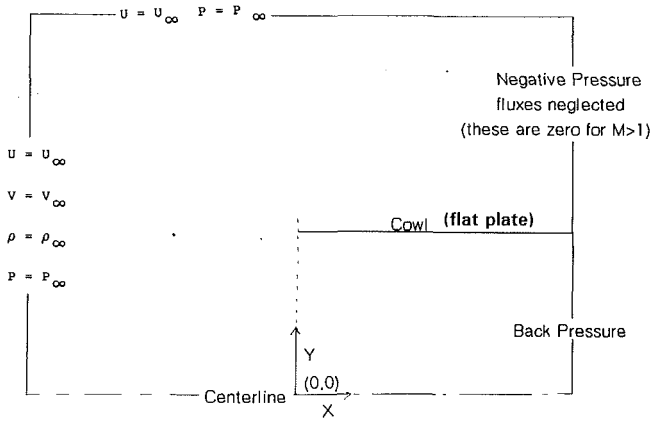

Fig. 1(a) Boundary conditions

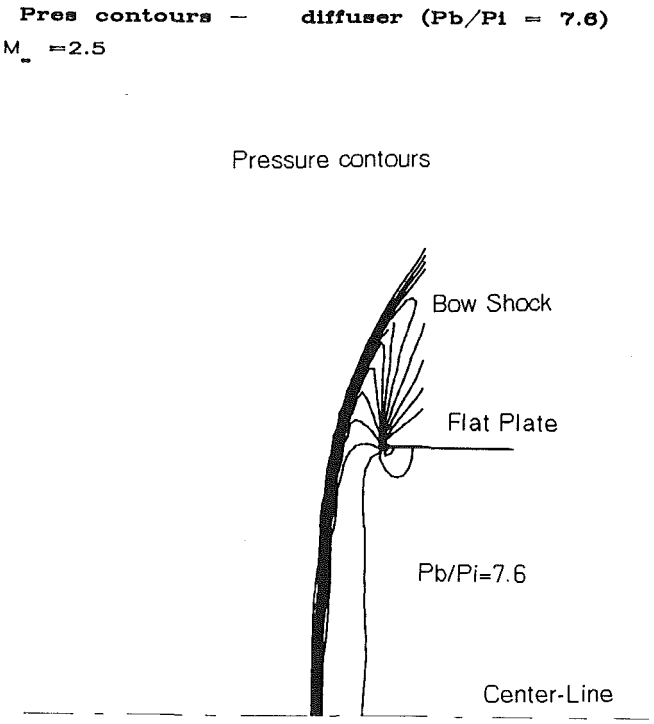

Fig. 1(b) Unstarted inlet

on applications to internal flows are available in earlier work by Pordal et al. (1989, 1991) and Reddy and Rubin (1988).

4 Discretization

The differencing has been described in previous references by Pordal et al. (1989, 1991), Rubin and Reddy (1983, 1986), Ramakrishnan and Rubin (1987, 1988) and Khosla and Lai (1983, 1987). All η derivatives are two point trapezoidal or three point central differenced and all convective ξ derivatives

Nomenclature

Cf = skin friction coefficient
Cp = specific heat at constant pressure
g = jacobian of transformation
H = total enthalpy
M = Mach number
P = pressure
Pb = back pressure at inlet exit
Pi = inflow pressure
Pr = Prandtl number
Re = Reynolds number
T = temperature
U, V = contravariant velocity components
X, Y = coordinates
γ = ratio of specific heats
ϕ = solution vector
ρ = density
τ = time
ω = flux splitting parameter
ξ, η = coordinates in transformed plane
μ = coefficient of viscosity

Subscripts

ξ, η = derivatives
∞ = free stream conditions

are upwind or flux vector differenced. The flux vector splitting (Rubin, 1988) for the stream wise pressure gradient term is in accordance with the flow physics and does not involve any discontinuous switching across shocks or contact discontinuities. The pressure gradient is differenced by

$$P_\xi = (\omega_{i-1/2})(P_i - P_{i-1})/\Delta\xi_i + (1. - \omega_{i+1/2})(P_{i+1} - P_i)/\Delta\xi_{i+1}$$

The parameter ω is computed as follows. For unsteady flows where a differential form of the energy equation is employed (Rubin, 1988), the cartesian form of ω is

$$\omega = M_\xi^2 \text{ for } M_\xi < 1 \text{ and } \omega = 1 \text{ for } M_\xi > 1$$

For a system of governing equations in curvilinear coordinates the eigenvalue analysis indicates that the parameter ω be redefined as

$$\omega = M_\xi^2 \cdot g^2/(Y_\eta^2 + X_\eta^2) \text{ for } M_\xi < 1 \text{ and } \omega = 1 \text{ for } M_\xi > 1$$

where Y_η, X_η, and g are metric quantities described previously in Section 2.

For computations where a constant stagnation enthalpy condition is used, in lieu of the differential energy equation, the parameter ω is given by the following relation first obtained by Vigneron (1978) and is also recovered by Rubin (1988), i.e., in cartesian form,

$$\omega = \gamma M_\xi^2/(1. + (\gamma - 1.)M_\xi^2) \text{ for } M_\xi < 1 \text{ and } \omega = 1 \text{ for } M_\xi > 1$$

This flux form of the streamwise pressure gradient term is capable of capturing very sharp normal shocks, e.g., three grid points. It should be noted that the flux splitting is employed only in the main flow or ξ direction. In the normal, and/or secondary flow direction, central differencing is currently applied. For blunt nosed regions, a form of flux vector splitting will be employed in both coordinate directions. This is currently under investigation. It must be noted that, though the convective streamwise derivatives are approximated using first-order differencing the accuracy of the overall scheme is somewhere between first and second-order for RNS solutions. This analysis has previously been discussed by Rubin (1982), Rubin and Reddy (1983, 1986), and Khosla and Lai (1983). In reversed flow regions, the streamwise convection terms in the ξ momentum and energy equation are flux vector or upwind differenced and this requires that the parameter ω be set to zero, see earlier work by Rubin and Reddy (1986), Himansu et al. (1989), Ramakrishnan and Rubin (1987) and Rubin (1988). The discretization is first order accurate and implicit in time. The time behavior of the RNS formulation has previously been explored by Ramakrishnan and Rubin (1987) and compared with results obtained from other computations. An unsteady solution for flow past a finite flat plate at incidence was described in order to demonstrate the time accuracy of the algorithm.

5 Solution Procedure

The discretized equations are quasilinearized using Newton's method and then written in a nine point star in delta form.

$$A_{ij}\delta\phi_{ij-1} + B_{ij}\delta\phi_{ij} + C_{ij}\delta\phi_{ij+1} + D_{ij}\delta\phi_{i-1j} + E_{ij}\delta\phi_{i+1j} + AM_{ij}\delta\phi_{i-1j-1} + CM_{ij}\delta\phi_{i-1j+1} + EM_{ij}\delta\phi_{i+1j-1} + EP_{ij}\delta\phi_{i+1j+1} = G_{ij} \quad (7)$$

where $\delta\phi$ denotes the error form of the solution vector ϕ and the coefficients A_{ij} . . . EM_{ij} are (5×5) matrices and G_{ij} is a (5×1) matrix. The elements of ϕ are U, V, ρ, P, and H. For unsteady flow H is not constant and the unsteady energy equation is solved. As a result there are five unknowns at each grid point. The equations of motion and the equation of state are solved in a coupled mode. The equation of state adds only diagonal elements in the coefficient matrix, and the band width is not affected. There is no additional computational cost in solving this completely coupled system.

For supersonic flows E_{ij}, EM_{ij}, and EP_{ij} are zero and the method reduces to a standard initial value problem. For supersonic flows there is no upstream influence. The above system of equations can be easily solved using a marching technique, such as line relaxation. However, for subsonic flow fields, it has been found that the convergence rate of such an iterative technique is very slow. Moreover, for unsteady flows the time step limitation for iterative solvers can also be severe (Ramakrishnan and Rubin, 1987). The experience of several researchers (Wigton, 1987, Bender and Khosla, 1988 and Salas and Kuruvila, 1989) has indicated that iterative techniques may not always be suitable for strong interaction flow problems and may be susceptible to false transients. It has been shown by Wigton (1987) for transonic flow over an airfoil, Salas and Kuruvila (1989) for vortex breakdown studies, Bender and Khosla (1988) for separated flows at large Reynolds number, that most of the difficulties encountered by iterative or approximate factorization techniques can be overcome by the use of a direct solver. It is for this reason that direct solution technique is chosen herein. In addition, iterative schemes degrade with fine or large aspect ratio meshes and the time required for convergence can become very large. Acceleration techniques such as multigrid or conjugate gradient methods are generally required. The direct solution technique applied here is time consistent, robust and is based on Newtons method so that it has quadratic convergence (Bender, 1988).

The Yale Sparse Matrix Package (YSMP), developed by Eisenstadt (1977) and modified for coupled systems (Bender, 1988) and for the boundary conditions detailed previously is applied here. This is an efficient solver as it stores only nonzero elements, and reorders the matrix using a minimum degree algorithm to minimize fill-in during the LU decomposition. For fine meshes and large numbers of mesh points, the memory requirement for the direct solver becomes significant. To overcome this limitation a domain decomposition strategy is employed. The computational domain is appropriately split into subdomains with suitable overlap between adjacent regions. Since we are dealing with flow fields that involve moving shocks, the overlap has to be sufficiently wide to accommodate the shock. Since the numerical scheme captures three point shocks, an overlap of five points is provided between adjacent regions. The entire flow field is computed by solving each subdomain sequentially, without any local iteractions on subdomain. Complete nonlinear convergence of the solution at each time step is obtained. The solution at each time level is assumed to be converged when the maximum residual is of order 10^{-4}. This is essential to maintain time consistency and accuracy of the solution. For inviscid flow computations, large time steps can be used ($\Delta\tau$ = .4, Courant number 16.), and complete convergence at each time step is achieved in about eight to ten local iterations. However, for viscous flow computations, to capture the correct transient flow physics related to recirculating flows, relatively small time steps are essential ($\Delta\tau$ = .04 to $\Delta\tau$ = .1, Courant numbers 1.6 to 4.), and for these computations convergence at each time level is attained in approximatedly four iterations.

6 Results

At supersonic flight conditions, inlet performance depends on the terminal shock in the diffuser. The shock location depends on the flight conditions, throat area and back pressure. The mass flow rate in an inlet is also dependent on these parameters. In the present study the effect of changing the back pressure and mass flow (bleed) on the terminal shock location is investigated. The unsteady flow behavior associated with unstart and restart of the inlet is efficiently captured.

The unstart and restart of an engine inlet are investigated for a Mach number of 2.5 and Reynolds number of 12000 (laminar flow). Since the flow is complex, the geometry is

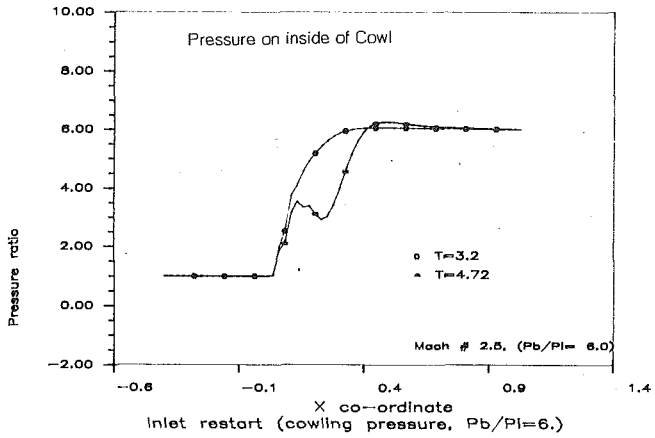

Fig. 2(*a*) Inlet restart

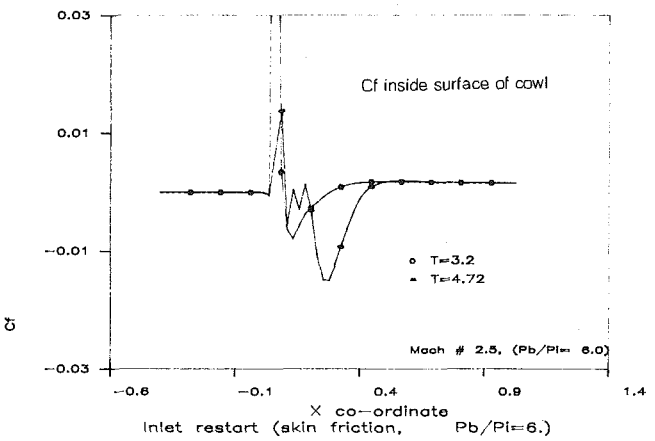

Fig. 2(*b*) Inlet restart

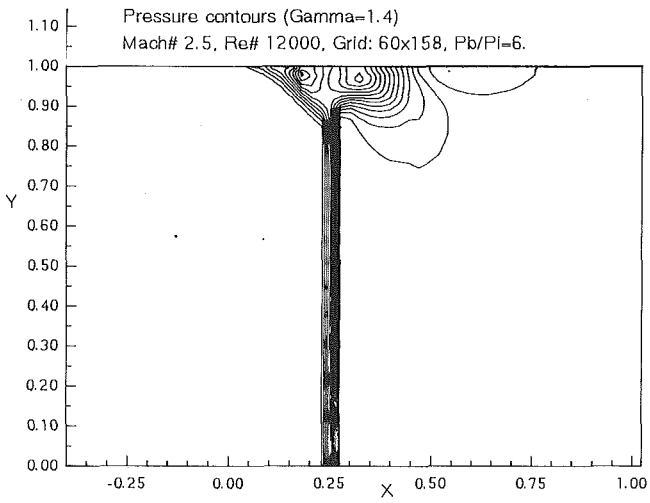

Fig. 3(*a*) Pressure contours

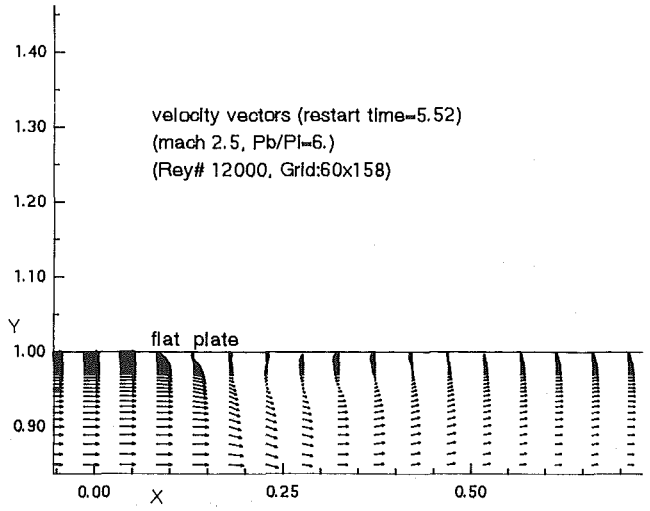

Fig. 3(*b*) Velocity vectors

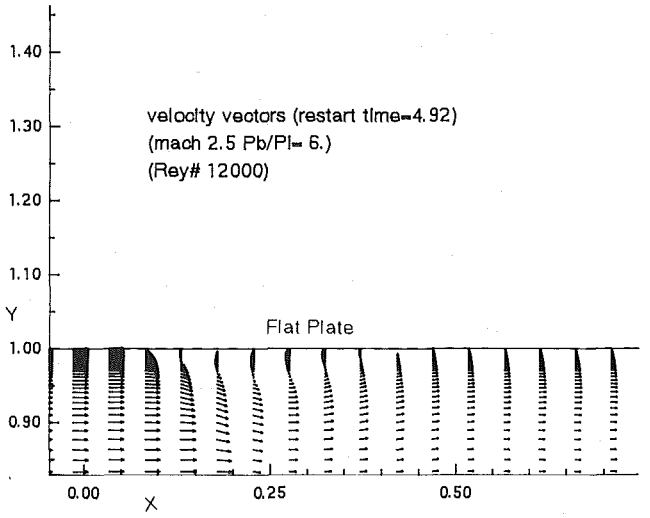

Fig. 4 Velocity vectors

simplified as a flat plate diffuser. Supersonic flow with a sufficiently high back pressure is computed. Rather interesting flow physics is highlighted even by this simple geometry. Similar flows are also encountered behind reflected shocks in shock tubes and shock tunnels. Computations were performed on a grid of 60 × 158 (ΔX = 0.023, ΔYmin = 0.0003). In the normal direction, 105 points are placed inside the diffuser and the rest are appropriately distributed outside. The internal flow field (between the center-line and cowling) and the external flow field are computed simultaneously. For this grid (47,400 unknowns), the direct solver requires 34 seconds of CPU time per iteration on the cray Y-MP8. The memory requirement for the above grid using a domain decomposition strategy (5 domains each of approximately 15 × 158) is a little over three mega-words.

The unstart and restart of an inlet can be achieved by changing the back pressure and/or by surface bleed. At unstart a bow shock stands ahead of the inlet (Fig. 1(*b*)). The inviscid solution for an unstarted inlet, as described by Pordal et al. (1989, 1991), was used as an initial solution to compute the viscous interaction. Steady viscous flow for an unstarted inlet was thus obtained. In the first example, the unstarted inlet, see Fig. 1(*b*) was restarted by decreasing the back pressure ratio to 6. This is well below the critical value. Once the shock is swallowed, the adverse pressure gradient associated with the shock generates a large reversed flow region. Since the shock location varies with time, the separation region is also in constant flux.

At time 3.2 (nondimensionalized time) the normal shock is swallowed and lies very close to the inlet lip. At this location the terminal normal shock merges with the inlet leading edge oblique shock. The cowling pressure distribution (Fig. 2(*a*)) indicates a single shock close to the inlet lip. The skin friction distribution (Fig. 2(*b*)) indicates a single recirculation zone close to the inlet lip. However, at time 4.72 the pressure distribution (Fig. 2(*a*)) is indicative of a double shock. Due to the separation, the boundary layer thickens considerably and

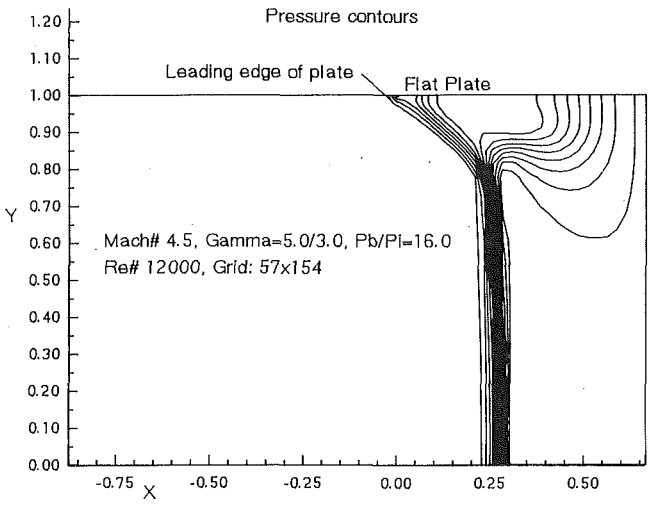

Fig. 5 Pressure contours

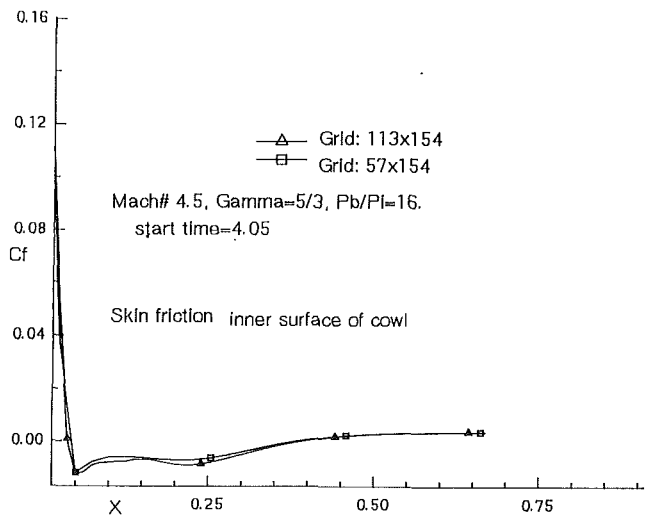

Fig. 6(*a*) Skin friction comparison

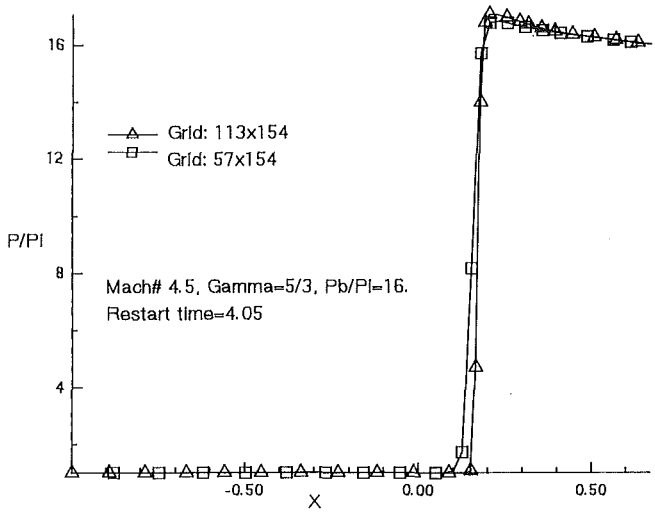

Fig. 6(*b*) Center-line pressure variation

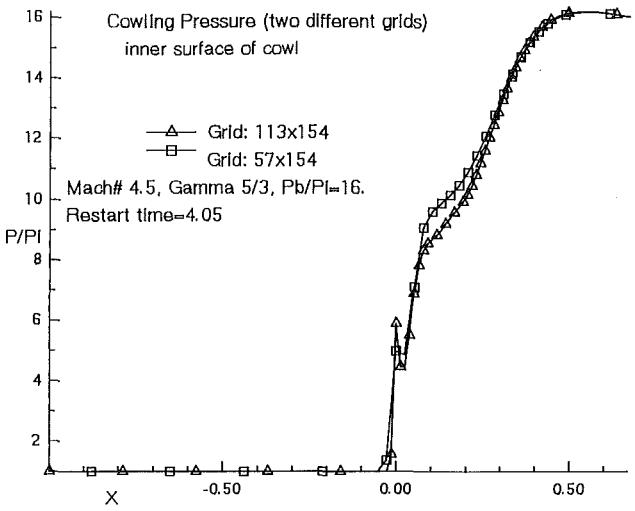

Fig. 6(c) Surface pressure comparison

this generates a strong leading edge shock. Therefore, both the terminal normal shock and the leading edge oblique shock, due to the displacement effect, are quite strong; this gives rise to the reversed flow. At the cowling surface, there is a positive pressure gradient associated with the leading edge shock. This is followed by a small expansion region associated with the convex displacement thickness generated by the separation bubble. This is followed by a steep pressure gradient associated with the terminal normal shock.

The skin friction (Fig. 2(*b*)) at time 4.72 indicates a leading edge separation bubble followed by a zone of large separation associated with the normal shock. The oscillation in the skin friction at time 4.72 (Fig. 2(*b*)) is probably due to lack of grid resolution. The separation zone at this point shows signs of "breaking up" into two vortical regions. At time 5.52, the pressure contours (Fig. 3(*a*) indicate a very complex shock structure close to the surface. An oblique shock originates from the leading edge of the plate and this shock intersects at the triple point associated with the terminal normal shock. The velocity vectors (Fig. 3(*b*)) indicate a double recirculation zone. The first is associated with the leading edge oblique shock and the second with the terminal normal shock. If we examine the velocity vectors at time 4.92 (Fig. 4), there is a single recirculation zone; however, at time 5.52 there are two distinct recirculation zones. This splitting takes place in a nondimensional time of about 0.6 or a real time of about 0.6×10^{-2} secs. This represents a very rapid change in flow properties.

The shock boundary layer interaction generates a very complex shock structure near the wall. Although there are no experimental observations for this type of inlet geometry, similar interaction is observed in shock tube flows (Herman, 1958). Shock tube experiments by Herman (1958) have indicated that a triple point shock structure exists for a range of Mach numbers and/or specific heats. For a Mach number within this regime the stagnation pressure of the energy deficient fluid in the boundary layer is exceeded by the pressure behind the shock. As a result, there is no steady flow of the energy deficit boundary layer fluid into the region behind the shock. The fluid gathers in a region adjacent to the foot of the shock, and is unable to pass into the high pressure region behind the shock. This complex region grows with time. If the Mach number and/or specific heats do not lie within this critical regime, the triple point intersection is not observed. The flow conditions in an inlet are considerably different from the flow conditions in a shock tube and always lie in the critical regime irrespective of the Mach number and/or specific heats; therefore, the triple point structure is always observed. In order to investigate the effect of specific heat ratio; computations for $\gamma = 5/3$ and $M_\infty = 4.5$ have also been considered. It can be noted from Fig. 5 that the triple point structure still presists.

The accuracy of the solution is examined with computations on a finer grid (113 × 154), for $\gamma = 5/3$ and $M_\infty = 4.5$. A comparison with the original grid (57 × 154) solution is pre-

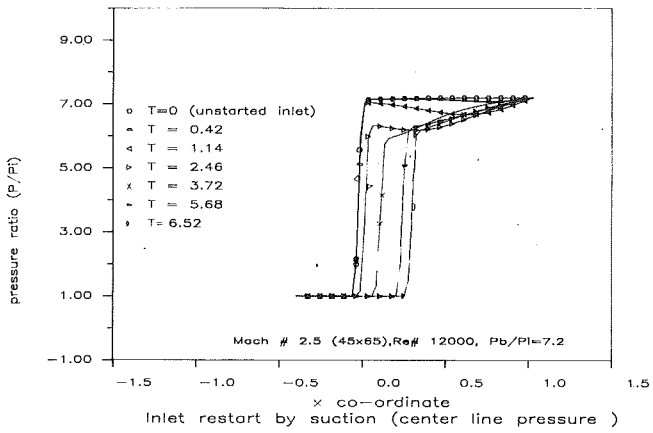

Fig. 7(*a*) Inlet restart by suction

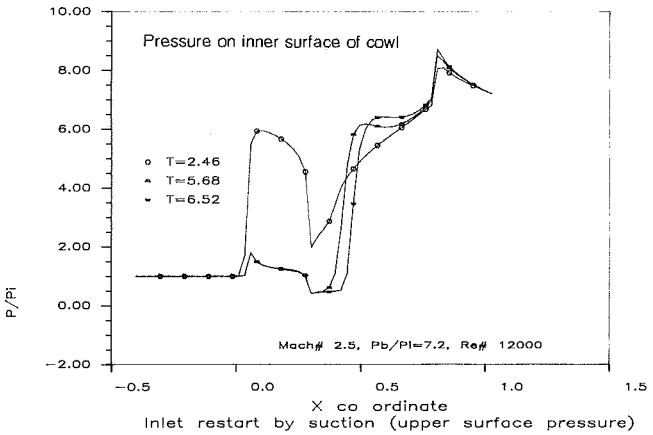

Fig. 7(*b*) Inlet restart by suction

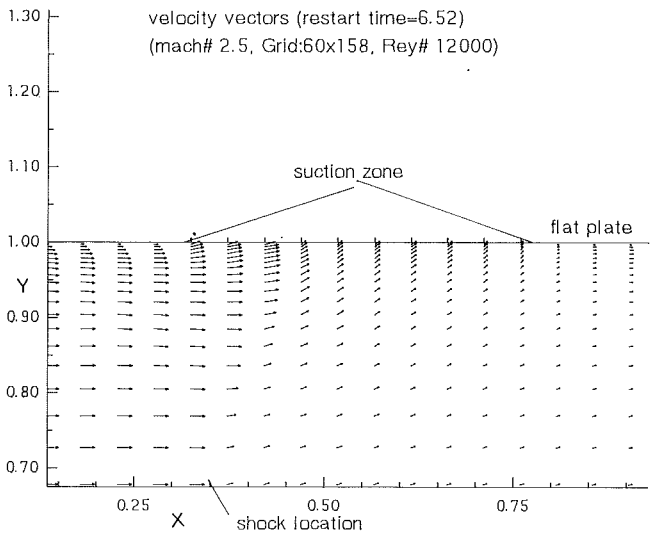

Fig. 8(*a*) Velocity vectors

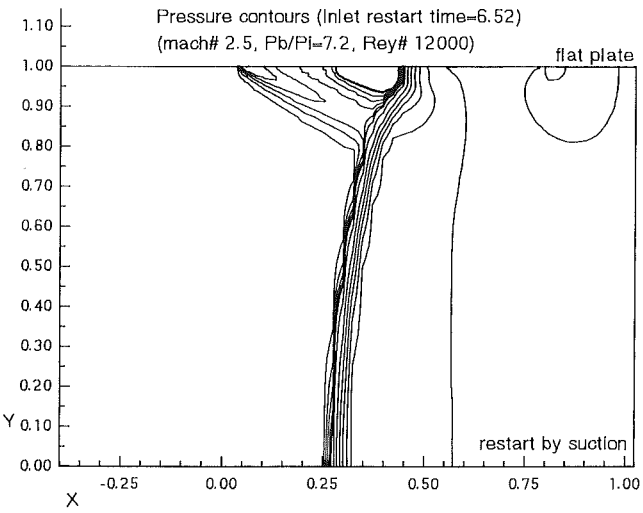

Fig. 8(*b*) Pressure contours

sented in Figs. 6(*a–c*). The overall accuracy of the original grid (57 × 154) solution is generally acceptable, except for a slight discrepancy in the pressure (Figs. 6(*b–c*)). This discrepancy arises due to the fact that, on the fine grid, the shock is spread over a smaller distance (always over three grid points). In order to investigate the effects of wall temperature on the shock boundary-layer interaction, computations at cold wall conditions have been carried out and the results are discussed in earlier work by Pordal et al. (1990).

Alternately, the inlet can also be restarted or unstarted by employing surface bleed. Inlet restart was investigated by applying bleed on the surface (a uniform nondimensional suction velocity of 0.28 is applied between $x = 0.3$ and $x = 0.78$; the back pressure is held constant). In this case the excess mass behind the normal shock is removed by providing bleed on the cowling surface. This causes the unstarted inlet to restart. The time history of the restart process is shown in Figs. 7(*a–b*). Application of bleed causes a reduction in the surface pressure. At a time 2.46, the inlet is restarted. The shock lies very close to the inlet tip and there is no separation. Due to suction the adverse pressure gradient associated with the normal shock is attenuated and the boundary layer is quite thin. As a result, the leading edge oblique shock is quite weak. At time 3.72, a single separation region is observed. This region is associated with the terminal normal shock. There is no separation associated with the leading edge oblique shock; however, as the terminal shock moves closer to the suction zone (time = 6.52) the adverse pressure gradient weakens and the separation zone vanishes (Fig. 8(*a*)). The surface pressure distribution (Fig. 7(*b*)) and the pressure contours (Fig. 8(*b*)) indicate a weak leading edge oblique shock intersecting the terminal normal shock.

This diffuser geometry represents a starting point for the simulation of transient inlet behavior. For this and similar geometries, other computational or experimental results are unavailable for comparison. However, qualitative agreement with flow visualization studies (Herman, 1958) for unsteady reflected shock wave boundary-layer interaction in a shock tube is obtained. Therefore, the only assessment of accuracy is the grid studies discussed herein. The code has been validated for other model geometries by comparison with other available solutions (Pordal et al., 1989). Turbulent flow computations have also been initiated. It is anticipated, that with turbulent boundary layers weaker shock boundary layer interaction, diminished recirculation bubbles and increased unsteadiness, e.g., buffetting, will result.

7 Summary

A flux-split relaxation procedure has been applied, with the RNS approximation, to investigate unstart and restart of an aircraft engine inlet. A simplified geometry (flat plate diffuser) was considered. A sparse matrix direct solver, combined with domain decomposition strategy, has been used to compute the unsteady flow field.

The restart of an unstarted inlet was initiated by decreasing the back pressure and also by surface bleed. Complex flow fields associated with strong shock-boundary layer interaction,

time varying shocks and time varying regions of separated flow have been captured. Efforts to capture the transient flow field associated with the unstart process are under consideration.

Acknowledgment

The work has been supported inpart by the NASA Lewis Research Center (T. Benson, Technical Monitor) under Grant No. NAG 3-1178 and in part by the AFOSR (L. Sakell, Technical Monitor) under grant No. 90-0096.

The computations have been performed on the Cray Y-MP at the Ohio Supercomputer center.

We are grateful to Dr. M. Dunn of Calspan for bringing the earlier work by Herman (1958) to our attention.

References

Bender, E. E., 1988, "The Use of Direct Sparse Matrix Solver and Newton Iteration for the Numerical Solution of Fluid Flow," Ph.D. Thesis, University of Cincinnati.

Bender, E., and Khosla, P. K., 1988, "Application of Sparse Matrix Solver and Newtons Methods to Fluid Flow Problems," 1st National Fluid Dynamics Congress, 88-3700, Cincinnati, Ohio.

Chyu, W. T., Kawamura, T., and Dencze, D. P., 1989, "Navier Stokes Solutions for Mixed Compression Axisymmetric Inlet Flow With Terminal Shock," *Journal of Propulsion*, Vol. 5, No. 1, pp. 4–5.

Eisenstadt, S. G., Gursky, M. C., Schultz, M. H., and Sherman, A. H., 1977, "Yale Sparse Matrix Package II. The Non-Symmetric Codes, Report 114," Yale University Department of Computer Science.

Herman, M., 1958, "The Interaction of a Reflected Shock Wave with the Boundary Layer in a Shock Tube," NACA TM-1418.

Himansu, A., Khosla, P. K., and Rubin, S. G., 1989, "Three-Dimensional Recirculating Flows," 27th Aerospace Sciences Meeting, AIAA 89-0552, Reno, Nevada.

Hsieh, T., Bogar, T. J., and Coakley, T. J., 1987, "Numerical Simulation with Experimental for Self Excited Oscillations in Diffuser Flow," *AIAA Journal*, Vol. 25, No. 7, pp. 936–943.

Khosla, P. K., and Lai, H. T., 1983, "Global PNS Solutions for Subsonic Strong Interaction Flow over a Cone-Cylinder Boat-Trail Configuration," *Computers and Fluids*, Vol. 11, No. 4, pp. 325–339.

Khosla, P. K., and Lai, H. T., 1987, "Global Relaxation Procedure for Compressible Solution of the Steady-State Euler Equations," *Computers and Fluids*, Vol. 15, No. 2, pp. 215–218.

Khosla, P. K., and Rubin, S. G., 1987, "Consistent Strongly Implicit Iterative Procedure for Two Dimensional Unsteady and Three Dimensional Space-Marching Flow Calculations," *Computers and Fluids*, Vol. 15, No. 4, pp. 361–377.

Knight, D. D., 1981, "Improved Calculation of High Speed Inlet Flows, Part I, Numerical Algorithm," *AIAA Journal*, Vol. 19, No. 1, pp. 34–41. Part II, Results, *AIAA Journal*, Vol. 19, No. 2, pp. 172–179.

Pordal, H. S., Khosla, P. K., and Rubin, S. G., 1989, "Flux-Split Solution Procedure for the Euler Equations," *International Conference on Computational Techniques and Applications*, Brisbane, Australia. pp. 437–444.

Pordal, H. S., Khosla, P. K., and Rubin, S. G., 1990, "A Flux-Split Solution Procedure for Unsteady Flow Calculations," *International Symposium on Nonsteady Fluid Dynamics*, Toronto, Canada, pp. 167–175.

Pordal, H. S., Khosla, P. K., and Rubin, S. G., 1991, "Inviscid Steady/Unsteady Flow Calculations," *Computers and Fluids*, Vol. 9, No. 1, pp. 93–118.

Ramakrishnan, S. V., and Rubin, S. G., 1984, "Global Pressure Relaxation for Steady, Compressible, Laminar, Two Dimensional Flows With Full Pressure Coupling and Shock Waves," Report AFL 84-100, University of Cincinnati.

Ramakrishnan, S. V., and Rubin, S. G., 1984, "Time Consistent Pressure Relaxation Procedure for Compressible Reduced Navier Stokes Equations," *AIAA Journal*, Vol. 25, No. 7, pp. 905–913.

Ramakrishnan, S. V., and Rubin, S. G., 1988, "Time Consistent RNS Solutions for Unsteady Subsonic Flow over Airfoils," 1st National Fluid Dynamics Congress, AIAA 88-3561-CP, Cincinnati, Ohio.

Reddy, D. R., and Rubin, S. G., 1988, "Consistent Boundary Condition for Reduced Navier Stokes Scheme Applied to Three Dimensional Internal Viscous Flows," ASME JOURNAL OF FLUIDS ENGINEERING, Vol. 110, pp. 306–314.

Rettle, I. H., Lewis, W. G. E., 1968, "Design and Development of an Intake for a Supersonic Transport Aircraft," *Journal of Aircraft*, Vol. 5, No. 6, pp. 513–521.

Reymner, T. A., and Hickox, T. E., 1972, "Combined Viscous-Inviscid Analysis of Supersonic Inlet Flow Fields," *Journal of Aircraft*, Vol. 9, No. 8, pp. 589–595.

Rubin, S. G., 1982, *A Review of Marching Procedures for PNS Equations, Proceedings of the a Symposium on Numerical and Physical Aspects of Aerodynamic Flows*, Springer-Verlag, CA, pp. 171–186.

Rubin, S. G., and Reddy, D. R., 1983, "Global PNS Solution for Laminar and Turbulent Flows, 6th Computational Fluid Dynamics Conference," AIAA 83-1911, Denver, MA.

Rubin, S. G., and Reddy, D. R., 1986, "Analysis of Global Pressure Relaxation for Flows With Strong Interaction and Separation," *Computers and Fluids*, Vol. 11, No. 4, pp. 281–306.

Rubin, S. G., 1988, "Reduced Navier Stokes/Euler Pressure Relaxation and Flux Vector Splitting," *Computers and Fluids*, Vol. 16, No. 4, pp. 285–290.

Rubin, S. G., and Himansu, A., 1989, "Convergence Properties of High Reynolds Number Separated Flow," *International Journal for Numerical Methods in Fluids*, Vol. 9, pp. 1395–1411.

Salas, M. D., and Kuruvila, G., 1989, "Vortex Breakdown Simulation; A Circumspect Study of the Steady, Laminar, Axisymmetric Model," *Computers and Fluids*, Vol. 17, No. 1, pp. 247–262.

Telcot, N. A., and Kumar, A., 1984, "Numerical Simulation of Flow Through Inlet/Diffuser with Terminal Shocks," 20th Joint Propulsion Conference, AIAA 84-1362, Cincinnati, OH.

Varner, M. O., Martindale, W. R., Phares, W. J., Kneille, K. R., and Adams, J. C., Jr., 1984, "Large Perturbation Flow Field Analysis and Simulation for Supersonic Inlets," NASA-CR 174676.

Vigneron, Y., 1978, "Calculation of Supersonic Viscous Flow over Delta Wings with Sharp Leading Edges," AIAA 78-11377, Seattle, Washington.

Wigton, L. B., 1987, "Application of MACSYMA and Sparse Matrix Technology to Multielement Airfoil Calculations," 8th Computational Fluid Dynamics Conference, AIAA 87-1142, Honolulu, Hawaii.

Blocked Flow Subchannel Simulation Comparison With Single-Phase Flow Data

A. Teyssedou

A. Tapucu

R. Camarero

École Polytechnique,
Montréal, Québec, Canada H3T 1J4

The time integral of the local instantaneous conservation laws has been used as the starting point to write a subchannel model. The assumption of an ergodic stationary process has made possible further spatial integration of the resulting equations. The SIMPLER algorithm is adapted for the numerical solution. An adequate blockage model assures an overall momentum balance over the discretized cell elements. Comparison of the predictions of the proposed model with the experimental data confirms that it is capable of handling blockages of up to 90 percent of the flow area. Presently, this model only accounts for the hydrodynamic aspect of vertical adiabatic flows.

1 Introduction

In pressurized water reactors, during the refilling and reflooding phases of a hypothetical loss-of-coolant-accident (LOCA), the temperature of the zircaloy fuel cladding may reach very high values. These high temperatures coupled with high internal pressures of the gaseous fission products, may trigger a ductile or brittle failure of the cladding. The ductile failure may result in a ballooning of the fuel rod, while a brittle failure will cause the rod to burst open. In both cases, the flow area within a rod bundle could be reduced. The grid spacers and, especially in CANDU reactors, the end plates may also significantly perturb the emergency core cooling fluid flow.

Within the above framework, experimental and theoretical investigation of blockages in fuel assemblies under single- and two-phase flow conditions, constitute an important subject of study (Tapucu et al., 1984, 1988a). Several computer codes have been developed and used to analyze thermohydraulics of rod-bundles. These codes are written by following different techniques and the most frequently used are reviewed by Sha (1980) and Van Doormaal (1980). One of these techniques, the subchannel model, consists of considering the complex rod-bundle geometry as formed by parallel cells called subchannels. Each subchannel is bounded by the solid walls of the rods or external pressure tubes and by imaginary boundaries placed between adjacent subchannels. Within each subchannel the flow is considered as one dimensional, therefore exchange mechanisms between adjacent subchannels should be taken into consideration. The overall conservation equations of mass, momentum, and energy are usually written for adequately defined elementary control volumes. A rational approach for obtaining the conservation equations consists of applying the transport theorem along with appropriate averaging techniques (Chawla and Ishii, 1978). Such an approach allows a better identification of the exchange mechanisms between adjacent subchannels. Usually these mechanisms are known as mixing effects, and they are quite complex and difficult to decompose into elemental ones. They are usually identified as (Lahey and Moody, 1984):

—*Diversion Cross Flow*, the directed flow caused by pressure gradients normal to the principal flow direction.
—*Turbulent Mixing*, which occurs due to stochastic pressure and flow fluctuations.
—*Void Drift*, that accounts for the tendency of the vapor phase to shift to higher velocity channels.
—*Buoyancy Drift*, that occurs due to density gradients submitted to a gravitational field.

From the designer's point of view it is important to determine flow and enthalpy distributions in the subchannels using inlet and outlet pressures as boundary conditions. Therefore, a multipoint boundary value problem has to be solved. Due to numerical difficulties, the codes usually solve an approximation of this problem by transforming it into an initial value problem. Thus, the inlet flow distributions are modified to satisfy the pressure boundary conditions.

In the early subchannel models, each subchannel was analized separately and the inlet flow was adjusted to give the same pressure drop. A considerable improvement was introduced later by including cross-flow, with the pressure difference between adjacent subchannels considered as the required driving force. Empirical cross-flow resistance coefficients were used to formulate a simplified lateral momentum equation where the inertial effects were neglected (Bowring, 1968 and Rowe, 1970). A more complete lateral momentum equation was introduced by Rowe (1971), where a transverse pressure loss term accounted for frictional and contraction-expansion losses occurring across the interconnection. However, the transverse momentum flux was neglected. Comparative analysis (Rouhani, 1973) have shown the importance of this term tied with the geometric characteristics of the subchannels and the gap, which can only be neglected when similar subchannels are considered.

Contributed by the Fluids Engineering Division for publication in the JOURNAL OF FLUIDS ENGINEERING. Manuscript received by the Fluids Engineering Division June 5, 1990. Associate Technical Editor: C. J. Freitas.

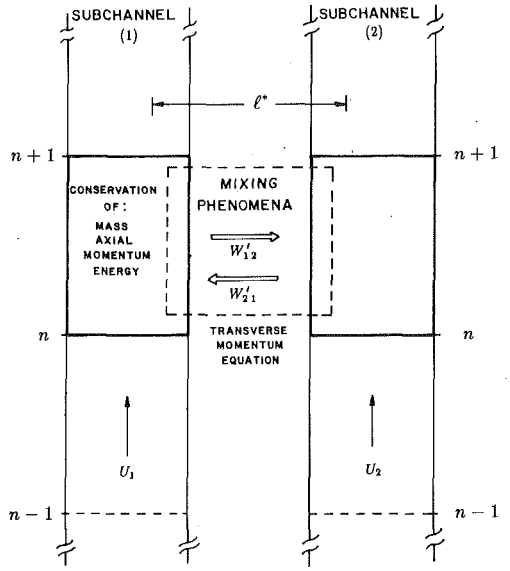

Fig. 1 Subchannel modeling concept

A more complete form of the transverse momentum equation is used in recent codes such as COBRA IV (Stewart et al., 1977), ASSERT (Carver et al., 1987), etc. In the ASSERT code the axial and transverse momentum equations, and the energy equation are written based on the relative velocity concept by using the two-phase drift flux model (Zuber, 1964). Thus, not only the transport mechanisms such as turbulent diffusion, buoyancy and void drift between subchannels are taken into account but also, diffusion of momentum and energy appear as consequence of the relative velocities between the phases.

It is apparent that a complete subchannel analysis can be only achieved if the elemental mixing mechanisms are adequately modelled. Their inclusion in a code eliminates partially the lack of consistency which results from treating a multidimensional problem as a one dimensional one. In general, the numerical solution of a subchannel model follows the scheme shown in Fig. 1. For each axial level, appropriate control volumes for the axial and the transverse flow are identified. There are no unified criteria to fix the boundaries of these control volumes. Some workers (Bernath et al., 1964 and St. Pierre, 1966) assumed that control volumes for the axial flow were conceptually separated by well defined mixing zones. In other cases (Fajeau, 1969), the step transition between adjacent subchannels are smoothed by including buffer regions into the numerical model formulation. On the other hand, it has been pointed out (Brown et al., 1975 and Tapucu, 1978) that the cross-flow induced by radial pressure differences between the subchannels can not be predicted with arbitrary control volumes for the transverse flow. Therefore, special care has to be taken when the centroid-centroid distance (l^* in Fig. 1) is used as the mixing length.

For the numerical solution of subchannel models the axial and transverse control volumes are considered as the nodes of a rod-bundle discrete space. Thereby, the use of appropriate finite difference schemes allows the reduction of the original set of equations into a discrete one. The non-linear character of the equations to be solved requires the use of iterative solution techniques. The step-by-step or marching method and simultaneous method of solution have been extensively used.

The simple marching procedure as used in the early versions of COBRA code can not handle a complete description of lateral flows under strong diversion cross-flow conditions. To deal with highly diverted flows a multi-pass marching technique as used in COBRA-IV is recommended. The technique of simultaneous solution of all axial intervals is used in SABRE (Gosman et al., 1973), SAGA (Tahir and Carver, 1982) and others (Siikonen, 1987). The numerical algorithm is adapted from the SIMPLE procedure (Patankar, 1980). Basically, the conservation equations are written in finite difference form using combined backward central differences. This procedure permits us to connect the values of the main variables for a particular control volume with those in neighboring control volumes. Staggered grids for velocities and pressures are used. The conservation equations are usually reduced to the following linearized form:

$$a_i\phi_i = \sum_{i \neq j} a_j\phi_j + S_j. \tag{1}$$

The solution of this system requires an initial guess for the pressure field. The axial momentum equation is solved to yield a first estimation on the flow velocities at each axial level. With this velocity field and the guessed pressures the transverse momentum equation permits the evaluation of the diverted flow everywhere. At this stage however, due to the non-linear nature of the problem, and due to the fact that the flow field has been calculated by starting from guessed pressures, the mass balance criterion is not satisfied. Consequently, the pressures have to be corrected and the iterative procedure has to be repeated until a mass convergence criterion is satisfied. Usually under relaxation factors of 0.5 and 0.8 are used respectively for the flow and pressure field calculations (Patankar, 1980).

The COBRA-IIIC code has been used to simulate interconnected blocked subchannels under single- and two-phase flow conditions (Tapucu et al., 1984, 1988a). However, it has been pointed out that this code failed in simulating plate blockages greater than 30 percent and smooth blockages greater than 60 percent. As a matter of fact comparisons of the simulations against experimental data show that the larger the blockage severity the lower the irreversible pressure loss coefficient re-

Nomenclature

A = subchannel cross-flow area, m^2
c = gap clearance, mm
G' = lateral mass flux, kg/sm^2
g = gravitational field constant, m/s^2
J = volumetric flux, m/s
$\hat{n}$ = unit vector
p = pressure, N/m^2
u = axial component of the flow velocity, m/s
$\mathbf{v}_k$ = phase velocity, m/s
$\mathbf{v}_i$ = interface velocity, m/s
v = transverse component of the flow velocity, m/s
x = dryness fraction or flow quality
α = void fraction
γ_w = wetted perimeter, m
$\bar{\epsilon}$ = average eddy diffusivity, m^2/s
$\hat{\imath}$ = unit vector
ξ_i = contour of a boundary, m
ρ' = momentum density, kg/m^3
$\bar{\bar{\sigma}}$ = viscous stress tensor, N/m^2
$\bar{\bar{\sigma}}'$ = turbulent stress tensor, N/m^2

Subscripts

d = donor channel
EQ = equilibrium
g = gas phase
l = liquid phase
r = recipient channel
w = solid wall

Special Notation

* = flow properties in the interconnection region
$\overline{\ }$ = time average
$\langle\ \rangle$ = line average
$\langle\langle\ \rangle\rangle$ = area average
$\sim$ = weighted average

quired by the code to produce acceptable results, i.e., for a case of 60 percent flow area reduction this coefficient drops to zero. These results are physically unrealistic, since an increase in the blockage severity increases the irreversibilities induced by the blockage (Tapucu et al., 1989). The same code has also been compared to experimental data obtained with up to 90 percent plate and sleeve blockages. The prediction of the code does not show a complete pressure recovery when the irreversible pressure loss coefficient is set equal to zero (Rowe et al., 1973), i.e., only acceleration effects are taken into account. For relatively complex geometries numerical instabilities have been reported when this code was used to simulate single-phase flows in subchannels containing 90 percent blockage severities (Creer et al., 1979). Therefore, the blockage model must involve further criteria other than the changes in the channel flow area and the dissipation of mechanical energy in the wake zone, i.e., momentum transport in the transverse direction. Furthermore, the numerical scheme must be appropriate to solve partially blocked subchannel. COBRA-IV (Stewart et al., 1977), seems to predict subchannel flows quite well (Tapucu et al., 1983, 1988b), however no satisfactory solutions of partially blocked subchannels have been obtained with this code (Tapucu, 1990).

In this paper a subchannel model capable of handling severe blocked flows is presented. The numerical solution of the model equations is carried out according to the SIMPLER (Patankar, 1980) (Semi Implicit Method for Pressure Linked Equation-Revised) algorithm. The predictions of the proposed model are then compared with single-phase flow data taken from Tapucu et al. (1984) and Tapucu and Gençay (1984).

2 Subchannel Model

The local instantaneous conservation laws have been used as the starting point to write a subchannel model for single- and two-phase flows. The local instantaneous equations were averaged in the time domain (Ishii, 1975). The fine structure due to phase interfaces was neglected, only the correlations of fluctuations involving turbulence were kept. The assumption that the flow follows a stationary-ergodic process, allows the local time averaged equations to be integrated over the subchannel geometry. Line and area averaging (Vernier and Delhaye, 1968) are used to express the equations in a calculable form.

2.1 Mass Balance Equations. According to the previously described procedure the mass balance for the phase k is written as:

$$\frac{\partial}{\partial t}\alpha_k A\langle\langle\overline{\rho_k}\rangle\rangle+\frac{\partial}{\partial z}\alpha_k A\langle\langle\overline{\rho_k}\rangle\rangle\,\widetilde{u_k}^{t,a}=-\sum_{i=k}\int_{\xi_{ik}}\overline{\rho_k}(\overline{\mathbf{v}}_k-\overline{\mathbf{v}}_i)\cdot\hat{n}_k\frac{dA_k}{dz}-\int_C\overline{\rho_k}\overline{\mathbf{v}}_k\frac{dA_{k\,dr}}{dz},\quad(2)$$

where $\widetilde{u_k}^{t,a}$ is the mass-weighted area averaged phase velocity. The two terms on the r.h.s. represent the phasic mass formation rates and the cross-flow of phase k at the interconnection respectively. Assuming that the phase densities and velocities are uniformly distributed within the cross-section of the subchannels, and adding the resulting equations for the liquid and the gas, the mixture mass conservation equation is written as:

$$\frac{\partial}{\partial t}A(\alpha\rho_g+(1-\alpha)\rho_l)+\frac{\partial}{\partial z}A(G_l+G_g)=-c(G_l'+G_g'),\quad(3)$$

2.2 Axial Momentum Equation. The local time-averaged axial momentum equation is integrated over the cross-sectional area of the subchannels and the no slip boundary conditions ($\mathbf{v}_{k,w}=\mathbf{v}_{k,w}'=0$) are used to simplify the resulting equation. Furthermore, the following interfacial terms are taken into account:

(i) *Solid wall interfaces.* The loss due to friction dissipation is written as:

$$\sum_{i=w}\int_{\xi_{iw}}\hat{\imath}_z(\bar{\bar{\sigma}}\cdot\hat{n}_k)\frac{dA_{kw}}{dz}=-\gamma_{kw}\tau_{kw},\quad(4)$$

The axial component force produced by the flow pressure acting on the subchannel walls becomes:

$$\sum_{i=w}\int_{\xi_{iw}}-\overline{p}_k\hat{\imath}_z\cdot(\bar{\bar{I}}\cdot\hat{n}_k)\frac{dA_{kw}}{dz}=\langle\overline{p}_k\rangle\frac{dA_k}{dz},\quad(5)$$

(ii) *Intersubchannel interfaces* (interconnected regions). The axial momentum convected by the transverse flow is modeled as:

$$\sum_{i=dr}\int_{\xi_{idr}}\overline{\rho_k u_k}(\overline{\mathbf{v}}_k-\overline{\mathbf{v}}_i)\cdot\hat{n}_k\frac{dA_{kdr}}{dz}=\int_C\overline{\rho_k}\,\widetilde{u_k'}(\overline{\mathbf{v}}_k\cdot\hat{n}_k)\frac{dA_{kdr}}{dz}\simeq\frac{G_{kdr}'}{c}u_k^*,\quad(6)$$

with, u_k^*, the average axial velocity at the gap. Since the information about the fine structure of the flow within each subchannel is unknown, some appropriate assumption should be introduced to estimate the axial flow velocity near the gap (Rouhani, 1973). In the rest of this paper u_k^* is defined as the arithmetic average of the subchannel axial velocities. The axial component of the viscous shear force taking place at the intersubchannel interface is given by:

$$\sum_{i=dr}\int_{\xi_{idr}}\hat{\imath}_z\cdot\bar{\bar{\sigma}}\hat{n}_k\frac{dA_{kdr}}{dz}\simeq-c_k\langle\overline{\tau}_{kdr}\rangle_z,\quad(7)$$

where $\langle\overline{\tau}_{kdr}\rangle_z$ is a line averaged quantity over the gap line c. Considering that $\hat{\imath}_z\cdot\sigma_{kdr}'=-\overline{\rho_k}\widetilde{v_k'v_k'}$, and applying the Boussinesq's approximation (Schlichting, 1968), the turbulent mixing between subchannels is modeled as:

$$\sum_{i=dr}\int_{\xi_{idr}}\hat{\imath}_z\cdot(\bar{\bar{\sigma}}'\cdot\hat{n}_k)\frac{dA_{kdr}}{dz}\simeq\int_C\overline{\rho_k}\epsilon\left(\frac{d\widetilde{u_k'}}{dy}\right)\frac{dA_{kdr}}{dz}.\quad(8)$$

The value of $(d\widetilde{u_k'}/dy)$ must be based on the local variations very near the boundary. Assuming that the axial velocity at the gap ($=u_k^*$) is the average of the axial velocities of each subchannel, and using the centroid-centroid distance ($=l^*$) as the mixing length, Eq. (8) yields:

$$\text{Turb. Mixing}=\frac{c\epsilon}{l^*}\sum_{k=g,l}\left\{(\alpha_k\overline{\rho_k})_d\left[\frac{G_{kr}}{\alpha_{kr}\rho_{kr}}-\frac{G_{kd}}{\alpha_{kd}\rho_{kd}}\right]\right\}.\quad(9)$$

Finally, the axial momentum equation for the two-phase mixture is written under the following form:

$$\begin{aligned}\frac{\partial}{\partial t}(AG)+\frac{\partial}{\partial z}\left\{A\left[\frac{x}{\alpha\rho_g}G_g+\frac{(1-x)}{(1-\alpha)\rho_l}G_l\right]G\right\}&+cF_m\left[\frac{x^*}{\alpha^*\rho_g^*}G_g'+\frac{(1-x^*)}{(1-\alpha^*)\rho_l}G_l'\right]G^*\\&+c\lambda\left\{x\left[\left(\frac{G_g}{\alpha\rho_g}\right)_r-\left(\frac{G_g}{\alpha\rho_g}\right)_d\right]\right.\\&\left.+(1-x)\left[\left(\frac{G_l}{(1-\alpha)\rho_l}\right)_r-\left(\frac{G_l}{(1-\alpha)\rho_l}\right)_d\right]\right\}G\\&=-A\frac{\partial}{\partial z}p+A\rho_m g+\gamma_w\tau_w+c(\tau_{dr})_z\\&\quad-A\frac{\partial}{\partial z}\left\{\beta\frac{(G')^2}{2\rho_m^*}\left[1-\left(\frac{c}{a}\right)^2\right]\right\},\end{aligned}\quad(10)$$

where the momentum transfer at the interfaces is neglected, i.e., no surface tension effects are taken into account. In order to consider the fraction of mechanical energy dissipated as heat under strong diversion cross-flow conditions, the axial momentum convected by the transverse flow is adjusted by means of a momentum factor, F_m (Tapucu and Merilo, 1977). The amount of axial momentum transported by turbulent exchanges between the channels is adjusted by means of a turbulent mixing coefficient ($0 < \lambda < 1$). The frictional dissipation at the walls of the subchannels and by the blockage is modeled as:

$$\gamma_w \tau_w = \Phi_L^2 \left(f_0 \frac{G^2}{2\rho_l} \frac{A}{D_h} \right) + K_{irrev} \frac{G^2}{2\rho'} \frac{A}{D_h}. \tag{11}$$

The first term on the r.h.s. represents the friction losses of the two-phase flow. The second term, takes into account the losses due to the presence of a blockage. The irreversible pressure loss caused by the blockage is adjusted by means of K_{irrev}. No attempt is made to model the inter-subchannel shear force, $c(\tau_{dr})_z$, in Eq. (10). However, in some particular cases, such as very dissimilar subchannels, the effects of this force should be not neglected.

Under strong diversion cross-flow conditions, i.e., severely blocked flows, the transverse flow acceleration across the gap may involve a non negligible fraction of the flow mechanical energy. In a three dimensional model, such a phenomenon should appear as a flow velocity divergence in the transverse directions. Since a subchannel model deals with one dimensional equations, an additional term is introduced into the axial momentum balance to account for these effects. Assuming that the lateral cross-flow expands from a contracted zone, identified with the interconnection, to the whole subchannel control volume, a simplified mechanical energy balance allows the last term on the r.h.s. of Eq. (10) to be written. The magnitude of the pressure gains or losses induced by the contraction-expansion of the cross-flow, are adjusted by means of an empirical factor (β).

2.3 Transverse Momentum Equation. The local time-averaged transverse momentum equation is integrated over a line bounded by the interconnection gap, and the acceleration terms are approximated as:

(i) *Local acceleration*

$$\frac{\partial}{\partial t} \int_{C_k} \overline{\rho_k}\, \widetilde{v_k^t} dc_k = \frac{\partial}{\partial t} W'_{k\,dr}. \tag{12}$$

(ii) *Convective terms*

$$\frac{\partial}{\partial z} \int_{C_k} \overline{\rho_k}\, \widetilde{u_k^t}\, \widetilde{v_k^t} dc_k \simeq \frac{\partial}{\partial z} \left(W'_{k\,dr} \widetilde{u^*_{k\,dr}}^{t,c} \right), \tag{13}$$

and,

$$\frac{\partial}{\partial y} \int_{C_k} \overline{\rho_k}\, \widetilde{v_k^{2t}} dc_k \simeq \frac{\partial}{\partial y} \left(W'_{k\,dr} \widetilde{v^*_{k\,dr}}^{t,c} \right), \tag{14}$$

where it is assumed that $\widetilde{u_k^t}\,\widetilde{v_k^t} \cong \widetilde{v_k^{2t}}$. The asterisks identify averaged values at the gap region. The solid wall phase interface term is simplified by using the no slip boundary condition ($\bar{v}_{kw} = 0$, $\bar{v}'_{kw} = 0$), thus, it is reduced to:

$$\frac{\partial}{\partial y} \int_{C_k} \hat{\imath}_y \overline{p}_k \bar{\bar{I}} dc_k = \frac{\partial}{\partial y} c_k \langle \overline{p}_k \rangle, \tag{15}$$

where $\langle \overline{p}_k \rangle$ is the line-averaged pressure acting over the gap boundary line. Furthermore, the interfacial pressure at the extremities of the segment c_k becomes:

$$\sum_{e=w} \overline{p}_k \hat{\imath}_y \cdot (\bar{\bar{I}} \cdot \hat{n}_k) \frac{dA_{kw}}{dzdy} \simeq - \langle \overline{p}_k \rangle \frac{d}{dy} \left(\frac{dA_{kwy}}{dz} \right), \tag{16}$$

with, $\hat{\imath}_y \cdot (\bar{\bar{I}} \cdot \hat{n}_k) dA_{kw} = -dA_{kwy}$. On the other hand, the viscous stress tensor yields:

$$\sum_{e=w} \hat{\imath} \cdot \bar{\bar{\sigma}} \cdot \hat{n}_k \frac{dA_{kw}}{dzdy} = - \langle \overline{\tau_{ky}} \rangle \frac{dA_{kw}}{dzdy}. \tag{17}$$

Assuming that there is no interfacial mass transfer, no surface tension effects, and the phase densities and velocities are uniformly distributed over the gap, the transverse momentum equation for a two-phase mixture can be written as:

$$\frac{\partial}{\partial t} cG' + \frac{\partial}{\partial z} c \left\{ G_g' \frac{G_g^*}{\alpha^* \rho_g^*} + G_l' \frac{G_l^*}{(1-\alpha^*)\rho_l} \right\} + \frac{\partial}{\partial y} c \left\{ \frac{G_g'^2}{\alpha^* \rho_g^*} + \frac{G_l'^2}{(1-\alpha^*)\rho_l} \right\} = -c \frac{\partial}{\partial y} p - \tau_{wy} \frac{dA_w}{dzdy} + c \rho_m g_y. \tag{18}$$

To obtain the total pressure difference between the channels, this equation is integrated over the mixing length l^*. Under the presence of a blockage the mixing length should change with the axial position then, $l^* = l^*(z)$. Assuming a linear variation of $l^*(z)$ within each control volume, using the Leibnitz theorem, and neglecting second order terms, integration of Eq. (18) yields:

$$\frac{\partial}{\partial t} A'G' + \frac{\partial}{\partial z} \left\{ A' \left[\frac{x^*}{\alpha^* \rho_g^*} G_g^* + \frac{1-x^*}{(1-\alpha^*)\rho_l} G_l^* \right] \right\} G' + \frac{\Delta_{dr}}{l^*} \left\{ A' \left[\frac{x^*}{\alpha^* \rho_g^*} G_g' + \frac{1-x^*}{(1-\alpha^*)\rho_l} G_l' \right] G' \right\} = -A' \frac{\Delta p_{dr}}{l^*} - K_{tr} \frac{(G')^2}{2\rho_m^*} \frac{A'}{c} + \rho_m A' g_y, \tag{19}$$

where $A' = cl^*$. The transverse viscous stress term, $\tau_{wy} dA_{kw}/dzdy$, is modeled by using Darcy's law and a transverse pressure loss coefficient (K_{tr}).

2.4 Energy Equation. Since the present paper deals with the simulation of adiabatic flows, the energy equation is not included. However, it is important to state that the total energy equation would be useful for taking into account the irreversible pressure losses induced by the cross-flow contraction-expansion and the obstructions (Tapucu et al., 1989).

3 Closure Equations

The set of Eqs. (3), (10), and (19) forms a system which contains five unknowns (G_l, G_g, G_l', G_g', p). It is apparent that two additional equations are required; a gas mass conservation, and a gas mixing equations. A gas mixing equation is obtained by using the drift-flux model to write the gas mass cross-flow across the interconnection. Other constitutive relationships are needed for calculating the frictional pressure losses, the void fraction as a function of the flow quality and the flow properties as functions of pressure and temperature. The transverse pressure drop coefficient (K_{tr}), the irreversible form pressure loss coefficient (K_{irrev}), the turbulent mixing factor (λ), the axial momentum factor (F_m), and the transverse flow expansion coefficient (β) are considered as convenable constants selected before starting the model calculations.

3.1 Gas Mixing Model. The drift flux model allows the averaged void weighted gas velocity to be written as:

$$\widetilde{v_g^\alpha} = C_0 \langle\langle \bar{J} \rangle\rangle + \widetilde{v_{gj}^\alpha}, \tag{20}$$

where C_0 is the distribution coefficient (Zuber and Findlay, 1965), and $\widetilde{v_{gj}^\alpha}$ the averaged void weighted drift velocity. By analogy to molecular diffusion (Hirschfelder et al., 1964) the

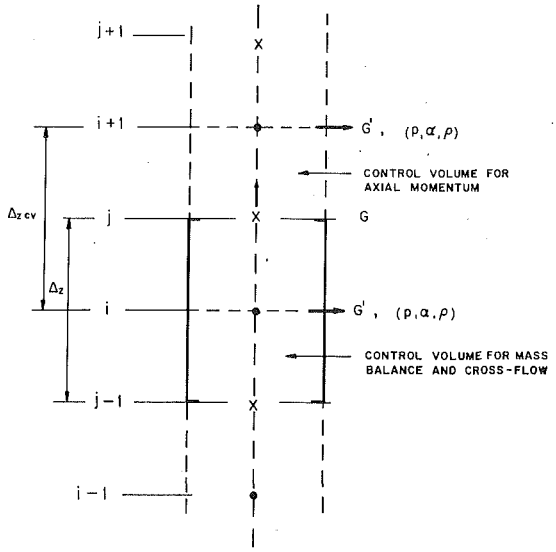

Fig. 2 Discretization scheme

drift velocity is expressed as function of the void fraction gradient. Applying Eq. (20) to the interconnected region yields:

$$G_g' = \alpha^* \rho_g^* \left\{ C_0 J_{dr} - D_\alpha \frac{\Delta_{dr}(\alpha)}{l^*} \right\}. \tag{21}$$

This equation gives the amount of gas mass cross-flow between the donor and the recipient subchannels. The first term on the r.h.s. represents the mass transferred mainly by diversion cross-flow, the second term represents mixing by turbulent void diffusion. The hypothesis that the two-phase mixing is proportional to the non equilibrium void fraction gradient implies that the net gas mass exchange due to turbulent mixing ceases when the equilibrium conditions are achieved. However, it is a well known fact that the void distribution tends toward a non uniform equilibrium void distribution (Lahey et al., 1972), thus non negligible void gradients may exist even if no net mass transfer is observed. This phenomenon is explained as a "void drift" mechanism. Modelling the void drift on the basis of a diffusion process yields:

$$G_g' = \alpha^* \rho_g^* \left\{ C_0 J_{dr} - D_\alpha \frac{\Delta_{dr}(\alpha)}{l^*} + D_{eq} \frac{\Delta_{dr}(\alpha)_{EQ}}{l^*} \right\}, \tag{22}$$

where D_α and D_{eq} are void diffusion coefficients.

4 Numerical Modelling

The numerical solution of the governing equations is based on the SIMPLER algorithm (Patankar, 1980). In order to apply this technique the equations are written in terms of total mass fluxes (G). These equations are then finite differenced using a staggered grid upwind scheme. The axial mass fluxes are defined at the computation cell boundaries (j), while the pressure, phase densities, void fraction, and cross-flow are defined at the cell centers (i). This scheme recognizes that the convected properties at the control volume faces represent averaged values of these properties taken at the neighboring points. Due to this fact the value of a property ϕ_i at an interface is taken equal to its value at a point on the upwind side face, this can be written as (Fig. 2):

$$(G\phi)_i = \| G_{j-1}, 0 \| \phi_{i-1} - \| -G_j, 0 \| \phi_{i+1}, \tag{23}$$

where the notation $\|\Psi, \Phi\|$ means the larger of Ψ and Φ. This formalism is used to write the discretized conservation equations, which are previously linearized and integrated over the control volumes. They are finally expressed under the form of linear systems with coefficients evaluated at the control volume faces. The overall form that the algorithm takes, for this case, is summarized as follows:

1) Start with a guessed mass flow distribution, i.e., axial mass fluxes taken equal to the inlet mass fluxes and cross-flows equal to zero everywhere.

2) From axial momentum balance calculate a flow pressure field.

3) Use this pressure field to actualize the axial mass flow distribution.

4) Using the transverse momentum equation, the pressures from step (2) and the mass fluxes from step (3), calculate the cross-flows everywhere.

5) Use mass imbalance to correct the axial flows and cross-flows without correcting the pressures.

6) Verify a mass convergence criterion. If convergence is not achieved, start a new iteration from step (2).

Since the present paper is concerned with the simulation of steady state flows, only the steady-state form of the discretized conservation equations are presented.

4.1 Mass Conservation Equation. The mass conservation equations are discretized as:

$$A_j G_j = A_{j-1} G_{j-1} - \Omega G_i', \tag{24}$$

with $\Omega = c(z_j - z_{j-1})$, which represents the element of gap area in the interconnected region.

4.2 Axial Momentum Equation. For steady-state flow conditions, the discretized form of Eq. (10) is written as the following linear system:

$$a_0 G_j - a_1 G_{j-1} - a_2 G_{j+1} = A_j (p_i - p_{i+1}) + b, \tag{25}$$

with the coefficients given by:

$$a_1 = \left\| A\Sigma_{k=g,l} \left(\frac{x_k G_k}{\alpha_k \rho_k} \right), 0 \right\|_i, \quad a_2 = \left\| -A\Sigma_{k=g,l} \left(\frac{x_k G_k}{\alpha_k \rho_k} \right), 0 \right\|_{i+1}$$

$$a_0 = a_1 + a_2 + \Delta_{i+1,i} \left[A\Sigma_{k=g,l} \left(\frac{x_k G_k}{\alpha_k \rho_k} \right) \right] + \left\| \Omega_{cv} \Sigma_{k=g,l} \left(\frac{x_k}{\alpha_k \rho_k} \right)^* G_k', 0 \right\|_j + \left[\lambda \Omega_{cv} \Sigma_{k=g,l} x_k \Delta_{r,d} \left(\frac{G_k}{\alpha_k \rho_k} \right) \right]_j + f_0 \Phi_L^2 \frac{G_i^0}{\rho_l} \frac{A_i \Delta z_{cv}}{D_{h_i}}$$

$$b = \frac{1}{2} f_o \Phi_L^2 \frac{|G_i^0| G_i^0}{\rho_l} \frac{A_i \Delta z_{cv}}{D_{h_i}} + \rho_m g A \Delta z_{cv} + \left\| -\Omega_{cv} \Sigma_{k=g,l} \left(\frac{q_k^x}{\alpha_k \rho_k} \right)^* G_k', 0 \right\|_j G_{dj} - K_{irrev} \Phi_L^2 \frac{G_i^2}{2\rho'} \frac{A_i \Delta z_{cv}}{D_{h_i}} - \frac{1}{2} \beta \left[1 - \left(\frac{c}{a} \right)^2 \right] \Delta_{i+1,i} \left[\frac{(G')^2}{\rho_m} \right]$$

The values at the cell boundaries (j) are calculated as the average between the values of the neighbor cell centers, (i). The source term which contains the wall friction is linearized by expanding it around the point (i). No linearization is needed for the irreversible pressure loss term.

4.3 Transverse Momentum Equation. The discretized form of the transverse momentum equation is written as the following linear system:

$$a_0' G_i' - a_1' G_{i-1}' - a_2' G_{i+1}' = \Omega (p_d - p_r)_i + b', \tag{26}$$

with the coefficients defined as:

$$a_1' = \left\| cl^*(x) \Sigma_{k=g,l} \left(\frac{x_k}{\alpha_k \rho_k} G_k \right)^*, 0 \right\|_{j-1},$$

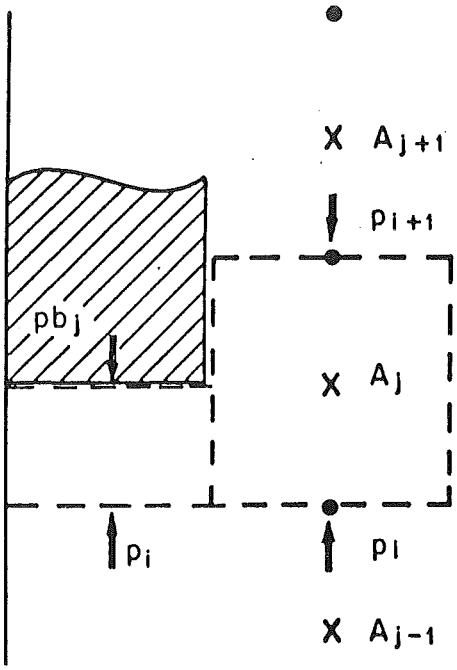

Fig. 3 Plate blockage

$$a_1' = \left\| cl^*(z)\Sigma_{k=g,l}\left(\frac{x_k}{\alpha_k\rho_k}G_k\right)^*, 0\right\|_{j-1},$$

$$a_2' = \left\| -cl^*(z)\Sigma_{k=g,l}\left(\frac{x_k}{\alpha_k\rho_k}G_k\right)^*, 0\right\|$$

$$a_0' = a_1' + a_2' + \Delta_{j,j-1}\left[cl^*(z)\Sigma_{k=g,l}\left(\frac{x_k}{\alpha_k\rho_k}G_k\right)^*\right] - \left[c\Sigma_{k=g,l}\left(\frac{x_k}{\alpha_k\rho_k}\right)^* G_k'\right]_i + K_{tr}\frac{(G')_i^2}{2\rho_m^*}\frac{l^*\Omega}{c}$$

$$b' = \frac{1}{2}K_{tr}\frac{|G_i'^0|G_i'^0}{\rho_{mi}^*}\frac{l^*\Omega}{c}$$

4.4 Pressure Equation. The pressure equation is obtained by combining the mass balance equation with the axial and transverse momentum equations. From these equations one may write:

$$G_j = \frac{a_1G_{j-1} + a_2G_{j+1} + b}{a_0} + \frac{A_j}{a_0}(p_i - p_{i+1}),$$

$$G_i' = \frac{a_1'G_{i-1}' + a_2'G_{i+1}' + b'}{a_0'} + \frac{\Omega}{a_0'}(p_d - p_r)_i.$$

Introducing this relationship into the mass balance equation yields:

$$(a_{p0})p_i - (a_{p1})p_{i-1} - (a_{p2})p_{i+1} = A_{j-1}\hat{G}_{j-1} - A_j\hat{G}_j - \Omega d_i' p_{ri}, \quad (27)$$

with the coefficients defined by:

$$a_{p1} = A_{j-1}d_{j-1},\ a_{p2} = (a_{p1})_{j+1},\ a_{p0} = a_{p1} + a_{p2} + \Omega d_i'$$

$$d_j = \left(\frac{A}{a_0}\right)_j,\ d_i' = \left(\frac{\Omega}{a_0'}\right)_i,$$

and;

$$\hat{G}_j = \frac{(a_1G_{j-1} + a_2G_{j+1} + b)}{a_0},\ \hat{G}_i' = \frac{(a_1'G_{i-1}' + a_2'G_{i+1}' + b')}{a_0'}.$$

4.5 Mass Flux Correction Equation. In order to correct the flow, an equation is derived by assuming that the mass fluxes and the pressures must be corrected. However, during the flow correction procedure *only the mass fluxes are affected.* Assuming corrected values of mass fluxes and flow pressure the axial and transverse momentum equations permit us to write:

$$\left.\begin{aligned} G_j &= G_j^0 + d_j(pc_i - pc_{i+1}) \\ G_i' &= G_i'^0 + d_i'(pc_d - pc_r)_i \end{aligned}\right\},$$

where G^0 and G'^0 are the old mass fluxes while G and G' are the new corrected values. In order to apply this correction procedure, it is necessary to know the values of pc everywhere. The equation used to calculate $[pc]$ is obtained by incorporating the corrected mass fluxes into the mass balance equation;

$$-(dApc)_{i-1} + [(dA)_j + (dA)_{j-1} + \Omega d_i']pc_i - d_jA_jpc_{i+1} = (AG^0)_{j-1} - (AG^0)_j - \Omega(G'^0 + d'pc_r)_i. \quad (28)$$

Appropriate boundary conditions permit us to reduce Eqs. (25)–(28) into tridiagonal forms. It is interesting to remark that the matrix which results from system (28) has the same elements as the matrix which results for system (27), only the source vectors differ. The system (28) is solved simultaneously for each subchannel, and the $[pc]$ vector is used to correct the mass fluxes. Since the axial pressures for each new iteration are calculated from corrected mass fluxes taken from the preceding iteration, it is not necessary to apply any corrective action to the flow pressure field.

5 Blockage Modeling

The staggered grid approach could produce a momentum imbalance when it is applied to the edge of a steep blockage (Fig. 3). The pressure difference $(p_{i+1} - p_i)$ could be substantial, hence the pressure force excerted over the blockage face can not be neglected. Two approaches can be used to reduce this induced momentum imbalance. The first one consists of increasing the number of mesh points in the blockage region. The second one consists of accounting for additional pressure terms which allow the axial momentum to be balanced at the blockage edge. The latter approach has been used in the present model. According to Fig. 3, the balance of forces due to pressure can be written as follows:

$$\Sigma Fp_x = A_j(p_i - p_{i+1}) + \frac{Ab_j}{2}(p_i - p_{i+1}), \quad (29)$$

with Ab_j the blockage cross-sectional area at point j, $(= A_{j-1} - A_j)$, and the pressure acting over the blockage face approached by; $pb_j \simeq \frac{1}{2}(p_i + p_{i+1})$. Comparing (27) with (29), it is apparent that the second term on the r.h.s. of (29) has to be added to the axial pressure equation. By carrying out this operation and putting all the pressures fully implicit, the coefficients of Eq. (27) take the following form:

$$a_{p0} = a_{p1} + a_{p2} + \Omega d_j',\ a_{p1} = A_{j-1}(d_{j-1} + db_{j-1}),$$

$$a_{p2} = (a_{p1})_{j+1},\ db_j = \frac{1}{2}A_jAb_j$$

6 Comparison of the Model Predictions With Single-Phase Flow Data

The predictions of the model presented in the former paragraphs have been compared with experimental data obtained by Tapucu et al. (1984) and Tapucu and Gençay (1984) under single-phase flow conditions. For simplicity, a given number of parameters have been a priori considered as constant values. The number of discretized mesh points is arbitrarily fixed at 120 for all the runs presented in this paper. An under-relaxation factor for the axial mass flow and the transverse equations (= 0.4) is used in all the cases. No attempt has been made to optimize any of these values.

Since the tests presented in this paper dealt with strong diverted flows, the turbulent mixing between the subchannels is set equal to zero ($\lambda = 0$). In other words, it is assumed that

RUN # 214 WITHOUT BLOCKAGE

FLOW INLET CONDITIONS

CHANNEL 1	CHANNEL 2
G_L = 4595.3 $Kg/m^2 s$	G_L = 790.2 $Kg/m^2 s$
G_G = 0.0 $Kg/m^2 s$	G_G = 0.0 $Kg/m^2 s$
α = 0.0 %	α = 0.0 %

GEOMETRIC CHARACTERISTICS

Gap Width = 1.0 mm — Gap Length = 3.2 mm

Flow Area Channel 1 = 162 mm^2 — Flow Area Channel 2 = 163 mm^2

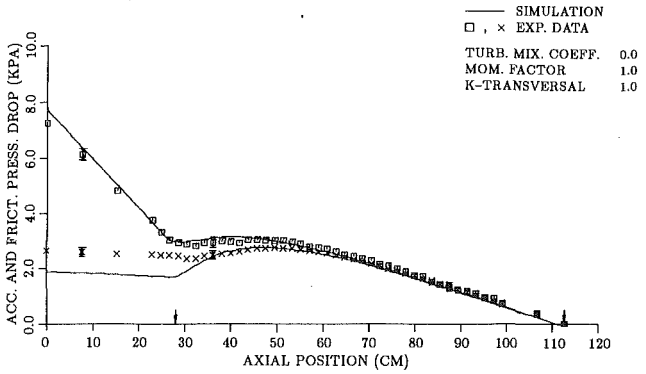

Fig. 4(*a*) Comparison of model's predictions with experimental data of Tapucu and Gençay (1984)

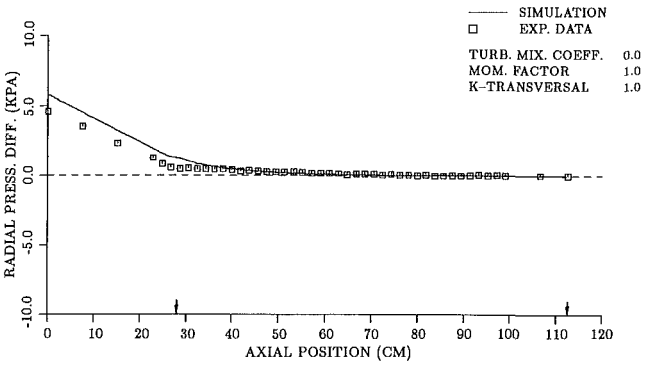

4(*b*)

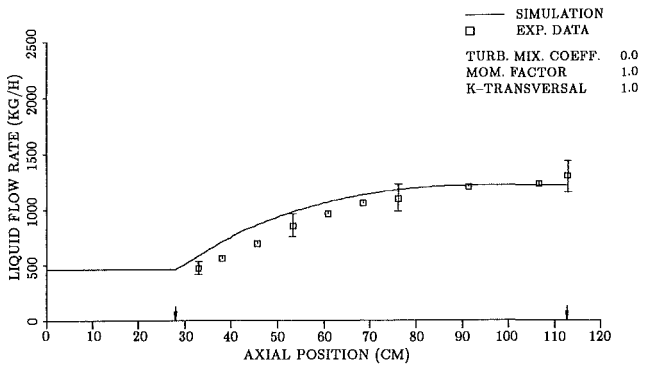

4(*c*)

RUN # 8 59.2% PLATE BLOCKAGE

FLOW INLET CONDITIONS

BLOCKED CHANNEL	UNBLOCKED CHANNEL
G_L = 3152.8 $Kg/m^2 s$	G_L = 3008.6 $Kg/m^2 s$
G_G = 0.0 $Kg/m^2 s$	G_G = 0.0 $Kg/m^2 s$
α = 0.0 %	α = 0.0 %

GEOMETRIC CHARACTERISTICS

Gap Width = 1.5 mm — Gap Length = 3.0 mm

Flow Area Channel 1 = 164 mm^2 — Flow Area Channel 2 = 163 mm^2

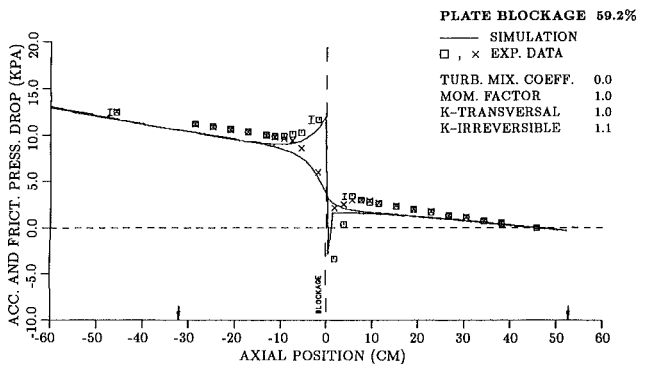

Fig. 5(*a*) Comparison of model's predictions with experimental data of Tapucu et al. (1984)

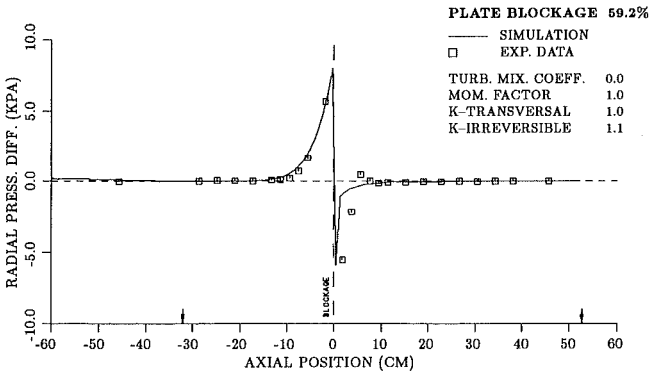

5(*b*)

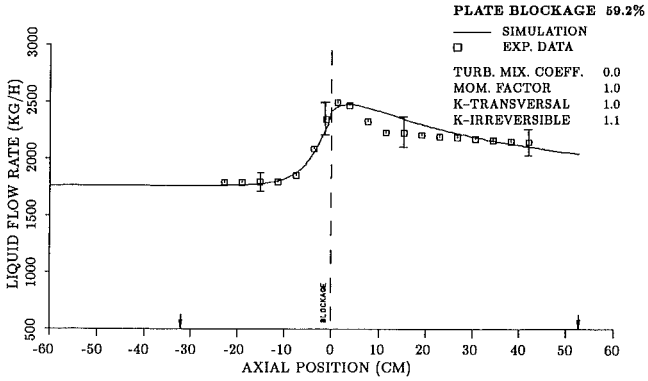

5(*c*)

turbulent mixing should not considerably change the predictions of the model when diversion cross-flow is the principal exchange mechanism between adjacent subchannels. The axial momentum factor (F_m) is taken equal to unity for all the present comparisons. Appropriate experimental support would be needed to determine the optimum value of this factor. The transverse pressure drop coefficient, introduced in Eq. (19), is taken always equal to unity. In turn, the irreversible form pressure loss coefficient in Eq. (11) is taken equal to the experimental values (Tapucu et al., 1984).

Comparison With Data Obtained on Single-Phase Flow Without Blockage. Comparison of the model's predictions with single-phase unblocked flow data are shown in Figs. 4(*a–c*), where the arrows indicate the extent of the interconnected region. These data (Tapucu and Gençay, 1984), have been obtained for dissimilar inlet flow conditions to the channels which produce an important cross-flow at the beginning of the interconnection. Therefore, it is expected that under such conditions, the flow will behave in a way similar to a partially blocked flow. The simulated acceleration and friction pressure drop in the interconnection shown in Fig. 4(*a*) follows the experimental trends very well. However, upstream of the be-

ginning of the interconnection, the pressures in the recipient channel are underestimated. This under-estimation may be related to three particular effects:

—Axial momentum imbalance due to the axial momentum convected by the transverse flow. Tapucu and Merilo (1977) used the same data to show that the axial momentum factors for the donor and recipient channels are not equal. As was stated before, a single value (= 1) of this factor has been used in this paper.
—Partial pressure recovery during the expansion of the cross-flow in the recipient channel. This phenomenon could be taken into account by selecting an appropriate value of β in Eq. (10).
—Dissipation of a fraction of the available mechanical energy as heat in the wake zone which develops at the beginning of the interconnection.

Figure 4(*b*) shows the radial pressure difference between the channels. Within the interconnection this difference drops to zero. However, before the beginning of the slot the trends observed in the axial pressure are reflected in the radial pressure difference. In general, the prediction of the liquid mass transfer (Fig. 4(*c*)), follows very closely the experimental trend and remains within the experimental error limits after 20 D_h downstream of the beginning of the interconnection.

Comparison With Data Obtained on Single-Phase Partially Blocked Flows. Two sets of experimental data on partially blocked single-phase flows are compared with the predictions of the model. The first set was obtained on a plate blockage with 59.2 percent of flow area reduction (Figs. 5(*a–c*)), and the second on a plate blockage with 88.8 percent of flow area reduction.

In general, the acceleration and friction pressure drop of the 59.2 percent plate blockage, Fig. 5(*a*), are very satisfactory simulated. The irreversible form pressure loss coefficient (K_{irrev}) for this blockage (= 1.1) is taken from Tapucu et al. (1984). Upstream of the obstruction the prediction is very close to the lower experimental error limits. Just downstream of the blockage the predicted pressure differs somewhat from the experimental observations. This is very likely due to the formation of a wake zone which is mainly a three-dimensional flow. After 20 D_h downstream of the blockage the prediction and the experimental data agree very well. The behavior observed just behind the blockage is also reflected in the radial pressure difference between the channels, shown in Fig. 5(*b*). However, the overall prediction of the radial pressure difference can be considered as excellent.

The predicted flow rate, Fig. 5(*c*), agrees very well with the data. A slight discrepancy taking place between 5 to 20 D_h downstream of the blockage is observed. This is very likely due to an overestimation of the liquid inertia which prevents the donor channel from having a fast flow recovery as suggested by the experimental data.

The acceleration and friction pressure drop simulation of an 88.8 percent plate blockage is shown in Fig. 6(*a*). The irreversible form pressure loss coefficient (= 2.8) is taken from Tapucu et al. (1984). The general behavior of the predicted pressure is quite similar to that of 59.2 percent plate blockage. Upstream of the blockage, an excellent agreement with data is observed. Downstream of the blockage a discrepancy which extends as far as 20 D_h is again observed. However, this feature does not prevent the radial pressure difference from following the experimental trends very well, as shown by Fig. 6(*b*).

The predictions of the liquid flow rates are given in Fig. 6(*c*). An excellent agreement with experimental data is observed. In this case the liquid inertia effects, as reported for 59.2 percent plate blockage, are almost negligible. Thus, the predicted flow recovery follows the experimental points very closely.

RUN # 5 88.8% PLATE BLOCKAGE

FLOW INLET CONDITIONS

BLOCKED CHANNEL	UNBLOCKED CHANNEL
G_L = 3056.1 $Kg/m^2 s$	G_L = 2796.7 $Kg/m^2 s$
G_G = 0.0 $Kg/m^2 s$	G_G = 0.0 $Kg/m^2 s$
α = 0.0 %	α = 0.0 %

GEOMETRIC CHARACTERISTICS

Gap Width = 1.5 mm — Gap Length = 3.0 mm

Flow Area Channel 1 = 164 mm^2 — Flow Area Channel 2 = 163 mm^2

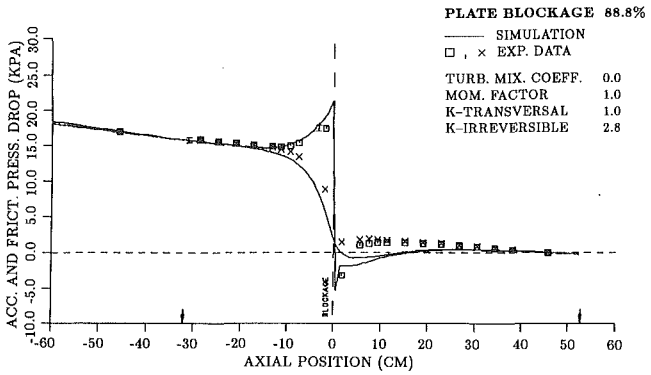

Fig. 6(*a*) Comparison of model's predictions with experimental data of Tapucu et al. (1984)

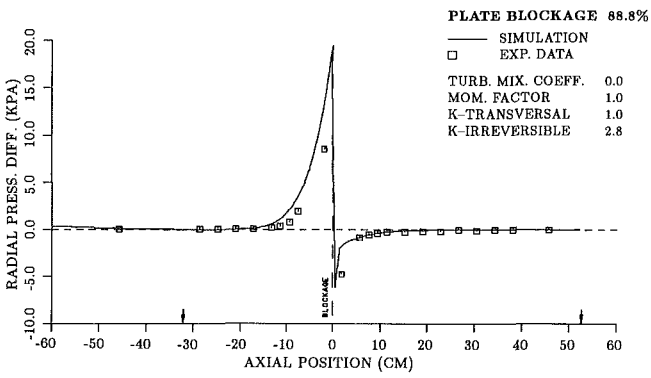

6(*b*)

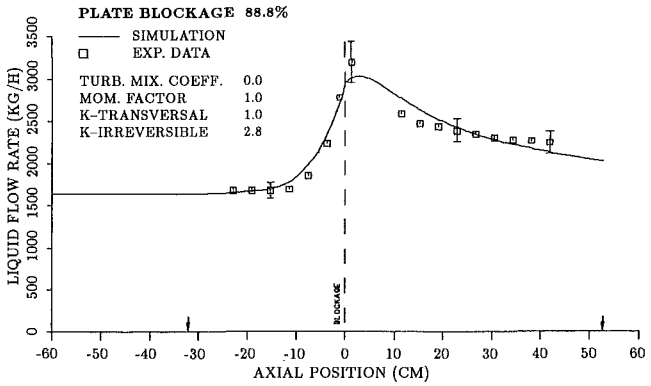

6(*c*)

Summary

A subchannel model has been written by evaluating the line and area average of the time-averaged local instantaneous conservation equations. The model has been finite differenced and the SIMPLER algorithm has been used to obtain the numerical solutions.

Comparison of the predictions of the model with experimental data showed that it is capable of handling severe blockages under single phase flow conditions. A correct adjustment of empirical parameters should improve the predictions at the

beginning of the interconnected region. However, the inaccuracies observed just downstream of the blockage are mainly due to the three-dimensional nature of the wake zone formed in this region, which cannot be adequately predicted by a one-dimensional model.

References

Bernath, L., Cohn, P. D., and Sadowski, T. J., 1964, "Forced Convection Burnout for Water in Rod Bundles at High Pressures," *International Journal of Heat and Mass Transfer*, Vol. 7, pp. 1385–1393.

Bowring, H., 1968, "HAMBO: A Computer Programme for the Subchannel Analysis of the Hydraulic and Burnout Characteristics of Rod Clusters," United Kingdom Atomic Energy Authority, AEEW-R-582.

Brown, W. D., Khan, E. U., and Todreas, N. E., 1975, "Prediction of Cross Flow Due to Coolant Channel Blockages," *Nuclear Science and Engineering*, Vol. 57, pp. 164–174.

Carver, M. B., Judd, R. A., Kiteley, J. C., and Tahir, A., 1987, "The Drift Flux Model in the ASSERT Subchannel Code," *Nuclear Journal of Canada*, Vol. 1, No. 2, pp. 153–165.

Chawla, F. C., and Ishii, M., 1978, "Equations of Motion for Two-Phase Flow in a Pin Bundle of a Nuclear Reactor," *International Journal of Heat and Mass Transfer*, Vol. 21, pp. 1057–1068.

Creer, J. M., Bates, J. M., Sutey, A. M., and Rowe, D. S., 1979, "Turbulent Flow in a Model Nuclear Fuel Rod Bundle Containing Partial Flow Blockages," *Nuclear Engineering and Design*, Vol. 52, pp. 15–33.

Fajeau, M., 1969, "Programme FLICA: Etude thermodynamique d'un réacteur ou d'une boucle d'essai," Centre d'études nucléaires, Saclay, France, CEA-R-3716.

Gosman, A. D., et al., 1973, "The SABRE Code for Prediction of Coolant Flows and Temperatures in Pin Bundle Containing Blockages," United Kingdom Atomic Energy Authority, AEEW-R905.

Hirschfelder, J. O., Curtiss, C. F., and Bird, R. B., 1964, *Molecular Theory of Gases and Liquids*, Wiley.

Ishii, M., 1975, *Thermo-Fluid Dynamic Theory of Two-Phase Flow*, Eyrolles, Paris, France.

Lahey, R. T., Shiralkar, B. S., Radcliffe, D. W., and Polomik, E. E., 1972, "Out-of-Pile Subchannel Measurements in a Nine-Rod Bundle for Water at 1000 psia," *Progress in Heat and Mass Transfer*, VI, Pergamon Press.

Lahey, R. T., Jr, and Moody, F. J., 1984, "The Thermal-Hydraulics of a Boiling Water Nuclear Reactor," American Nuclear Society, Third printing, USA.

Patankar, S. V., 1980, *Numerical Heat Transfer and Fluid Flow*, Hemisphere Publishing Co., McGraw-Hill.

Rouhani, Z., 1973, "Axial and Transverse Momentum Balance in Subchannel Analysis," SDS-46, AE-TPM-RL-1400.

Rowe, D. S., 1970, "COBRA II: A Digital Computer Program for Thermal Hydraulic Subchannel Analysis of Rod Bundle Nuclear Fuel Elements," BNWL-1229.

Rowe, D. S., 1971, "COBRA III: A Digital Computer Program for Steady State and Transient Thermal Analysis of Rod Bundle Nuclear Fuel Elements," Interim Report, BNWL-B-82.

Rowe, D. S., Wheeler, C. L., and Fitzsimmons, D. E., 1973, "An Experimental Study of Flow and Pressure in Rod Bundle Subchannels Containing Blockages," BNWL-1771.

Schilchting, H., 1968, *Boundary Layer Theory*, McGraw-Hill.

Sha, W. T., 1980, "An Overview on Rod-Bundle Thermal-Hydraulic Analysis," *Nuclear Engineering and Design*, Vol. 62.

Siikonen, T., 1987, "Numerical Method for One-Dimensional Two-Phase Flow," *Numerical Heat Transfer*, Vol. 12, pp. 1–18.

Stewart, C. W., Wheeler, C. L., Cena, R. J., McMonagle, C. A., Cuta, J. M., and Trent, D. S., 1977, "COBRA-IV: The Model and the Method," BNWL-2214, NRC-4.

St. Pierre, C. C., 1966, "SASS Code I, Subchannel Analysis for the Steady-State," AECL, APPE-41.

Tahir, A., and Carver, M. B., 1982, "Numerical Analysis of Two-Phase Flow in Horizontal Channels, SAGA-III code User's Guide," AECL-7613.

Tapucu, A., and Merilo, M., 1977, "Studies on Diversion Cross-Flow Between Two Parallel Channels Communicating by a Lateral Slot, II: Axial Pressure Variations," *Nuclear Engineering and Design*, Vol. 42, pp. 307–318.

Tapucu, A., 1978, "Diversion Cross-Flow Between Two Flows Communicating by a Lateral Slot," Institut de génie nucléaire, École Polytechnique de Montréal, IGN-284, Project P-420.

Tapucu, A., Troche, N., and Sami, S., 1983, "Comparison of Subchannel Code COBRA-IIIC and COBRA-IV with Experimental Data Obtained on Two-Laterally Interconnected Flows," Document IGN-465, École Polytechnique, Université de Montréal.

Tapucu, A., and Gençay, S., 1984, "Experimental Investigation of Mass Exchanges Between Two Laterally Interconnected Two-Phase Flows, Part I: Experimental Results on Vertical Flow," IGN-354, École Polytechnique, Montréal.

Tapucu, A., Gençay, S., and Troche, N., 1984, "Experimental Study of Diversion Cross-Flow Caused by Subchannel Blockages, Single-Phase Flow," NP-3459, Vol. 1, EPRI, Ca.

Tapucu, A., Teyssedou, A., Geçkinli, M., and Troche, N., 1988a, "Experimental Study of Diversion Cross-Flow Caused by Blockages, Part II: Two-Phase Flow," NP-3459, Vol. 2, EPRI, Ca.

Tapucu, A., Geçkinli, M., Troche, N., and Girard, R., 1988b, "Experimental Investigation of Mass Exchanges Between Two Laterally Interconnected Two-Phase Flows," *Nuclear Engineering and Design*, Vol. 105, pp. 295–312.

Tapucu, A., Teyssedou, A., Troche, N., and Merilo, M., 1989, "Pressure Losses Caused by Area Changes in a Single-Channel Flow Under Two-Phase Flow Conditions," *International Journal of Multiphase Flow*, Vol. 15, No. 1, pp. 51–64.

Tapucu, A., 1990, Personal Communication, École Polytechnique, Université de Montréal.

Van Doormaal, L. P., 1980, "A Review of Pertinent Methods Used in Multi-Dimensional Rod Bundle Thermal-Hydraulic Analysis," AECL, WNRE Project 907-16, University of Waterloo.

Vernier, P., and Delhaye, J. M., 1968, "Equations générales des écoulements diphasiques appliquées à la thermohydrodynamique des réacteurs nucléaires à eau bouillante," *Énergie Primaire*, Vol. IV, No. 1–2, pp. 5–46.

Zuber, N., 1964, "On the Problem of Hydrodynamic Diffusion in Two-Phase Flow Media," *Proceedings of the Second All Union Conference on Heat and Mass Transfer*, Minsk USSR, Vol. 3, pp. 419–442.

Zuber, N., and Findlay, J. A., 1965, "Average Volumetric Concentration in Two-Phase Flow Systems," ASME *Journal of Heat Transfer*, pp. 453–468.

M. J. Hughes
Graduate Student.

S. A. Kinnas
Principal Research Engineer and Lecturer.

J. E. Kerwin
Professor of Naval Architecture.

Department of Ocean Engineering,
Massachusetts Institute of Technology,
Cambridge, Mass. 02139

Experimental Validation of a Ducted Propeller Analysis Method

A ducted propeller model was tested in the MIT water tunnel. A hub apparatus was designed which allowed for the duct and propeller forces to be measured separately. The forces on the duct and propeller were measured over a range of advance coefficients. Velocities were measured upstream and downstream from the duct using a Laser Doppler Velocimetry system. Using these velocities the experimental values for the spanwise distribution of circulation on the propeller blades were then calculated. The experimental results were compared to the results from a propeller lifting surface/duct and hub surface panel analysis code over the same range of advance coefficients showing very good agreement for the duct and propeller forces and the circulation in the region of attached flow.

1 Introduction

The objective of the research described in this paper was to perform an extensive experiment on a ducted propeller in different flow conditions and measure the forces and flow-field velocities around it, and then use those measurements to validate the peformance of an existing Ducted Propeller Steady Flow (DPSF-2) analysis method.

Various methods exist for the design and analysis of ducted propellers. Those methods combine different models for the duct and the propeller. In the original methods the duct was represented in linearized theory by distributing ring vortices and sources on an approximate mean surface, and the propeller was modeled by using an actuator disk, lifting line or lifting surface method (Morgan, 1962; Caster, 1967; Dyne, 1967). The representation of the duct in non-linear theory was then introduced by distributing surface vorticity on the duct surface and with the propeller modeled with actuator disk or lifting line theory (Ryan and Glover, 1972; Gibson and Lewis, 1973; Falcão de Campos, 1983). Finally the complete non-axisymmetric flow around ducted propellers has been addressed in Van Houten (1986) and Kerwin et al. (1987).

In Kerwin et al. (1987) a potential based panel method has been utilized for the representation of the duct and, a vortex lattice lifting surface method for the representation of the propeller. The corresponding computer code, DPSF-2, is described in Kinnas (1989). Detailed nonaxisymmetric pressure distributions on the duct as well as the duct and propeller forces have been produced as a result of this method. The method was subsequently extended to determine the optimum loading of a propeller inside a given duct with the duct represented in nonlinear theory (Kinnas and Coney, 1988). The method was finally applied to the ultimate design of a ducted propeller using a systematic technique for designing the propeller as well as the duct (Kinnas and Coney, 1989). The numerical validation of DPSF-2, i.e., comparison with analytic solutions for simple configurations and convergence of the results with number of panels, has been established and is documented in Kerwin et al. (1987).

In this work, we initiated an effort to complete the validation of DPSF-2 by comparison with experimental results. In lack of detailed flow field measurements around a ducted propeller model, we decided to perform our own experiment at the MIT water tunnel. A duct was designed for an existing propeller along with a hub apparatus to test this ducted propeller system in the MIT variable pressure water tunnel. The forces on the duct and propeller on this model were measured for different flow conditions. The velocity flow field upstream and downstream of the duct was measured by using a Laser Doppler Velocimetry (LDV) system. The panel method, DPSF-2, was then used to analyze some of the operating conditions studied

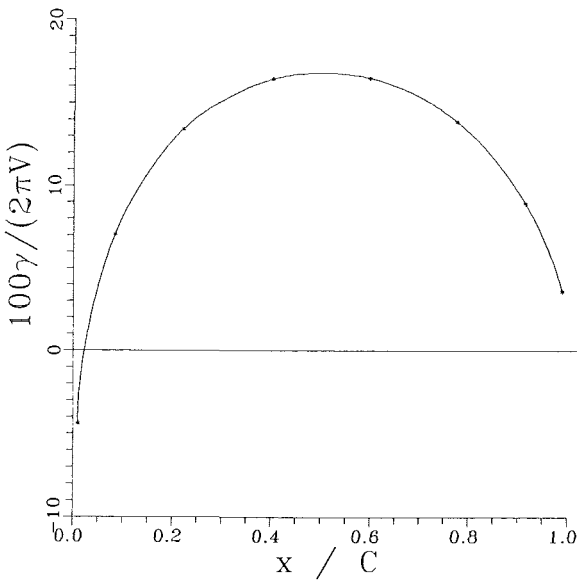

Fig. 1 Chordwise velocity distribution at 0.7 radius on propeller blade as predicted by DPSF-2 at the design advance coefficient $J = 0.30$

Contributed the Fluids Engineering Division for publication in the JOURNAL OF FLUIDS ENGINEERING. Manuscript received by the Fluids Engineering Division January 3, 1991. Associate Technical Editor: T. T. Huang.

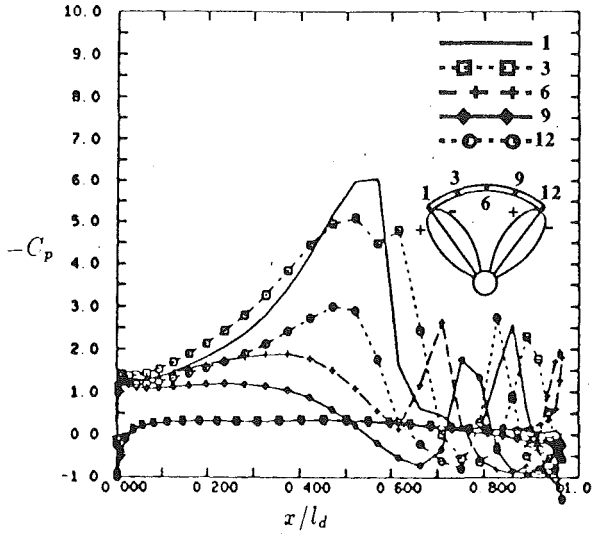

Fig. 2 Chordwise distribution of pressure on the duct cross section at different circumferential positions within two consecutive blades. The pressures have been produced by applying DPSF-2, Design $J = 0.30$.

in the tests. This paper includes a description of the experimental procedure and the theoretical calculations, and a discussion of both the theoretical and experimental results with a comparison between the two. Comparisons are also made between the experimental results from the ducted propeller and the same propeller operating without a duct.

2 Experimental Procedure

In order to perform the experimental investigation a ducted propeller model was needed. It was most efficient to design a duct which would be well suited to an existing propeller which could be obtained free of cost. A propeller was chosen from the archives at the MIT propeller tunnel. The DPSF-2 program was then used to design a duct which would provide some positive thrust without separation when operating in the propeller flow field, while maintaining the propeller blade sections near their ideal angle of attack. A complete description of the procedure used to design the duct is given by Hughes (1990). A complete description of the geometry of the duct and propeller is given in Appendix A. The loading distribution on the propeller blades and the pressure distribution on the duct for the final duct iteration are shown in Figures 1 and 2 respectively. The tests were performed at the MIT variable pressure water tunnel. A description of the water tunnel facility and of the Laser Doppler Velocimetry system can be found in Eccles (1990). A hub apparatus was developed to hold the duct to the propeller shaft. This apparatus, a drawing of which is shown in Fig. 3, was designed to allow for two configurations. In one configuration the forces on both the duct and propeller are measured by the propeller dynamometer and in the second configuration only the propeller forces are measured. The apparatus consists of a sleeve which slides over the outer nonrotating shaft in the propeller tunnel. The upper half of the drawing in Fig. 3 shows the first configuration in which the sleeve floats on the outer propeller shaft and is connected to the propeller dynamometer through a thrust bearing. The lower half of the drawing shows the second configuration in which the thrust bearing has been removed and the sleeve is clamped to the outer propeller shaft using a series of set screws. The duct is connected to this sleeve by four symmetric struts located upstream of the propeller. Experience has shown that the propeller force measurements are repeatable within one percent.

Using this apparatus, experiments were performed. The duct was manufactured from a transparent plastic in order that the propeller could be observed during the experiment. By saturating the water in the tunnel with air bubbles, the streamlines along the duct on both the inside and the outside could be observed. This showed that the flow around the duct remained unseparated over a wide range of conditions ranging from advance coefficients of 0.1 to 0.5. This indicated that the duct was truly operating near its ideal angle of attack at the design advance coefficient of 0.3. Force measurements were made over a wide range of advance coefficients in both the ahead and astern conditions. These measurements were made first using the configuration in which only the propeller forces are measured and then using the configuration in which the combined forces on the duct and propeller are measured. In this manner the forces on the duct alone could be obtained by simply subtracting the forces measured in each of the configurations. Force measurements were also made for the propeller without the presence of the duct.

The radial distributions of the axial, radial, and tangential velocity were measured at three axial positions aft of the duct trailing edge and two axial positions upstream of the duct for several advance coefficients using a Laser Doppler Velocimetry system. The circumferential mean velocities were measured by recording the average of the time varying velocities measured at a specified axial location and radius. It has been shown by Min (1978) that the accuracy of a LDV system is within one percent. A more complete description of the experimental results is given in Hughes (1990).

From the values of the tangential velocity in the wake of the duct it was possible to determine an experimental value for the spanwise distribution of circulation on the propeller blades. This was done by applying Kelvin's theorem to the propeller problem. The method used to measure the velocities and determine the circulation is described in detail by Wang (1985) and will not be restated here.

Nomenclature

C = blade section chord length
C_p = pressure coefficient, $(p-p_\infty)/(1/2\rho U_\infty^2)$
D = diameter of the propeller
f = maximum propeller blade section camber at a given radius
J = advance coefficient, $V/(nD)$
K_q = nondimensionalized torque, $Q/(\rho n^2 D^5)$
K_t = nondimensionalized thrust, $T/(\rho n^2 D^4)$
l_d = duct section chord length
N = propeller rotational speed in revolutions per minute
n = propeller rotational speed in revolutions per second
P = propeller pitch
p = pressure
p_∞ = ambient pressure
Q = propeller torque
r = radial coordinate
R = propeller radius
T = thrust
t = maximum blade thickness at a given radius
U_∞ = freestream velocity
V = inflow velocity
V_s = ship speed
x = axial coordinate
Γ = circulation around blade section
γ = strength of bound vorticity
η = open water propeller efficiency, $(JK_t)/(2\pi K_q)$
ρ = mass density of fluid
DPSF-2 = Ducted Propeller Steady Flow 2 computer analysis code
PSF-2 = Propeller Steady Flow 2 computer analysis code

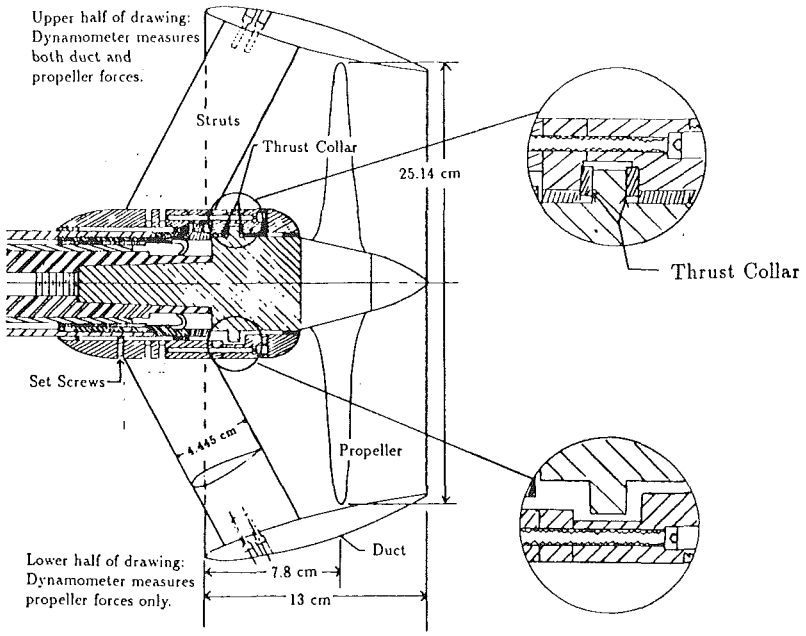

Fig. 3 The experimental apparatus

In order to calculate the proper value of the inflow velocity with which to non-dimensionalize the measured velocities, the effects of the tunnel walls had to be taken into account. When measuring the forces, the tunnel walls were accounted for by using the principles of momentum and continuity in a linearized manner to determine the corrected value for the advance coefficient and K_t, as described in Glauert (1947). The velocities measured using the LDV system were nondimensionalized with respect to the velocity corresponding to the corrected value of the advanced coefficient at the same propeller rpm.

3 Theoretical Calculations

Theoretical computations were performed using the DPSF-2 program. In DPSF-2 the flow around the duct and the hub is analyzed via a discretized boundary element method, or *panel method.* The duct and the hub are treated as a single unit. From now on the existence of the hub will be implied when discussing the duct solution. The propeller is modeled by a lifting surface method. The program is currently being extended to also include a panel method representation of the propeller. This will result in a more accurate representation of the propeller leading edge flow, but is not expected to affect the force calculation substantially, as it is more essential that the thickness effects be represented more accurately for the duct than for the propeller. The duct and the propeller are treated as independent devices. However, the effects of the duct on the propeller and of the propeller on the duct are computed in an iterative manner. A complete description of the DPSF-2 program, including discussions of numerical convergence, is provided in Kerwin et al. (1987) and Kinnas (1989). In the original version of this code the panels on the duct were set up to match the pitch of the propeller blades at the propeller tip in order to reduce the numerical error. However, in the present case the propeller had a very low pitch and a rounded tip which resulted in very elongated, oddly shaped panels being formed on the duct. On the other hand, the relatively large gap between the tip of the propeller and the duct made the alignment of these two grids less important. For this reason the program was modified to have the option of paneling the duct with a different pitch from the propeller tip.

Sixty circumferential and sixty-two chordwise panels, thirty-one on each side, were used when modeling the duct. For the propeller eight chordwise and eight spanwise vortex segments were used. The resulting panel arrangement can be seen in Fig. 4. For most of the DPSF-2 runs nine iterations were used for the duct and propeller solutions. However, at very low advance coefficients, eleven iterations were required in order to achieve adequate convergence. Convergence of the calculated forces with grid size for this particular geometry is shown in Table 1.

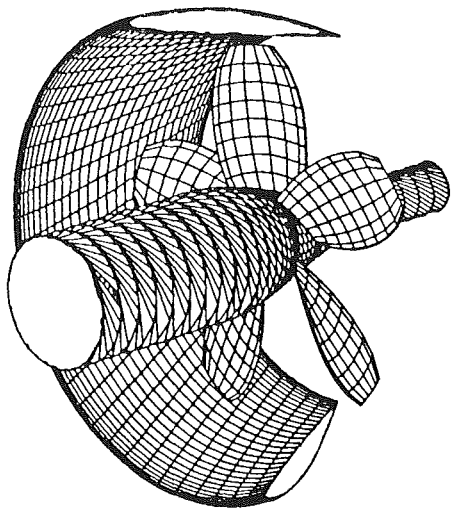

Fig. 4 Panel management for propeller, hub. Only half of the duct panels are shown.

Table 1 Convergence of calculated forces with grid size, $J = 0.300$

Duct Paneling	Propeller Grid	Propeller K_t	Total K_t	K_q
62×60	8×8	0.170	0.1898	0.0203
82×80	12×12	0.172	0.1897	0.0205

The output from the theoretical calculations consists of K_t and K_q for the propeller, the velocities at the plane of the propeller, the pressure distribution over the duct, and the circulation on the duct and propeller. Examples of the pressure distributions at two off design advance coefficients are shown in Fig. 5. DPSF-2 also calculates a nondimensionalized force

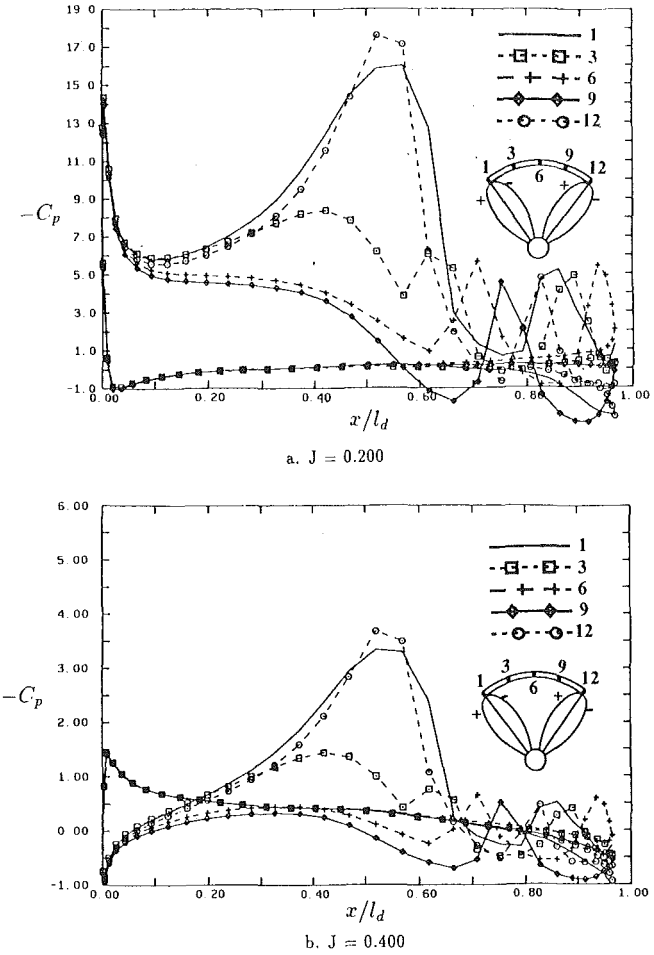

Fig. 5 Dust pressure distributions as predicted by DPSF-2 at off-design conditions, shown at different circumferential positions within two consecutive blades.

coefficient for the duct by integrating the pressure distribution. This is converted to a K_t value for the duct in order to compare against experimental results. The viscous drag on the duct is taken into account by assuming that the drag coefficient of the duct profile is 0.0085. Although the propeller was modeled with a vortex lattice, the forces on the propeller were calculated using lifting line theory, where the circulation at the control point radii on the lifting line was taken to be the sum of the vorticity at the chordwise control points at that radii. This will later be modified so that the propeller forces are computed by integrating the pressure distribution over the blade surfaces (Kinnas et al., 1990).

The program was extended to calculate the velocity at any point in the flow field. As with the experimental case, the velocity calculated is the mean circumferential velocity at a given axial location and radius. This value is obtained by first calculating the velocities at a series of angular positions at the same axial and radial location and then taking the average of these values. It is essential to avoid computing the velocity at points in the vicinity of the propeller and duct panels, where the discretization error is substantial. The velocities induced by the duct and propeller are calculated separately and then added to the unperturbed velocity to produce the total velocity at any point in the flow field. The velocities induced by the propeller singularities were calculated by following the method described by Greeley and Kerwin (1982). The velocities induced by the duct were calculated by superimposing the velocities due to the dipole and source panels on the duct and its wake. A more detailed description of this procedure is given in Kinnas et al. (1990b).

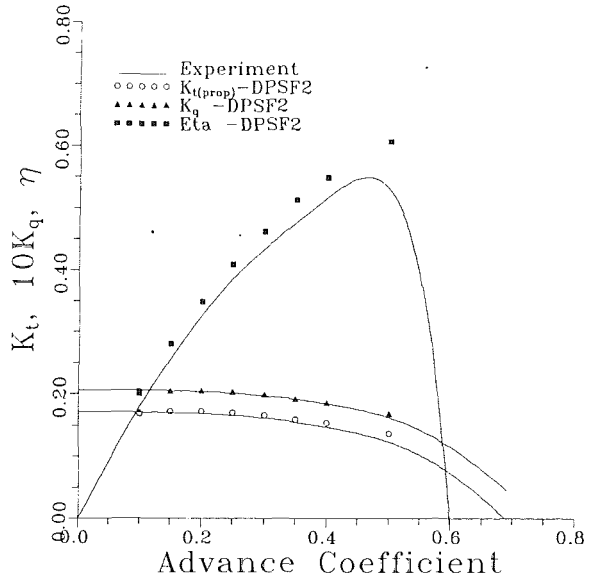

Fig. 6 Comparison of experimental and theoretical forces, propeller force only

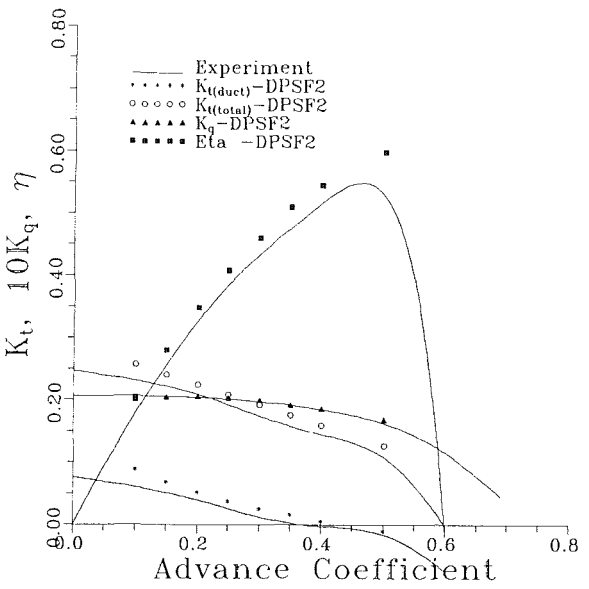

Fig. 7 Comparison of experimental and theoretical forces, propeller and duct forces

4 Comparison of Theoretical and Experimental Results

Comparison between the experimental results and the results from DPSF-2 are shown in Figs. 6 and 7. Figure 6 shows the results for the forces measured on the propeller alone in the presence of the duct compared with the same forces from DPSF-2. Figure 7 shows the same comparison including the forces on the duct.

It can be seen in Fig. 6 that the K_t and K_q for the propeller are predicted very accurately over the full range of advance coefficients. The value for K_t on the duct is slightly overpredicted at all values of advance coefficients, although the shape of this curve is predicted correctly. This could possibly be due to separation occurring on the internal surface of the duct aft of the propeller. The pressure distribution on the duct shows a negative pressure gradient aft of the propeller which indicates that the flow might separate there. This would tend to decrease the thrust produced by the duct. The overprediction of duct thrust results in the total thrust and open water efficiency predicted by DPSF-2 being slightly higher than its experimental

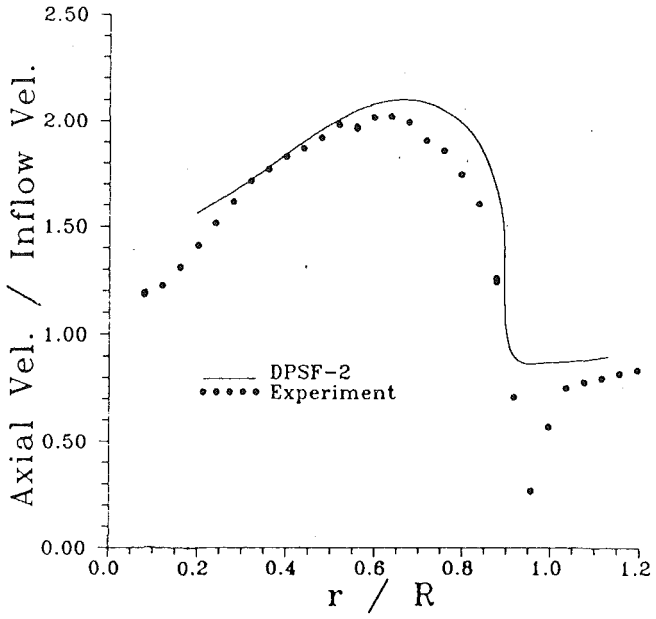

a. Comparison for axial velocities

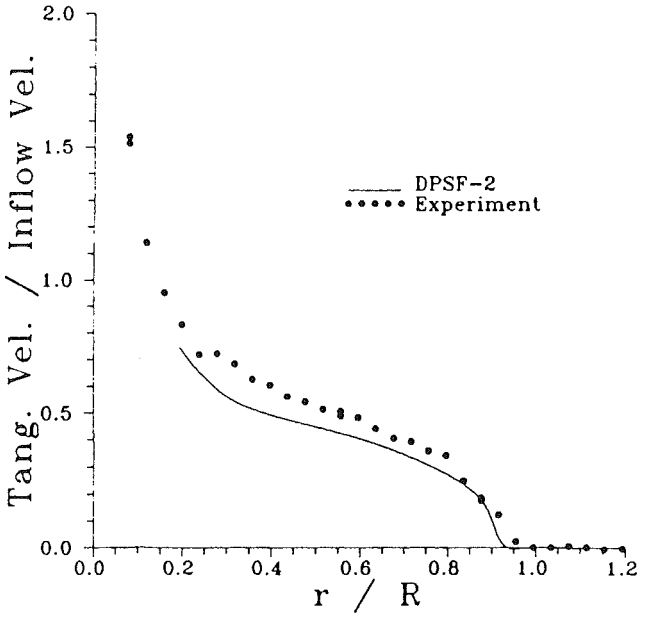

b. Comparison for tangential velocities

Fig. 8 Comparison of experimental and theoretical velocities at an axial location of 1 cm aft of the duct tracking edge, $J = 0.373$

value. Overall, however, the results show a very good correlation between theory and experiment.

Figure 8 shows a comparison between the axial and tangential velocities measured one centimeter behind the trailing edge of the duct and those calculated using DPSF-2 at J = 0.373. The correlation is relatively good. The shape of the curve for the axial and tangential velocities is accurately predicted, but the values obtained from DPSF-2 are shifted slightly over the span. This discrepancy may disappear if a more systematic method of accounting for the tunnel wall effects were incorporated into the program (Shih, 1988). Comparisons at other operating conditions can be found in Hughes (1990).

From the values of tangential velocity versus radial position, the radial distribution of circulation around the propeller can be calculated. A comparison was also made between the spanwise distribution of circulation calculated from DPSF-2 and that obtained from the tangential velocities in the wake as described in Section 3. This comparison was made at three advance coefficients and is shown in Fig. 9. A good correlation was achieved between experimental and the theoretical values of the spanwise circulation.

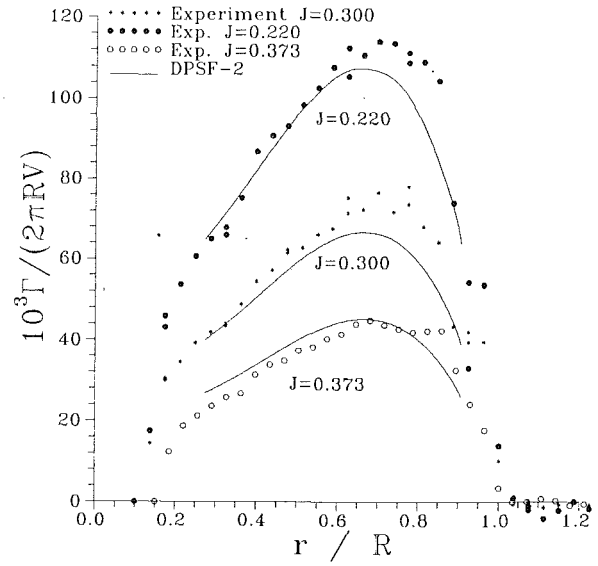

Fig. 9 Comparison of experimental and theoretical distributions for the spanwise distribution of circulation on the propeller

5 Conclusions and Future Research

The following has been accomplished in the present work:

- Experiments on a ducted propeller were performed in the MIT Variable Pressure Water Tunnel. A hub apparatus was designed which allowed for the duct and propeller forces to be measured separately.
- The ducted propeller was analyzed using the DPSF-2 computer program. Very good agreement over a large range of advance coefficients was shown between the theoretical and experimental values for the forces on the duct and propeller and the circulation on the propeller.
- Velocity measurements were made using the LDV system at the MIT propeller tunnel. The velocity field measured behind the ducted propeller model behaved as expected. The analysis code was also extended to predict the velocity at any field point in the region surrounding a ducted propeller. The predicted velocities showed reasonable agreement with those measured experimentally.

The above shows that the utilized potential based panel method (DPSF-2) is a useful and reliable tool for the design and analysis of ducted propellers. Our current research concerns the analysis of ducted propellers operating in combination with preswirl stator vanes. Since a ducted propeller often requires struts to support the duct, it appears logical to use these supports as a set of pre-swirl stator vanes if a gain in efficiency could be achieved. The ducted propeller analysis code DPSF-2 has been modified to include the presence of pre-swirl stators. This extended version of the code has been used to design a combination of duct and stators to operate efficiently with an existing propeller. Tests were performed on this ducted propeller and stator combination. A description of the analysis method and comparisons with experiments can be found in Hughes and Kinnas (1991).

Acknowledgments

Support of the research was provided by the Charles Stark Draper Laboratory Internal Research and Development Program. At this point the authors wish to thank Mr. Peter Sebelius and Mr. John Chiffer of Draper Laboratory for their valuable comments and discussions during the course of this work.

References

Caster, E. B., 1967, "A Computer Program for Use in Designing Ducted Propellers," Technical Report 2507, NSRDC.

Dyne, G., 1967, "A Method for the Design of Ducted Propellers in a Uniform Flow," Technical Report 62, Swedish State Shipbuilding Tank, Goteberg, Sweden.

Eccles, T. J., 1990, "Measurement of Hydrodynamic Forces and Moments and Flow Field Mapping of a Model in Coning Motion," Master's thesis, Department of Ocean Engineering, MIT, Cambridge, Mass.

Falcão de Campos, J. A. C., 1983, "On the Calculation of Ducted Propeller Performance in Axisymmetric Flows," Technical Report 696, Netherlands Ship Model Basin, Wageningen, The Netherlands.

Gibson, I. S., and Lewis, R. I., 1973, "Ducted Propeller Analysis by Surface Vorticity and Actuator Disc Theory," *Proceedings of the Symposium on Ducted Propellers*, No. 1-10, Teddington, England, The Royal Institution of Naval Architects.

Glauert, H., 1974, *The Elements of Aerofoil and Airscrew Theory*, 2nd Edition, Cambridge University Press, NY.

Greeley, D. S., and Kerwin, J. E., 1982, "Numerical Methods for Propeller Design and Analysis in Steady Flow," *Trans. SNAME*, Vol. 90.

Hughes, M. J., 1990, "A Comparison of Experiment and Analysis for a Ducted Propeller," Master's thesis, Department of Ocean Engineering, MIT, Cambridge, Mass.

Hughes, M. J., and Kinnas, S. A., 1991, "An Analysis Method for a Ducted Propeller with Pre-Swirl Stator Blades," *Proceedings of the Propellers/Shafting '91 Symposium*, No. 15, SNAME, Virginia Beach, VA.

Kerwin, J. E., Kinnas, S. A., Lee, J.-T., and Shih, W.-Z., "1987, "A Surface Panel Method for the Hydrodynamic Analysis of Ducted Propellers," *Trans. SNAME*, Vol. 95.

Kinnas, S. A., 1989, *Ducted Propeller Steady Flow, MIT-DPSF2, User's Manual*, MIT, Department of Ocean Engineering Report.

Kinnas, S. A., Hsin, C.-Y., and Keenan, D. P., 1990, "A Potential Based Panel Method for the Unsteady Flow Around Open and Ducted Propellers," *Proceedings of the Eighteenth Symposium on Naval Hydrodynamics*, Ann Arbor, Mich.

Kinnas, S. A., Hughes, M. J., and Kerwin, J. E., 1990b, "Comparison of Analysis and Experiment for a Ducted Propeller," *Proceedings of the Second International Symposium on Performance Enhancement for Marine Applications*, Newport, RI.

Kinnas, S. A., and Coney, W. B., 1988, "On the Optimum Ducted Propeller Loading," *Proceedings of the Propellers '88 Symposium*, No. 1, SNAME, Virginia Beach, VA.

Kinnas, S. A., and Coney, W. B., 1988, "A Systematic Method for the Design of Ducted Propellers," *Proceedings of the Fourth International PRADS89 Symposium*, Vol. 4, Varna, Bulgaria.

Min, Keh-Sik, 1978, "Numerical and Experimental Methods for the Prediction of Field Point Velocities Around Propeller Blades," Technical Report 78-12, Department of Ocean Engineering, MIT.

Morgan, W. B., 1962, "Theory of the Annular Airfoil and Ducted Propeller," *Fourth Symposium on Naval Hydrodynamics*, No. ACR-73, pp. 151-197.

Table 2 Description of propeller geometry

r/R	*P/D*	RAKE/D	SKEW	*C/D*	*f/C*	*t/D*
0.20	0.5734	0.00	0.00	0.1698	0.0459	0.0416
0.30	0.6031	0.00	0.00	0.2057	0.0380	0.0359
0.40	0.6317	0.00	0.00	0.2359	0.0331	0.0303
0.50	0.6560	0.00	0.00	0.2562	0.0304	0.0248
0.60	0.6707	0.00	0.00	0.2667	0.0284	0.0198
0.70	0.6764	0.00	0.00	0.2667	0.0258	0.0152
0.80	0.6714	0.00	0.00	0.2505	0.0210	0.0109
0.90	0.6515	0.00	0.00	0.2101	0.0147	0.0069
0.95	0.6296	0.00	0.00	0.1719	0.0115	0.0050
1.00	0.5969	0.00	0.00	0.1094	0.0062	0.0030

Table 3 Offsets for the duct

Duct inner surface		Duct outer surface	
x	*r*	*x*	*r*
0.000	1.177	0.000	1.177
0.006	1.165	0.015	1.187
0.029	1.150	0.053	1.192
0.076	1.128	0.102	1.191
0.133	1.103	0.177	1.184
0.201	1.083	0.253	1.172
0.279	1.057	0.336	1.157
0.365	1.031	0.410	1.141
0.455	1.006	0.516	1.112
0.546	0.983	0.619	1.077
0.663	0.958	0.714	1.038
0.770	0.939	0.788	1.006
0.848	0.926	0.860	0.972
0.900	0.918	0.915	0.944
0.942	0.912	0.947	0.928
0.960	0.909	0.963	0.920
0.965	0.909	0.965	0.919

Ryan, P. G., and Glover, E., 1972, "A Ducted Propeller Design Method: A New Approach Using Surface Vorticity Distribution Techniques and Lifting Line Theory," *Trans. RINA*, Vol. 114.

Shih, Wei-Zen, 1988, "Effective Wake Calculations by Solving The Euler Equation, Technical Report No. 88-2, Department of Ocean Engineering, MIT.

Van Houten, R. J., 1986, "Analysis of Ducted Propellers in Steady Flow," Technical Report 4.76-1, Airflow Research and Manufacturing Corp., Watertown, Massachusetts.

Wang, Mo-Hwa, 1985, "Hub Effects in Propeller Design and Analysis," Technical Report No. 85-12, Department of Ocean Engineering, MIT.

A Geometry of the Propeller and Duct

The propeller model used for this research was DTRC propeller model 3745. This propeller had 5 blades and a diameter of 25.14 cm. The propeller blades had parabolic arc camber and a NACA-16 thickness form. A description of the propeller geometry at various sections is given in Table 2. The offsets for the duct are given in Table 3. These offsets have been nondimensionalized with respect to the duct chord. The origin is located on the propeller axis at the duct leading edge.

Prediction of Confined Three-Dimensional Impinging Flows With Various Turbulence Models

T. M. Liou
Professor.

Y. H. Hwang
Graduate Student.

L. Chen
Graduate Student.

Department of Power Mechanical Engineering,
National Tsing Hua University,
Hsin-Chu, Taiwan 30043

This paper deals with three-dimensional, turbulent, confined impinging flows. Various turbulence models are examined with reported laser-Doppler velocimetry data and flow-visualization photographs. The turbulence models considered are the $k-\epsilon$, $k-\epsilon$ with the Richardson number correction for swirling and recirculating flows ($k-\epsilon$ w/scm), algebraic Reynolds stress ($k-\epsilon-A$), and modified $k-kl$ models. The $k-\epsilon$ and $k-\epsilon-A$ models are found to be superior to the $k-\epsilon$ w/scm and modified $k-kl$ models in predicting the main flow characteristics. The $k-\epsilon-A$ model provides a better quantitative agreement with the experimental data than can be achieved with the $k-\epsilon$ model, however, less computational effort is spent with the $k-\epsilon$ model than with the $k-\epsilon-A$ model. Also, the effect of the inlet velocity profile on the characteristics of the confined impinging flows is addressed in this study.

Introduction

The impingement of two jets on each other in a closed-end cylindrical duct with side-inlet ports is an important feature of the flow fields involved in internal biofluiddynamics, utility boiler furnaces, and side-dump ramjet combustors. In fact, the flow fields associated with these applications consist of a number of diverse flow moduli such as the inlet jets, the jet-jet head-on collision, the jet-wall impingement, the recirculating flow in the separated regions, and the developing duct flow far downstream of the inlet ports. For the case of combustors, the flow fields in the side-dump combustors are certainly more complicated than in the coaxial-dump combustors. The latter case has been intensively studied in the past. In contrast, the impingement flow in the side-dump combustors has not been fully addressed in the literature. Therefore, a better understanding of such a complicated flow field is highly desirable.

Shahaf et al. (1980) investigated the two-dimensional flow field in a square cross-sectional channel with two side inlets both analytically and experimentally. They characterized the isothermal flow patterns by calculating the distributions of stream function and vorticity. The turbulence closure scheme was achieved by modifying the $k-kl$ turbulence model proposed by Launder and Spalding (1972). For brevity, this modified version of $k-kl$ model will be referred to as $k-kl$ model in this paper. Large discrepancies between the measured and calculated axial mean-velocity profiles were found along the channel axis and in the recirculating zones. No measurements were made in the head region (i.e., the region between the closed end and the upstream edge of the intake ports). Choudhury (1982) experimentally tested for the combustor performance of a gas generator ramjet with four side inlets and concluded that the system of vortices in the head region is crucial to the stable operation of the combustor. Moreover, he found that the inlet flow angle does not have any influence on the vortex system in the head region and the flame blowoff data for both side inlet angles, $\theta=45$ and $\theta=70$ deg (Fig. 1) are identical within the range of data scatter. Stull et al. (1983) performed water flow visualization and combustion test of a side dump combustor with two side inlets separated by an azimuthal angle of 90°. They reported that combustor performance was not sensitive to variations in head height and only mildly affected by inlet entry angle. Subsequently, Vanka et al. (1983) calculated the three-dimensional cold mean-flow field with the $k-\epsilon$ turbulence model (Launder and Spalding, 1974) in the combustor of Stull et al. Their calculations, however, did not predict a vortex pattern in the head region in the $\theta_c=180$ deg plane (Fig. 1) shown by the flow visualization of Stull et al. Vanka et al. (1985) further performed calculations of the three-dimensional reacting flow in the same combustor using the $k-\epsilon$ model. The effects of the head height and the side-inlet angle were studied in terms of the combustion efficiency. They found the combustion efficiency increased with steepening of the side-inlet angle (30–60 deg), a result inconsistent with that of Stull et al. They also found an optimal head height for the best combustion efficiency. Additionally, Cherng et al. (1988) calculated the detailed three-dimensional turbulent reacting flow in a cylindrical combustor with four side inlets and fuel-gas injectors using the $k-\epsilon$ turbulence model with streamline curvature modification ($k-\epsilon$ w/scm) (Srinivasan et al., 1983). Their results are informative but lacking of direct comparison with experimental data.

In view of the lack of quantitative data related to the flow field, particularly the turbulence data, with which to compare with computational predictions, Liou and Wu performed de-

Contributed by the Fluids Engineering Division for publication in the JOURNAL OF FLUIDS ENGINEERING. Manuscript received by the Fluids Engineering Division June 8, 1989. Associate Technical Editor: C. J. Freitas.

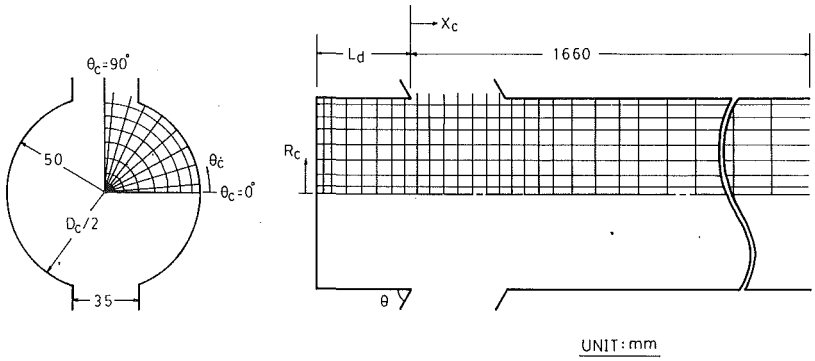

Fig. 1 Sketch of configuration, coordinate system, dimensions and grid system of dual-inlet closed-end cylindrical duct (Uncertainty in X_c position: less than ±0.3 mm, in R_c position: less than ±0.3 mm, in θ_c: less than ±1.5 deg, in D_c: less than ±0.3 mm, in L_d: less than ±0.5 mm)

tailed mean velocity and turbulence measurements in curved 60 deg inlet ducts (Liou and Wu, 1986) and in a three-dimensional side-dump cylindrical combustor (Liou and Wu, 1988) using laser-Doppler velocimetry (LDV); nevertheless, their measurements were carried out only at a single side-inlet angle. Recently, Liou et al. (1990b) performed both LDV measurements and theoretical computations ($k-\epsilon$ model) for the flow field in a two-dimensional side-inlet rectangular duct. They found the three-dimensional nature of a two-dimensional side-inlet duct flow due to the presence of streamwise and vortex structures which were also observed by Nosseir and Behar (1986) using smoke flow visualization.

From the above literature review, a computational study of three-dimensional jet-jet impingement flow, including comparisons with available experimental results, would be worthwhile. The applicability of different turbulence models, including the $k-kl$, $k-\epsilon$, $k-\epsilon$ w/scm, and the algebraic Reynolds stress ($k-\epsilon-A$) (Rodi, 1976) model, to confined impinging flows has not been previously documented and, therefore, was made in the present study. Furthermore, the influence of the inlet velocity profile on the flow characteristics is also important and was analyzed in the present work.

In the following sections of this paper, the details of the theoretical treatment, including the equations solved, boundary conditions specified, and solution algorithm used, are stated first. The computed flow patterns using the $k-\epsilon$ model are subsequently discussed. Then, the comparisons with LDV measurements and with the results predicted with the $k-kl$, $k-\epsilon$ w/scm, and $k-\epsilon-A$ models are given. Finally, the effect of the inlet velocity profile on the flow characteristics is addressed.

Theoretical Formulation

The computations were performed by numerically solving the fully elliptic, three-dimensional Navier-Stokes equations. To simplify the problem, the flow was considered to be isothermal, incompressible and steady-state in the mean.

The Mean Flow Equations. The time averaged equations for conservation of mass and momentum in a cylindrical coordinate system (R_c, θ_c, X_c) can be expressed as follows:

$$\frac{\partial}{R_c\partial R_c}(R_c\rho V)+\frac{\partial}{R_c\partial\theta_c}(\rho W)+\frac{\partial}{\partial X_c}(\rho U)=0 \tag{1}$$

$$\frac{\partial}{R_c\partial R_c}(R_c\rho V\phi)+\frac{\partial}{R_c\partial\theta_c}(\rho W\phi)+\frac{\partial}{\partial X_c}(\rho U\phi)$$
$$=\frac{\partial}{R_c\partial R_c}\left(R_c\mu_l\frac{\partial\phi}{\partial R_c}\right)+\frac{\partial}{R_c\partial\theta_c}\left(\mu_l\frac{\partial\phi}{R_c\partial\theta_c}\right)+\frac{\partial}{\partial X_c}\left(\mu_l\frac{\partial\phi}{\partial X_c}\right)+S_\phi \tag{2}$$

Table 1 shows the source terms appearing in Eq. (2). Note that the body force term has been neglected in the momentum equation and the turbulent correlation $\overline{u_iu_j}$ is the time-average of u_iu_j and stands for the Reynolds stresses which must be modeled to close the above set of equations.

The Turbulence Models. In the present calculations, the general Boussinesq eddy viscosity concept is adopted to express

Nomenclature

C_{A1} = constant in the $k-\epsilon-A$ turbulence model (=1.5)
C_{A2} = constant in the $k-\epsilon-A$ turbulence model (=0.6)
$\hat{C}_{A1}$, $\hat{C}_{A2}$ = modified constants for C_{A1} and C_{A2}, respectively
C_b = constant in the $k-kl$ turbulence model (=1.0)
C_{kl} = constant in the $k-kl$ turbulence model (=0.22)
C_l = constant in the $k-kl$ turbulence model (=1.0)
$C_{l\epsilon}$ = constant in the $k-kl$ turbulence model (=0.416)
C_s = constant in the $k-kl$ turbulence model (=0.057)
C_1 = constant in the $k-\epsilon$ turbulence model (=1.44)
C_2 = constant in the $k-\epsilon$ turbulence model (=1.92)
C_μ = constant in the $k-\epsilon$ turbulence model (=0.09)
$\hat{C}_2$ = modified constant for C_2
D_c = combustor diameter
E = constant in near-wall description of velocity profile
k = turbulence kinetic energy
L_d = dome height of combustor
L_d^* = nondimensional dome height $L_d^* = L_d/(D_c/2)$
l = turbulent length scale
MIC = measured inlet condition
P = pressure
P_{ij} = production rate of $\overline{u_iu_j}$
P_k = production rate of k ($=1/2\ P_{ii}$)
R_c = combustor radial coordinate
R_c^* = normalized combustor radial coordinate $R_c^* = R_c/(D_c/2)$
R_{cu} = radius of flow curvature
Re_c = combustor Reynolds number $\mathrm{Re}_c = \rho U_{\mathrm{ref}}D_c/\mu_l$
$\mathrm{R_{ic}}$ = Richardson number for recirculating flow
$\mathrm{R_{is}}$ = Richardson number for swirling flow

Table 1 Source terms in Eq. (2) for various ϕ

ϕ	S_ϕ
U	$-\frac{\partial P}{\partial X_c}+\frac{\partial}{R_c\partial R_c}\left(R_c\mu_l\frac{\partial V}{\partial X_c}\right)+\frac{\partial}{R_c\partial\theta_c}\left(\mu_l\frac{\partial W}{\partial X_c}\right)+\frac{\partial}{\partial X_c}\left(\mu_l\frac{\partial U}{\partial X_c}\right)$ $-\frac{\partial}{R_c\partial R_c}(R_c\rho\overline{u_ru_x})-\frac{\partial}{R_c\partial\theta_c}(\rho\overline{u_\theta u_x})-\frac{\partial}{\partial X_c}(\rho\overline{u_xu_x})$
V	$+\frac{\rho W^2}{R_c}-\frac{\partial P}{\partial R_c}+\frac{\partial}{R_c\partial R_c}\left(R_c\mu_l\frac{\partial V}{\partial R_c}\right)+\frac{\partial}{R_c\partial\theta_c}\left[R_c\mu_l\frac{\partial}{\partial R_c}\left(\frac{W}{R_c}\right)\right]$ $+\frac{\partial}{\partial X_c}\left(\mu_l\frac{\partial U}{\partial R_c}\right)-2\frac{\mu_l}{R_c}\left(\frac{\partial W}{R_c\partial\theta_c}+\frac{V}{R_c}\right)-\frac{\rho\overline{u_\theta u_\theta}}{R_c}-\frac{\partial}{R_c\partial R_c}(R_c\rho\overline{u_ru_r})$ $-\frac{\partial}{R_c\partial\theta_c}(\rho\overline{u_ru_\theta})-\frac{\partial}{\partial X_c}(\rho\overline{u_ru_x})$
W	$-\frac{\rho VW}{R_c}-\frac{\partial P}{R_c\partial\theta_c}+\frac{\partial}{R_c\partial R_c}\left[R_c\mu_l\left(\frac{\partial V}{R_c\partial\theta_c}-\frac{W}{R_c}\right)\right]$ $+\frac{\partial}{R_c\partial\theta_c}\left[\mu_l\left(\frac{\partial W}{R_c\partial\theta_c}+\frac{2V}{R_c}\right)\right]$ $+\frac{\partial}{\partial X_c}\left(\mu_l\frac{\partial U}{R_c\partial\theta_c}\right)+\frac{\mu_l}{R_c}\left[R_c\frac{\partial}{\partial R_c}\left(\frac{W}{R_c}\right)+\frac{\partial V}{R_c\partial\theta_c}\right]$ $-\frac{\rho\overline{u_ru_\theta}}{R_c}-\frac{\partial}{R_c\partial R_c}(R_c\rho\overline{u_ru_\theta})-\frac{\partial}{R_c\partial\theta_c}(\rho\overline{u_\theta u_\theta})-\frac{\partial}{\partial X_c}(\rho\overline{u_\theta u_x})$

the Reynolds stresses for the $k-\epsilon$, $k-kl$, and $k-\epsilon$ w/scm models.

$$
\begin{aligned}
-(\overline{u_ru_r}) &= 2\frac{\mu_t}{\rho}\left(\frac{\partial V}{\partial R_c}\right)-\frac{2}{3}k\\
-(\overline{u_ru_\theta}) &= \frac{\mu_t}{\rho}\left(\frac{\partial V}{R_c\partial\theta_c}-\frac{W}{R_c}+\frac{\partial W}{\partial R_c}\right)\\
-(\overline{u_ru_x}) &= \frac{\mu_t}{\rho}\left(\frac{\partial V}{\partial X_c}+\frac{\partial U}{\partial R_c}\right)\\
-(\overline{u_\theta u_\theta}) &= 2\frac{\mu_t}{\rho}\left(\frac{\partial W}{R_c\partial\theta_c}+\frac{V}{R_c}\right)-\frac{2}{3}k\\
-(\overline{u_\theta u_x}) &= \frac{\mu_t}{\rho}\left(\frac{\partial U}{R_c\partial\theta_c}+\frac{\partial W}{\partial X_c}\right)\\
-(\overline{u_xu_x}) &= 2\frac{\mu_t}{\rho}\left(\frac{\partial U}{\partial X_c}\right)-\frac{2}{3}k
\end{aligned}
\tag{3}
$$

where δ_{ij} is the Kronecker-Delta function and μ_t is the turbulent viscosity that may be related to the turbulent variables as k, ϵ, kl etc. In addition to the Boussinesq eddy viscosity concept, an algebraic Reynolds stress model ($k-\epsilon-A$) is also used to model Reynolds stresses. The detailed formulations of various turbulence models are given below and values of the empirical constants in the turbulent transport equations have been specified in the Nomenclature.

(*i*) The $k-\epsilon$ model

$$\mu_t = C_\mu\rho k^2/\epsilon \tag{4}$$

The differential equations for k and ϵ are

$$
\begin{aligned}
&\frac{\partial}{R_c\partial R_c}(R_c\rho Vk)+\frac{\partial}{R_c\partial\theta_c}(\rho Wk)+\frac{\partial}{\partial X_c}(\rho Uk)\\
&\quad=\frac{\partial}{R_c\partial R_c}\left(R_c\Gamma_k\frac{\partial k}{\partial R_c}\right)+\frac{\partial}{R_c\partial\theta_c}\left(\Gamma_k\frac{\partial k}{R_c\partial\theta_c}\right)\\
&\qquad+\frac{\partial}{\partial X_c}\left(\Gamma_k\frac{\partial k}{\partial X_c}\right)+\rho\overline{P}_k-\rho\epsilon
\end{aligned}
\tag{5}
$$

$$
\begin{aligned}
&\frac{\partial}{R_c\partial R_c}(R_c\rho V\epsilon)+\frac{\partial}{R_c\partial\theta_c}(\rho W\epsilon)+\frac{\partial}{\partial X_c}(\rho U\epsilon)\\
&\quad=\frac{\partial}{R_c\partial R_c}\left(R_c\Gamma_\epsilon\frac{\partial\epsilon}{\partial R_c}\right)+\frac{\partial}{R_c\partial\theta_c}\left(\Gamma_\epsilon\frac{\partial\epsilon}{R_c\partial\theta_c}\right)\\
&\qquad+\frac{\partial}{\partial X_c}\left(\Gamma_\epsilon\frac{\partial\epsilon}{\partial X_c}\right)+C_1\rho\overline{P}_k\epsilon/k-\rho\epsilon^2/k
\end{aligned}
\tag{6}
$$

where $\overline{P}_k$ is given in Appendix A and

$$\Gamma_k=\mu_t/\sigma_k$$

$$\Gamma_\epsilon=\mu_t/\sigma_\epsilon$$

(*ii*) The modified $k-kl$ model

$$\mu_t = C_{kl}\rho k^{1/2}l \tag{7}$$

The differential equations for k and kl are

$$
\begin{aligned}
&\frac{\partial}{R_c\partial R_c}(R_c\rho Vk)+\frac{\partial}{R_c\partial\theta_c}(\rho Wk)+\frac{\partial}{\partial X_c}(\rho Uk)\\
&\quad=\frac{\partial}{R_c\partial R_c}\left(R_c\Gamma_k\frac{\partial k}{\partial R_c}\right)+\frac{\partial}{R_c\partial\theta_c}\left(\Gamma_k\frac{\partial k}{R_c\partial\theta_c}\right)+\frac{\partial}{\partial X_c}\left(\Gamma_k\frac{\partial k}{\partial X_c}\right)\\
&\qquad+\rho\overline{P}_k-C_{l\epsilon}\rho k^{3/2}/l
\end{aligned}
\tag{8}
$$

Nomenclature (cont.)

SI = swirl intensity
U = axial mean velocity
UIC = uniform inlet condition
U_{ref} = combustor bulk mean velocity
V = radial mean velocity
V_p = velocity parallel to the wall
V_R = resultant velocity of U and V
W = azimuthal mean velocity
X_c = combustor axial coordinate
X_c^* = normalized combustor axial coordinate $X_c \le 0$; $X_c^* = X_c/L_d$, $X_c \ge 0$; $X_c^* = X_c/D_c$
z_p = distance normal to the wall
α_c = constant in the $k-\epsilon$ w/scm turbulence model (=0.2)
α_s = constant in the $k-\epsilon$ w/scm turbulence model (=0.2)
κ = von Karman's constant (=0.4187)
θ = angle of side-inlet jet
θ_c = combustor azimuthal coordinate
ϵ = dissipation rate of turbulence kinetic energy
Γ = turbulent diffusion coefficient
ρ = fluid density
μ_l = molecular dynamic viscosity
μ_t = turbulent dynamic viscosity
σ_k = turbulent Prandtl number of k (=1.0)
σ_{kl} = turbulent Prandtl number of kl (=1.2)
σ_ϵ = turbulent Prandtl number of ϵ (=1.217)

Superscript

$\bar{}$ = turbulent properties of Boussinesq part
$\tilde{}$ = turbulent properties of deviation part

$$\frac{\partial}{R_c\partial R_c}(R_c\rho Vkl)+\frac{\partial}{R_c\partial\theta_c}(\rho Wkl)+\frac{\partial}{\partial X_c}(\rho Ukl)$$
$$=\frac{\partial}{R_c\partial R_c}\left(R_c\Gamma_{kl}\frac{\partial kl}{\partial R_c}\right)+\frac{\partial}{R_c\partial\theta_c}\left(\Gamma_{kl}\frac{\partial kl}{R_c\partial\theta_c}\right)$$
$$+\frac{\partial}{\partial X_c}\left(\Gamma_{kl}\frac{\partial kl}{\partial X_c}\right)+C_b l\rho\bar{P}_k$$
$$-kl\left\{\frac{C_s k^{1/2}\rho}{l}+\frac{\rho C_l l\left[\left(\frac{\partial k}{\partial X_c}\right)^2+\left(\frac{\partial k}{\partial R_c}\right)^2+\left(\frac{\partial k}{R_c\partial\theta_c}\right)^2\right]}{k^{3/2}}\right\} \quad (9)$$

Note that the last term on the right-hand side of Eq. (9) is proposed by Shahaf et al. (1980) and is different from that in the original $k-kl$ model (Launder and Spalding, 1972).

(*iii*) The $k-\epsilon$ *w/*scm model

All equations are the same as those in the standard $k-\epsilon$ model, but the C_2 in ϵ Eq. (6) is substituted by $\hat{C}_2$ which accounts for both the recirculating and swirling effects. For recirculating flows, the Richardson number is defined as

$$\mathrm{R_{ic}}=\frac{k^2}{\epsilon^2}\frac{V_R}{R_{cu}^2}\frac{\partial}{\partial R_{cu}}(R_{cu}V_R) \quad (10)$$

where the resultant velocity, V_R, and the radius of curvature, R_{cu}, are defined as

$$V_R=(U^2+V^2)^{1/2} \quad (11)$$

$$R_{cu}=V_R^3\Big/\left[UV\left(\frac{\partial V}{\partial R_c}-\frac{\partial U}{\partial X_c}\right)+U^2\frac{\partial V}{\partial X_c}-V^2\frac{\partial U}{\partial R_c}\right] \quad (12)$$

For swirling flows, the corresponding Richardson number is defined as

$$\mathrm{R_{is}}=\left(\frac{W}{R_c^2}\right)\frac{\partial}{\partial R_c}(R_cW)\Big/\left\{\left(\frac{\partial U}{\partial R_c}\right)^2+\left[R_c\frac{\partial}{\partial R_c}\left(\frac{W}{R_c}\right)^2\right]\right\} \quad (13)$$

The modified constant $\hat{C}_2$ is given by the following equation (Srinivasan et al., 1983)

$$\hat{C}_2=C_2\exp(-\alpha_s\mathrm{R_{is}}-\alpha_c\mathrm{R_{ic}}) \quad (14)$$

(*iv*) The $k-\epsilon-A$ model

Besides the differential equations of k and ϵ, an algebraic Reynolds stress equation proposed by Rodi (1976) is used to replace the Boussinesq Eqs. (3).

$$\frac{\overline{u_iu_j}}{k}\left(-\overline{u_mu_n}\frac{\partial U_m}{\partial X_n}-\epsilon\right)=-\left(\overline{u_iu_m}\frac{\partial U_j}{\partial X_m}+\overline{u_ju_m}\frac{\partial U_i}{\partial X_m}\right)-\frac{2}{3}\delta_{ij}\epsilon$$
$$-C_{A1}\frac{\epsilon}{k}\left(\overline{u_iu_j}-\frac{2}{3}\delta_{ij}k\right)-C_{A2}\left[-\left(\overline{u_iu_m}\frac{\partial U_j}{\partial X_m}+\overline{u_ju_m}\frac{\partial U_i}{\partial X_m}\right)\right.$$
$$\left.+\frac{2}{3}\delta_{ij}\overline{u_mu_n}\frac{\partial U_n}{\partial X_m}\right] \quad (15)$$

After manipulation, the algebraic form of Reynolds stresses is obtained as below.

$$\overline{u_iu_j}-\frac{2}{3}\delta_{ij}k=k(1-C_{A2})\frac{\left(P_{ij}-\frac{2}{3}\delta_{ij}P_k\right)}{P_k+\epsilon(C_{A1}-1)} \quad (16)$$

Equations (5) and (6) are also used here to solve for k and ϵ except that $\bar{P}_k$ is substituted by $\bar{P}_k+\tilde{P}_K$ where $\tilde{P}_K$ is given in Appendix A.

The local effect of a rigid solid wall on the pressure strain correlation can be expressed through the modification of the constants C_{A1} and C_{A2} with the following relationships (Launder et al., 1975), respectively.

$$\hat{C}_{A1}=C_{A1}-0.125\frac{k^{3/2}}{\epsilon z_p} \quad (17)$$

$$\hat{C}_{A2}=C_{A2}-0.015\frac{k^{3/2}}{\epsilon z_p} \quad (18)$$

where z_p is the distance between the node point and its neighboring wall.

In the present calculations the Reynolds stresses are decomposed into a Boussinesq part, defined by Eqs. (3) and representing the standard $k-\epsilon$ formulation, and a deviation part. This is done to facilitate the comparison with the original $k-\epsilon$ model, and to reduce the numerical instability inherent from the nonlinearity of the governing equations. Note that the above decomposition allows a portion of the Reynolds stresses to be inserted into the diffusion terms of the momentum equations rather than the entire quantity being incorporated into the source terms. The resulted coefficient matrix is found to be more diagonally dominant and, therefore, to converge more quickly, as illustrated by Fig. 2.

$$-\overline{u_iu_j}=(-\overline{u_iu_j})_B+(-\overline{u_iu_j})_d \quad (19)$$

The 6 nonlinear algebraic equations for $(u_iu_j)_d$ are listed in Appendix A.

Boundary Conditions. The above set of three-dimensional differential equations are elliptic in nature, and therefore require that boundary conditions be specified on all surfaces surrounding the flow field.

(i) Symmetry planes ($\theta_c=0$ deg and $\theta_c=90$ deg)

$$\frac{\partial U}{\partial\theta_c}=\frac{\partial V}{\partial\theta_c}=\frac{\partial k}{\partial\theta_c}=\frac{\partial\epsilon}{\partial\theta_c}\left(\text{or }\frac{\partial kl}{\partial\theta_c}\right)=0;\ W=0 \quad (20)$$

(ii) Exit plane

$$\frac{\partial U}{\partial X_c}=\frac{\partial k}{\partial X_c}=\frac{\partial\epsilon}{\partial X_c}\left(\text{or }\frac{\partial kl}{\partial X_c}\right)=0;\ V=W=0 \quad (21)$$

The location of the downstream boundary is determined both by measured results and by computational tests. In fact, the computational tests showed that there was no noticeable change in the computed flow field as long as the location of the exit plane was far enough to allow the flow to become unidirectional.

(iii) Inlet plane

There are two categories of inlet conditions that are considered in the present work: the measured and the assumed inlet conditions. For the former case, the distributions of the mean velocity and turbulent kinetic energy at the inlet ports are taken directly from LDV measurements Liou and Wu (1986), while for the latter case, the mean velocity profile is assumed to be uniform and the turbulent intensity has a constant value of 0.015. For both cases the inlet profiles of ϵ and kl are deduced from the uniform turbulent length scale $(k^{3/2}/\epsilon)$ which is estimated to be 0.5 percent of the inlet width.

(iv) Walls

These turbulence models are not valid in the viscous sublayer where molecular diffusion is greater than turbulent diffusion. In addition, the steep change of flow properties in the wall region requires an extremely fine grid distribution and tends

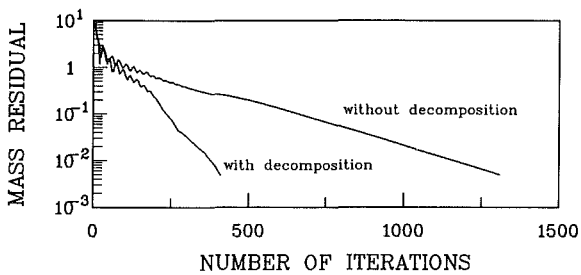

Fig. 2 A comparison of convergence rate for the computations with and without decomposition of Reynolds stresses

to make the computational effort impractical. Therefore, in this study the flow properties in the near-wall region are simulated by the two-zone model, i.e., a viscous sublayer model and fully turbulent zone model, and wall-functions (Launder and Spalding, 1974) are used to bridge these models. The wall function approach consists of the assumption that at those grid points nearest to the solid wall, or at a distance y_p (3 mm in this study) normal to the solid wall but outside the viscous sublayer, the velocity component parallel to the wall (V_p) obeys the logarithmic law of the wall:

$$V_p/(\tau_w/\rho)^{1/2}=\frac{1}{\kappa}\ln[E\cdot y_p\cdot(\tau_w/\rho)^{1/2}/\nu] \tag{22}$$

and the assumption that at the same location the production of k is in equilibrium with dissipation of k. If k_p and ϵ_p are the k and ϵ at the $y=y_p$, then it can be shown that the conditions imposed on the k equation and the ϵ equation instead of solid-wall boundary conditions are:

$$k_p=(\tau_w/\rho)/C_\mu^{1/2} \tag{23}$$

$$\epsilon_p=(\tau_w/\rho)^{3/2}/\kappa y_p \tag{24}$$

Solution Procedure. Figure 1 shows the grid arrangement for all scalar variables. A staggered grid system is employed. The total flux (convective plus diffusive) across the control volume boundary is approximated by the Power-law scheme (Patankar, 1980). Although the $k-\epsilon-A$ model appears attractive for accounting for effects of rotation and streamline curvature (Pletcher, 1988), it should be mentioned that to reduce numerical diffusion associated with the one-dimensional power-law discretization scheme, as large cross-flow gradients exist and the flow cuts across the grid lines at a large angle (Raithby, 1976), the finite difference scheme SCSUDS (Smoothed Hybrid Central/Skew Upstream Difference Scheme) proposed by Liou et al. (1990a) will be adopted in the future study of turbulent flow field in a simulated combustor with axial and side inlets.

To account for the nonlinear coupling between the pressure and velocity field, an iterative scheme based on the SIMPLE (Semi-Implicit Pressure-Linked equations) algorithm (Patankar and Spalding, 1972) is used. The integrated finite-difference equation system is solved by repeated alternate line sweep in all coordinate directions. At each line, a line by line TDMA (Tri-Diagonal Matrix algorithm) is used. To solve the system of nonlinear algebraic equations deduced from the algebraic Reynolds stress model, a global convergent secant method employing Broyden update with an analytical Jacobian matrix (Dennis and Schuahel, 1983) is used with subiterations. Further iterations are needed until the continuity and momentum equations are simultaneously satisfied to the requisite degree of accuracy. The maximum tolerance of the nondimensionalized mass and momentum residuals is mostly 0.005. The k and ϵ equations (or kl) are also solved line by line simultaneously with the mean velocity distribution. To prevent numerical instability, the flow variables are underrelaxed. The underrelaxation factors are 0.5 for U, V, W, k, ϵ, μ_t, and 0.3 for P, $\overline{(u_iu_j)}_d$, respectively.

The calculations were made using a $9\times10\times40$ grid (Fig. 1) in the radial, azimuthal, and axial directions, respectively. A larger number of grid points were placed in the areas where steep variations in velocities were revealed from the previous experimental results. To ensure grid independence, solutions were calculated using different grid sizes of $6\times8\times28$, $9\times10\times40$, $16\times14\times54$, and $18\times20\times80$. Less than 27, 5 and 2 percent (relative to the local U of $18\times20\times80$) differences in the computed results were found between grid sizes of $6\times8\times28$ and $18\times20\times80$, $9\times10\times40$ and $18\times20\times80$, $16\times14\times54$ and $18\times20\times80$, respectively. However, the maximum error (5 percent) between grid systems of $9\times10\times40$ and $18\times20\times80$ is only restricted to the narrow region around

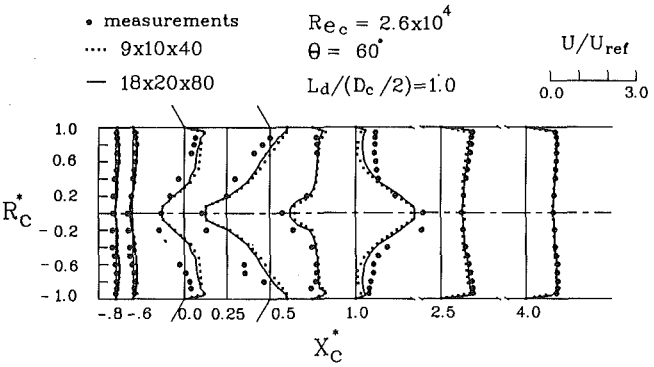

Fig. 3 An example of grid independence test

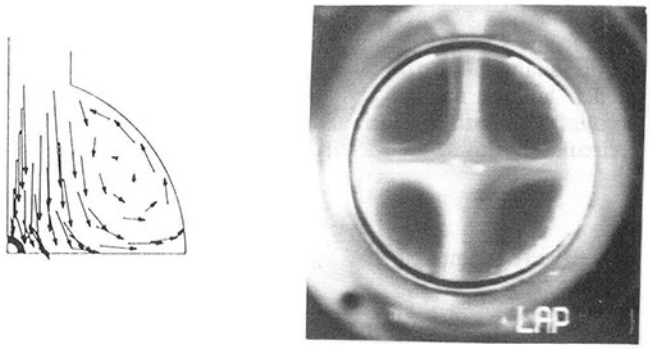

Fig. 4 (*a*) Vector plot of azimuthal flow structure at $X_c^*=0.25$; (*b*) the corresponding flow-visualization photograph (Wu, 1990)

$X_c^*=0.5$, as shown by Fig. 3 which is plotted using Richardson Extrapolation between the two grid resolutions. In addition, the computational time for $9\times10\times40$ is much more economical than for $16\times14\times54$. Consequently, the grid size of $9\times10\times40$ was chosen in the present work. Typically, convergence required 400 iterations for the $k-\epsilon$ model, and the corresponding CPU time on a CDC-CYBER 180/840 computer system was about 0.75 hours. The CPU time for the $k-\epsilon$ w/ scm, $k-kl$, and $k-\epsilon-A$ models was typically of 0.6, 1.5, and 4.5 hours, respectively.

Results and Discussion

The experimental conditions of Liou and Wu (1988), are used in the present computations ($R_e=2.6\times10^4$, $\rho=1.18$ Kg/m^3, $U_{ref}=4.15$ m/s, $D=0.1$m, $\mu=1.88\times10^{-5}$ Kg/m•s). Because the inlet ducts are located symmetrically about two diametrical planes which are perpendicular to each other, only one quarter of the configuration is solved for (Fig. 1).

Flow Pattern. In this section, the calculations are based on the $k-\epsilon$ turbulence model. Figure 4(*a*) shows the calculated streamwise vortex, generated by the jet-jet impingement in a quarter of the configuration at $X_c^*=.25$, i.e., the cross sectional plane passing through the centers of the intake ports. Figure 4(*b*) is the smoke flow-visualization photograph at the same plane taken by Wu (1990) using a laser light-sheet method. The camera was located in front of head plate ($X_c^*=-1.0$) and aligned along the duct axis. It is seen that the actual flow is rather symmetric and the qualitative agreement between Fig. 4(*a*) and Fig. 4(*b*) is reasonably good. Consequently, the symmetric predictions of the present work appear justified.

To display the three-dimensional nature of the flow, the computed contours of the mean axial and azimuthal velocities and turbulent kinetic energy at various X_c^* stations are plotted in Fig. 5. The jet-jet impingement occurs at $X_c^*=0.46$. The locations of peak U/U_{ref} at various X_c^*, as shown in Fig. 5(*a*), clearly reveal the three-dimensional spiraling flow both upstream and downstream of $X_c^*=0.46$. Similar behavior can

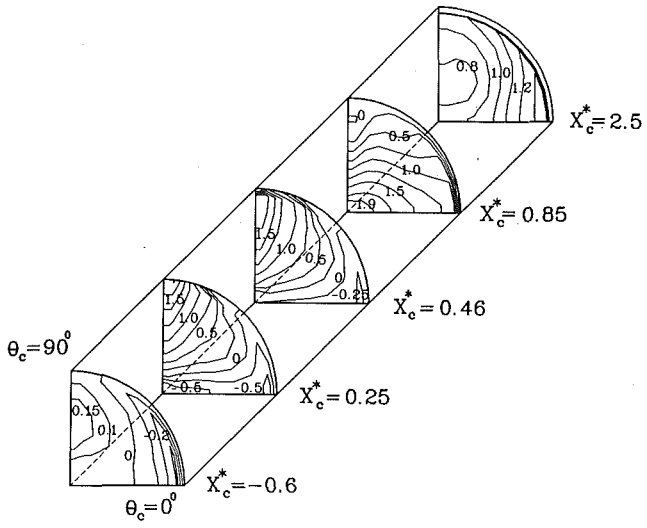

Fig. 5(*a*) U/U_{ref} contour at various axial stations

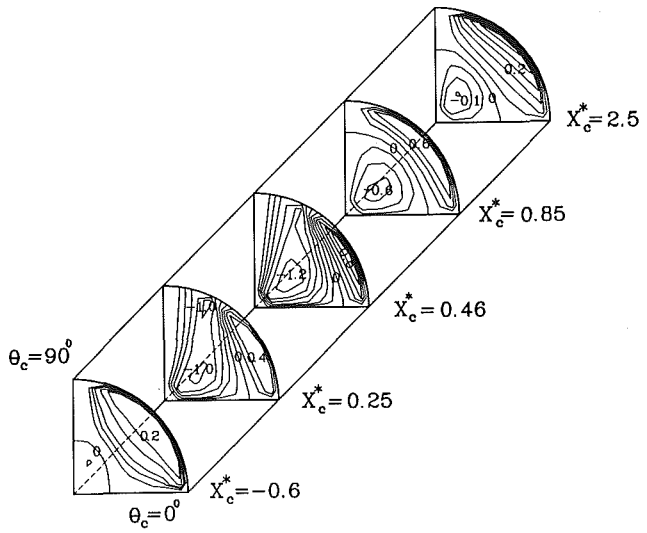

Fig. 5(*b*) W/U_{ref} contour at various axial stations

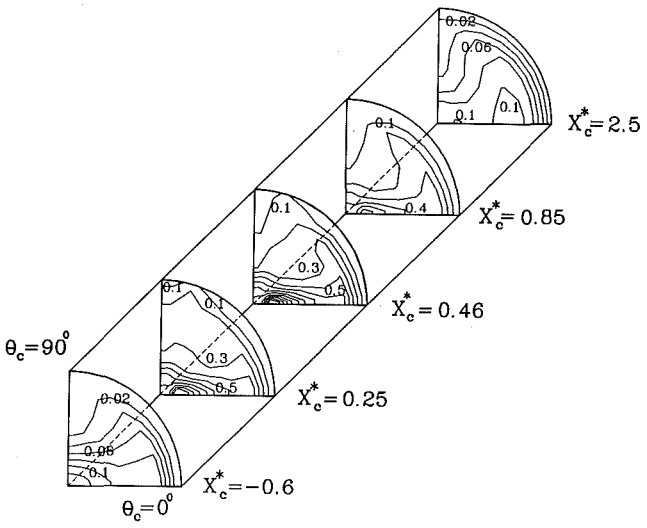

Fig. 5(*c*) k/U^2_{ref} contour at various axial stations

also be characterized in terms of the variation of the streamwise vortex center with X_c^* shown n Fig. 5(*b*). Figure 5(*c*) further indicates that around the jet impingement zone ($0 < X_c^* < 0.5$) that high turbulent kinetic energy levels prevail only at $R_c^* \approx 0.2$

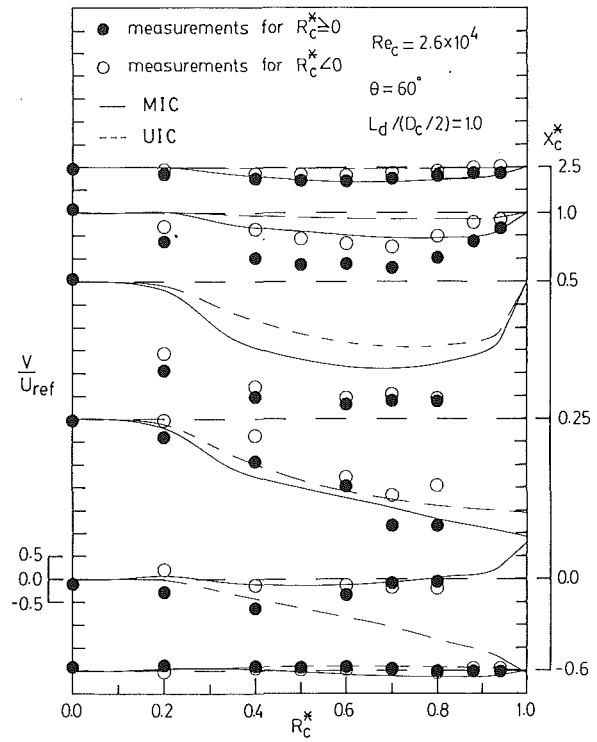

Fig. 6 Calculated and measured profiles of mean radial velocity at various X_c^* for $\theta_c = 90$ deg (Experimental uncertainty reported in (Liou and Wu 1988)

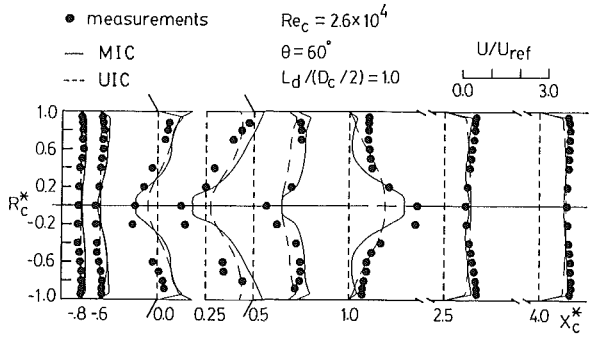

Fig. 7 Calculated and measured profiles of mean axial velocity at various X_c^* for $\theta_c = 90$ deg

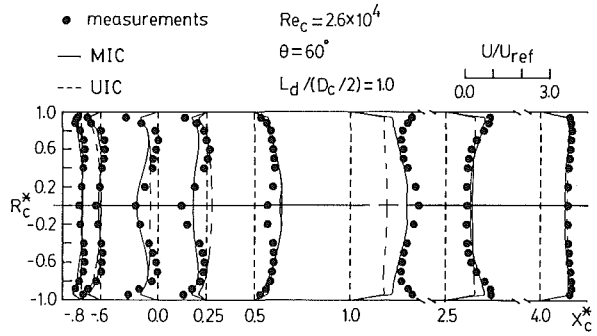

Fig. 8 Calculated and measured profiles of mean axial velocity at various x_c^* for $\theta_c = 0$ deg

in the $\theta_c = 0$ deg plane and the maximum value of k can be as high as 120 percent of U^2_{ref} at ($X_c^* = 0.46$). Further downstream and upstream, the region where local maximum k appears move toward the duct wall and axis, respectively, and the turbulent energy levels are much smaller.

Figure 6 displays calculated and measured mean radial velocity at various X_c^* for $\theta_c = 90$ deg. The calculated and measured streamwise mean velocity distributions at $\theta_c = 90$ deg and $\theta_c = 0$ deg planes are displayed in Fig. 7 and Fig. 8, respectively.

These figures indicate that the streamwise mean velocity in the head region is much smaller than those of other regions in the duct. The same observation can also be made for the radial mean velocity shown in Fig. 6. This low velocity in the head region ensures ready anchorage for the flame. Note that a comparison between the calculated results based on the measured inlet condition (MIC) and the assumed uniform inlet condition (UIC) is depicted in Figs. 6, 7, and 8, and will be discussed in a later section.

Figures 7 and 8 further show that the counterrotating vortices with their vortex axes perpendicular to the $X_c^* - R_c^*$ planes are mainly generated in the impingement region ($0 < X_c^* < 0.5$) and decay toward the head plate. These vortices obviously enhance mixing and are driven by the upstream bifurcating flow of the jet-jet impingement and by the shear of the inlet jets. Additionally, Figs. 6–8 suggest that the flow tends to become unidirectional at about four times the duct diameter, downstream.

Comparison of Turbulence Models. A comparison of mean velocity profiles between measurements and predictions obtained with several turbulence models is shown in Figs. 9 through 11. Note that the measured data for $R_c^* < 0$ have been plotted together with those for $R_c^* \geq 0$. Discrepancies between predicted and measured profiles are partly due to inaccuracies in the specification of the inlet conditions. In order to mount the rectangular inlet duct on the cylindrical combustion chamber, a 20-mm-thick flange was needed (Liou and Wu, 1986). However, the position of the flange made the LDV measurements at the inlet plane impossible. Consequently, the inlet velocity profiles used for calculations were actually measured at a plane of 20 mm above the inlet plane. Figure 9 reveals significant overprediction of the negative radial mean velocity and thus the entrainment of the intake jet at $\theta_c = 90$ deg plane by the $k-kl$ and $k-\epsilon$ w/scm models. In addition, the results of streamwise mean velocity shown in Fig. 9 further displays that the $k-kl$ and $k-\epsilon$ w/scm models predict a too strong recirculating flow with extraordinarily large centerline mean velocity which indicates a too strong upstream bifurcating flow of the jet-jet impingement. For the intake-jet region at $X_c^* = 0.25$, Fig. 10 demonstrates that the results predicted by these turbulence models differ little. It is believed that the convective transport overwhelms the diffusive transport in the intake-jet region and, therefore, the choice of individual turbulence model results in no difference. Figure 10 also shows that the mean radial jet velocity monotonically decreases from the inlet jet velocity to zero as the intake jet flows from the intake port to the impingement plane. It should be mentioned that a comparison of measured data between $R_c^* < 0$ and $R_c^* \geq 0$ reveals some degree of asymmetry in the jet-jet impingement region. As the flow proceeds further downstream, Fig. 11 shows that the $k-kl$ and $k-\epsilon$ w/scm models still overpredict the jet entrainment and centerline mean velocity of the downstream bifurcating flow.

Because large discrepancies between the measured mean velocity data and the results predicted with the $k-kl$ and $k-\epsilon$ w/scm turbulence models were found around the centerline, a further comparison of the measured and predicted turbulent kinetic energy profiles along the centerline is shown in Fig. 12. All the profiles, except the one obtained by using the $k-kl$ model, depict a maximum in the jet impingement region ($0 < X_c^* < 0.5$) and a decay toward the head plate and toward the far downstream end. This trend is physically appropriate, since jet-jet impingement results in a steep variation of the velocity field and, therefore, high turbulent kinetic energy. The decay of the turbulent kinetic energy is due to retardation caused by the presence of the head plate in the head region and due to the tendency toward a unidirectional flow for $X_c^* \geq 4.0$. Quantitatively, the $k-kl$, $k-\epsilon$ w/scm, $k-\epsilon$, and $k-\epsilon-A$ models underpredict the measured peak value of k/U_{ref}^2 by 110, 95, 50, and 8 percent, respectively. In summary,

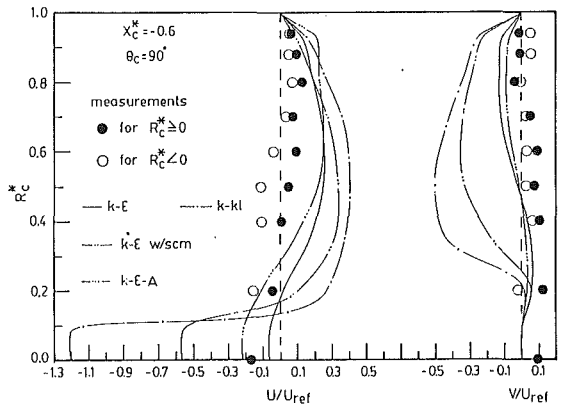

Fig. 9 Calculated and measured profiles of mean radial and streamwise velocities at $X_c^* = -0.6$ for $\theta_c = 90$ deg

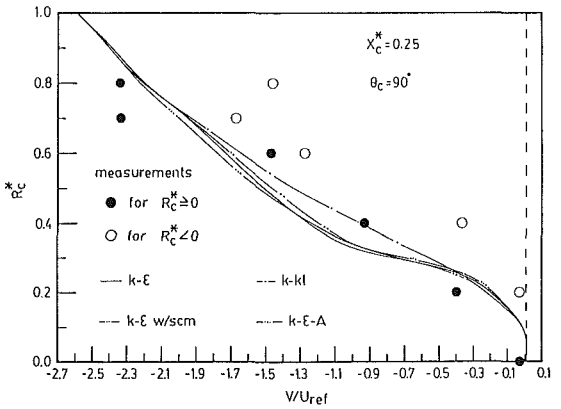

Fig. 10 Calculated and measured profiles of mean radial velocity at $X_c^* = 0.25$ for $\theta_c = 90$ deg

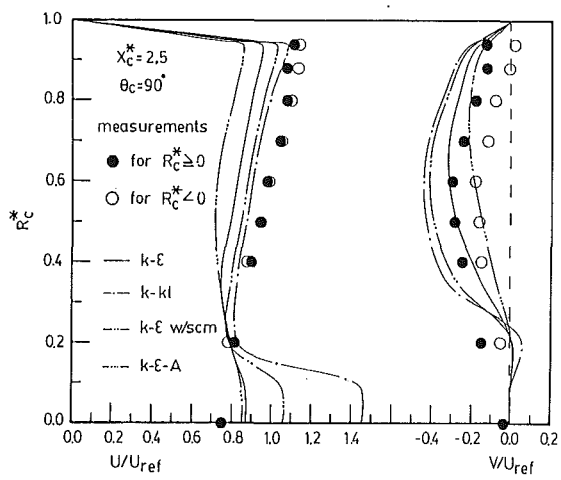

Fig. 11 Calculated and measured profiles of mean radial and streamwise velocities at $X_c^* = 2.5$ for $\theta_c = 90$ deg

among the turbulence models tested the best agreement with the measured k/U_{ref}^2, especially in the jet-jet impingement region and in the head region of multi-vortices, is obtained by using the $k-\epsilon-A$ model which gives an overall discrepancy within 10 percent.

Additionally, the centerline distribution of k/U_{ref}^2 predicted by using the $k-kl$ model displays three maxima, i.e., at $X_c^* = -0.8$, 0.25, and 3.2, as shown in Fig. 12. This distribution fails to follow the measured trend and is not consistent with the physical conjecture mentioned above. The poor performance of the $k-kl$ model in predicting the present three-dimensional flow field and the two-dimensional flow field mentioned in the Introduction may be attributed to the in-

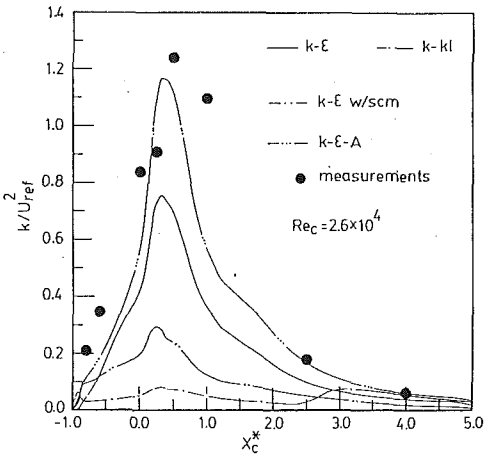

Fig. 12 Calculated and measured turbulent kinetic energy along the centerline

appropriate modification made by Shahaf et al. (1980). In addition, the poor results obtained by the $k-\epsilon$ w/scm model may partly be due to the fact that the predictions using the streamline curvature modification, proposed by Srinivasan et al. (1983) and subsequently applied by Cherng et al. (1988) to a ramjet combustor, have recently been found more suitable for high swirl flows (Cherng, 1990). Consequently, the choice of different turbulence models does significantly affect the computed axial mean velocity as illustrated in Figs. 9 and 11.

From the results presented and discussed above, it is concluded that the $k-\epsilon$ and $k-\epsilon-A$ models are obviously superior to the $k-kl$ and $k-\epsilon$ w/scm models in predicting the confined impinging flow field. Furthermore, the $k-\epsilon-A$ model provides better agreement with the measured data than the $k-\epsilon$ model for the flow field investigated, although both models reasonably predict the qualitatively trend. Because the calculated k by using the $k-\epsilon-A$ model is more accurate than using the $k-\epsilon$ model, the $k-\epsilon-A$ model should be more suitable for simulating the flow characteristics in the regions, such as the head region, where the diffusion effect is more prevalent ($\mu_t=\rho k^2/\epsilon$) due to low mean velocity. To show this point, Figs. 13(b), (c) and 14(b), (c) display the calculated mean flow pattern using the $k-\epsilon-A$ (Liou and Hwang, 1989) and $k-\epsilon$ models for the combustor conditions of Stull et al. (1983) mentioned in the Introduction, i.e., with water properties at a Reynolds number of 2.675×10^5. The vector plots in Fig. 13 depict the swirling motion in the cross-sectional plane of inlet jets where convective effects are prevalent. The predictions of both models are in excellent accord with the corresponding flow visualization photograph of Stull et al. (Fig. 13(a)). There is very little difference between Fig. 13(b) and Fig. 13(c). However, the counter-clockwise recirculating flow structure in the low-speed head region of the $\theta_c=180$ deg plane is more intact and more close to the flow-visualization photograph (Fig. 14(a)) as predicted by the $k-\epsilon-A$ model (Fig. 14(c)) than as predicted by the $k-\epsilon$ model (Fig. 14(b)). These differences are attributed to the ability of the $k-\epsilon-A$ model in accounting for effects of rotation and streamline curvature as mentioned previously in the Solution Procedure. Note that the recirculating fluids in the $\theta_c=180$ deg plane result from two turns of inlet jets. Jet-Jet impingement gives the flow a turn from $\theta_c=90$ deg plane to $\theta_c=180$ deg plane. A subsequent turn occurs in the $\theta_c=180$ deg plane, due to the deflection of spreadout flow of jet-jet impingement by the chamber wall.

Effect of Inlet Velocity Profile. In the present work, two inlet velocity profiles, MIC and UIC, are studied. The calculated results corresponding to these two inlet-velocity profiles are compared with the measured data in Figs. 6 to 8, 15, and 16. From Fig. 6, the radial mean velocities at most X_c^* stations predicted with UIC are smaller than those predicted with MIC. Two opposite trends are found from these two calculations at $X_c^*=0.0$ and near $R_c^*=1.0$. The reason is because that the calculation with UIC fails to account for flow retardation and separation occurring in the inlet duct and near the upstream edge of the inlet port as reported in Liou and Wu (1986). Furthermore, the radial mean-velocity profiles at $X_c^*=2.5$ (Fig. 6) indicate that the flow investigated can attain

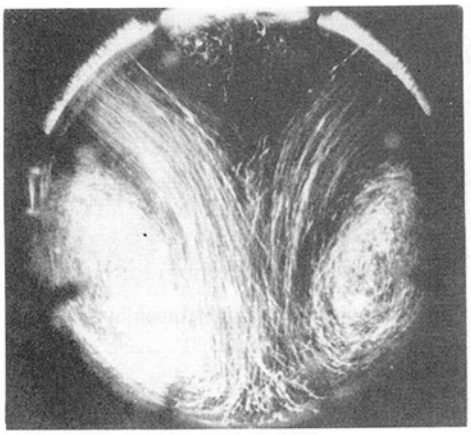

Fig. 13(a) Flow visualization photograph of Stull et al. (1985)

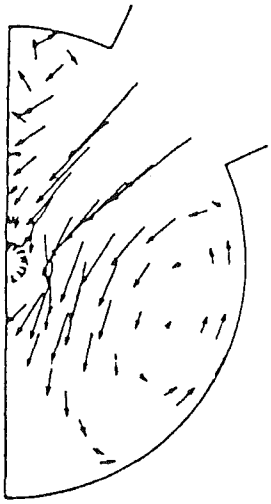

Fig. 13(b) Computational result with the $k-\epsilon$ turbulence model

Fig. 13(c) Computational result with the $k-\epsilon-A$ turbulence model

Fig. 14(*a*) Flow visualization photograph of Stull et al. (1985)

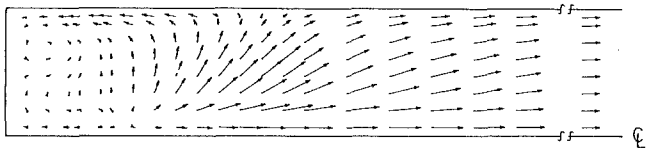

Fig. 14(*b*) Computational result with the $k-\epsilon$ turbulence model

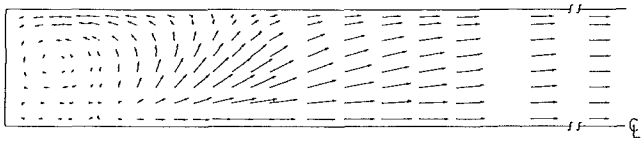

Fig. 14(*c*) Computational result with $k-\epsilon-A$ turbulence model

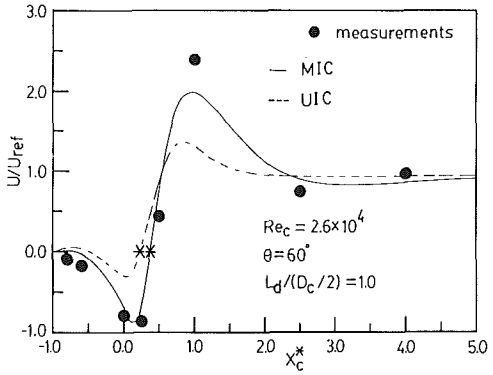

Fig. 15 Calculated and measured centerline distributions of streamwise mean velocity

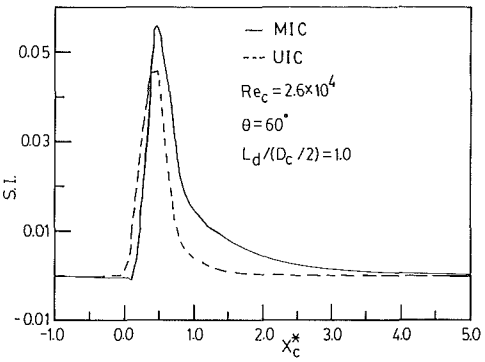

Fig. 16 Calculated swirl intensity distributions

unidirectionality earlier if the inlet flow has a uniform profile. This fact is because the radial component of the inlet jet is smaller for the assumed uniform profile than for the measured profile, as shown in Figs. 6. The positions of impinging stagnation points (denoted as * in Fig. 15), defined as the point dividing the upstream and downstream bifurcating flows at the centerline, also support the above observation. Additionally, the swirl intensity (SI) (Fig. 16), which is defined as the ratio of the axial flux of the swirling mean kinetic energy at a given X_c^* to the flux of the total mean kinetic energy at the inlet and is a useful parameter to characterize the circumferential motion, is weaker and has a more confined distribution for the UIC case than for the MIC case. The swirling motion vanishes at about $X_c^* = 2.0$ and $X_c^* = 4.0$ for the UIC and MIC cases, respectively. This result further supports the conclusion made above that the flow investigated tends to become unidirectional more quickly if the inlet flow has a uniform profile. Nevertheless, from the point of view of validating both the turbulence models and numerical schemes, the measured inlet velocity profile should be used, as can be seen from Figs. 6–8 and 15.

Conclusions

In this study, the $k-\epsilon$, $k-\epsilon$ w/scm, $k-\epsilon-A$, and modified $k-kl$ turbulence models have been used to predict three-dimensional confined impinging flows. The predicted results have also been compared with LDV measured data and flow visualization photographs. The comparison reveals that the $k-\epsilon-A$ model is the most satisfactory in predicting the vortex structure in the head region, which is important to predicting flame anchorage, combustion instability, and turbulent kinetic energy distribution. Quantitatively, an overall discrepancy less than 10 percent in predicting the turbulent kinetic energy along the centerline is achieved by using the $k-\epsilon-A$ model. In addition, realistic inlet velocity profiles and turbulence quantities are crucial to the accuracy of the flow field simulation. In the present work, it is found that the flow investigated tends to attain unidirectionality more quickly if the inlet flow has a uniform profile. Finally, the decomposition of $\overline{u_i u_j}$ into a Boussinesq and deviation part in implementing the algebraic stress model is found to promote the numerical stability and save the computing time.

Acknowledgment

Support for this work was partially provided by the National Science Council of the Republic of China under contract NSC-80-0401-E007-02.

References

Cherng, D. L., Yang, V., and Kuo, K. K., 1988, "Simulations of Three-Dimensional Turbulent Reacting Flows in Solid-Propellant Ducted Rocket Combustors," AIAA paper 88-3042, July.

Cherng, D. L., Private Communication, 1990.

Choudhury, P. R., 1982, "Characterization of a Side Dump Gas Generator Ramjet," AIAA paper 82-1258, Jan.

Dennis, J. E. Jr., and Schnahel, R. B., 1983, *Numerical Methods for Unconstrained Optimization and Nonlinear Equations*, Prentice-Hall, NJ.

Hwang, Y. H., 1989, *Theoretical Analysis on Flow Fields in Side-Inlet Dump Combustors*, PhD. thesis, Department of Power Mechanical Engineering, National Tsing Hua University, Hsin-Chu, Taiwan.

Launder, B. E., Reece, G. J., and Rodi, W., 1975, "Progress in the Development of a Reynolds Stress Turbulence Closure," *Journal of Fluid Mechanics*, Vol. 68, Part 3, pp. 537–566.

Launder, B. E., and Spalding, D. B., 1972, *Lectures in Mathematical Model of Turbulence*, Academic Press, London.

Launder, B. E., and Spalding D. B., 1974, "The Numerical Computation of Turbulent Flows," *Computer Methods in Applied Mechanics and Engineering*, Vol. 3, pp. 269–289.

Liou, T. M., Chang, Y., and Hwang, D. W., 1990a, "Experimental and Computational Study of Turbulent Flows in a Channel with Two Pairs of Turbulence Promoters in Tandem," ASME JOURNAL OF FLUIDS ENGINEERING, Vol. 112, pp. 302–310.

Liou, T. M., and Hwang, Y. H., 1989, "Calculation of Flow Fields in Side-Inlet Ramjet Combustor with an Algebraic Reynolds Stress Model," accept by *Journal of Propulsion and Power*.

Liou, T. M., and Wu, S. M., 1986, "Application of Laser Velocimetry to the Curved Inlet Duct of a Side Dump Combustor," *Third International Symposium on Application of Laser-Doppler Anemometry to Fluid Mechanics*, Ladon-Instituto Superior Tecnico, July, pp. 9.3.1–9.3.6.

Liou, T. M., and Wu, S. M., 1988, "Flow Field in a Dual-Inlet Side-Dump Combustor," *Journal of Propulsion and Power*, Vol. 4, No. 1, Jan.

Liou, T. M., Wu, S. M., and Hwang, Y. H., 1990b, "Experimental and

Theoretical Investigation of Turbulent Flow in a Side-Inlet Rectangular Combustor," *Journal of Propulsion and Power*, Vol. 6, No. 2, pp. 131–138.

Nossier, N. S., and Behar, S., 1986, "Characteristics of Jet Impingement in a Side-Dump Combustor," *AIAA Journal*, Vol. 24, No. 11, pp. 1752–1757.

Patankar, S. V., 1980, *Numerical Heat Transfer and Fluid Flow*, Hemisphere Publishing Co., New York.

Patankar, S. V., and Spalding, D. B., 1972, "A Calculation Procedure for Heat, Mass, and Momentum Transfer in Three-Dimensional Parabolic Flows," *International Journal of Heat and Mass Transfer*, Vol. 15, pp. 1787–1806.

Pletcher, R. H., 1988, "Progress in Turbulent Forced Convection," ASME *Journal of Heat Transfer*, Vol. 110, pp. 1129-1144.

Raithby, G. D., "Skew Upstream Difference Schemes for Problems Involving Fluid Flow," *Computer Methods in Applied Mechanics and Engineering*, Vol. 9, pp. 153–164.

Rodi, W., 1976, "A New Algebraic Relation for Calculating the Reynolds Stresses," *ZAMM*, Vol. 56, T219–T221.

Shahaf, M., Goldman, Y., and Greenberg, J. B., 1980, "An Investigation of Impinging Jets in Flow with Sudden Expansion," *Proceedings of the 22nd Israel Annual Conference on Aviation and Astronautics*, Israel Ministry of Transport, Mar., pp. 100–106.

Srinivasan, R., Reynolds, R., Ball I., Berry, R., Johnson, K., and Mongia, H., 1983, "Aerothermal Modelling Program Phase I Final Report," NASA-CR-168243, Aug.

Stull, F. D., Craig, R. R., Streby, G. D., and Vanka, S. P., 1985, "Investigation of a Dual Inlet Side Dump Combustor Using Liquid Injection," *Journal of Propulsion and Power*, Vol. 1, No. 1, Jan., pp. 83–86.

Vanka, S. P., Stull, F. D., and Craig, R. R., 1983, "Analytical Characterization of Flow Field in Side Inlet Dump Combustor," AIAA paper 83-1399, June.

Vanka, S. P., Craig, R. R., and Stull, F. D., 1985, "Mixing, Chemical Reaction and Flow Field Development in Ducted Rockets," AIAA paper 85-1271.

Wu, S. M., 1990, "Investigation on Turbulence Structure in Dual-Inlet Side Dump Combustors Using a Two-Component Laser Doppler Velocimetry," PhD. thesis, Department of Power Mechanical Engineering, National Tsing Hua University, Taiwan.

APPENDIX A

The nonlinear equation of deviated Reynolds stress are given in the following:

$$\left[(\overline{u_r u_r})_d - 2\frac{\mu_t}{\rho}\left(\frac{\partial V}{\partial R_c}\right)\right][\tilde{P}_k + \overline{P}_k + \epsilon(C_{A1}-1)] - \left[\tilde{P}_{rr} + \overline{P}_{rr} - \frac{2}{3}(\tilde{P}_k + \overline{P}_k)\right](1-C_{A2})k = 0 \quad \text{(A1)}$$

$$\left[(\overline{u_r u_\theta})_d - \frac{\mu_t}{\rho}\left(\frac{\partial V}{R_c \partial \theta_c} + \frac{\partial W}{\partial R_c} - \frac{W}{R_c}\right)\right][\tilde{P}_k + \overline{P}_k + \epsilon(C_{A1}-1)] - (\tilde{P}_{r\theta} + \overline{P}_{r\theta})(1-C_{A2})k = 0 \quad \text{(A2)}$$

$$\left[(\overline{u_r u_x})_d - \frac{\mu_t}{\rho}\left(\frac{\partial V}{\partial X_c} + \frac{\partial U}{\partial R_c}\right)\right][\tilde{P}_k + \overline{P}_k + \epsilon(C_{A1}-1)] - (\tilde{P}_{rx} + \overline{P}_{rx})(1-C_{A2})k = 0 \quad \text{(A3)}$$

$$\left[(\overline{u_\theta u_\theta})_d - 2\frac{\mu_t}{\rho}\left(\frac{\partial W}{R_c \partial \theta_c} + \frac{V}{R_c}\right)\right][\tilde{P}_k + \overline{P}_k + \epsilon(C_{A1}-1)] - \left[\tilde{P}_{\theta\theta} + \overline{P}_{\theta\theta} - \frac{2}{3}(\tilde{P}_k + \overline{P}_k)\right](1-C_{A2})k = 0 \quad \text{(A4)}$$

$$\left[(\overline{u_\theta u_x})_d - \frac{\mu_t}{\rho}\left(\frac{\partial U}{R_c \partial \theta_c} + \frac{\partial W}{\partial X_c}\right)\right][\tilde{P}_k + \overline{P}_k + \epsilon(C_{A1}-1)] - (\tilde{P}_{\theta x} + \overline{P}_{\theta x})(1-C_{A2})k = 0 \quad \text{(A5)}$$

$$\left[(\overline{u_x u_x})_d - 2\frac{\mu_t}{\rho}\left(\frac{\partial U}{\partial X_c}\right)\right][\tilde{P}_k + \overline{P}_k + \epsilon(C_{A1}-1)] - \left[\tilde{P}_{xx} + \overline{P}_{xx} - \frac{2}{3}(\tilde{P}_k + \overline{P}_k)\right](1-C_{A2})k = 0 \quad \text{(A6)}$$

where

$$\tilde{P}_{rr} = -\left[2(\overline{u_r u_r})_d\left(\frac{\partial V}{\partial R_c}\right) + 2(\overline{u_r u_\theta})_d\left(\frac{\partial V}{R_c \partial \theta_c} - \frac{W}{R_c}\right) + 2(\overline{u_r u_x})_d\left(\frac{\partial V}{\partial X_c}\right)\right]$$

$$\tilde{P}_{r\theta} = -\left[(\overline{u_r u_r})_d\left(\frac{\partial W}{\partial R_c}\right) + (\overline{u_r u_\theta})_d\left(\frac{\partial W}{R_c \partial \theta_c} + \frac{V}{R_c} + \frac{\partial V}{\partial R_c}\right) + (\overline{u_r u_x})_d\left(\frac{\partial W}{\partial X_c}\right) + (\overline{u_\theta u_\theta})_d\left(\frac{\partial V}{R_c \partial \theta_c} - \frac{W}{R_c}\right) + (\overline{u_\theta u_x})_d\left(\frac{\partial V}{\partial X_c}\right)\right]$$

$$\tilde{P}_{rx} = -\left[(\overline{u_r u_r})_d\left(\frac{\partial U}{\partial R_c}\right) + (\overline{u_r u_\theta})_d\left(\frac{\partial U}{R_c \partial \theta_c}\right) + (\overline{u_r u_x})_d\left(\frac{\partial V}{\partial R_c} + \frac{\partial U}{\partial X_c}\right) + (\overline{u_\theta u_x})_d\left(\frac{\partial V}{R_c \partial \theta_c} - \frac{W}{R_c}\right) + (\overline{u_x u_x})_d\left(\frac{\partial V}{\partial X_c}\right)\right]$$

$$\tilde{P}_{\theta\theta} = -\left[2(\overline{u_r u_\theta})_d\left(\frac{\partial W}{\partial R_c}\right) + 2(\overline{u_\theta u_\theta})_d\left(\frac{\partial W}{R_c \partial \theta_c} + \frac{V}{R_c}\right) + 2(\overline{u_\theta u_x})_d\left(\frac{\partial W}{\partial X_c}\right)\right]$$

$$\tilde{P}_{\theta x} = -\left[(\overline{u_r u_\theta})_d\left(\frac{\partial U}{\partial R_c}\right) + (\overline{u_r u_x})_d\left(\frac{\partial W}{\partial R_c}\right) + (\overline{u_\theta u_\theta})_d\left(\frac{\partial U}{R_c \partial \theta_c}\right) + (\overline{u_\theta u_x})_d\left(\frac{\partial U}{\partial X_c} + \frac{\partial W}{R_c \partial \theta_c} + \frac{V}{R_c}\right) + (\overline{u_x u_x})_d\left(\frac{\partial W}{\partial X_c}\right)\right]$$

$$\tilde{P}_{xx} = -\left[2(\overline{u_r u_x})_d\left(\frac{\partial U}{\partial R_c}\right) + 2(\overline{u_\theta u_x})_d\left(\frac{\partial U}{R_c \partial \theta_c}\right) + 2(\overline{u_x u_x})_d\left(\frac{\partial U}{\partial X_c}\right)\right]$$

$$\tilde{P}_k = (\tilde{P}_{rr} + \tilde{P}_{\theta\theta} + \tilde{P}_{xx})/2$$

and

$$\overline{P}_{rr} = \frac{\mu_t}{\rho}\left[4\left(\frac{\partial V}{\partial R_c}\right)^2 + 2\left(\frac{\partial V}{R_c \partial \theta_c} - \frac{W}{R_c}\right)^2 + 2\left(\frac{\partial V}{\partial X_c}\right)^2 + 2\left(\frac{\partial W}{\partial R_c}\right)\left(\frac{\partial V}{R_c \partial \theta_c} - \frac{W}{R_c}\right) + 2\left(\frac{\partial U}{\partial R_c}\right)\left(\frac{\partial V}{\partial X_c}\right)\right]$$

$$\overline{P}_{r\theta} = \frac{\mu_t}{\rho}\left[2\left(\frac{\partial W}{\partial R_c}\right)\left(\frac{\partial V}{\partial R_c}\right) + \left(\frac{\partial W}{R_c \partial \theta_c} + \frac{V}{R_c} + \frac{\partial V}{\partial R_c}\right)\left(\frac{\partial V}{R_c \partial \theta_c} - \frac{W}{R_c} + \frac{\partial W}{\partial R_c}\right) + \left(\frac{\partial W}{\partial X_c}\right)\left(\frac{\partial U}{\partial R_c} + \frac{\partial V}{\partial X_c}\right) + 2\left(\frac{\partial V}{R_c \partial \theta_c} - \frac{W}{R_c}\right)\left(\frac{\partial W}{R_c \partial \theta_c} + \frac{V}{R_c}\right) + \left(\frac{\partial V}{\partial X_c}\right)\left(\frac{\partial W}{\partial X_c} + \frac{\partial U}{R_c \partial \theta_c}\right)\right]$$

$$\overline{P}_{rx} = \frac{\mu_t}{\rho}\left[2\left(\frac{\partial U}{\partial R_c}\right)\left(\frac{\partial V}{\partial R_c}\right) + \left(\frac{\partial U}{R_c \partial \theta_c}\right)\left(\frac{\partial V}{R_c \partial \theta_c} - \frac{W}{R_c} + \frac{\partial W}{\partial R_c}\right) + \left(\frac{\partial U}{\partial X_c} + \frac{\partial V}{\partial R_c}\right)\left(\frac{\partial U}{\partial R_c} + \frac{\partial V}{\partial X_c}\right) + \left(\frac{\partial V}{R_c \partial \theta_c} - \frac{W}{R_c}\right)\left(\frac{\partial U}{R_c \partial \theta_c} + \frac{\partial W}{\partial X_c}\right) + 2\left(\frac{\partial V}{\partial X_c}\right)\left(\frac{\partial U}{\partial X_c}\right)\right]$$

$$\overline{P}_{\theta\theta}=\frac{\mu_t}{\rho}\left[2\left(\frac{\partial W}{\partial R_c}\right)^2+4\left(\frac{\partial W}{R_c\partial\theta_c}+\frac{V}{R_c}\right)^2+2\left(\frac{\partial W}{\partial X_c}\right)^2+2\left(\frac{\partial W}{\partial R_c}\right)\left(\frac{\partial V}{R_c\partial\theta_c}-\frac{W}{R_c}\right)+2\left(\frac{\partial W}{\partial X_c}\right)\left(\frac{\partial U}{R_c\partial\theta_c}\right)\right]$$

$$\overline{P}_{\theta x}=\frac{\mu_t}{\rho}\left[\left(\frac{\partial U}{\partial R_c}\right)\left(\frac{\partial V}{R_c\partial\theta_c}-\frac{W}{R_c}+\frac{\partial W}{\partial R_c}\right)+\left(\frac{\partial W}{\partial R_c}\right)\left(\frac{\partial U}{\partial R_c}+\frac{\partial V}{\partial X_c}\right)+2\left(\frac{\partial U}{R_c\partial\theta_c}\right)\left(\frac{\partial W}{R_c\partial\theta_c}+\frac{V}{R_c}\right)+\left(\frac{\partial U}{\partial X_c}+\frac{\partial W}{R_c\partial\theta_c}+\frac{V}{R_c}\right)\left(\frac{\partial U}{R_c\partial\theta_c}+\frac{\partial W}{\partial X_c}\right)+2\left(\frac{\partial W}{\partial X_c}\right)\left(\frac{\partial U}{\partial X_c}\right)\right]$$

$$\overline{P}_{xx}=\frac{\mu_t}{\rho}\left[2\left(\frac{\partial U}{\partial R_c}\right)^2+2\left(\frac{\partial U}{R_c\partial\theta_c}\right)^2+4\left(\frac{\partial U}{\partial X_c}\right)^2+2\left(\frac{\partial U}{\partial R_c}\right)\left(\frac{\partial V}{\partial X_c}\right)+2\left(\frac{\partial W}{\partial X_c}\right)\left(\frac{\partial U}{R_c\partial\theta_c}\right)\right]$$

$$\overline{P}_k=(\overline{P}_{rr}+\overline{P}_{\theta\theta}+\overline{P}_{xx})/2$$

Velocity Characteristics of Multiple Impinging Jets Through a Crossflow

J. M. M. Barata

D. F. G. Durão

M. V. Heitor

Mechanical Engineering Department,
Instituto Superior Técnico,
Technical University of Lisbon,
1096 Lisbon Codex,
Portugal

The mean and turbulent velocity characteristics of the flowfield resulting from the impingement of two and three jets against a wall through a low-velocity crossflow are quantified in detail making use of a laser-Doppler velocimeter and are discussed together with the visualization of the flow. The experiments have been carried out for a velocity ratio between the jets and the crossflow of 30, for a Reynolds number based on the jet exit of 105,000, and for the jet exit five jet-diameters above the ground plate, and provided a basis to improve knowledge of several related complex flow fields in engineering applications. The results characterize the turbulent transport typical of multiple impinging flows associated with a large penetration of the impinging jets through a crossflow, and quantify the formation of fountain flows due to collision of consecutive wall jets. The turbulence measurements include those of Reynolds shear stress and identify large effects of flow distortion on the turbulence structure parameters that determine the empirical constants in engineering models of turbulence.

1 Introduction

The flow of single or multiple jets issuing into a confined crossflow is of great practical relevance in many situations, such as those typical of the discharge of exhaust gases or waste liquids, of the impingement cooling in a range of process industries and of the flowfield beneath a vertical/short take-off and landing, VSTOL, aircraft close to the ground. In this application the impingement height is usually in the range $1 < H/D < 6$ and the jet-to-crossflow velocity ratio, V_j/U_o, is always higher than 20 (e.g., Kotansky, 1981) and the consequent occurrence of jet-induced effects during hover and transition to horizontal flight include strong lift losses due to enhanced entrainment, which induces low pressure zones in the neighborhood of the jets (suckdown) and engine thrust losses following re-ingestion of the exhaust gases. In addition, the lifting jets impinge on the ground and the resulting wall jets collide to form a fan-shaped upwash flow which impinges on the fuselage resulting in a positive contribution to the lift force. However, the deflection of the fountain by a cross-wind may produce adverse pitch and roll moments, as identified by Gentry and Margason (1966) and Jenkins and Hill (1977), and affect the performance of the aircraft. Knowledge of the fountain upwash flow is therefore, essential to the successful development of VSTOL aircraft technology. Further, current needs to improve the performance of impingement cooling in industry and the high standards in aircraft technology require accurate prediction methodologies able to simulate the dependence of impingement and fountain flows upon geometrical and flow conditions. To achieve these objectives detailed measurements of the velocity characteristics of impinging jets in mutual interaction should be obtained and discussed. This paper is aimed to help to fulfil these requirements and presents a detailed analysis of two and three impinging jets through a crossflow giving rise to the formation of fountain flows.

Earlier detailed measurements of the mean and turbulent flow properties of multiple impinging jets are scarce and have been presented essentially in the absence of crossflow and using probe techniques. Examples include the works of Jenkins and Hill (1977), Kotansky and Glaze (1980), Kind and Suthanthiran (1980) and Gilbert (1983), which are limited in extent due to the difficulties associated with the use of pitot probes and hot films in complex 3-D flows. A laser Doppler velocimeter (e.g., Durst et al., 1981) meets the requirements of a non-intrusive technique with the ability to sense the direction of the instantaneous flow in turbulent recirculating regions, but only Saripalli (1987) reports laser-Doppler measurements, including those of shear stress, for twin axisymmetric impinging jets in the absence of crossflow. His results show that the regions of the flow where impingement and the fountain upwash flow occur are characterized by high turbulence levels with intensities up to 60 percent. The upwash flows are characterized by considerably large mixing growth rates compared to conventional turbulent shear flows and exhibit a linear rate of spread independent of the impingement height.

Measurements of impinging jets in the presence of a crossflow are even more scarce and have concentrated on single jets for large impinging heights (predominantly for $H/D > 10$), and for small jet-to-crossflow velocity ratios in the context of V/STOL technology. Examples include the works of Sugiyama and Usami (1975), Andreopoulos and Rodi (1984) and Shayesteh et al. (1985), which report hot-wire measurements for ratios H/D higher than 24 and for values of V_j/U_o respectively up to 1.96, 2 and 16. Kamotani and Greber (1972) present

Contributed by the Fluids Engineering Division for publication in the JOURNAL OF FLUIDS ENGINEERING. Manuscript received by the Fluids Engineering Division October 25, 1988. Associate Technical Editor: C. J. Freitas.

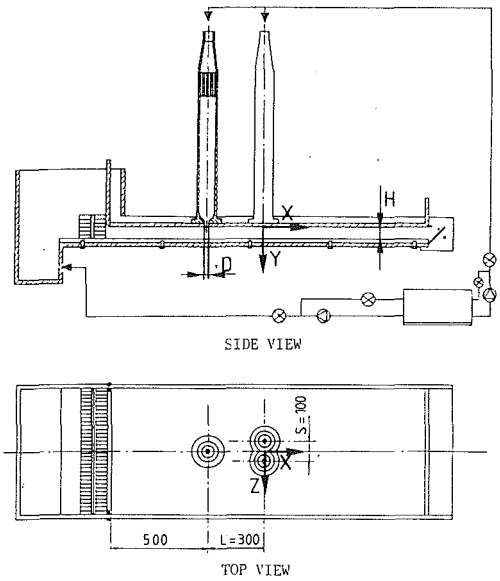

Fig. 1 Schematic diagram of flow configuration

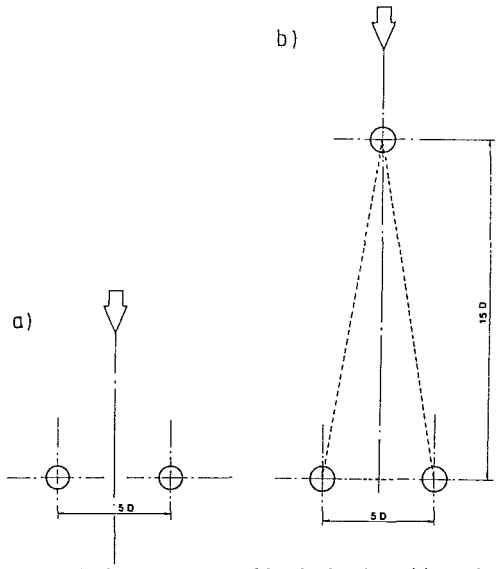

Fig. 2 Geometrical arrangement of impinging jets: (*a*) two-jet configuration; (*b*) three-jet configuration

results for $H/D = 12$ and Stoy and Ben-Hain (1973) give pitot tube measurements for values of H/D of 3 and for jet-to-crossflow velocity ratios up to 6.8. Only Crabb et al. (1981) report LDV measurements, but again for a single jet and for values of $H/D = 12$ and velocity ratios up to 2.3.

This paper is one of a series on turbulent impinging jets, which have first addressed the question of the lack of available data on impinging jets through a low-velocity crossflow for low impingement heights. The results for single jets were obtained for jet-to-crossflow velocity ratios in the range $30 \leq V_j/U_o \leq 73$ (which correspond to momentum ratios between 5 and 33) and for an impingement height of $H/D = 5$ (see Barata et al., 1991a and b) and have quantified the time-averaged vortex structure developed in this type of flows, as well as large effects of flow distortion on the turbulence structure parameters that determine the empirical constants in engineering models of turbulence. Here the analysis is extended to the flow resulting from the impingement of two and three jets on a ground plane set normally to the jet nozzle axis and located five jet diameters below the jet exits. The experiments were performed for a Reynolds number based on the jet exit conditions of $\mathrm{Re} = 105{,}000$ and for a jet-to-crossflow velocity rate of 30 and provide a basis for better understanding of several related but more complex practical flow fields.

The remainder of this paper includes three sections. The next section describes the experimental method, gives details of the flow configuration, of the laser-Doppler velocimeter and of the errors incurred in the measurements. Section 3 presents and discusses the results and section 4 summarizes the main findings and conclusions of this work.

2 Experimental Method

2.1 Flow Configuration and Measurement Procedure. The experiments were carried out in a horizontal water channel, 1.50m long and 0.5m wide, made of perspex, as shown schematically in Fig. 1. The apparatus was built to allow multi-jet impingement experiments with variable impinging heights, H, but in the present study two and three jets of 20mm exit diameter have been used at a fixed impingement height of five jet diameters. The crossflow duct extends 20D upstream and 55D downstream of the central upstream jet entry, which is located 12.5D from each side wall. The twin-jets are separated by 5D, Fig. 2, and are located 10D from the nearest side wall. Each jet unit comprises a 7 deg flow distributor for decelerating the flow, a settling chamber 0.56m long with a honeycomb and a set of screens to establish a uniform flow, and a nozzle with an area contraction ratio of 16 to provide a jet with an uniform potential core with a low turbulence intensity. The facility has a recirculating system whereby both jet and crossflow water are drawn from a discharge tank and pumped to a constant-head tank or supplied to each jet unit via control valves. The uniformity of the crossflow was ensured by straighteners and screens.

The origin of the horizontal, X, and vertical, Y, coordinates is taken at the center of the twin jets, in the upper wall of the tunnel: X is positive in the crossflow direction and Y is positive vertically downwards.

The present results were obtained for a jet exit velocity profile typical of a potential jet with a centerline mean velocity of 5.1m/s, giving rise to a Reynolds number based on jet exit conditions of 105,000. The nozzle exit turbulence intensity was measured to be approximately 2 percent (see Barata, 1989). The crossflow mean velocity was set to give rise to a velocity ratio between the jets and the crossflow of $V_j/U_o = 30$ for all the flows studied: the resulting momentum ratio was equal to

Nomenclature

D = diameter of the jet
H = height of the crossflow channel
k = turbulent kinetic energy
L = distance between the center of the jets along longitudinal direction
Re = Reynolds number, $\mathrm{Re} = V_j D/\nu$
S = distance between the center of the jets along transversal direction
U = horizontal velocity, $U = \overline{U} + u'$
V = vertical velocity, $V = \overline{V} + v'$
X = horizontal coordinate (positive in the direction of the crossflow)
Y = vertical coordinate (positive in the direction of the jet flows, i.e., downwards)
Z = transverse coordinate (zero at central plane; positive in the direction towards the lateral walls)
ν = kinematic viscosity

Subscripts

j = jet-exit value
o = crossflow value

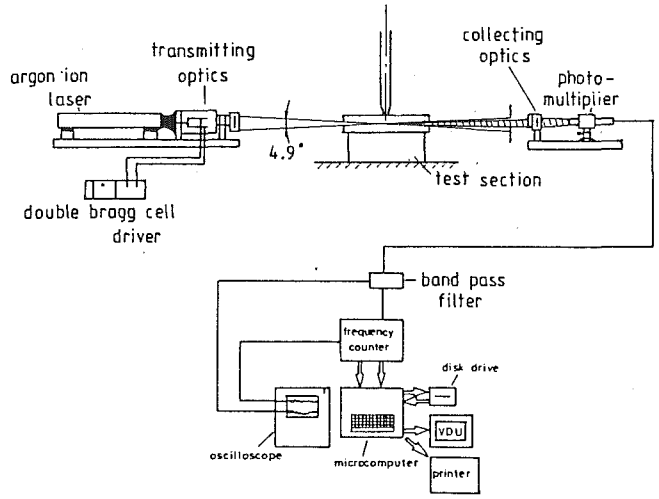

Fig. 3 Diagram of laser-Doppler velocimeter

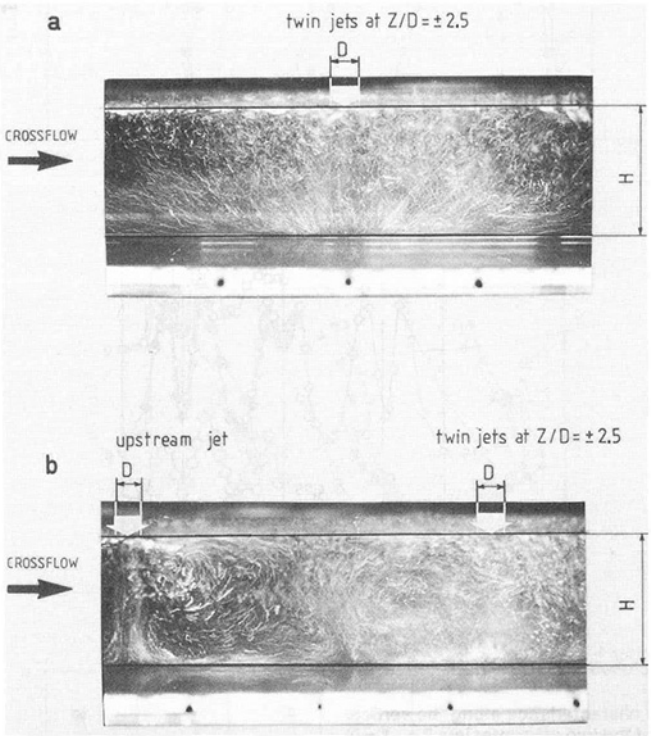

Fig. 4 Visualization of the fountain upwash flow in the vertical plane of symmetry for $Re_j = 105{,}000$, $H/D = 5$, $V_j/U_o = 30$: (*a*) two-jet case, $S/D = 5$; (*b*) three-jet case, $S/D = 5$, $L/D = 15$

5.65. Measurements obtained in the crossflow without the jets have shown that the wall boundary layer in the jet impingement regions has a uniform thickness around 10mm. The uniform velocity of the external stream of 0.17m/s and the local turbulence intensity was about 18 percent. This is due to the straighteners and screens used to uniformize the flow and do not affect the turbulent structure of the impingement and fountain regions, as analyzed in detail by Barata (1989).

2.2 Experimental Techniques. Flow visualization has been conducted using air bubbles as tracer particles or by introducing a fluorescent dye into the jet flow. Illumination of the flow was achieved by a sheet of light, about 2mm thick, obtained by spreading a laser beam (Argon-ion, 2W, at 488nm) with a cylindrical lens.

The velocity field was measured by a dual-beam, forward-scatter laser velocimeter, Fig. 3, which comprised an argon-ion laser operated at a wavelength of 514.5nm and a nominal power of around 1W, sensitivity to the flow direction provided by light-frequency shifting from acousto-optic modulation (double Bragg cells), a 310mm focal length transmission lens and forward-scattered light collected by a 150mm focal lens at a magnification of 0.76. The half-angle between the beams was 3.48 deg (4.64 deg in air) and the calculated dimensions of the measuring volume at the e^{-2} intensity locations were 2.225 and 0.135mm. The horizontal, U, and vertical, V, mean and turbulent velocity components were determined by a non-commercial frequency counter interfaced with a microprocessor, as described by Heitor et al. (1984). The fluctuating velocity components were also used, together with those at 45 deg, to compute the local shear stress distribution, $\overline{u'v'}$ in the way described by Melling and Whitelaw (1978). In order to measure the vertical component in near wall regions, the transmitting optics were inclined half-angle of beam intersection and the scattered light was collected off-axis. Measurements could then be obtained up to 2mm from the ground plane without a significant deterioration of the Doppler signals. Results obtained 20mm away from the ground plate with both the on-axis and the off-axis arrangements have shown a close agreement, within the precision of the equipment.

It should be pointed out that the use of water, rather than air, as the working fluid has two advantages when using laser-Doppler velocimetry. Water is naturally laden with particles which are suitable for use as scattering centers, so that seeding of the flow is usually unnecessary. Second, the required Reynolds number can be achieved at relatively low velocities, which correspond to Doppler frequencies, together with light frequency shifting, of a few megahertz which can be conveniently modulated by most data processing systems.

2.3 Experimental Accuracy The error sources associated with the measurements are briefly considered here together with assessments of accuracy. The arguments associated with these assessments are based on previous experiments and are provided in condensed form. Details can be found in Barata (1989).

Error incurred in the measurements of velocity by displacement and distortion of the measuring volume due to refraction of light on the duct walls and the change in refractive index were found to be negligibly small and within the accuracy of the measuring equipment. No corrections were made for sampling bias, and the systematic errors that could have arisen were minimized by using high data rates in relation to the fundamental velocity fluctuation rate, as suggested for example by Dimotakis (1983) and Erdman and Tropea (1981). Non-turbulent Doppler broadening (systematic) errors due to gradients of mean velocity across the measuring volume, e.g., Durst et al. (1981), may affect essentially the variance of the velocity fluctuations, but for the present experimental conditions are sufficiently small for their effect to be neglected: the maximum error is of the order of $10^{-4}V_j^2$ and occurs at the edge of the jet. Transit broadening has been shown by Zhang and Wu (1987) to be the principal source of error in laser velocimetry, but for the present optical configuration (with a signal-to-noise ratio about 69) and counting processor the error is negligible. Systematic errors incurred in the measurements of Reynolds shear stress can arise from lack of accuracy in the orientation angle of the normal to the anemometer fringe pattern and can be particularly large in the vicinity of the zones characterized by zero shear stress. For the present experimental conditions, and based on the results of Melling and Whitelaw (1976), the largest error is expected to be smaller than -2.5 percent.

The number of individual velocity values used in the experiments to form the averages was always above 10,000. As a result, the largest statistical (random) errors were 1.5 and 3 percent, respectively for the mean and variance values, ac-

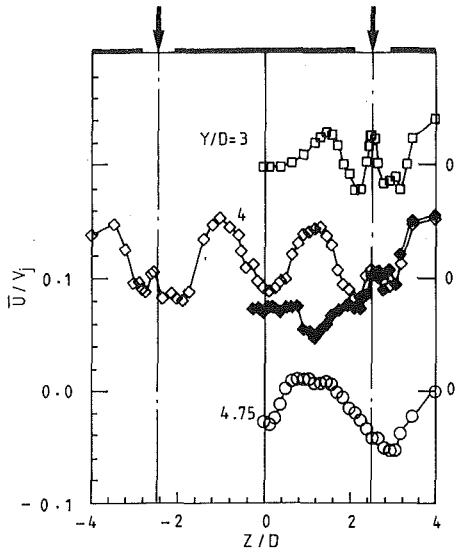

Fig. 5(*a*) Mean horizontal velocity, $\overline{U}/V_j$

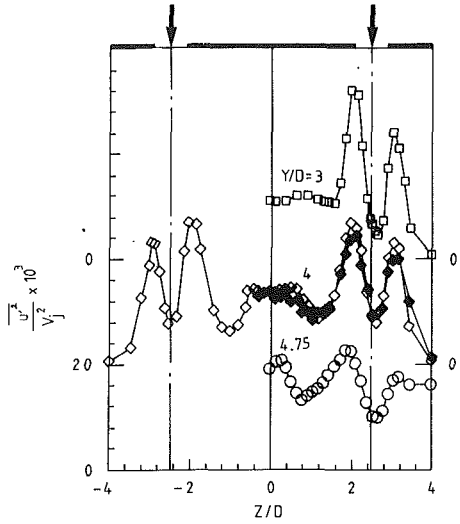

Fig. 5(*c*) Horizontal normal stress, $\overline{u'^2}/V_j^2 \times 10^3$

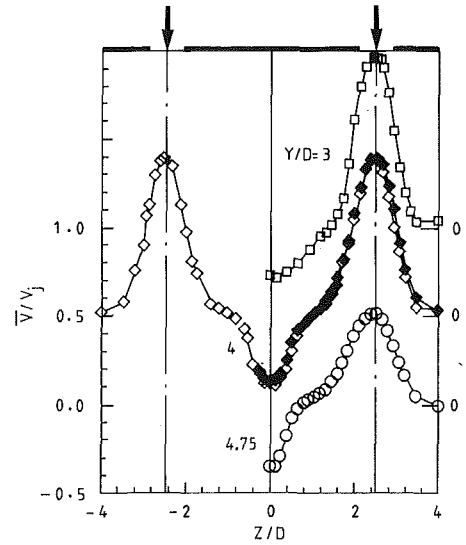

Fig. 5(*b*) Mean vertical velocity, $\overline{V}/V_j$

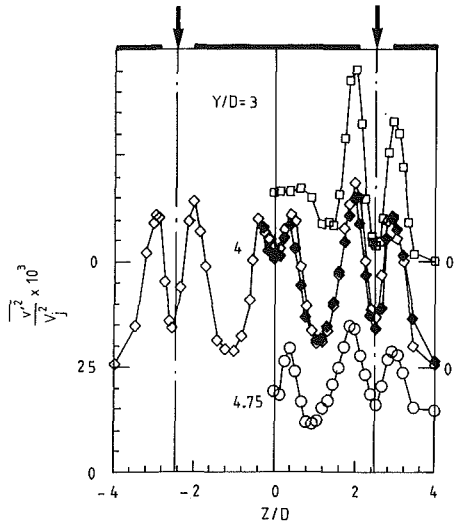

Fig. 5(*d*) Vertical normal stress, $\overline{v'^2}/V_j^2 \times 10^3$

Key: Open Symbols—two-jet case; closed symbols—three-jet case

Fig. 5 Horizontal profiles of velocity characteristics along the vertical transversal plane crossing the center of the two off-center jets (i.e., $X=0$) for $Re_j=105{,}000$; $V_j/U_o=30$; $H/D=5$, $S/D=5$, $L/D=15$

cording to the analysis of Yanta and Smith (1978) for a 95 percent confidence interval.

3 Results and Discussion

Prior to the detailed measurements, extensive visualization studies were performed to provide a qualitative picture of the flows considered here and to guide the choice of the flow configurations characterized by $Re_j=105{,}000$, $V_j/U_o=30$, $H/D=5$ and $S/D=5$ for the basic benchmark data for the two and three-jet flows.

For all the flows studied the results have shown for each jet a pattern similar to that for a single impinging jet, comprising an initial potential core jet region and an impingement region characterized by considerable deflection of the jets. After impingement the flow becomes almost parallel to the ground plate and resembles a wall jet, which interacts with the crossflow giving rise to a ground vortex wrapped around the impingement jet. The nature of the flow is similar to the "horseshoe" vortex structure known to be generated by the deflection of a boundary layer by a solid obstacle, e.g., Baker (1981), but is independent of the vortex pair known to exist in a "bent-over" jet in crossflow far from the ground, e.g., Andreopoulos and Rodi (1984). Two counter-rotating streamwise vortices trail away from the impingement zone and develop further downstream by skewing of pre-existing spanwise vorticity.

For the double-jet configuration an upwash fountain flow is formed in the center of the two impinging jets due to the collision of the individual wall jets. Figure 4(*a*) identifies the upwash flow in the vertical plane of symmetry, which contains a straight stagnation line on the bottom wall of the channel, in a way similar to that reported by Saripalli (1983) for twin-jet impingement in the absence of crossflow. A considerable entrainment of surrounding fluid into the jets and fountain was also observed in the present experiments, but in contrast with the results of Saripalli (1983) the upwash flow is asymmetric in relation to $X=0$, in that the crossflow lifts from the

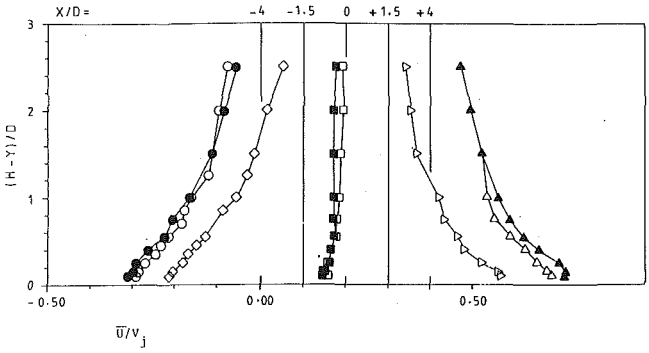

Fig. 6(*a*) Mean horizontal velocity, $\overline{U}/V_j$

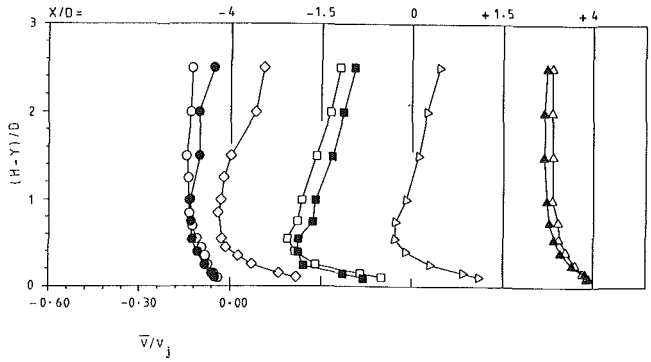

Fig. 6(*b*) Mean vertical velocity, $\overline{V}/V_j$

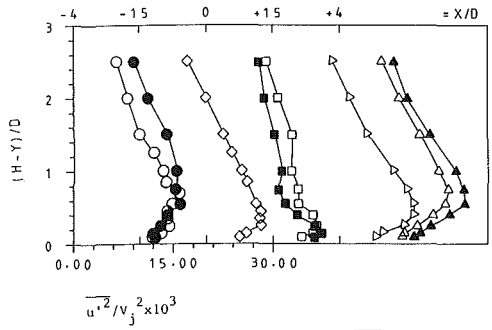

Fig. 6(*c*) Horizontal normal stress, $\overline{u'^2}/V_j^2 \times 10^3$

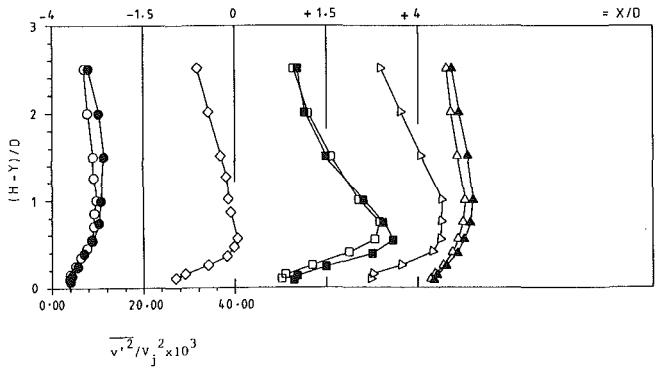

Fig. 6(*d*) Vertical normal stress, $\overline{v'^2}/V_j^2 \times 10^3$

ground in the upstream part of the flow (i.e., for $X<0$) in relation to that for $X>0$.

Figure 4(*b*) shows typical visualization of the flow along the vertical plane of symmetry for the three-jet configuration and identifies the interaction between the fountain flow formed in the center of the two downstream impinging jets and the wall jet derived from the upstream impinging jet. This gives rise to an extended upwash fountain flow which is inclined due to the relative strengths of the upstream thin wall jet and the cross-

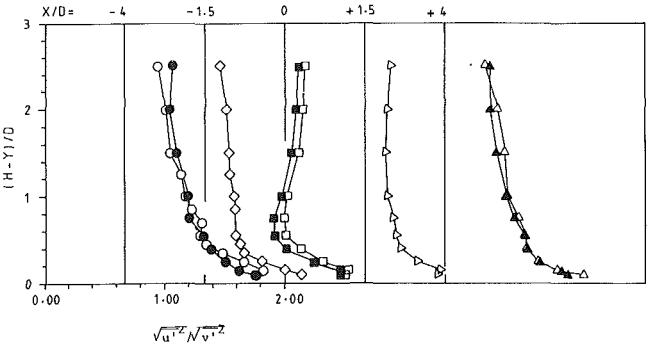

Fig. 6(*e*) Distribution of the relative magnitude of the normal stresses, $\sqrt{u'^2}/\sqrt{v'^2}$

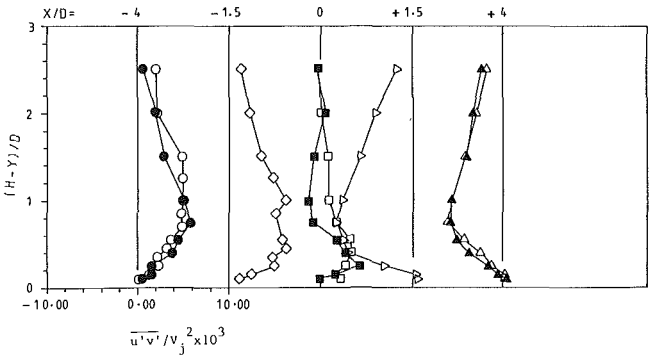

Fig. 6(*f*) Reynolds shear stress, $\overline{u'v'}/V_j^2 \times 10^3$

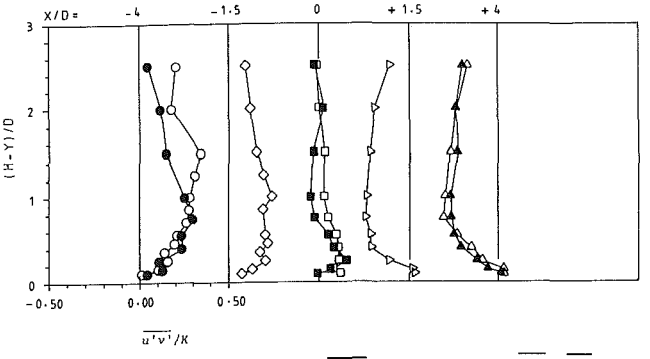

Fig. 6(*g*) Structure parameter, $\overline{u'v'}/k$, where $k = 3/4(\overline{u'^2} + \overline{v'^2})$

Key: Open Symbols—two-jet case; closed symbols—three-jet case

Fig. 6 Vertical profiles of velocity characteristics along the longitudinal plane of symmetry. $Re_j = 105{,}000$, $V_j/U_o = 30$, $H/D = 5$, $S/D = 5$, $L/D = 15$

flow. The confinement of the upwash flow and its interaction with the upstream impinging jet gives rise to the recirculation zone shown in Fig. 4(*b*) downstream of the first impinging jet. It should be noted that visualization of the flows under analysis in several transversal planes have shown that the lateral walls do not disturb the upwash flows described above. In addition, it should be recalled that one of the main purposes of the present experiments is to validate calculation methods of the flow which have to assume the lateral boundary conditions of the experiments and, therefore, the presence of the lateral walls in our rig does not affect the conclusions to be drawn from the measurements.

The previous paragraphs have considered a qualitative analysis of the most salient features of the upwash flows considered in this paper. We now turn to the description of the detailed laser Doppler measurements of mean on turbulent velocities, which quantify those features. The results are presented in the form of profiles obtained in the vertical plane crossing the center of the two off-center jets (i.e., $X=0$) and in the lon-

gitudinal, vertical, plane of symmetry (i.e., $Z=0$) for the two flow configurations studied, and care was taken to provide all data with the same uniformity of precision.

Figures 5(*a*) and (*b*) show the most revealing horizontal transversal profiles of axial, $\overline{U}$, and vertical, $\overline{V}$, mean velocity components for the two- and three-jet cases in the vicinity of the ground plane, i.e., for $Y/D>3$, and quantify the development of the impinging jets and of the central fountain upwash flows. The measurements, and particularly those of the vertical velocity component, clearly identify for the two configurations a centrally located fountain rising from the ground plate without interference from the main jets, as it occurs in practical VSTOL applications (e.g., Kotansky, 1981). This shows that the inter-jet spacing, S, used in the present experiments is large enough to avoid a sensible deflection of the jets perpendicular to the crossflow. The symmetry of the flow about the central plane between the two jets is also clearly demonstrated in Fig. 5 along the horizontal profiles obtained at $Y/D=4$ for the two-jet configuration and is an indication of the precise matching of the jet-exit velocities.

The initial profiles of the horizontal velocity, $\overline{U}$, show peaks along the jet boundaries, which are considerably small in magnitude (about 0.4 percent V_j) and may be associated with the transversal recirculatory flows originated by the central and lateral collisions of the wall jets. It should be noted that the measurements obtained 2mm downstream the jet exit have established precise boundary conditions typical of a jet flow with a potential core and zero horizontal mean velocities. Based upon the detailed measurements of Barata et al. (1991) for single impinging jets for $V_j/U_o=30$, it is observed that the influence of the ground plate on the jet flows extend to about 3D above the plate, while the impinging region is about 1D high. The maximum differences that occur between the mean flows for the two- and three-jet configurations are identified in the profiles of the mean horizontal velocity at $Y/D=4$ and are explained by the upstream confinement of the fountain flow in the three-jet configuration.

The deflection of the impinging jets by the crossflow is identified close to the ground plate, i.e. at $Y/D=4.75$, by the negative values of the mean horizontal velocity, $\overline{U}$, at the geometrical axis of the jet, i.e. $Z/D=2.5$. The negative values of $\overline{U}$ at $Z=0$ are a consequence of the longitudinal (i.e., along the crossflow direction) asymmetry of the fountain flow discussed above and indicates that the central stagnation point is displaced downstream by the crossflow. These features of the mean flow field can be readily analyzed by the vertical profiles of the mean axial velocity shown in Fig. 6(*a*): the values at $X=0$ are negative along the full profile and, in particular, the profiles at $X/D=\pm 1.5$ are asymmetric with increased absolute magnitudes for $X<0$. As expected, the displacement of the central stagnation point increases for the three-jet configuration, as well as the downstream wall jet velocities.

The analysis of the upwash flows can be further documented with help of Figs. 7 and 8, which show horizontal profiles of velocity characteristics along the central plane of symmetry. For the two-jet configuration (i.e., Fig. 7) the mean axial velocities increase in absolute magnitude at least up to $X/D=\pm 2.7$ and, then, decay with increased rates closer to the ground plate. The vertical velocities show maximum upward values around the central stagnation zone and decay monotonically to zero with X. At $X/D=8$ the maximum upward vertical velocities increase with the distance to the ground plate and are below 0.08 V_j. In agreement with the qualitative analysis given above, the distributions of the mean velocity components are asymmetric with respect to $X=0$, with higher upward vertical velocities for $X<0$. For example, at $X/D=-4$ the inclination of the mean velocity vector reaches values three times larger than that at $X/D=+4$.

For the three-jet configuration, Fig. 8, the upwash flow around $X=0$ is similar to that described previously, although with increased asymmetries. The interaction between the upstream wall jet and the upwash flow noted in Fig. 4 is identified between $X/D=-3$ and $X/D=-7$ with a plateau in the values of the upward vertical velocity between $X/D=-4$ and $X/D=-6$. Around $X/D=-15$, the profiles of Figs. 8(*a*) and (*b*) identify the upstream impinging jet and, in general, show features similar to those discussed by Barata et al. (1991) for a single impinging jet. It is noted that the impingement point on the ground plane occurs at $X/D=-0.1$ due to deflection by the crossflow.

Figures 5 to 8, (*c*) and (*d*), show horizontal and vertical profiles of the normal stresses, $\overline{u'^2}$ and $\overline{v'^2}$, and show three regions of intense velocity fluctuations, namely the shear layer surrounding the impinging jets, the impinging zones themselves and the fountain upwash flow with maximum values similar to those found by Saripalli (1987) for a two-jet impingement flow in the absence of a crossflow. These regions are characterized by the highest mean velocity gradients and are associated with near-Gaussian velocity probability distributions, suggesting the absence of discrete frequency oscillations. The development of the horizontal velocity profiles of Figs. 5(*c*) and (*d*) quantify the turbulent diffusion along the jets: the peaks of the normal stresses spread along the jet and the minima in the center of the jets increase in magnitude as Y increases. The consistent asymmetry of the distributions of the normal stresses along the jets is associated probably with convection from the highly turbulent upwash flow, which exhibits maximum fluctuating values close to the group plate.

The flows are anisotropic in that, with exception of the initial potential core, $\overline{v'^2}$ is largest around the impinging jets and in the upwash flows, with $0.6<\sqrt{\overline{u'^2}}/\sqrt{\overline{v'^2}}<1$ while, based on the results of Fig. 8, $\overline{u'^2}$ is largest along the wall jets, with $1<\sqrt{\overline{u'^2}}/\sqrt{\overline{v'^2}}\leq 1.4$. The anisotropy of the upwash flows is particularly observed along the vertical plane of symmetry, Figs. 7 and 8: close to the ground plate, $\overline{u'^2}$ is largest, with $1<\sqrt{\overline{u'^2}}/\sqrt{\overline{v'^2}}\leq 1.4$ at $X/D=\pm 4$, while away of the ground plate and downstream of $X/D=+4$, $\overline{v'^2}$ is largest with $\sqrt{\overline{u'^2}}/\sqrt{\overline{v'^2}}=0.65$ at $X/D=0$.

The distribution of the shear stress $\overline{u'v'}$ away from the fountain upwash flow may be analyzed on the basis of Fig. 8(*e*), which is similar to the results of Barata et al. (1991). The impinging jets and the wall jets are dominated respectively by the mean strains $\partial\overline{V}/\partial X$ and $\partial\overline{U}/\partial Y$, and the sign of the shear stress is related with that of each shear strain in accordance with a turbulent viscosity hypothesis. Around the impinging point the values of the two mean strains have the same order of magnitude and the "thin shear layer" approximation, as discussed by Bradshaw (1973) and Castro and Bradshaw (1976), is no more valid. The Reynolds shear stress decrease in the region of high stabilizing curvature typical of the impinging zones, but the remarkable feature is its rapid increase further away of the impinging zones, reaching values of $\overline{u'v'}/V_j^2$ higher than those typical of "well-behaved" plane shear layers. Further, the values of turbulence structure parameters such as the correlation coefficient for shear stress, $\overline{u'v'}/\sqrt{\overline{u'^2}\cdot\overline{v'^2}}$, and the ratio between Reynolds shear stress and turbulent kinetic energy, $\overline{u'v'}/k$, also confirm that the impingement zone is significantly affected by streamline curvature which increases the shear stress on the upper side and decreases it on the lower side in agreement with the results of Castro and Bradshaw (1976). For example, the values of $\overline{u'v'}/k$ plotted along a curved line following the center of the shear layers bounding the impingement and wall jets fall from around 0.3 to 0.1 in the impinging zone and, then, overshoot again the typical value of 0.3 (e.g., Harsha and Lee, 1970) along the wall jets before decreasing further away of the impinging zone.

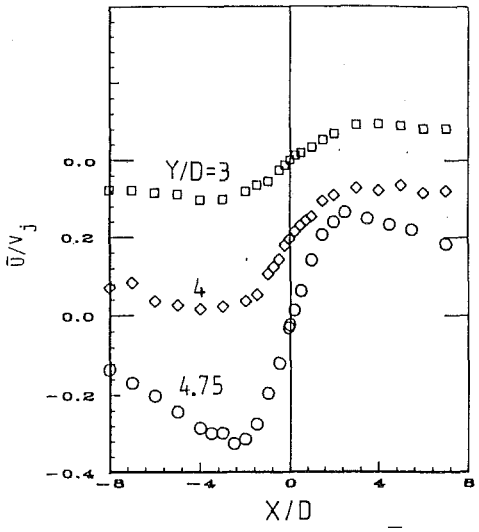

Fig. 7(*a*) Mean horizontal velocity, $\bar{U}/V_j$

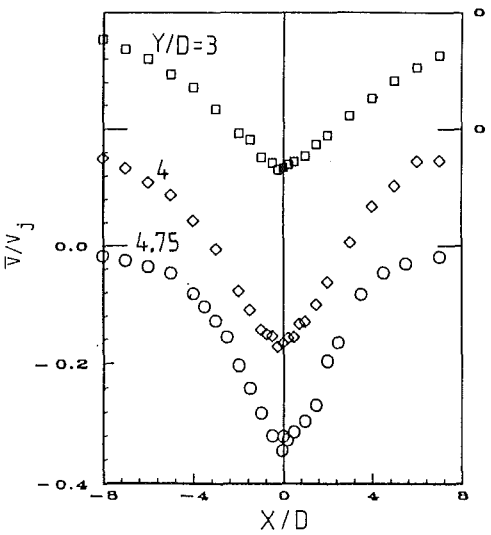

Fig. 7(*b*) Mean vertical velocity, $\bar{V}/V_j$

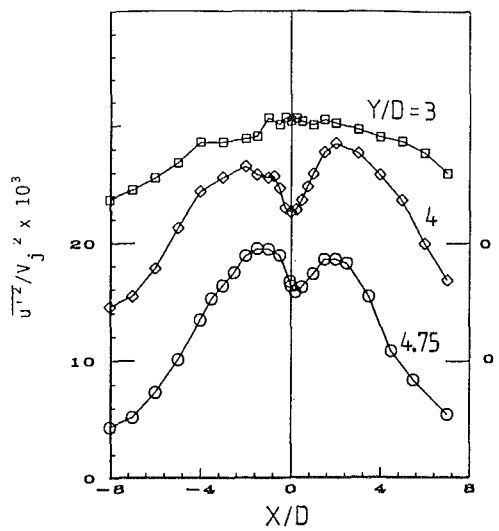

Fig. 7(*c*) Horizontal normal stress, $\overline{u'^2}V_j^2 \times 10^3$

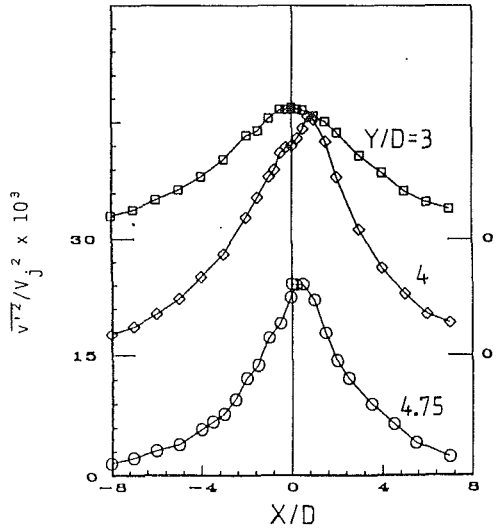

Fig. 7(*d*) Vertical normal stress, $\overline{v'^2}/V_j^2 \times 10^3$

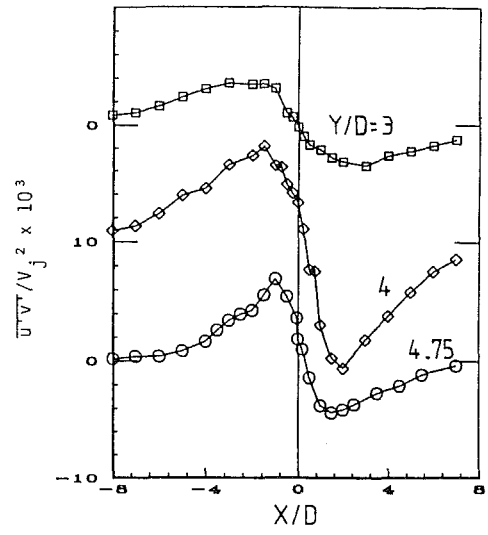

Fig. 7(*e*) Reynolds shear stress, $\overline{u'v'}/V_j^2 \times 10^3$

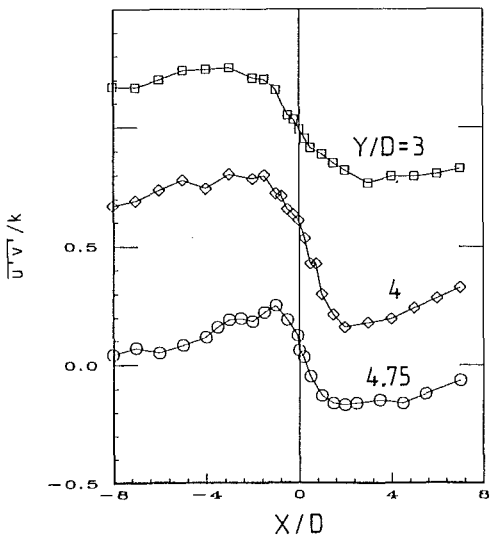

Fig. 7(*f*) Structure parameter, $\overline{u'v'}/k$, where $k = 3/4(\overline{u'^2} + \overline{v'^2})$

Fig. 7 Horizontal profiles of velocity characteristics along the longitudinal plane of symmetry (i.e., $Z = 0$) for the two-jet configuration. $Re_j = 105{,}000$, $V_j/U_o = 30$, $H/D = 5$, $S/D = 5$, $L/D = 15$

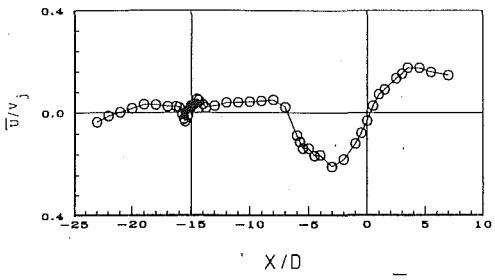

Fig. 8(*a*) Mean horizontal velocity, $\overline{U}/V_j$

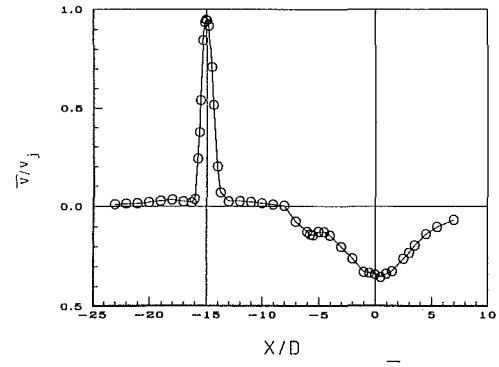

Fig. 8(*b*) Mean vertical velocity, $\overline{V}/V_j$

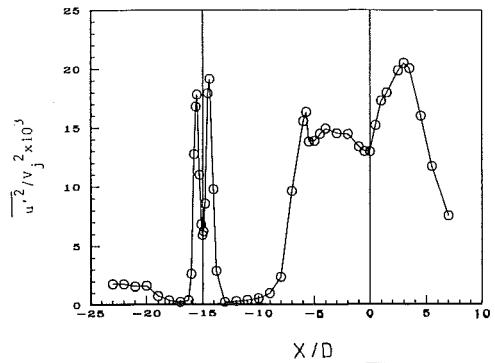

Fig. 8(*c*) Horizontal normal stress, $\overline{u'^2}/V_j^2 \times 10^3$

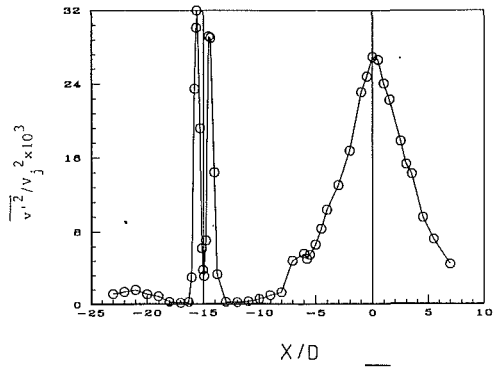

Fig. 8(*d*) Vertical normal stress, $\overline{v'^2}/V_j^2 \times 10^3$

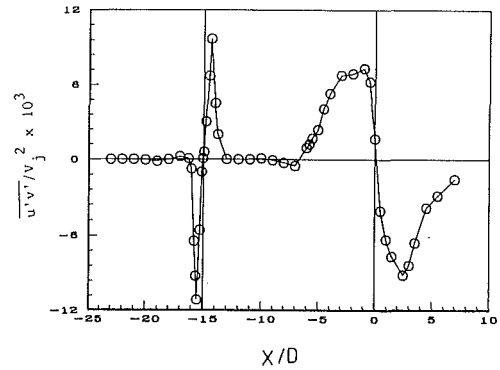

Fig. 8(*e*) Reynolds shear stress, $\overline{u'v'}/V_j^2 \times 10^3$

Fig. 8 Horizontal profiles at $Y/D = 4$ of velocity characteristics along the longitudinal plane of symmetry (i.e., $Z = 0$) for the three-jet configuration. $Re_j = 105{,}000$, $V_j/U_o = 30$, $H/D = 5$, $S/D = 5$, $L/D = 15$

Around the fountain flows the profiles of Reynolds shear stress, which are shown along the vertical plane of symmetry, are consistent with the longitudinal asymmetry of the upwash flow and, in general, with the direction of mean flow. For $X < 0$, the shear stress is positive because faster moving elements of upward fluid ($v' < 0$) tend to move far upstream ($u' < 0$). Similarly, the shear stress downstream of the jets, i.e., $X > 0$, is negative because there the upward movement of fluid particles is associated with positive axial velocity fluctuations.

The present results also show that the turbulence structure of the fountain upwash flows is subject to the effects of flow distortion and influenced by the competing magnitudes of the mean strains $\partial\overline{U}/\partial Y$ and $\partial\overline{V}/\partial X$. The shear stress around the stagnation point is close to zero in the zones of zero shear strain, but the high turbulent levels measured may be explained by the interaction of normal stresses and normal strains. In addition, the values of the turbulence structure parameter $\overline{u'v'}/k$, Figs. 6(*g*) and 7(*f*), show considerably departures from the conventional value of plane shear layers, implying unconventional behavior of the dimensionless "constants" in any turbulence model that is adjusted to fit the data.

The relevance of the present results to the development of engineering calculation methods is that many of the principles used in current schemes for "well-behaved" shear layers and undermined, such as the estimation of a length scale from the shear layer thickness or the gradient-diffusion hypothesis for turbulent transport. Based on the detailed results of Castro and Bradshaw (1976) for a mixing layer bounding a normally impinging plate jet with a irrotational core, one is forced towards the conclusion that a further level of allowance for history effects on the distortion of the turbulent flow in the impingement and fountain zones is necessary, for instance through transport equations for one or more of the empirical constants in engineering models of turbulence. This requires analysis of quantities which are not directly measurable and should involve a more detailed study of length scales in complex flows than we have been able to make in the present case.

4 Conclusions

Laser-Doppler measurements have provided information of the mean and turbulent velocity characteristics of the flows created by two and three round jets impinging on a ground plate through a low-velocity confined crossflow with fountain formation, for $Re_j = 105{,}000$, $V_j/U_o = 30$ and $H/D = 5$.

The experiments have shown a large penetration of the impinging jets, which exhibit a similar pattern for two- and three-jet configurations and give rise to fairly thin wall jets. The collision of consecutive wall jets gives rise to fountain upwash flows, which interact with the crossflow originating a complex vortical structure wrapped around the impinging jets. For the three jet case the fountain upwash flow formed by collision of the wall jets is extended by the interaction with the third wall jet.

The shear layer surrounding the jets, the impingement region and the fountain are zones of intense velocity fluctuations, along which it is noted large effects of flow distortion on the turbulence structure parameters that determine the empirical constants in engineering models of turbulence. The results suggest that the calculation of complex impinging flows must be found from modeled transport equations rather than from

a turbulent viscosity hypothesis, and that the distortion of turbulent length scales have to be considered if the turbulence levels of the impingement and fountain flows are to be predicted.

Acknowledgments

We are pleased to record many useful discussions with Dr. J. J. McGuirk of the Fluids Section of the Imperial College throughout this work. The experiments were performed at the "Centro de Termodinâmica Aplicada e Mecânica dos Fluidos da Universidade Técnica de Lisboa" (CTAMFUTL-INIC).

References

Andreopoulos, J., and Rodi, W., 1984, "Experimental Investigation of Jets in a Crossflow," *J. Fluid Mech.*, Vol. 138, p. 127.

Baker, O. J., 1981, "The Turbulent Horseshoe Vortex," *J. Wind Engng. and Indust., Aerod.*, Vol. 6, p. 9.

Barata, J. M. M., "Experiments and Numerical Study on the Aerodynamics of Impinging Jets in a Crossflow," (in Portuguese), Ph.D. thesis, 1989, Instituto Superior Técnico, Tech. University of Lisbon.

Barata, J. M. M., Durão, D. F. G., Heitor, M. V., and McGuirk, J. J., 1991a, "The Turbulent Characteristics of a Single Impinging Jet Through a Crossflow," *Exp. Thermal and Fluid Science*, in press.

Barata, J. M. M., Durão, D. F. G., Heitor, M. V., and McGuirk, J. J., 1991b, "The Impingement of Single and Twin Turbulent Jets Through a Crossflow," *AIAA J.*, Vol. 29(4), pp. 595–602.

Bradshaw, P., 1973, "Effects of Streamline Curvature on Turbulent Flow," *Agardograph*, Vol. 169.

Castro, I. P., and Bradshaw, P., 1976, "The Turbulence Structure of a Highly Curved Mixing Layer," *J. Fluid Mech.*, Vol. 73, pp. 265–304.

Crabb, D., Durão, D. F. G., and Whitelaw, J. H., 1981, "A Round Jet Normal to Crossflow," ASME JOURNAL OF FLUIDS ENGINEERING, Vol. 103, pp. 142–153.

Dimotakis, F., 1978, "Single Scattering Particle Laser-Doppler Measurements of Turbulence," AGARD CP 13, paper 10.7., 1978.

Durst, F., Melling, A., and Whitelaw, J. H., 1981, *Principles and Practice of Laser-Doppler Anemometry*, 2nd ed., Academic Press, London.

Erdmann, J. C., and Tropea, C. D., 1981, "Turbulence-Induced Statistical Bias in Laser Anemometry," *Proc. 7th Biennal Symp. on Turbulence*, Rolla-Missouri.

Gentry, G. L., and Margason, R. J., 1966, "Jet-Induced Losses on VTOL Configurations Hovering In and Out of Ground Effect," NASA TN D-3166.

Gilbert, B. L., 1983, "Detailed Turbulence Measurements in a Two Dimensional Upwash," AIAA paper No. 83-1678, AIAA 16th Fluid and Plasma Dynamics Conference, July 12–14, Danvers, Mass.

Harsha, P. T., and Lee, S. C., 1970, "Correlation Between Turbulent Shear Stress and Turbulent Kinetic Energy," *AIAA J.*, Vol. 8, pp. 1508–1510.

Heitor, M. V., Laker, J. R., Taylor, A. M. K. P., and Vafidis, C., 1984, "Introduction Manual for the FS Model 2 Doppler-Frequency Counter," Imperial College, Mech. Engng. Dept. Report FS/84/10.

Jenkins, R. C., and Hill, W. G., Jr., 1977, "Investigation of VTOl Upwash Flows Formed by Two Impinging Jets," Grunman Research Department Report RE-548.

Kamotani, Y., and Greber, I., 1972, "Experiments on a Turbulent Jet in a Cross Flow," *AIAA Journal*, Vol. 10, pp. 1425–1429.

Kind, R. J., and Suthanthiran, K., 1980, "The Interaction of Two Opposing Plane Turbulent Wall Jets," AIAA paper 72-211.

Kotansky, D. R., 1981, "The Modelling and Prediction of Multiple Jet VTOL Aircraft Flow Fields in Ground Effect," AGARD CP 308, paper 16.

Kotansky, D. R., and Glaze, L. W., 1980, "The Effects of Ground Wall-Jet Characteristics on Fountain Upwash Flow Formation and Development," Report ONR-CR212-216-1F.

Melling, A., and Whitelaw, J. H., 1978, "Turbulent Flow in a Rectangular Duct," *J. Fluid Mech.*, Vol. 78, pp. 289–315.

Saripalli, K. R., 1983, "Visualization of Multijet Impingement Flow," *AIAA Journal*, Vol. 21, pp. 483–484.

Saripalli, K. R., 1987, "Laser Doppler Velocimeter Measurements in 3-D Impinging Twin-Jet Fountain Flows," *Turbulent Shear Flows*, Vol. 5, ed. Durst et al., Springer-Verlag, pp. 147–168.

Shayesteh, M. V., Shabaka, I. M. N. A., and Bradshaw, P., 1985, "Turbulent Structure of a Three-Dimensional Impinging Jet in a Crossflow," AIAA 23rd Aerospace Sciences Meeting, Reno, Nevada, Jan. 14–17.

Stoy, R. L., and Ben-Haim, Y., 1973, "Turbulent Jets in a Confined Crossflow," ASME JOURNAL OF FLUIDS ENGINEERING, Vol. 95, pp. 551–556.

Sugiyama, Y., and Usami, Y., 1979, "Experiments on the Flow in and Around Jets Directed Normal to a Crossflow," *Bulletin JSME*, Vol. 22, pp. 1736–1745.

Yanta, W. J., and Smith, R. A., 1978, "Measurements of Turbulent-Transport Properties with a Laser-Doppler Velocimeter," AIAA paper 73-169, 11th Aerospace Science Meeting, Washington.

Zhang, Z., and Wu, J., 1987, "On Principal Noise of the Laser Doppler Velocimeter," *Exp in Fluids*, Vol. 5, pp. 193–196.

A. S. Lyrintzis
Assistant Professor.
Assoc. Mem. ASME;
Formerly, Cornell and Syracuse Universities

Y. Xue
Graduate Research Assistant;
Formerly, Syracuse University

Aerospace Engineering and Mechanics,
University of Minnesota,
Minneapolis, MN 55455

Acoustics of Transonic Flow Around an Oscillating Flap

Investigation of noise mechanisms due to unsteady transonic flow is important for aircraft noise reduction. In this work, the near-field impulsive noise due to an oscillating flap is simulated numerically. The problem is modeled by the two-dimensional high frequency transonic small disturbance equation (VTRAN2 code). The three types of unsteady shock wave motion have been identified. Two different important disturbances exist in the pressure signal. The disturbances are related to the unsteady motion of the supersonic pocket and fluctuating lift, and drag forces. Pressure wave signatures, noise frequency spectra, and noise directivity are shown.

Introduction

Flow generated sound has been familiar to man since prehistoric days. However, very little study of these mechanisms was made until after World War II. Since then the increased use of airplanes and helicopters has drawn attention to the noise they generate. For an aircraft or a helicopter, aerodynamic noises generated from fluids are usually very important. There are many kinds of aerodynamic noises including turbine jet noise, impulsive noise due to unsteady flow around wings and rotors, broadband noise due to inflow turbulence and boundary layer separated flow, etc. Here we are particularly interested in studying the impulsive noise due to unsteady flow around an airfoil, which usually dominates the other noise sources when it occurs.

The transonic flow region is extremely interesting because flight in the transonic regime is efficient and because typical helicopters in forward flight develop transonic conditions on their rotors. The appearance of unsteady shock waves on a blade creates shock-related noise that can be studied computationally. The physics of the noise generation due to unsteady transonic flow is not adequately understood and we will focus our research on this problem. We will concentrate on the noise generated by an oscillating flap with the hope that these results will be very helpful when a more complicated motion (such as BVI) is studied.

The oscillating flap (Fig. 1) is a typical unsteady airfoil flow that is widely studied experimentally and computationally. Tijdeman (1977) used an oscillating flap to experimentally identify the three types of unsteady shock motion.

Unsteady transonic flow problems have been solved numerically in the past. The low frequency approximation of the unsteady two-dimensional Transonic Small Disturbance (TSD) equation was first solved by Ballhaus and Goorjian (1977) and the LTRAN2 code was created. Since then the code has been updated to include high frequency effects (Rizetta and Chin, 1979), viscosity (Guruswamy and Goorjian, 1984), monotone switches (Goorjian et al., 1985) and second order effects (Goorjian and Van Buskirk, 1985). However, the acoustic waves resulting from the unsteady motion have not been adequately studied.

A comprehensive code, VTRAN2 was developed (George and Chang, 1984; Lyrintzis, 1988) as a modification to LTRAN2, to study unsteady transonic flow including Blade-Vortex Interactions (BVI) using the high frequency transonic small disturbance equation. A direct comparison of the results obtained from the different methods (from small disturbance to Navier Stokes equations) shows that the results are very similar (George and Chang, 1984). In fact the results tend to coincide the further away we move from the airfoil surface. Thus the small disturbance equation was chosen because of simplicity. At great distances from the airfoil though, the waves become very difficult to follow because of numerical diffusion and dispersion errors. The Kirchhoff method was introduced (George and Lyrintzis, 1988; Lyrintzis and George, 1989a, 1989b) to extend the numerically calculated nonlinear aerodynamic results to the linear acoustic far-field.

In this paper (a version of which was presented by Lyrintzis and Xue, 1990), we will examine the noise due to an oscillating flap. An oscillating flap is chosen because its well-defined periodicity creates a simple motion. We will attempt to explain the physics governing the acoustics of an oscillating flap with the hope that these results will be very helpful when a more complicated motion (such as BVI) is studied. All the work will be done on a typical airfoil NACA 64A006. The different types of shock-wave motion (type A, B, and C) will be observed. The results will be examined and compared with previous ex-

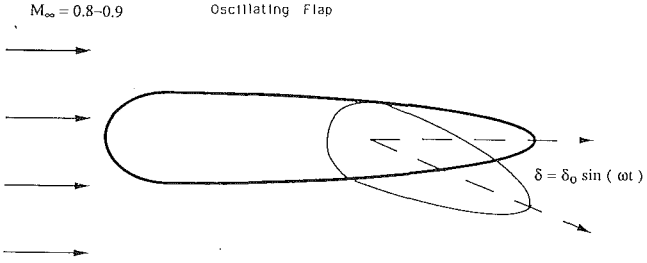

Fig. 1 Oscillating flap

Contributed by the Fluids Engineering Division and presented at the International Symposium on Nonsteady Fluid Dynamics, Toronto, Canada, June 1990. Manuscript received by the Fluids Engineering Division July 16, 1990. Associate Technical Editor: C. J. Freitas.

perimental and computational results. The acoustic analysis will be emphasized. The directivity patterns of noise will be studied, and Fast Fourier Transform (FFT) technique will be applied to obtain noise frequency spectra. The noise mechanisms will be explained physically and we will show the relation between the noise signal and oscillating lift and drag forces and the unsteady shock wave motion.

The Numerical Method (VTRAN2)

VTRAN2 is a code developed for analyzing unsteady transonic flow using transonic small disturbance theory (George and Chang, 1984; Lyrintzis, 1988). It is based on the ADI implicit scheme of the LTRAN2 code (Ballhaus and Goorjian, 1977) with the inclusion of the high frequency term and the addition of regions of convected vorticity for the study of BVI.

The equation for the unsteady inviscid transonic small-disturbance potential ϕ is:

$$A\phi_{tt} + 2B\phi_{xt} = C\phi_{xx} + \phi_{yy} \tag{1}$$

where

$$A = \frac{k^2M^2}{\tau^{2/3}}, \quad B = \frac{kM^2}{\tau^{2/3}}, \quad C = \frac{1-M^2}{\tau^{2/3}} - (\gamma+1)M^m\phi_x$$

The quantities x, y, t, ϕ in Eq. (1) have been scaled by c, $c/\tau^{1/3}$, ω^{-1}, and $c\tau^{2/3}\,U_o$, respectively. The exponent m in the nonlinear term is chosen as $m = 2$, which is suitable for stronger shocks as it locates the shocks more accurately (Ballhaus, 1978).

For the oscillating flap cases we sometimes have comparatively high values of k (0.3–0.4) that also justify the need for the high frequency term (the high frequency term can be dropped for $k < 0.1$–0.2). There are several advantages to adopting the fast and simple small disturbance theory. The principal advantage is the simplified treatment of the boundary conditions which can be written as:

1. Upstream outer boundary condition:

$$\phi_x = \phi_y = 0 \qquad \text{as } x -> -\infty \tag{2}$$

2. Lateral outer boundary condition:

$$\phi_x = \phi_y = 0 \qquad \text{as } y -> \pm\infty \tag{3}$$

3. Downstream outer boundary condition:

$$\phi_x + k\phi_t = 0 \qquad \text{as } x -> +\infty \tag{4}$$

4. Airfoil surface boundary condition (applied at $y = 0$):

$$\phi_y = \frac{\partial Y\pm}{\partial x} + \frac{k\partial Y\pm}{\partial t} = 0 \qquad \text{as } x -> -\infty \tag{5}$$

where $Y\pm$ defines the airfoil surface.

The oscillating flap motion will be represented by the boundary condition on the surface of the airfoil which includes an unsteady term as shown in Eq. (5). The classical Kutta condition is satisfied by this small disturbance formulation. We are interested in cases for which the reduced frequency range is much less than 4, which is the limit for the application of the Kutta condition (Poling and Telionis, 1986).

The pressure coefficient C_p in the unsteady small-disturbance theory is:

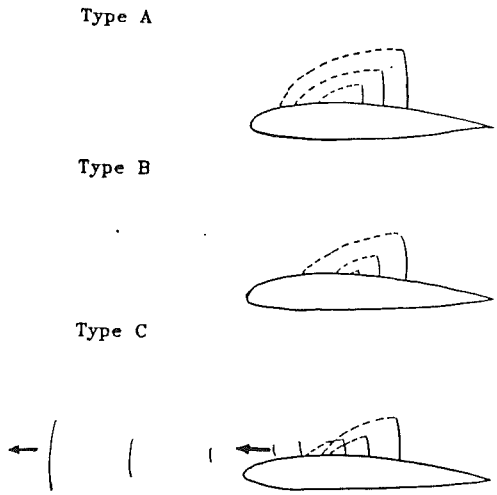

Fig. 2 Tijdeman's unsteady types of shock motion

$$C_p = -2\tau^{2/3}(\phi_x + k\phi_t) \tag{6}$$

In addition, the wake condition

$$\Gamma_x + k\Gamma_t = 0 \tag{7}$$

implies that a branch cut exists between the trailing edge and the downstream outer boundary, across which the potential jump, $\Delta\phi = \Gamma$, where Γ is the circulation.

An alternating direction implicit (ADI) method is used for the solution of the equation, where the high frequency term is added in the y-sweep. An approximate factorization technique (AF2) is used for the steady calculation which provides a start-up solution. Special care is taken for the conservative differentiation along the uneven mesh. Details of the differencing technique were given by Lyrintzis (1988).

A coarse (113 × 99) and a fine (213 × 119) mesh are used for the calculations. The computational mesh points are clustered more densely near and in front of the airfoil and then are stretched exponentially from the near airfoil region to about 200 chordlengths from the airfoil in both x and y directions. Since the stronger waves propagate primarily upstream, more mesh points were added in the x-direction in front of the airfoil. We should note that, although the outer boundary conditions used are reflective, the large computational region used (−200, 200 chords) insures that the reflections from the boundaries are very small by the time they arrive back in the region near the airfoil, and, in any case, they arrive much later than the time of interest for the purposes of this study. We should also note that moving far from the airfoil (e.g., one chord) the mesh becomes coarse and it is very difficult to follow the propagating waves because of numerical diffusion.

The VTRAN2 code was shown to agree well with other, more complex approaches including Euler and thin-layer Navier-Stokes computations (George and Chang, 1984). VTRAN2 can be used for calculations of the effects of airfoil shape, angle of attack, Mach number, vortex strength, and vortex miss distance on the flow and on the radiated sound. The CPU time for each two-dimensional case on a VAX 8820 computer

Nomenclature

A, B = coefficients of unsteady terms in Eq. (1)
C = coefficient of nonlinear term
c = airfoil chordlength
k = reduced frequency: $\omega c/U_o$
m = exponent in the nonlinear term of Eq. (1)
M = free-stream Mach number
U_o = free stream velocity
t = time, scaled by ω^{-1}
x, y = horizontal and vertical coordinates, scaled by c, $c/\tau^{1/3}$
$Y_\pm$ = equation of the upper (+) and lower (−) surface
Γ = circulation
γ = ratio of specific heats (= 1.4 for air)
δ = angle of the oscillating flap
δ_o = amplitude angle of the oscillating flap
θ = angle below the horizontal (see Fig. 3)
τ = airfoil thickness ratio
ϕ = disturbance-velocity potential, scaled by $c\tau^{2/3}U_o$
ω = characteristic frequency of the unsteady motion

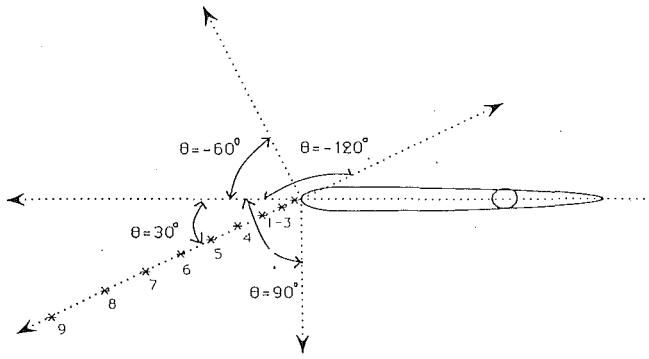

Point #	x	y
1	-0.015	-0.013
2	-0.037	-0.020
3	-0.082	-0.045
4	-0.158	-0.095
5	-0.300	-0.188
6	-0.500	-0.297
7	-0.870	-0.515
8	-1.219	-0.696
9	-1.704	-0.977

Fig. 3 Positions of points for calculation of the noise signals

is about 21 minutes for a mesh (113 × 119), 1024 time-marching steps, and about 39 minutes for a fine mesh (213 × 119), 1024 time-marching steps, which are enough for a complete history of the oscillating flap. For Cray-2 the CPU time is about one minute.

Types of Unsteady Shock Motion

Tijdeman (1977) showed experimentally using an oscillating flap, that varying airfoil surface boundary conditions can give three different types of unsteady shock motion (Fig. 2):

Type A shock motion, where the shock at the rear of the supersonic region merely moves back and forth with concurrent changes in strength.

Type B shock motion, where the shock moves similarly to type A, but disappears temporarily during the unsteady motion.

Type C shock motion, where the supersonic region disappears, but a shock wave leaves the airfoil and propagates forward to the far field.

The above three types of unsteady shock motions affect heavily the characteristics (e.g., lift, drag) of all unsteady transonic flows. The type of shock motion that occurs in a given situation depends on the flow characteristics (e.g., free-stream Mach number, airfoil shape, amplitude and frequency of the unsteady motion). Their existence has been verified by different experiments and calculations for various types of unsteady shock motion (e.g., Ballhaus and Goorjian, 1977).

Results and Discussion

Some mid-field calculations for an oscillating flap on NACA 64A006 were performed using VTRAN2 with a refined mesh to follow the waves of interest. The calculations were made in an airfoil fixed reference frame. Figure 3 demonstrates the positions of nine points on a line which is 30 deg below the horizontal. Different directions as shown in Fig. 3 will also be investigated.

Most results are presented as $C_p(t)$ plots where the vertical axis is C_p and the horizontal axis stands for time. The noise frequency spectrum is always important for studying noise characteristics. Therefore, the Fast Fourier Transform (FFT) technique is applied to transform the $C_p(t)$ signals to noise frequency spectra SPL(f) (SPL = Sound Pressure Level).

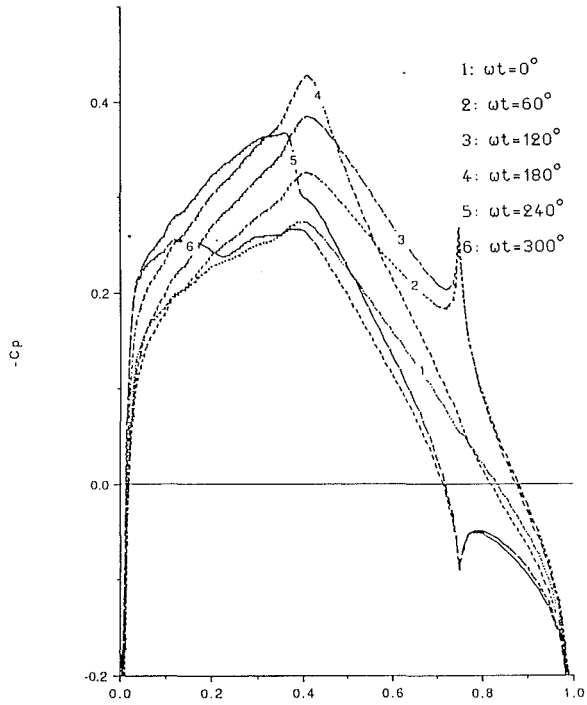

Fig. 4 C_p distribution on airfoil surface for oscillating flap, type C shock motion, fine mesh (213 × 119); 64A006, M = 0.822, k = 0.496, δ_o = 1.5 deg

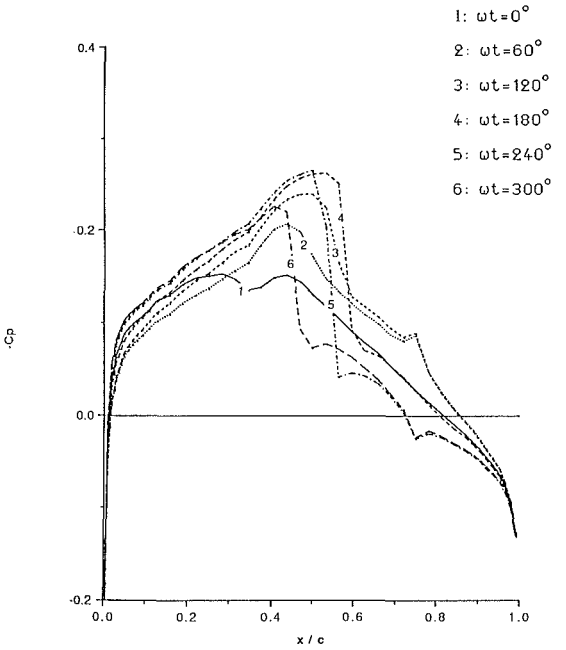

Fig. 5 C_p distribution on airfoil surface for oscillating flap, type B shock motion, coarse mesh (113 × 97); 64A006, M = 0.854, k = 0.358, δ_o = 1 deg

We again have a 64A006 airfoil at Mach numbers 0.875, 0.854, and 0.822 which correspond to shock wave motions of type A, B, and C, respectively, as shown also by Ballhaus and Goorjian (1977). The flap has a length of 25 percent of the chord (starts at x/c = 0.75), the reduced frequency k of the motion varies: 0.468, 0.358 and 0.496, respectively, and the amplitude of the flap motion δ_o is 1, 1, and 1.5 deg, respectively. k and δ_o vary to correspond to cases reported by Ballhaus and Goorjian, (1977). The solution starts with the flap at rest; then the flap starts to oscillate ($\delta = \delta_o \sin(\omega t)$). Thus, it takes some time for the initial transients to die out. In the subsequent

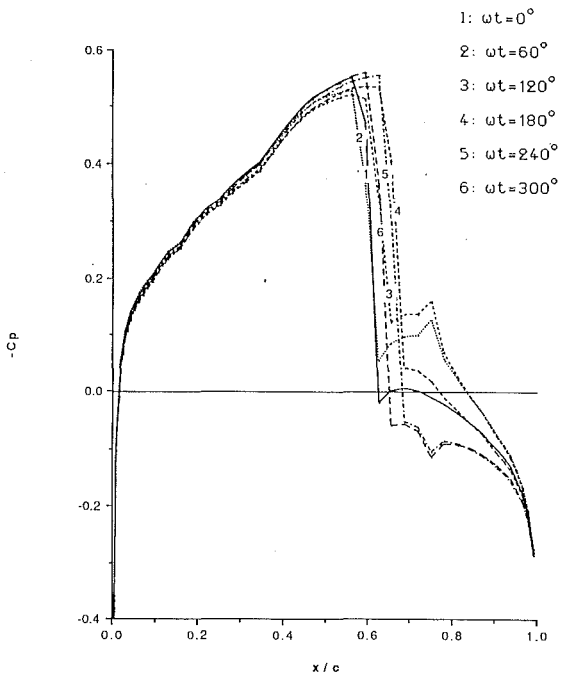

Fig. 6 C_p distribution on airfoil surface for oscillating flap, type A shock motion, coarse mesh (113 × 97); 64A006, M = 0.875, k = 0.468, δ_0 = 1 deg

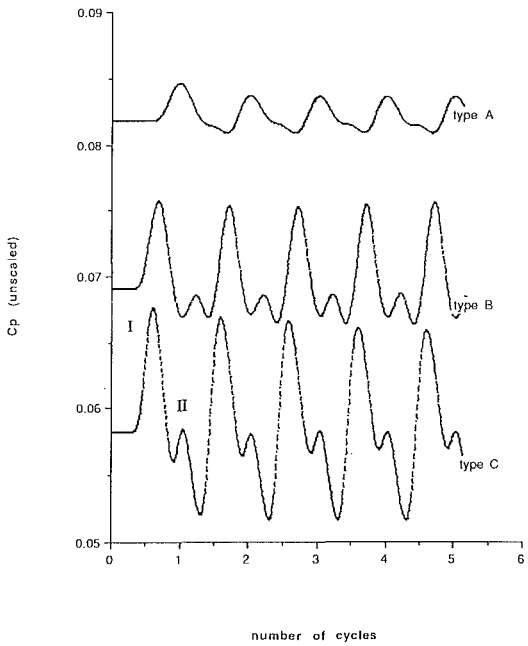

Fig. 7 Comparison of the $C_p(t)$ signal for oscillating flap, types A, B, C; point 5

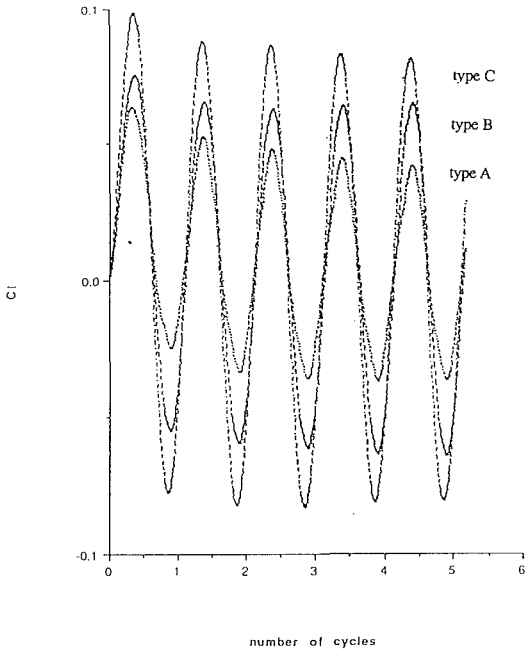

Fig. 8 Comparison of the C_l signal for oscillating flap types A, B, C

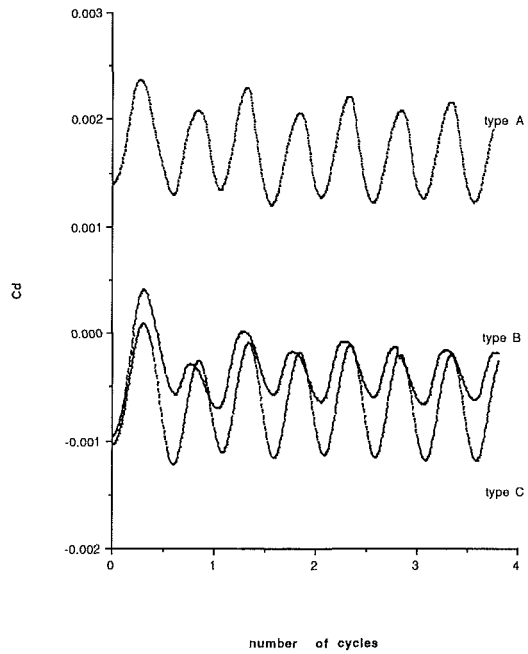

Fig. 9 Comparison of the C_d signal for oscillating flap types A, B, C

figures we will present results starting at the third cycle which was shown to be adequate (Xue, 1989).

The number of mesh points can have an influence on type C shock motion. Coarse mesh (113 × 97) calculations (not shown) did not capture the type C shock wave motion for these conditions, whereas finer mesh (213 × 119) calculations (Fig. 4) show the type C shock motion. Figures 5 and 6 show the type B and A shock motion on the surface of airfoil for a coarse mesh (the coarse mesh is adequate in these cases). The irregularities near x/c = 0.75 are due to flap (the airfoil is not smooth there when the flap is moving). These computational results compare well with results by Ballhaus and Goorjian (1977).

Figure 7 shows the relative amplitude of the unscaled $C_p(t)$ signal for the three types of shock motion (A, B, C) for the oscillating flap case. We can see that in every cycle there are two main propagating disturbances (I, II). The first disturbance (I) is the main oscillating flap noise and it is related to the fluctuating lift coefficient C_l. The second disturbance II corresponds to the unsteady shock motion and depends on the motion of the entire supersonic region induced by the vortex passage. It depends heavily on the type of shock motion. It is also somehow related to the fluctuating drag coefficient C_d. In order to check the effect of the oscillating drag alone, we examined the subcritical case (not shown). We found that the disturbance II exists in the subcritical case and it is very weak. Thus the main part of the disturbance II signal is due to the unsteady shock motion. The directivity of the two disturbances is very different, as will be shown later. The relative amplitude

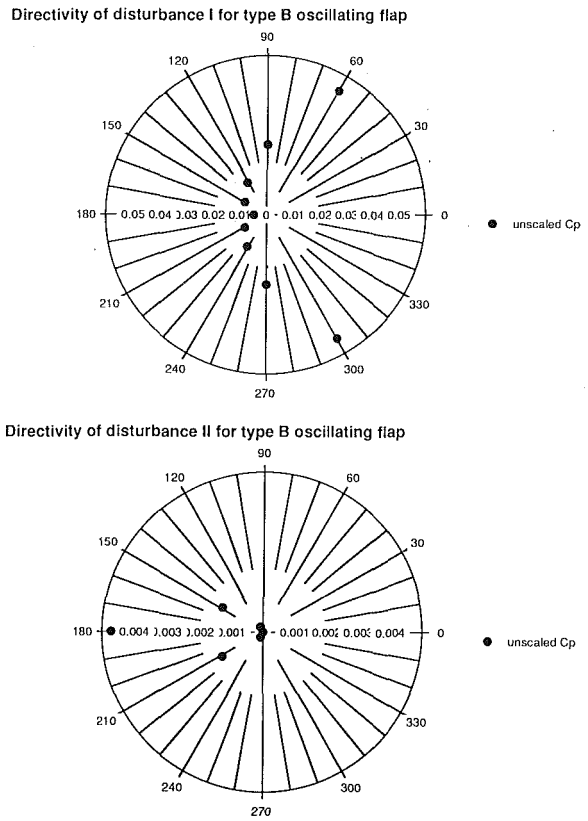

Fig. 10 Polar plot of the directivity of disturbances I and II for oscillating flap, type B, r = 0.35 chords measured from the leading edge

of the second disturbance compared to the first, seems to increase as we move from type A to type C shock motion, because the induced shock motion is more severe for the type C case. The actual disturbance amplitude is not fully indicative, since we have a different k, and amplitude δ_0 of the flap motion. The existence of the second disturbance for the BVI case was observed computationally (George and Chang, 1984; Owen and Shenoy, 1987; and George and Lyrintzis, 1989a) and experimentally (Caradonna et al., 1984 and Shenoy, 1989), but it has not been detected in the oscillating flap case. Finally, the acoustic properties (such as amplitude, directivity etc.) behave continuously through the three different types of shock motion. However, the amplitude of disturbance II can be directly related to the type of shock motion, as shown in Fig. 7.

Figure 8 compares the C_l variations for the three types of shock motion. We can see that the first disturbance (I) shown in Fig. 7 relates well to the C_l oscillations shown in Fig. 8 whereas there is no disturbance (II) in the C_l signal. Thus, the first disturbance (I) is associated with the C_l oscillations caused by the periodic flow changes.

The inviscid C_d was also calculated. (C_d can be easily calculated if the pressure distribution is known.) It is well known that in subcritical inviscid flow the drag coefficient C_d is negative (propulsion). In fact it oscillates between zero and a negative value and the frequency is twice the frequency of the unsteady shock motion. When the flow becomes supercritical the formation of supersonic pockets increases the average value of C_d, but the fluctuations stay about the same. Figure 9 compares the C_d variations for the three types of shock motion (only four cycles are shown for a better identification of disturbance II). C_d has twice the frequency of C_l, as expected. It is also very interesting to note, that, as expected, for the type C case the C_d variation resembles the subsonic case (oscillating propulsion). As the Mach number increases the mean value of C_d increases, as expected, but the fluctuations remain about the same.

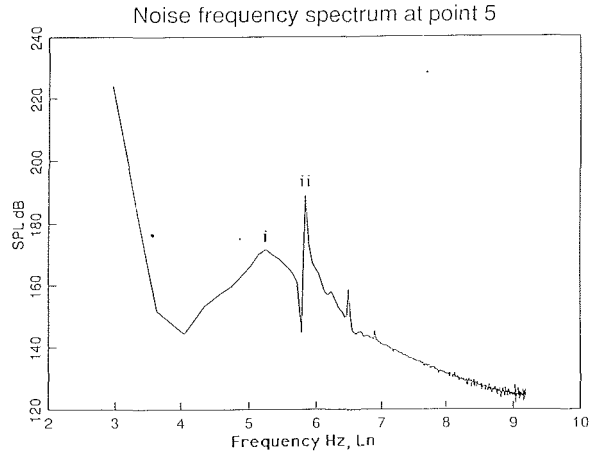

Fig. 11 Noise frequency spectra SPL(f) for type B shock motion, θ = 0 deg

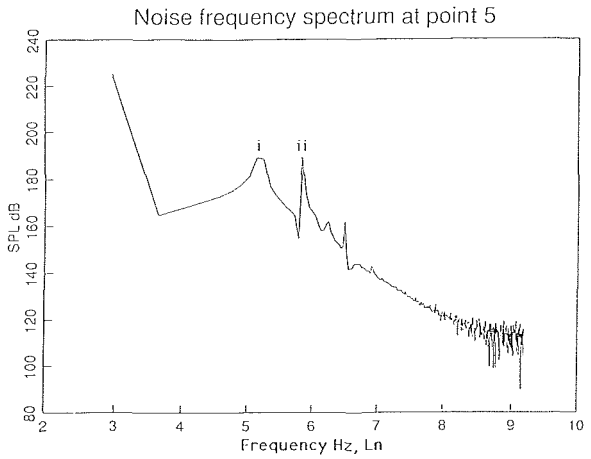

Fig. 12 Noise frequency spectra SPL(f) for type B shock motion, θ = 30 deg

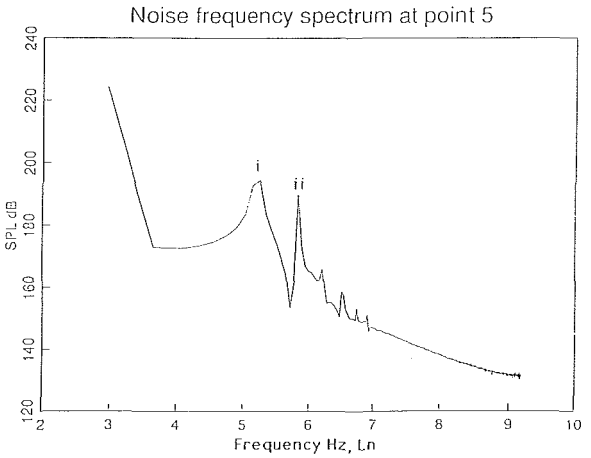

Fig. 13 Noise frequency spectra SPL(f) for type B shock motion, θ = 60 deg

Unsteady forces become acoustic dipole sources as it is implied by the Ffowcs Williams Hawkings equation. Thus an unsteady lift is expected to create a dipole in the y-direction. For a pure dipole the pressure disturbance will be zero for θ = 0 and 180 deg, and reach a maximum for θ = 90 deg. An unsteady drag creates a dipole in the x-direction, where the directivity is shifted 90 deg (i.e., max for θ = 0 deg). This behavior is modified because of the different traveled distances (Doppler effect). However, a moving shock creates a nonlinear quadrupole source that has a strong forward directivity.

The directivity of the noise signal was investigated (plots of the $C_p(t)$ signal for different directions can be found in Xue (1989)). Figure 10 shows the polar plot (i.e., amplitude as a function of θ) for disturbances I and II for type B. By analyzing this plot, we can see that the first disturbance (I) (which is believed to be caused by fluctuating C_l) is getting stronger as the direction angle increases from 0 to 90 deg. These are unscaled results at an actual distance $r = 0.35$ chords from the leading edge. In fact, the waves propagating that distance upstream have an effective distance of propagation higher than the ones propagating downstream, because of the free stream velocity. If this distance is scaled out (not shown), then the first disturbance (I) keeps increasing (but slower) between 0 and 90 deg, and drops after 90 deg. Similar behavior was obtained in the subsonic case, where a good dipole behavior was detected. The dipole-like dependence looks very weak for the supercritical case. A plausible explanation is that the shock wave motion influences disturbance, causing an increase in the forward direction. The second disturbance (II) is getting weaker as the direction angle increases from 0 to 90 deg. This second disturbance seems to have a strong forward directivity. Adding the effect of scaling will make this forward directivity even stronger.

Similar graphs can be obtained for types A and C. In the subcritical case the polar directivity graphs show that we have two dipoles at right angles from each other. The dipoles are associated with the lift and drag forces. (Note that the dipole associated with the drag is very weak.) This idea is not new, (see e.g., Chanaud, 1977), but it was not mentioned by previous investigators in the analysis of the noise due to unsteady flow. In supercritical cases though, the directivity observed is not the one described by a pure dipole, because of various nonlinearities (i.e., shock waves) and source noncompactness. In particular, noise due to shock wave motion has a strong forward directivity, and it influences disturbance I and dominates disturbance II.

Noise frequency spectra SPL(f) are shown in Figs. 11, 12, 13 for angles (θ) 0, 30, and 60 deg, respectively and constant distance ($=0.35$ chordlengths) from the airfoil leading edge. Disturbance I corresponds to the frequency of the unsteady motion. Disturbance II corresponds to twice the frequency of the unsteady motion. The high value of the curve at very low frequencies is due to the initial transient. The very high frequency fluctuations are mesh dependent. Since the mesh is finer in the y-direction around point 5 the high frequency fluctuations are stronger at $\theta = 30$ deg (Fig. 12). (In fact, we run the finer mesh for this case the high frequency fluctuations diminished (Xue, 1989).) We can see that the first disturbance is broader-band in character, while the second disturbance is more narrow, more sinusoidal in character. Looking at the noise signals at different directivity angles we can verify the behavior observed from the polar graphs.

A parametric study shows that the disturbance amplitude decreases as the reduced frequency k increases. Also an increase in the amplitude of the flap motion increases the resulting disturbance with the results being very sensitive to small changes in the amplitude of the oscillation angle.

Conclusions

An existing numerical finite difference code VTRAN2 was modified to analyze noise due to unsteady transonic flow. Oscillating flap flows were analyzed. The unsteady transonic small disturbance equation was solved numerically using ADI techniques. Examining the C_p distribution on the airfoil surface, the three types of unsteady shock motion (A, B, and C) were identified in both cases and matched previous results.

The unsteady pressure coefficients $C_p(t)$ showed the existence of two main disturbances. In the subcritical cases the two disturbances correspond to the fluctuating life and drag forces and have a dipole directivity. In supercritical cases the first disturbance (I) is associated mainly with the fluctuating lift coefficient (C_l), but the added nonlinear sound due to the shock motion affects its directivity; the second disturbance (II) has a higher frequency and is mainly due to the shock motion, since the effect of the oscillating drag forces is not significant.

Noise frequency spectra SPL(f) were obtained at different points, and the two disturbances were observed. It is evident from the frequency spectra that the second disturbance has a higher frequency.

We hope that this work will contribute towards the better understanding of the mechanisms of noise due to unsteady transonic flow, especially in more applied cases like blade-vortex interaction.

Acknowledgments

The authors want to thank Professor A. R. George of Cornell University for some stimulating discussions about the research subject. Some of the calculations were performed at the computational facilities of Minnesota Supercomputer Institute (MSI).

References

Ballhaus, W. F., and Goorjian, P. M., 1977, "Implicit Finite-Difference Computations of Unsteady Transonic Flows about Airfoil," *AIAA J.*, Vol. 15, No. 12, pp. 1728–1735.

Ballhaus, W. F., 1978, "Some Recent Progress in Transonic Flow Computations," *Numerical Methods in Fluid Dynamics*, ed. Wirz H. J., and Smolderen J. J., McGraw-Hill, NY pp. 155–235.

Caradonna, F. X., Laub, G. H., and Tung, C., 1984, "An Experimental Investigation of the Parallel Blade-Vortex Interaction," 10th European Rotorcraft Forum, The Hague, Netherlands.

Chanaud, R. C., 1977, "Basic Mechanisms of Noise Generations by Fluids," *Noise and Fluids Engineering*, the Winter Annual Meeting of ASME, Atlanta, GA.

George, A. R., and Chang, S. B., 1984, "Flow Field and Acoustics of Two-dimensional Transonic Blade-Vortex Interactions," AIAA Paper 84-2309, AIAA 9th Aeroacoustics Conference, Williamsburg, VA.

George, A. R., and Lyrintzis, A. S., 1988, "Acoustics of Transonic Blade-Vortex Interactions," *AIAA Journal*, Vol. 26, No. 7, pp. 769–776.

Goorjian, P. M., Meagher, M. E., and Van Buskirk, R. D., 1985a, "Monotone Switches in Implicit Algorithms for Potential Equations Applied to Transonic Flows," *AIAA Journal*, Vol. 23, No. 4, pp. 492–498.

Goorjian, P. M., and Van Buskirk, R. D., 1985b, "Second-Order-Accurate Spatial Differencing for the Transonic Small-Disturbance Equation," *AIAA Journal*, Vol. 23, No. 11, pp. 1693–1699.

Guruswamy, P., and Goorjian, P. M., 1984, "Effects of Viscosity on Transonic Aerodynamic and Aeroelastic Characteristics of Oscillating Airfoils," *AIAA Journal*, Vol. 21, No. 9, pp. 700–707.

Lyrintzis, A. S., 1988, "Transonic Blade-Vortex Interactions," Ph.D. dissertation, Mechanical and Aerospace Engineering Department, Cornell University, Ithaca, NY.

Lyrintzis, A. S., and George, A. R., 1989a, "Far-Field Noise of Transonic Blade-Vortex Interactions," *American Helicopter Society Journal*, Vol. 34, No. 3, pp. 30–39.

Lyrintzis, A. S., and George, A. R., 1989b, "The Use of Kirchhoff Method in Acoustics," *AIAA Journal*, Vol. 27, No. 10, pp. 1451–1453.

Lyrintzis, A. S., and Xue, Y., 1990, "Acoustics of Unsteady Transonic Flow," *Proceedings of the International Symposium on Nonsteady Fluid Dynamics*, Toronto, Canada, pp. 187–199.

Lyrintzis, A. S., and Xue, Y., 1991, "A Study of the Noise Mechanisms of Transonic Blade-Vortex Interactions," to appear in *AIAA Journal* (scheduled for Sept. 1991), also University of Minnesota Supercomputer Institute Research Report, UMSI 90/141, Minneapolis, MN, July 1990.

Owen, S. T., and Shenoy, R. K., 1987, "Numerical Investigation of Two-Dimensional Blade-Vortex Interaction," *Proceedings of the AHS National Specialists' Meeting on Aerodynamics and Aeroacoustics*, Arlington, Texas.

Poling, D. R., Telionis, D. P., 1986, "The Response of Airfoils to Periodic Disturbances—The Unsteady Kutta Condition," *AIAA Journal*, Vol. 24, No. 2, pp. 193–199.

Rizzetta, D. P., and Chin, W. C., 1979, "Effect of Frequency in Unsteady Transonic Flow," *AIAA Journal*, Vol. 17, No. 7, pp. 779–781.

Shenoy, R. K., 1989, "Aeroacoustic Flowfield and Acoustics of a Model Helicopter Tail Rotor at a High Advance Ratio," *Proceedings of the 45th Annual Forum of the American Helicopter Society*, Boston, MA.

Tijdeman, H., 1977, "Investigations of the Transonic Flow Around Oscillating Airfoils," NLR TR 77090-U, NLR The Netherlands.

Xue, Y., 1989, "Numerical Simulation of Acoustic Sources in Unsteady Transonic Flow," Master of Science Thesis, Department of Mechanical & Aerospace Engineering, Syracuse University, Syracuse, NY.

R. Srikanth
Graduate Student.

E. Rathakrishnan
Associate Professor.

Department of Aerospace Engineering,
Indian Institute of Technology,
Kanpur, India 208106

Application of Digital Moire Interferometry for Mapping Conical Flows

Digital Moire Interferometry (DMI)—a low cost and sufficiently sensitive geometric interference technique with very low stability requirement analyzed through digital image processing, has been applied to compressible conical flows. An inverse Abel transform algorithm for image reconstruction from moire deflectograms has been developed.

Introduction

Quantitative evaluation of compressible flow visualization photographs through digital image processing (DIP) has been investigated during the past few years. A recent extensive review on this topic, by Hesselink (1988), classifies the application technique for the first time. Under line-of-sight measurements, most methods are directed toward turbulent structure evaluation from shadowgraph images. Other methods include evaluation of conventional and holographic interferometry images for steady flows. To develop a low cost and easy to set up system, with lower sensitivity than conventional interferometry but sufficient for most practical purposes, a tunable moire system was demonstrated on conical flows by Stricker et al. (1983). This axisymmetric flow system, though applied successfully, lacked generalization as the analysis was carried out with functional form assumptions on the observed data. Integration of geometric interferometry through a tunable moire system and digital image processing avoids the assumptions made by Stricker et al. (1983), and renders the application more general, thereby opening it for further applications and developments.

Image reconstruction from line-integrated effects is done in several fields, each demanding a separate approach. In moire interferometry, with paraxial approximation, the refractive index function in the flow is Abel transformed into fringe shift functions. The inverse Abel transform is a convergent improper integral with the observed function, fringe shift, present as a zeroth order derivative within the integral for evaluating the required refractive index field. The existing algorithms are all suitable for the case when the observed function exists as a first order derivative within the integral. The algorithm developed in this work is developed following a recent suggestion (Nestor and Olsen, 1960) but modified to suit the contrary purpose mentioned. In this paper it is aimed to carry out the application to a conical flow and show how flexible the method is. The photograph evaluated is that of a flow over a 23 deg right circular cone at zero angle of attack taken from Stricker et al. (1983) for the purpose of easy comparison. To the best of the authors knowledge the integrated technique shown in this work is the first such application.

Contributed by the Fluids Engineering Division for publication in the JOURNAL OF FLUIDS ENGINEERING. Manuscript received by the Fluids Engineering Division April 23, 1991. Associate Technical Editor: D. M. Bushnell.

Analysis Using Digital Moire Interferometry (DMI)

A tunable moire system consists of two similar, parallel line gratings separated by Δ and oriented to each other by angle θ. Figure 1 shows a schematic of the setup. The orientation of the parallel fringe system which develops when collimated light travels from one grating to the other is perpendicular to the axis bisecting angle θ. Laser light is expanded and collimated by a lens pair. The collimated light passes through the flow system, which has to be a phase object, and falls on grating G_1. The shadow of this straight line grating G_1 falls on G_2. The interference pattern formed falls as an image on the mat screen (ground glass) S which is flush with G_2. The image is photographed from behind S. Two images, one without the flow and the other with the flow system on, are captured. The fringe shift when the flow is turned on, thereby distorting the parallel fringes. The shift at a point on the fringe is measured perpendicular to the original straight fringe axis. The shift at a point is proportional to the gradient of the refractive index field integrated along the path of the light passing through the point. A fringe can only respond to the refractive index gradient component along a line parallel to the fringe axis. The collimated light beam travels perpendicular to the flow axis undeviated in the paraxial approximation, and their wave fronts are twisted through angles that change the shadow of G_1 and G_2, thereby distorting the fringe system. The y-gradient effects

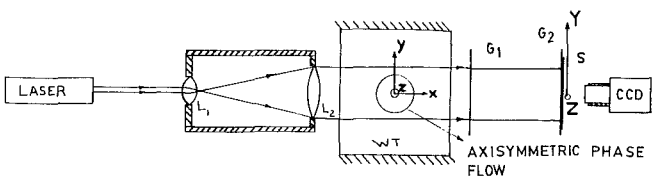

Fig. 1 DMI setup; L1, L2: lens pair; WT: windtunnel; G1, G2: gratings; S: mat screen

are observed when the angle θ between G_1 and G_2 is bisected by the z-axis; therefore, the vertical Y-fringes shift in the Z-direction.

DIP is a vast field by itself and certain tools developed will be helpful in analyzing the moire deflectograms. Jain (1989) gives great details about DIP in general. Details of the methodology for applying DIP to moire interferometry of compressible flows are given by Srikanth and Rathakrishnan (1991). Intensity gradient thinning is a technique by which an intensity pattern can be reduced to a contour pattern along chosen intensity gradients. Another thinning technique is geometric in nature which reduces intensity patterns to lines along constant geometric features observed in the pattern after edge detection.

A hybrid thinning algorithm, capable of multi-directional scanning, was used. Each scan determines the regions of specified intensity gradient and marks them. Then an intersection of the data sets obtained from each scan is done by a sequence of logical AND and OR operations which yield the true thinned lines. Since the photograph was taken from a print with a close-up lens, the image was partially binary in nature. To suppress this, the photograph printing was done with a slight blur. This operation did not affect the information as will be seen from the results. This resulted in thinned bands, rather than lines, after zero intensity gradient thinning was carried out on the dark fringes. The bands were further thinned geometrically to their mid points to obtain perfect thinned lines. This operation was carried out after a factor of 17 magnification was obtained on the image through a macro lens fitted to a CCD camera. The images were stored in files to carry out thinning operations on a PC-XT, configured with an image processing card (Matrox, PIP). Two images are normally required as mentioned. Comparison of two image files, i.e., location of corresponding points throughout the images, is extremely tedious. For this purpose an on-line CCD camera is most preferable. For situations where photographs are unavoidable, as in the present case, thinned straight fringes of the undisturbed part of the disturbed photograph are extrapolated to the disturbed parts.

A conical flow has constant properties on constant conical surface emanating from the apex of the cone symmetrically about the conical body axis. In this work, conical shock is attached at the apex of a 23 deg right circular cone at zero angle of attack in Mach 1.98 stream which deflects the flow over the conical surface.

Image Reconstruction From Fringe Shift Data

The coordinate systems considered are polar (r, θ, z) for the flow system and cartesian (Y, Z) for the fringe plane. (Y, Z) of the fringe plane is equivalent to (y, z) of the flow system. The refractive index gradient field $\nabla n(r, \theta, z)$ is Abel transformed (A) to produce fringe shift functions $g(y, z)$ and $h(y, z)$ for Z and Y fringe systems through the total angle of twist functions $\psi(y, z)$ and $\phi(y, z)$, respectively. The Y-fringe shift function, $h(y, z)$, is the one and only that can map an axisymmetric field radially. The function $\phi(y, z) \equiv \phi(y, z_0) \equiv \phi(y)$ for a given fringe plane is related to the r-gradient of refractive index $n(r, \theta, z) \equiv n(r, z_0) \equiv n(r)$ through

$$\phi(y) = [A] * (\partial n(r)/\partial r)](y) = 2y \int_y^{r_s} \frac{(\partial n(r)/\partial r) dr}{\sqrt{(r^2 - y^2)}} \quad (1)$$

The function to be determined, $n(r)$, can be obtained by an inverse Abel transform (A^{-1}) through

$$\Delta n(r) = [A^{-1} * \phi(y)](r) = -\pi^{-1} \int_r^{r_s} \frac{\phi(y) dy}{\sqrt{(y^2 - r^2)}} \quad (2)$$

The integral on the right-hand side of Eq. (2) is improper and converges only for certain $\phi(y)$ types whose functional form is not known. Stricker et al. (1983) made assumptions about the functional form of $\phi(y)$. In the region $r_c \le y \le r_s$ a linear fringe form was assumed and at $y = r_s$ a step function was introduced. This approach cannot be generalized for all types of flow systems for two reasons. First, a functional form cannot be easily fitted to the distorted shape of a fringe and, secondly, Eq. (2) cannot be integrated analytically for all $\phi(y)$ types.

$\phi(y)$ is related to the fringe shift function $h(y, z_0)$ through

$$\phi(y) = \frac{\theta h(y)}{\Delta} \quad (3)$$

The sensitivity of the tunable moire can be increased by increasing Δ. But this introduces parallax if laser light is not used. The gratings have to be perfectly flat, without warps, so that when the flow is not turned on the fringes do not distort as Δ is increased. For this reason the rulings are done on perfectly flat glass plates. Details about the sensitivity, accuracy and dynamic range of the system are given by Srikanth and Rathakrishnan (1991). Substituting Eq. (3) into Eq. (2),

$$\Delta n(r) = \frac{-\theta}{\pi \Delta} \int_{y=r}^{r_s} \frac{h(y)\, dy}{\sqrt{y^2 - r^2}} = K \int_{y=r}^{r_s} \frac{h(y)\, dy}{\sqrt{y^2 - r^2}} \quad (4)$$

The constant K includes the magnification factor associated with the photograph. To solve Eq. (4), where $h(y)$ is in the zeroth order derivative form and the integral is singular at $y = r$, Nestor and Olsen (1960) algorithm was modified in the following way. Figure 5 shows the diagrammatic form of the numerical scheme. If r_c and r_s are cone and shock radii at any $z = z_0$ plane, then breaking up $r_c \le y \le r_s$ into M equal zones of width f gives

$$\Delta n(r) = \Delta n_k = -\pi^{-1} \sum_{m=k}^{M} \int_{r_m}^{r_{m+1}} \frac{\phi_m(y)\, dy}{\sqrt{(y^2 - r_k^2)}},$$

where $r_i = f(i-1)$. Substituting Eq. (3), taking f to be small and linearly approximating $h_m(y)$, gives

$$h_m(y) = S_m y + C_m,$$

where S_m and C_m are the slope and y-intercept, respectively. Substituting $h_m(y)$ and rewriting Δn_k gives

$$\Delta n_k = K \sum_{m=k}^{M} \left[S_m \int_{r_m}^{r_{m+1}} \frac{y\, dy}{\sqrt{(y^2 - r^2)}} + C_m \int_{r_m}^{r_{m+1}} \frac{dy}{\sqrt{(y^2 - r^2)}} \right].$$

Analytically integrating the definite integrals in the above equation gives

$$\Delta n_k = K \sum_{m=k}^{M} (S_m A_{mk} + C_m B_{mk}) \quad (5)$$

where

$$A_{mk} = [\sqrt{(r_{m+1}^2 - r_k^2)} - \sqrt{(r_m^2 - r_k^2)}] \quad (6)$$

$$B_{mk} = [Ln(r_{m+1} + \sqrt{r_{m+1}^2 - r_k^2}) - Ln(r_m + \sqrt{r_m^2 - r_k^2})] \quad (7)$$

$$S_m = \frac{h(r_{m+1}) - h(r_m)}{f} \quad (8)$$

$$C_m = \frac{r_m(h(r_m) - h(r_{m+1})) + f(h(r))}{f}. \quad (9)$$

The refractive index change is related to density change through

$$\Delta \rho = 4.4\, \Delta n \ (\mathrm{g/cm^3}). \quad (10)$$

In Fig. 5, the lower end of the kth zone is where Δn_k has to be determined and mth zone takes all zones between $k \le m \le M$. It is clear that the sub-zone analytical integral estimates very closely to the actual convergent value of Eq. (2). Equations (5) to (10) were used to analyze Fig. 2.

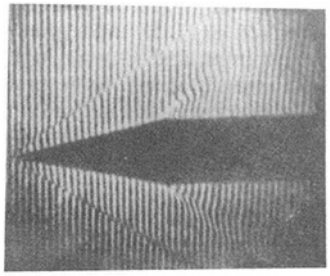

Fig. 2 Deflectogram of a 23 deg cone in a flow at zero angle of attack taken from Stricker et al. (1983) $M = 1.98$; $P_{st} = 3.15$ atm

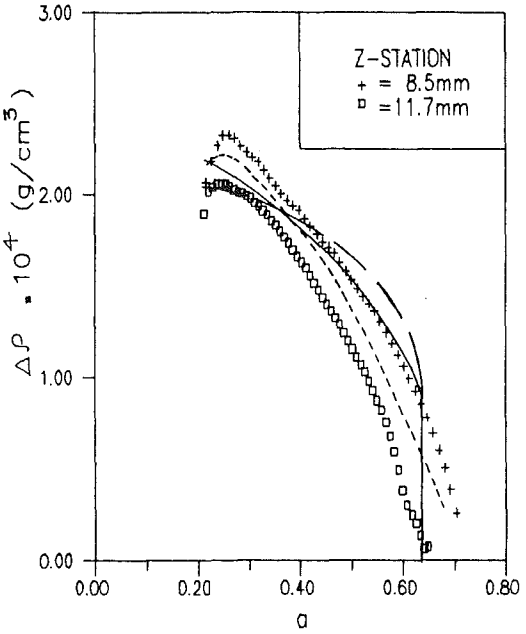

Fig. 3 Density change distribution at Z-station and comparison of results; continuous curve: theory; long-dashed curve: Stricker et al. (1983); short-dashed curve: average expt. curve

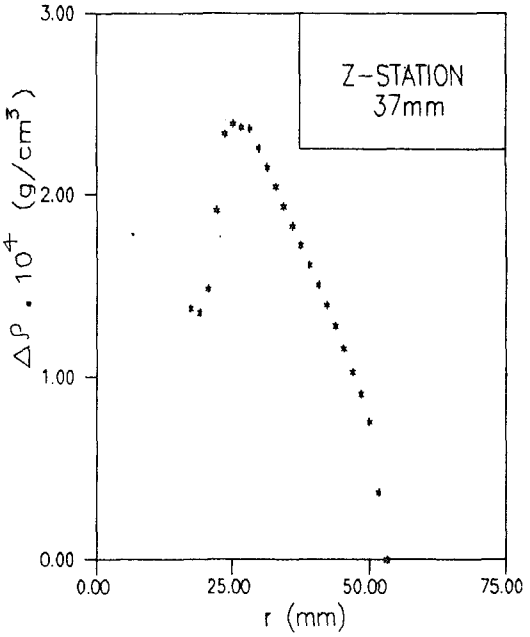

Fig. 4 Density change distribution for a Z-station after expansion over cone shoulder

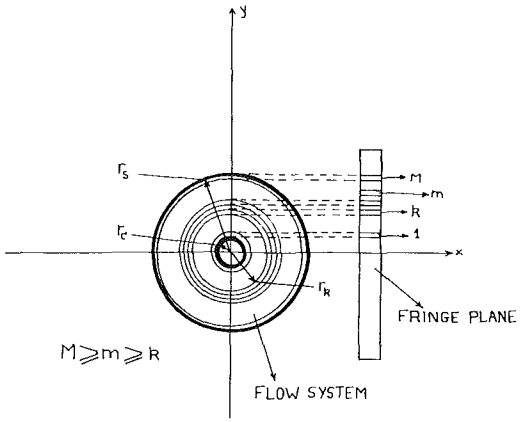

Fig. 5 Representation of sub-zone analytical integration scheme for Abel transforms

Analytical Setup

The photograph on Fig. 2 was captured and stored in an image file through a CCD camera fitted with a macro lens of fixed focal length. The image processing was carried out on a PC-XT configured with Matrox PIP card. Spatial averaging to remove electrical noise was carried out. The image was then thinned through a multi-directional scanning and thinning algorithm. The pixel fringe shifts were inverse Abel transformed to actual length scales by taking several fringes and transforming with Eqs. (5) to (10) using a zone width of five pixels. One pixel is equivalent to 0.01934(mm) on the photograph.

Results and Discussion

Figure 3 shows the results of the Abel transform inversion algorithm. The plots are made for $\Delta\rho = \rho - \rho_\infty$ against conical variable 'a' defined as $a = r/z$. The data points shown for two fringes are selected to show the extreme variation. The average curve agrees very well with the Taylor and Maccoll (1933) theoretical curve. But after the shock the fringe shifts have carried over further to give an erroneous prediction. This anomalous situation is due to the paraxial approximation considered. In the zone $y \cong r_c$, the highly refracting shock is intercepted by light rays at almost right angles. This is somewhat reduced as the changes caused by the force part of the shock are somewhat undone by the aft part of the shock when light passes through it. However, as one considers light rays at $y \cong r_s$, the interception angle is close to 180 deg and both fore and aft parts of the shock (fore and aft parts of shock are in with respect to the light ray path) destroys the straight path. This can be solved by considering Δn_s only up to the shock and discarding the carried over values. But for a complete solution, ray tracing has to be carried by considering the flow to be strongly refracting. Results of Stricker et al. (1983) agree well at $y = r_s$ with the theoretical curve; however, this is owing to the use of a step function assumption at $y = r_s$. Though the agreement of the present result at $y = r_s$ with theoretical result is not good, it is to be noted that the analysis does not assume any functional forms for fringe shift data. Attributing this disagreement to the paraxial approximation, as mentioned above, there are reasons to see that the present analysis is completely general, unlike the method suggested by Stricker et al. (1983).

Figure 4 shows $\Delta\rho$ mapped for a z-plane location on the photograph after expansion through the fan centered at the shoulder rim. The density change distribution after expansion over the cone shoulder, at a particular z-station, is shown in this figure.

Uncertainty of Analysis of the Fringe System

It is not straightforward to measure or estimate the uncertainty that creeps in due to (1) the paraxial approximation, (2) video, photograph and CCD array noise, and (3), linear approximation of the fringe form in the small zones over which the Abel inversion is carried out. At the present, it is only possible to point out these sources for error. However, the uncertainty due to spatial resolution is magnification dependent and in the presented analysis a magnification of 17 has been used on Fig. 2. All data points shown have their associated uncertainty of ± 1 pixel. The uncertainty in intensity is the minimum irradiance value, which finally surfaces in the spatial uncertainty (i.e., since an irradiance uncertainty of ± 1 level is the minimum, the location of thinned line can be uncertain only by its product with gradient of intensity). Since the thinned line was positioned at zero gradient, uncertainty due to intensity measurements is seen to be negligible compared to the spatial uncertainty. For ± 1 pixel shift uncertainty, the density change uncertainty varies from a maximum of $\pm 1 \times 10^{-5}$ (g/cm^3) at $r = r_c$ to $\pm 2 \times 10^{-7}$ (g/cm^3) at $r = r_s$.

Summary

Application of DMI for mapping conical flows has been demonstrated. The modifications made to a previously suggested algorithm for image reconstruction from Abel-transformed data has been shown. Various improvements and modifications on the presented methodology has been suggested for further work.

Acknowledgments

The authors wish to thank B. R. Pramod, Mechanical Engineering Department, Utah State University and V. Phankawala, Mechanical Engineering Department, Indian Institute of Technology, Kanpur for their help rendered in DIP. Dr. K. Ramesh, Mechanical Engineering Department, Indian Institute of Technology, Kanpur is acknowledged for making available the DIP facilities of the experimental stress analysis laboratory for this work.

References

Hesselink, L., 1988, "Digital Image Processing in Flow Visualization," *Ann. Rev. Fluid Mech.*, Vol. 20, pp. 421–485.

Jain, A. K., 1989, *Fundamentals of Digital Image Processing*, Prentice-Hall Inc., NJ.

Nestor, O. H., and Olsen, H. N., 1960, "Numerical Methods for Reducing Line and Surface Probe Data," *SIAM Rev.*, Vol. 2, No. 3, pp. 200–207.

Srikanth, R., and Rathakrishnan, E., 1991, "Digital Moire Interferometry in Experimental Analysis of Compressible Flows," *Journal of Mechanics Research Comm.*, Vol. 18, No. 6, pp. 345–358.

Stricker, J., Keren, E., and Kafri, O., 1983, "Axisymmetric Density Field Measurements by Moire Deflectometry," *AIAA*, Vol. 21, No. 12, pp. 1767–1769.

Taylor, G. I., and Maccoll, J. W., 1933, *Proceedings of the Royal Society*, Series A, Vol. 139, p. 278.

C. Dugué

D. H. Fruman

Groupe Phénomènes d'Interface,
Ecole Nationale Supérieure
de Techniques Avancées,
91120 Palaiseau, France

J-Y. Billard

P. Cerrutti

Laboratoire d'Hydrodynamique,
Ecole Navale,
29240 Brest Naval, France

Dynamic Criterion for Cavitation of Bubbles

The classical criterion for cavitation of bubbles is based on the assumption that the bubbles are subjected to a quasi-steady pressure change and that the non condensible gas within the cavity behaves isothermally. No simple criterion accounting for the dynamic terms in the Rayleigh-Plesset equation is presently available. In this paper, a criterion for cavitation of bubbles, which takes into account the contribution of the dynamic terms in the Rayleigh-Plesset equation, is obtained and presented in a new useful form which allows rapid computation of the critical pressure whatever the fluid and the nuclei initial conditions are. The impact of these results on different flow situations are analyzed and discussed.

1 Introduction

Inception of cavitation in a liquid flow is directly related to the size and population of nuclei within the fluid. In particular, explosive bubble growth depends on the size of the nucleus and the surface tension, as the usual quasi-steady criterion tells. This criterion is, however, unable to account for the dynamic effects which prevail in numerous practical situations when the pressure changes can be assimilated to a sudden, stepwise, pressure reduction and, in particular, when small amplitude pressure fluctuations are superimposed to a mean pressure much larger than the critical one, Billard et al. (1988). Practically, these late situations can be those associated, for example, to turbulent pressure fluctuations and active sonar pressure waves. For a stepwise reduction of the ambient pressure and water at 20°C, Matsumoto and Beylich (1985) have numerically computed the (dynamic) critical pressure and compared their results with those of Sato and Shima (1979). However, these results can not be directly used to determine the dynamic critical pressure for, say, water at other temperatures and initial ambient pressure or for other fluids.

In this paper, a more general approach, without considering either evaporation and condensation or water compressibility effects, is taken. By properly nondimensionalizing the Rayleigh-Plesset equation, a general method to compute the critical conditions for an instantaneous pressure step and any value of the polytropic coefficient of the gas within the nucleus is proposed. A range of critical pressures for which the nuclei can grow asymptotically is determined. The major conclusion, applicable for example to venturi susceptibility meters or to sudden pressure drops on the succion side of foils, is that, depending on the pressure evolution and thermodynamics of the noncondensible gas within the bubble, nuclei can display very different critical pressures and radii.

Contributed by the Fluids Engineering Division for publication in the JOURNAL OF FLUIDS ENGINEERING. Manuscript received by the Fluids Engineering Division February 22, 1991. Associate Technical Editor: M. L. Billet.

2 The Rayleigh-Plesset Equation and the Quasi-Static Criterion

The Rayleigh-Plesset equation is,

$$\rho\left(rr'' + \frac{3}{2}r'^2\right) = \left(p_{\infty 0} - p_v + \frac{2\gamma}{r_0}\right)\left(\frac{r_0}{r}\right)^{3k} - p_\infty(t) + p_v - \frac{2\gamma}{r} \quad (1)$$

where ρ, μ, and γ are the density, the viscosity and the surface tension of the liquid respectively, r_0 is the radius of the nucleus in equilibrium at pressure $p_{\infty 0}$ before the pressure change is applied, r is the radius at time t, p_v the vapor pressure $p_\infty(t)$ the pressure at time t and k is the polytropic coefficient. The symbol $'$ indicates a time derivative.

If the evolution of the pressure field $p_\infty(t)$ is such that its characteristic time is much larger than the natural period of the nucleus, the terms on the left-hand side of Eq. (1) can be neglected. Since the equation is now independent of time, we set $p_\infty(t) = p_\infty$ and k equal to one. We have then,

$$p_\infty = p_v + \left(p_{\infty 0} - p_v + \frac{2\gamma}{r_0}\right)\left(\frac{r_0}{r}\right)^3 - \frac{2\gamma}{r} \quad (2)$$

It leads to the well-known condition for explosive growth,

$$r_{cs} = r_0\sqrt{3\left(\frac{p_{\infty 0} - p_v}{2\gamma}r_0 + 1\right)} \quad (3)$$

where the subscript "*cs*" is used to specify the "critical steady" conditions. The corresponding value of the pressure is,

$$p_{cs} = p_v - \frac{4\gamma}{3r_{cs}} \quad (4)$$

The values of r_{cs} and p_{cs} are obtained as a function of r_0 and $p_{\infty 0}$.

A more convenient presentation can be achieved by recalling that Eq. (2) is equivalent to,

$$\frac{p_\infty - p_v}{2\gamma} r = \frac{p_g}{2\gamma} r - 1 \tag{5}$$

where p_g is the partial pressure of the gas within the nucleus. The right-hand term is equivalent to a Weber number which characterizes the instantaneous condition of the noncondensible gas. We therefore set,

$$\mathcal{W}_0 = \frac{p_{\infty 0} - p_v}{2\gamma} r_0; \quad \mathcal{W} = \frac{p_\infty - p_v}{2\gamma} r; \quad \mathcal{W}^* = \frac{p_\infty - p_v}{2\gamma} r_0;$$

$$\alpha = \frac{1}{\beta} = \frac{p_\infty - p_v}{p_{\infty 0} - p_v} \tag{6}$$

and notice that the Weber numbers can be negative and that Eq. (5) implies that,

$$\mathcal{W}_0 \geq -1 \text{ and } \mathcal{W} \geq -1 \text{ since } p_g > 0.$$

Equation (2), generalized to any polytropic coefficient, can then be written as,

$$\mathcal{W}_0 = -1 + \mathcal{W}^* \left(1 + \frac{1}{\mathcal{W}}\right) \left(\frac{\mathcal{W}}{\mathcal{W}^*}\right)^{3k} \tag{7}$$

from which the critical Weber number is obtained for $d\mathcal{W}_0/d\mathcal{W} = 0$,

$$\mathcal{W}_{cs} = -\frac{3k-1}{3k} < 0 \tag{8}$$

Following (6), $\mathcal{W}_{cs} < 0$ implies that $\mathcal{W}^* < 0$. Thus, by replacing (8) into (7), the steady criterion is given by,

$$1 + \mathcal{W}_0 = \frac{(3k-1)^{3k-1}}{(3k)^{3k} |\mathcal{W}^*_{cs}|^{3k-1}} \tag{9}$$

For $k = 1$ the system of Eqs. (8) and (9) is equivalent to Eqs. (3) and (4). The main advantage of this presentation is that Eq. (9) provides, for each value of k, a single curve relating the initial conditions summarized by $\mathcal{W}_0$ to the final ones summarized by $\mathcal{W}^*_{cs}$.

3 The Dynamic Criterion

3.1 The General Situation. In more general situations, when the time scale of the pressure reduction, mean or instantaneous, is of the same order of magnitude or smaller than the natural period of the bubble, the left hand terms of Eq. (1) must be taken into account. These are called here "rapidly varying pressure fields."

Since equation (1) is nonlinear, no general results concerning the behavior of the nucleus can be explicitly obtained. It is also clear that, as for all dynamical systems, the existence of static stability does not guarantee dynamic stability. This fact is often ignored in problems regarding cavitation. In order to obtain explicit results, only the case of an instantaneous pressure drop from a constant initial value $p_{\infty 0}$ to a constant final value p_∞, which is a situation opposite to the quasi-static case, will be considered here. Between these two extreme cases, the critical pressure will change continuously depending on the $dp_\infty(t)/dt$ value.

Equation (1), nondimensionalized using expressions (6) and a time scale $1/\omega$, is rewritten as,

$$\frac{4\rho\omega^2\gamma^2}{(p_\infty - p_v)^3} \left(\mathcal{W}\mathcal{W}'' + \frac{3}{2}\mathcal{W}'^2\right) = \left(\beta + \frac{1}{\mathcal{W}^*}\right) \left(\frac{\mathcal{W}^*}{\mathcal{W}}\right)^{3k} - 1 - \frac{1}{\mathcal{W}} \tag{10}$$

By choosing ω such that the coefficient of the left-hand side be equal to one,

$$\omega = \frac{1}{2\gamma} \sqrt{\frac{|p_\infty - p_v|^3}{\rho}} \tag{11}$$

Eq. (10) becomes,

$$\pm \left(\mathcal{W}\mathcal{W}'' + \frac{3}{2}\mathcal{W}'^2\right) = \left(\beta + \frac{1}{\mathcal{W}^*}\right) \left(\frac{\mathcal{W}^*}{\mathcal{W}}\right)^{3k} - 1 - \frac{1}{\mathcal{W}} \tag{12}$$

The positive sign holds for $p_\infty > p_v$ and the negative one for $p_\infty < p_v$. Consideration of equation (12) clearly shows that it is a function of a single parameter,

$$\left(\beta + \frac{1}{\mathcal{W}^*}\right) |\mathcal{W}^*|^{3k} = (1 + \mathcal{W}_0) |\mathcal{W}^*|^{3k-1} \tag{13}$$

which relates the initial conditions, $\mathcal{W}_0$, to the final ones, $\mathcal{W}^*$.

Using the following identity,

$$2\mathcal{W}^2\mathcal{W}' \left(\mathcal{W}\mathcal{W}'' + \frac{3}{2}\mathcal{W}'^2\right) = (\mathcal{W}^3\mathcal{W}'^2)' \tag{14}$$

equation (12) can be integrated once to obtain,

$$\pm \mathcal{W}'^2 = -\frac{2}{3(k-1)} \left(\beta + \frac{1}{\mathcal{W}^*}\right) \left(\frac{\mathcal{W}^*}{\mathcal{W}}\right)^{3k} - \frac{1}{\mathcal{W}} - \frac{2}{3} + \frac{K}{\mathcal{W}^3} \tag{15}$$

where the constant of integration K is obtained for the initial conditions $\mathcal{W}' = 0$ at $t = 0$,

$$K = \frac{2}{3(k-1)} (1 + \beta\mathcal{W}^*)\mathcal{W}^{*2} + \frac{2}{3}\mathcal{W}^{*3} + \mathcal{W}^{*2} \tag{16}$$

The interesting situation to be considered corresponds to the case $p_\infty < p_v$; thus a negative sign affects the left-hand term in Eq. (15). Therefore, only solutions for which the right-hand side is negative will have a physical significance. Analysis of Eq. (15) shows that three cases are possible (represented graphically in Fig. 1): a single root corresponding to asymptotic growth of the bubble from the very beginning (case *a*), three roots corresponding to the oscillation of the bubble between the first and the second root (case *b*) and two roots, with one double, corresponding to the critical situation (case *c*). The double root determines the conditions for the critical dynamic criteria, with,

$$\mathcal{W}'^2 = 0 \text{ and } \frac{d\mathcal{W}'^2}{d\mathcal{W}} = 0 \tag{17}$$

which is equivalent to,

$$\mathcal{W}' = 0 \text{ and } \mathcal{W}'' = 0 \tag{18}$$

The criterion just appears as the bifurcation condition of the nonlinear Eq. (12).

From the above conditions it follows that in Eq. (12) the left-hand side term is zero,

$$\pm \left(\mathcal{W}\mathcal{W}'' + \frac{3}{2}\mathcal{W}'^2\right) = \left(\beta + \frac{1}{\mathcal{W}^*}\right) \left(\frac{\mathcal{W}^*}{\mathcal{W}}\right)^{3k} - 1 - \frac{1}{\mathcal{W}} = 0 \tag{19}$$

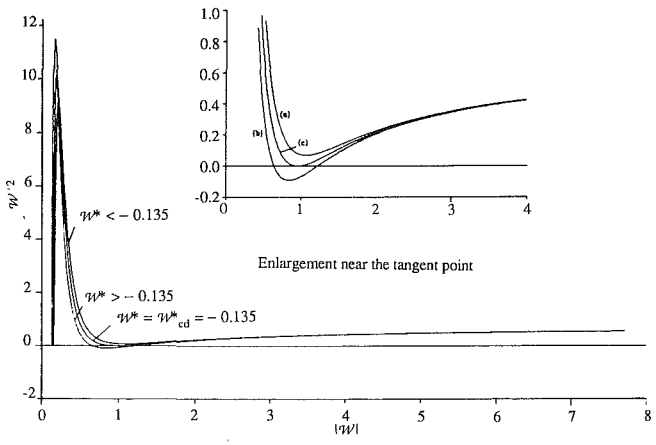

Fig. 1 Example of curves given by Eqs. (15) and (16) for $k = 1.2$, $p_{\infty 0} = 101325$ Pa, $r_0 = 10$ μm, $\mathcal{W}_0 = 6.5$

and the right-hand side is strictly equal to Eq. (7),

$$(1+\mathcal{W}_0)\left(\frac{\mathcal{W}^*_{cd}}{\mathcal{W}_{cd}}\right)^{3k}-\mathcal{W}^*_{cd}\left(1+\frac{1}{\mathcal{W}_{cd}}\right)=0 \tag{20}$$

This means that the Rayleigh-Plesset equation behaves quasi-steadily in the neighborhood of the critical point. Equation (15) is now equal to zero,

$$-\frac{2}{3(k-1)}\left(\beta+\frac{1}{\mathcal{W}^*_{cd}}\right)\left(\frac{\mathcal{W}^*_{cd}}{\mathcal{W}_{cd}}\right)^{3k}-\frac{1}{\mathcal{W}_{cd}}-\frac{2}{3}+\frac{K}{\mathcal{W}^3_{cd}}=0 \tag{21}$$

with the constant given by,

$$K=\frac{2}{3(k-1)}(1+\beta\mathcal{W}^*_{cd})\mathcal{W}^{*2}_{cd}+\frac{2}{3}\mathcal{W}^{*3}_{cd}+\mathcal{W}^{*2}_{cd} \tag{22}$$

Substituting (20) into (21) and (22), we have,

$$2k\mathcal{W}^3_{cd}+(3k-1)\mathcal{W}^2_{cd}-2(1+\mathcal{W}_0)\mathcal{W}^{*2}_{cd}-(k-1)(2\mathcal{W}^*_{cd}+3)\mathcal{W}^{*2}_{cd}=0 \tag{23}$$

Equations (20) and (23) are analogous to (8) and (9) in the quasi-steady situation. The critical pressure $\mathcal{W}^*_{cd}$ is obtained as a function of the initial condition $\mathcal{W}_0$ by equating $\mathcal{W}_{cd}$ in Eqs. (20) and (23).

It is possible to present the criterion in a more explicit way by introducing the ratio between the initial nucleus radius and the critical value r_{cd}. Let z be that radius,

$$z=\frac{r_0}{r_{cd}}=\frac{\mathcal{W}^*_{cd}}{\mathcal{W}_{cd}} \tag{24}$$

then, Eqs. (20) and (23) can be rewritten as,

$$(1+\mathcal{W}_0)z^{3k-1}-(\mathcal{W}_{cd}+1)=0 \tag{25}$$

$$2k\mathcal{W}_{cd}+(3k-1)-2(1+\mathcal{W}_0)z^2-(k-1)(2z\mathcal{W}_{cd}+3)z^2=0 \tag{26}$$

It is easy then to obtain an explicit relation between $\mathcal{W}_0$ and z,

$$1+\mathcal{W}_0=\frac{k-1}{2z^2}\,\frac{1+2z^3-3z^2}{[(k-1)z^3-k]z^{3(k-1)}+1} \tag{27}$$

which can be solved in a very simple way: firstly, either $\mathcal{W}_0$ or z are imposed and by equation (27) either z or $\mathcal{W}_0$ are obtained; secondly, $\mathcal{W}_{cd}$ is obtained by Eq. (25) and finally $\mathcal{W}^*_{cd}$ is obtained from Eq. (24). Two specific situations, $k=1$ for which Eq. (15) is singular and $k=4/3$ for which an explicit solution can be obtained will be considered next.

3.2 Case $k=1$. When $k=1$, Eq. (12) can be integrated,

$$\pm\mathcal{W}'^2=2(1+\beta\mathcal{W}^*)\mathcal{W}^{*2}\,\frac{\mathrm{Log}|\mathcal{W}|}{\mathcal{W}^3}-\frac{1}{\mathcal{W}}-\frac{2}{3}+\frac{K}{\mathcal{W}^3} \tag{28}$$

where K is equal to,

$$K=-2(1+\beta\mathcal{W}^*)\mathcal{W}^{*2}\mathrm{Log}|\mathcal{W}^*|+\mathcal{W}^{*2}+\frac{2}{3}\mathcal{W}^{*3} \tag{29}$$

These two equations are the counterpart of (15) and (16) for all values of k different than one. They differ from the equation already discussed by Darrozès and Chahine (1983, Eq. (11)) by the fact that the surface tension has been taken into account. This is a major new element since otherwise asymptotic growth occurs as soon as p_∞ becomes equal to p_v, i.e., cavitation is not moderated by surface tension effects.

With Eq. (24) remaining unchanged, Eqs. (25) and (27) become,

$$(1+\mathcal{W}_0)z^2-(\mathcal{W}_{cd}+1)=0 \tag{30}$$

$$1+\mathcal{W}_0=\frac{1}{2z^2}\,\frac{1+2z^3-3z^2}{z^3-3\,\mathrm{Log}\,z-1} \tag{31}$$

which can be solved using the procedure described in the previous paragraph.

3.3 Case $k=4/3$. When $k=4/3$, Eqs. (20) and (21) become polynomials and, after some lengthy and tedious computation, an explicit relation between $\mathcal{W}_0$ and $\mathcal{W}^*_{cd}$ can be obtained,

$$1+\mathcal{W}_0=\frac{(\mathcal{W}^*_{cd}+3/2)^2}{81\mathcal{W}^{*2}_{cd}}\left(3-7\mathcal{W}^*_{cd}+(3-4\mathcal{W}^*_{cd})\sqrt{\frac{3-4\mathcal{W}^*_{cd}}{3+2\mathcal{W}^*_{cd}}}\right) \tag{32}$$

This expression can be compared to the quasi-steady criterion issued from expression (9),

$$1+\mathcal{W}_0=\frac{27}{256|\mathcal{W}^*_{cs}|^3} \tag{33}$$

4 Results and Discussion

The values of $\mathcal{W}^*_{cs}$, $\mathcal{W}^*_{cd}$, r_{cd}/r_0, r_{cs}/r_0, computed for some values of $\mathcal{W}_0$ and $k=1$, 1.25, and 1.4, are presented in Tables 1 to 3. By using these tables the critical dynamic conditions can be easily determined for any practical situation by linear interpolation. For values of $\mathcal{W}_0$ comprised between -1 and 5, Fig. 2 shows $\mathcal{W}^*_{cs}$ and $\mathcal{W}^*_{cd}$ for the limiting cases corresponding to isothermal and adiabatic behavior of the noncondensible gas within the bubbles

Before discussing these results it is interesting to compute the values of $\mathcal{W}_0$, Eq. (6), for some practical situations which can exist in the case of water at ambient temperature ($\gamma=0.071$). For a marine propeller of a surface ship at a depth of 5 m, $p_{\infty 0}=1.5\ 10^5$ Pa and $r_0=1$ μm, $\mathcal{W}_0\approx 1$. For a submarine operating at a depth of 300 m, $p_{\infty 0}=31\ 10^5$ Pa and $r_0=4.6$ μm, $\mathcal{W}_0\approx 100$. At intermediate depths, for example 20 meters, $p_{\infty 0}=3\ 10^5$ Pa and $r_0=5$ μm, $\mathcal{W}_0\approx 10$. Thus, depending on the operating conditions, large variations of $\mathcal{W}_0$ can be achieved.

Detailed analysis of the data in Tables 1 to 3 leads to the following:

1 for all values of k and $\mathcal{W}_0$ the critical radii issued from the dynamic criterion are larger than those obtained from the quasi-steady criterion. Thus, a nucleus of given initial radius will grow asymptotically, in a slowly varying pressure field, after reaching a smaller radius than in a rapidly varying pressure field.

2 since for all values of k and $\mathcal{W}_0$, $\mathcal{W}^*_{cs}(\mathcal{W}_0,k)<\mathcal{W}^*_{cd}(\mathcal{W}_0,k)$,

Table 1 Critical Weber numbers and radii as a function of the initial Weber number for $k=1$

$k=1.00$ $\qquad \frac{3k-1}{k}=0.6667$

$\mathcal{W}_0$	$\lvert\mathcal{W}^*_{cd}\rvert$	$\lvert\mathcal{W}^*_{cs}\rvert$	r_{cd}/r_0	r_{cs}/r_0
-0.6	0.6067	0.6086	1.147	1.095
-0.3	0.4401	0.4600	1.757	1.449
0.0	0.3525	0.3849	2.301	1.732
0.3	0.2980	0.3376	2.798	1.975
0.6	0.2606	0.3043	3.259	2.191
1.0	0.2255	0.2722	3.829	2.449
1.3	0.2060	0.2538	4.230	2.627
1.5	0.1952	0.2434	4.486	2.739
2.0	0.1736	0.2222	5.095	3.000
2.5	0.1572	0.2057	5.667	3.240
3.0	0.1444	0.1925	6.207	3.464
4.0	0.1253	0.1721	7.213	3.873
5.5	0.1063	0.1510	8.580	4.416
6.5	0.0972	0.1405	9.420	4.743
8.0	0.0868	0.1283	10.597	5.196
9.5	0.0789	0.1188	11.695	5.612
12	0.0693	0.1068	13.387	6.245
15	0.0611	0.0962	15.245	6.928
18	0.0551	0.0883	16.959	7.550
20	0.0519	0.0840	18.037	7.937
35	0.0377	0.0642	25.029	10.392
50	0.0307	0.0539	30.822	12.369
70	0.0253	0.0457	37.479	14.595
100	0.0207	0.0383	46.065	17.407
200	0.0140	0.0271	68.553	24.556
400	0.0095	0.0192	101.581	34.684
1000	0.0057	0.0122	169.825	54.800

Table 2 Critical Weber numbers and radii as a function of the initial Weber number for $k = 1.25$

$k = 1.25 \qquad \frac{3k-1}{k} = 0.7333$

$\mathcal{W}_0$	$\lvert\mathcal{W}^*_{cd}\rvert$	$\lvert\mathcal{W}^*_{cs}\rvert$	r_{cd}/r_0	r_{cs}/r_0
-0.6	0.6265	0.6328	1.252	1.159
-0.3	0.4896	0.5163	1.721	1.420
0.0	0.4125	0.4535	2.115	1.617
0.3	0.3618	0.4122	2.462	1.779
0.6	0.3254	0.3822	2.777	1.919
1.0	0.2898	0.3524	3.159	2.081
1.3	0.2693	0.3350	3.424	2.189
1.5	0.2577	0.3250	3.592	2.257
2.0	0.2340	0.3041	3.988	2.411
2.5	0.2156	0.2876	4.354	2.550
3.0	0.2008	0.2739	4.697	2.677
4.0	0.1783	0.2526	5.328	2.903
5.5	0.1550	0.2296	6.172	3.194
6.5	0.1436	0.2180	6.684	3.365
8.0	0.1303	0.2040	7.394	3.595
9.5	0.1200	0.1929	8.049	3.803
12	0.1072	0.1784	9.048	4.110
15	0.0960	0.1655	10.131	4.432
18	0.0877	0.1554	11.118	4.718
20	0.0832	0.1499	11.735	4.893
35	0.0627	0.1232	15.657	5.952
50	0.0523	0.1085	18.827	6.756
70	0.0440	0.0962	22.405	7.619
100	0.0367	0.0847	26.935	8.661
200	0.0258	0.0659	38.482	11.124
400	0.0181	0.0513	54.883	14.300
1000	0.0114	0.0368	87.528	19.944

Table 3 Critical Weber numbers and radii as a function of the initial Weber number for $k = 1.4$

$k = 1.40 \qquad \frac{3k-1}{k} = 0.7619$

$\mathcal{W}_0$	$\lvert\mathcal{W}^*_{cd}\rvert$	$\lvert\mathcal{W}^*_{cs}\rvert$	r_{cd}/r_0	r_{cs}/r_0
-0.6	0.6391	0.6479	1.282	1.176
-0.3	0.5139	0.5439	1.694	1.401
0.0	0.4413	0.4866	2.032	1.566
0.3	0.3924	0.4483	2.326	1.700
0.6	0.3566	0.4201	2.591	1.814
1.0	0.3210	0.3918	2.911	1.945
1.3	0.3003	0.3751	3.132	2.031
1.5	0.2884	0.3654	3.272	2.085
2.0	0.2640	0.3452	3.599	2.207
2.5	0.2448	0.3289	3.902	2.316
3.0	0.2291	0.3155	4.185	2.415
4.0	0.2051	0.2942	4.704	2.589
5.5	0.1798	0.2711	5.396	2.811
6.5	0.1674	0.2592	5.815	2.939
8.0	0.1527	0.2449	6.395	3.111
9.5	0.1412	0.2334	6.929	3.265
12	0.1268	0.2183	7.742	3.490
15	0.1141	0.2046	8.621	3.724
18	0.1046	0.1939	9.422	3.930
20	0.0994	0.1879	9.922	4.055
35	0.0757	0.1588	13.090	4.799
50	0 0634	0.1424	15.643	5.350
70	0.0537	0.1284	18.518	5.933
100	0.0449	0.1150	22.153	6.624
200	0.0318	0.0928	31.392	8.213
400	0.0224	0.0748	44.479	10.192
1000	0.0142	0.0562	70.466	13.564

a nucleus can be subjected to a premature asymptotic growth in a rapidly varying pressure field.

3 for the larger values of $\mathcal{W}_0$ the critical radius issued from the dynamic criterion can be three (isothermal conditions) to five (adiabatic conditions) times larger than that obtained from the quasi-steady criterion.

4 for $\mathcal{W}_0 = -(3k-1)/3k$, $\mathcal{W}^*_{cs}(\mathcal{W}_0,k) = \mathcal{W}^*_{cd}(\mathcal{W}_0,k)$, because nuclei are not stable even for small perturbations. The limiting values of $\mathcal{W}_0$ are -0.762 and -0.666 for the adiabatic and the isothermal cases, respectively.

5 the values of $\mathcal{W}^*_{cs}$ for $k = 1$ are practically equal to those of $\mathcal{W}^*_{cd}$ for $k \approx 1.25$. There is a region where, depending on the values of k, the critical values of $\mathcal{W}^*$ issued from the dynamic and the quasi-steady criterion overlap.

What these results clearly show is that the isothermal quasi-steady criterion usually employed to analyze cavitation inception data in a variety of flow situations can not provide a definite response concerning either the size of the nuclei or the critical pressures. Indeed, depending on the way the pressure variation is applied and the effective thermodynamic behavior of the noncondensible gas included in the bubble, very different results can be obtained. As the example, let us consider the case of salt water (≈ 25 grams salt per liter) at ambient temperature ($\gamma = 0.0767$) and atmospheric pressure ($p_{\infty 0} = 101325$ Pa). Figure 3 shows the critical pressure obtained with the isothermal quasi-steady criterion and with the dynamic criterion for isothermal and adiabatic conditions. For an initial nucleus radius of 10 μm, the value of $\mathcal{W}_0$ is 6.45, the corresponding value of $\mathcal{W}^*_{cd}$ is -0.1674 for the adiabatical case and -0.0972 for the isothermal case. They lead to a dynamic critical pressure comprised between a minimum of -230 Pa and a maximum of 846 Pa depending on the noncondensible gas behaving adiabatically or isothermally respectively. For the same conditions the critical radius are respectively 58.1 and 94.2 μm. Matsumoto and Beylich (1985) obtained for a nucleus having the same radius and a complete numerical computation, which takes into account gas diffusion, evaporation, condensation and liquid compressibility, a critical pressure of 839.8 Pa and a critical radius of 82.6 μm. These two values are very close to those given by the present criterion in the case of an isothermal evolution. Moreover, the values obtained using the present criterion are only a few percent different of those computed numerically by Sato and Shima (1979) taking into account the effect of the viscosity. The viscosity effect is, in any event, small as compared to the one associated with a change of the polytropic constant. Finally, for the isothermal

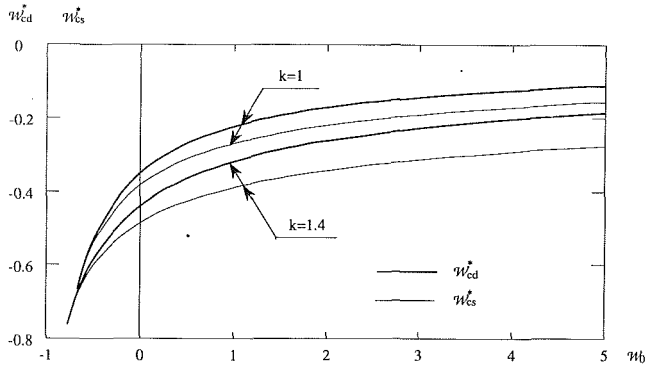

Fig. 2 Critical Weber numbers as a function of the initial Weber number for $k = 1$ and $k = 1.4$

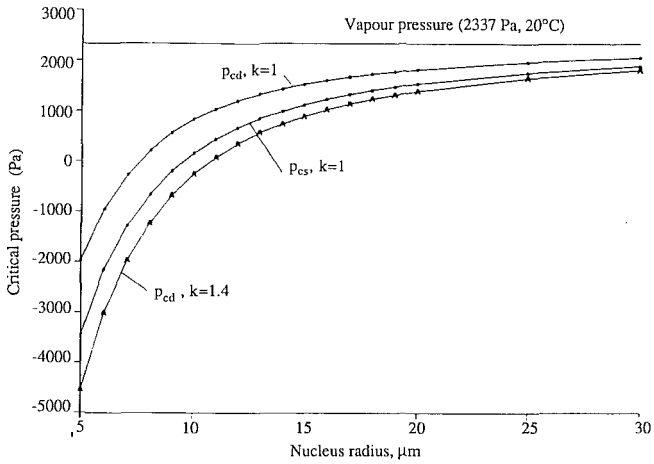

Fig. 3 Critical pressures as a function of the nucleus radius for $p_{\infty 0} = 101325$ Pa

quasi-steady criterion we have a critical pressure of 181 Pa and a critical radius of 47 μm. Thus, the critical pressure can vary over a range of 1000 Pa (0.01 bar) depending on the dynamics of the pressure transient and the thermodynamic behavior of the noncondensible gas.

If the range of the above pressure variation is within the precision of measurements of most of marine applications and its implication, from the practical point of view, can be considered as limited, for tests in cavitation tunnels the results can be significantly altered as it will be seen next. What is important to consider is the difference between the vapor pressure, used in the definition of the cavitation number,

$$\sigma = \frac{p_{\infty 0} - p_v}{\frac{1}{2}\rho U_\infty^2} = \frac{\mathcal{W}_0 \frac{2\gamma}{r_0}}{\frac{1}{2}\rho U_\infty^2}$$

and the critical pressure $p_{\infty c}$ such that a cavitation number defect,

$$\Delta\sigma = \frac{p_v - p_{\infty c}}{\frac{1}{2}\rho U_\infty^2} = \frac{|\mathcal{W}_c^*|}{\mathcal{W}_0}\,\sigma$$

can be defined.

For a nucleus of 10 μm radius, $\sigma = 1$ and two cavitation tunnels; one in which the maximum velocity is 15 m/s and the other 8 m/s, the $\mathcal{W}_0$ values are, respectively, 7.92 and 2.25. From Tables 1 and 3, it is easy to obtain the values of $\mathcal{W}_{cd}^*$ and to compute the cavitation number defect. For the largest test velocities it is comprised between 1 and 2 percent of the cavitation number depending the isothermal or the adiabatic case are taken into account. The relative difference reaches, respectively, 7 and 11 percent in the case of the low free-stream velocity. If the free-stream velocity is still lowered the relative differences increase significantly. For example, if the free stream velocity is further reduced by a factor two, $\mathcal{W}_0 = 0.56$, the relative cavitation defect is, respectively, 90 and 108.6 percent. Thus, for the same nuclei size:

(i) the cavitation number at very low free-stream velocity will be a factor two larger than the one determined at the large velocity;

(ii) the thermodynamics of the noncondensible gas will justify, at the low velocity, a difference of about 20 percent between cavitation numbers.

The only possible way of keeping things equal at any given velocity will be to have the same value of $\mathcal{W}_0$ and thus to modify the size of the nuclei which, for the present situation, should be of 142, 35 and 10 μm radius, respectively, for 4, 8, and 15 m/s. However, because in all cavitation tunnels nuclei above a certain dimension will separate, comparison of cavitation tunnel test results obtained at low and high velocities might be meaningless.

Although similar conclusions can be reached if the quasi-steady criterion is used instead of the dynamic one, the latter one has the advantage of making more physically plausible the possibility for the noncondensible gas in the nuclei to obey to a polytropic thermodynamic behavior. Indeed, for slow pressure transients it can be safely assumed that the gas will behave isothermally. Moreover, even in the case of a pressure step, Matsumoto and Beylich (1985) have shown that during the growth phase isothermal conditions prevail.

Another example is given by the cavitation susceptibility meters in which bubble sizes are determined from the measurement of a critical pressure, p_c, in the throat of a venturi. Let's assume this pressure as well as the pressure upstream, $p_{\infty 0}$, where the nucleus size is r_0, be known. We have then,

$$\left|\frac{p_c - p_v}{p_{\infty 0} - p_v}\right| = \frac{|\mathcal{W}_c^*|}{\mathcal{W}_0}$$

and by using Tables 1 to 3 it is easy to determine the value of $\mathcal{W}_0$ for which such ratio is obtained and thus the value of r_0. As an example, computations were carried out for $p_{\infty 0} = 5\ 10^4$ Pa, $p_c = -2\ 10^3$ Pa and $p_v = 2337$ Pa and the nuclei size obtained were 7.9 and 5.7 μm for the dynamic criterion in adiabatic and isothermal situations. For the quasi-steady criterion in isothermal conditions the nucleus radius is 6.8 μm, in between those given by the dynamic criterion. Therefore, it would be advisable to consider, in analyzing CSM data, a range of nuclei radius instead of a single one.

5 Conclusion

A criterion for cavitation of bubbles which takes into account the contribution of the dynamic terms in the Rayleigh-Plesset equation is proposed. By a suitable choice of dimensionless parameters, results for any initial pressure and nucleus radius are obtained in a very simple and useful form. Tables allowing a rapid computation of the critical pressure and radius for various values of the polytropic coefficient are given. It is shown that critical pressures and nuclei radii obtained using the classical isothermal quasi-steady criterion are comprised between those computed using the dynamic criterion for the limiting cases of isothermal and adiabatic gas behavior.

Acknowledgment

The authors wish to express their deep appreciation to the reviewers for pertinent and useful comments. The Direction des Recherches, Etudes et Techniques from the Ministry of Defense, France, partially supported this work through grant DRET 88/1040.

References

Darrozès, J. S., and Chahine, G. L., 1983, "Les Recherches sur le Phénomène de Cavitation Effectuées à l'ENSTA," Sciences et Techniques de l'Armement, Paris, Imprimerie Nationale.

Billard, J. Y., Grosjean, F., and Fruman, D. H., 1988, "Effect of a Step Pressure Pulse with a Superimposed Périodic Pressure Wave on the Growth and Collapse of Cavitation Bubble," *Cavitation and Multiphase Flow Forum*, ASME FED64.

Matsumoto, Y., and Beylich, A. E., 1985, "Influence of Homogeneous Condensation Inside a Small Gas Bubble on its Pressure Response," ASME JOURNAL OF FLUIDS ENGINEERING, Vol. 107, pp. 281–286.

Sato, Y., and Shima, A., 1979, "The Growth of Bubbles in Viscous Incompressible Liquids," Report of Institute of High Speed Mechanics, 40-319, pp. 23–49.

Occurrence of Bubbles in a Thin Wire at Low Reynolds Number

K. Sato
Professor,
Mechanical Engineering Department,
Kanazawa Institute of Technology,
Ishikawa 921, Japan

Thin wires of various diameters from 0.07 to 0.7 mm are examined about appearances and characteristics of bubble occurrence behind them in the range of low Reynolds numbers. The appearance of bubbles is very dependent on diameters of wires. Two different types of bubbles can be observed in the present experiment. One is a streamer-type bubble for smaller wires and the other is a small unspherical bubble for larger wires. The incipient and the desinent values of cavitation number also change greatly with the bubble types. The streamer-type bubble is related to the presence of laminar separation zone and the growth due to air diffusion. The small unspherical bubble can be mainly attributed to the motion of rolled-up vortices and the growth due to vaporization.

1 Introduction

The present investigation has three purposes: 1) to make clear a role of thin or very small separation zone in bubble growth, 2) to investigate the mechanism of gaseous growth within a separation zone at inception, 3) to examine cavitation characteristics of a circular cylinder at low Reynolds numbers.

The presence of separation zone plays a very important role in inception of cavitation bubbles. For example, the band-type bubbles in a hemispherical-nosed body (Arakeri and Acosta, 1973) or the streamer bubbles in a Venturi tube (Ito and Oba, 1982) are closely related to laminar separation bubbles on bodies. Vortex-cavitation bubbles are connected with micro-vortices on a separated free shear layer or vortices rolled-up within a vortex formation region. On the other hand, it has been made clear (Arakeri et al., 1981; Arakeri and Ramarajan, 1981) that the appearance of bubble-ring cavitation varies with the thickness of laminar separation bubble. Therefore, it is very interesting to systematically examine characteristics of bubble occurrence for bodies with a thin or a small separation zone such as a thin wire.

Cavitation can be divided into two types of vaporous and gaseous cavitation (Holl, 1969). Vaporous cavitation has received the most attention because of its importance on industry. It is, however, generally accepted that cavitation nuclei are small gas bubbles in a liquid or a crevice on a solid surface. In addition, it has been indicated (Parkin, 1981) that gaseous growth occurs inside laminar separation zone to initiate bubble-ring cavitation on a hemispherical-nosed body. There are also many other works for air content effects on cavitation inception, erosion, and performance of machinery (for example, Hammitt, 1972; Arndt, 1981). Gaseous growth, especially, has an important influence on bubble inception in flows with separation zone. Nuclei or small gas bubbles can grow by the gaseous diffusion in the separation zone because they can be exposed to low pressure during a long time within the vortrices or the separation zone which can be easily oversaturated by local pressure reduction due to formation of vortices.

It should be noted that circular cylinders have not been examined systematically about their cavitation inception mechanism in a wide Reynolds number range though they are one of the typical bluff bodies and their flow patterns have been investigated in detail in the field of noncavitating flows.

In the present investigation, thin wires with a circular section were chosen as a test body to examine the characteristics of gaseous or vaporous growth of bubbles in the flow with a thin and small separation zone. The velocities and the wire diameters used in the experiment were relatively small, and thus the range of Reynolds number was less than 3×10^3. The static pressure in the test section was decreased to a level sufficient for growth of bubbles. As a result, two kinds of bubbles were observed with changing the wire diameter.

2 Experimental Facilities

The experiments were carried out in the small cavitation tunnel with a resorber of Kanazawa Institute of Technology as shown in Fig. 1. The working section with acrylic-resin windows has a rectangular cross section 60 mm × 80 mm. A test wire was placed vertically in the middle location of the section. The location was at 145 mm downstream of the nozzle exit. The wire diameters of 0.07, 0.1, 0.14, 0.19, 0.28, 0.54, and 0.7 mm were used under flow velocities from 0 to about 4.5 m/s. The details of wire dimensions and the measurement uncertainties are shown in Table 1. The wires from 0.1 to 0.7 mm in diameter were made of stainless steel and the wires from 0.07 to 0.19 mm were made of nichrome or iron-chrome. Two kinds of materials were used for the wire of 0.1 mm in diameter. The maximum deflection of wires due to flow resistance was less than 2.5 percent of the full wire length 80 mm. The natural frequencies of wires were approximately estimated to be less than half the vortex shedding frequencies in the velocity range used in the present bubble observations.

The flow rate was measured with an electromagnetic flowmeter. The measurement values from the flowmeter was cal-

Contributed by the Fluids Engineering Division and presented at the Winter Annual Meeting, San Francisco, Calif., December 10–15, 1989 of THE AMERICAN SOCIETY OF MECHANICAL ENGINEERS. Manuscript received by the Fluids Engineering Division February 22, 1990. Associate Technical Editor: A. Prosperetti.

Table 1 Details of wire-diameter

Wire Diameter	Measured Value	
d	Mean Value	Uncertainty
0.07 mm	0.068 mm	±0.001 mm
0.10	0.102	±0.001
0.14	0.141	±0.001
0.19	0.193	±0.001
0.28	0.283	±0.001
0.54	0.544	±0.002
0.70	0.695	±0.002

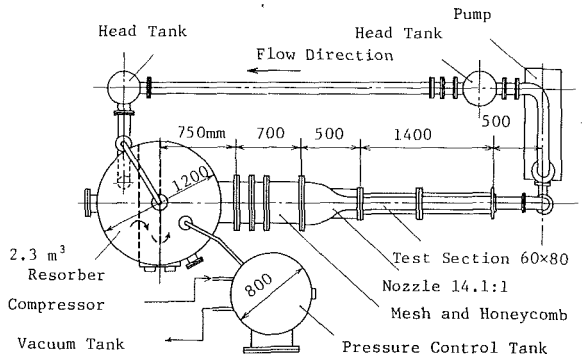

Fig. 1 Cavitation test tunnel

ibrated with the free-stream velocity upstream of the wire using a two-dimensional, laser-doppler velocimeter (LDV). The uncertainty of velocity measurement was estimated to be ±1 percent. The LDV consists of a 4-watt argon-ion laser, TSI inc. optics and counter-type signal processors. The profile of free-stream velocity in the test section was flat to within 0.8 percent in the direction perpendicular to the wire axis. The profile in the direction of wire axis was flat to within 1.0 percent. The thickness of boundary layer on the upper or lower wall surface of test section was estimated to be less than 5 mm. The zone (5 mm) near the wall could not be measured because of the finite beam-crossing angles of laser beams. The turbulence level of the free stream was estimated to be less than 0.5 percent with the LDV (Bogard and Gan, 1987).

The static pressure in the working section was measured with pressure transducers and mercury manometers. The uncertainty in the pressure measurement was estimated to be ±0.2 percent. The amount of air dissolved in water was controlled with a deaerating system and measured with a van-Slyke device. In the measurement of air content, the maximum deviation from averaged values fell within 0.08. A small hole was drilled on the wall surface at the lower end of the wire in order to examine the effect of injection of small bubbles as shown in Fig. 2. The hole was also used to fix the wire and completely sealed at usual experiments without ventilation.

3 Experimental Methods

The present bubble observations were conducted under stroboscopic light. The appearance of bubbles was examined with micro-flash photographs (flash period: 3 μs) and video tapes. Most of the present experiments was conducted under a constant rate of pressure reduction $\Delta P/\Delta t$ in the test section. The reduction rate of pressure $\Delta P/\Delta t$ was very slow (mostly about 7 Pa/s).

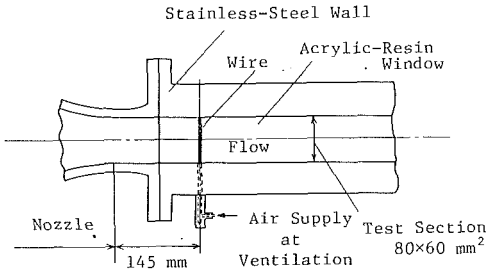

Fig. 2 Details of working section

The air content was set to be from 0.5 to 0.6 at the beginning of tests because there was no large variation during the tests for the value less than 0.6. In addition, Peterson (1972) reported that there were few gas bubbles larger than 25 μm in the case of air content less than 0.6. The change of air content during the tests were less than 0.1. As a result, the air content ranged from 0.42 to 0.58 in the present experiments.

In the first of tests, the static pressure in the tunnel reduced to a low pressure level around 20 KPa. After a circulation of tested water for 1 minute at low velocity, the flow velocity was slowly increased under a constant pressure-reduction rate until inception of bubbles behind a wire. After the development of bubbles, the flow velocity was decreased until the disappearance of bubbles. The typical duration per measurement was about 20 minutes for smaller wire diameters from 0.07 to 0.14 mm and about 60 minutes for larger wire diameters from 0.19 to 0.7 mm. The difference was due to the reason that bubbles occurred earlier for smaller wires.

4 Appearance of Bubbles

In the present experiments, two kinds of bubbles were observed with variation in diameter of wire. For wires larger than 0.19 mm in diameter, unspherical small bubbles were observed at a definite place behind the wires. For wires smaller than 0.14 mm in diameter, streamer-type bubbles were observed. The incipient and the desinent cavitation numbers were widely different from each other.

4.1 The Case of Wire Diameter From 0.07 to 0.14 mm. Figure 3 shows typical appearances of bubbles in various wire diameters. Figures 3(*a*), (*b*) and (*c*) show streamer-type bubbles behind the wires for $d \leq 0.14$ mm. The spatial intervals between each bubble are almost equal. The reason for this regular arrangement of bubbles has not been known clearly though it may be indicated that the regular pattern can be caused by an interference effect between neighboring bubbles

Nomenclature

C_{pb} = base pressure coefficient: $C_{pb} = 2(P_b - P)/\rho V^2$
d = wire diameter
P_b = base pressure behind wire
P_v = vapor pressure of water
P = static pressure in working section
Q = injection rate of air
R_e = Reynolds number: $R_e = V \cdot d/\nu$
S = surface tension of water
T_w = temperature of water
t = time in experiment
V = free-stream velocity
V_i = free-stream velocity at inception of bubble
V_d = free-stream velocity at desinence of bubble
W_e = Weber number: $W_e = \rho d^2 V/S$
α = actual air content of water
α_s = air content at saturation
α/α_s = air content in terms of percent of saturation at water and at atmospheric pressure
σ = cavitation number: $\sigma = 2(P - P_v)/\rho V^2$
σ_i = incipient cavitation number
σ_d = desinent cavitation number
ν = kinetic viscosity of water
ρ = density of water

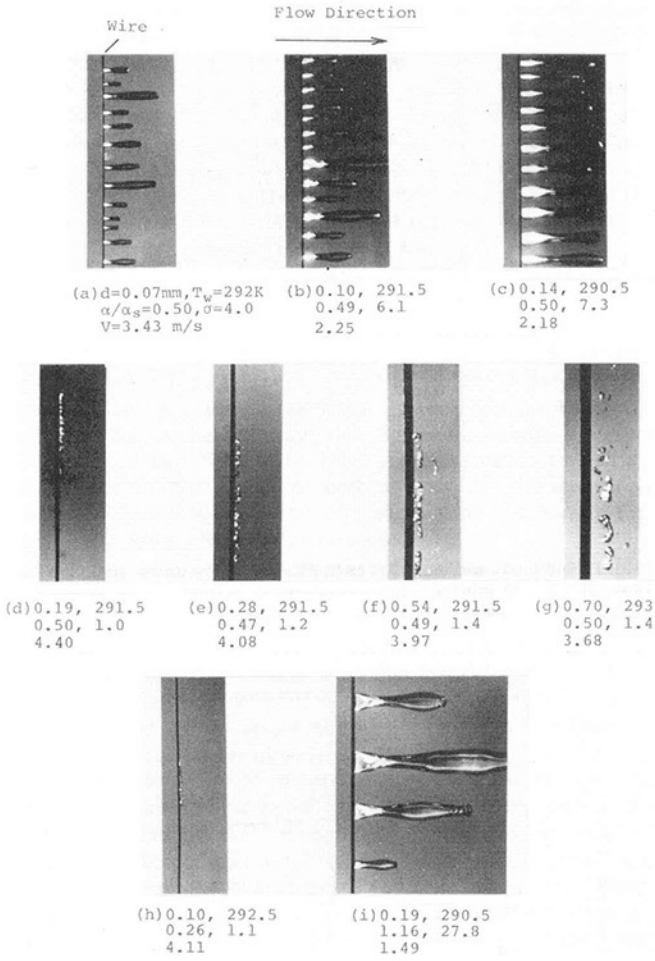

Fig. 3 Typical examples of bubble appearance for wires of various diameters

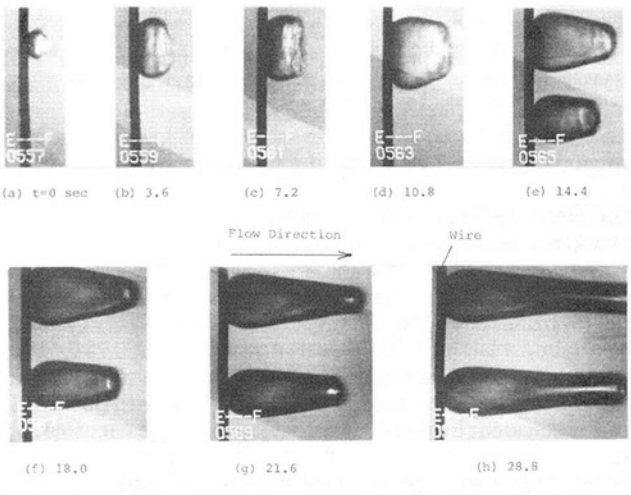

Fig. 4 Appearance of bubble growth in streamer type; d = 0.14 mm, α/α_s = 0.47, T_w = 291 K, V = 2.05 m/s, σ = 7.3

or the presence of a three-dimensional structure within separated wake (Ito and Oba, 1981). The bubbles just behind the wire are flat in shape and approximately equal to the diameter of wire in thickness. The bubble behind the flat part shows an appearance like a waist because of the surface tension. The width of bubbles and the length from the wire to the waist

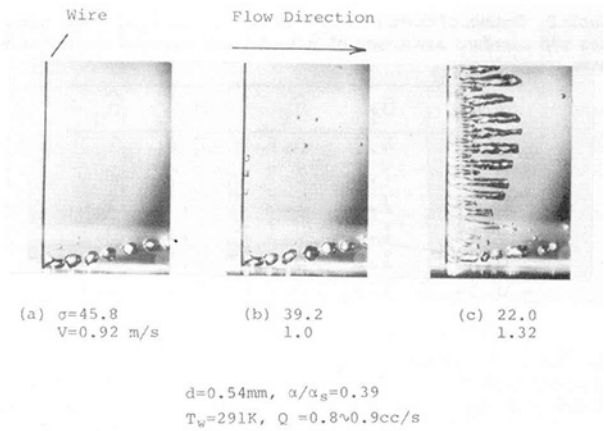

Fig. 5 Appearance of ventilated bubbles

increase with an increase in the diameter of wires. Figure 4 copied from video-tapes shows a typical process of growth in streamer-type bubbles. Figure 4(*a*) shows a small bubble of which the scale approximately corresponds to that of the wire or the vortex formation region behind the wire. The bubbles as shown in Figs. 4(*b*) and (*c*) appear to be unstable and their rear portions appear to be fluctuating. It was sometimes observed around this stage that some of bubbles were swept away to a downstream direction. Bubbles after this stage steadily grew into streamer-type cavities. Figure 4(*e*) shows two bubbles divided from the bubble shown in Fig. 4(*d*).

Figure 5 shows an appearance in the growth of ventilated bubbles for a wire of 0.54 mm in diameter. Air bubbles were injected from the lower end of wire. It can be observed from Fig. 5(*b*) that secondary small bubbles rise along the wire axis within the wake and are swept away to a downstream direction. Figure 5(*c*) shows streamer-type bubbles rising upward behind a wire. These pictures confirm that (i) small bubbles of which dimensions are approximately equal to that of the vortex formation zone can move within the formation zone, (ii) some of the bubbles can be swept away by the flow drag or the motion of vortex and (iii) the streamer-type bubbles can also occur for larger wires in the case where large air bubbles were artificially injected into the wake.

4.2 The Case of Wire Diameter From 0.19 to 0.7 mm. Figures 3(*d*), (*e*), (*f*), and (*g*) show typical appearances of bubbles for wires from 0.19 to 0.7 mm in diameter. These bubbles appear as small unspherical cavities similar to vortex-cavitation bubbles. With an increase in the wire diameter, the bubbles move to a downsteam direction and increase in scale. The location of bubbles appears to be near the place of vortex roll-up though for smaller wires it slightly approaches to the wire surface. These results suggest that this type of cavitation bubbles is related to pressure reduction due to the rotating motion of vortices within the vortex formation region.

4.3 Special Cases of Bubble Occurrence. Exceptional examples of bubble occurrence are shown in Figs. 3(*h*) and (*i*). Figure 3(*h*) presents that the small unspherical bubbles can also occur for small wires of diameter less than 0.14 mm in the case of sufficiently low air content in water. Streamer-type bubbles can be suppressed for low air content and replaced by small unspherical bubbles. On the other hand, Fig. 3(*i*) displays streamer-type bubbles in larger wires for high air content. It indicates that the occurrence of streamer-type bubbles much depends on the air content or the nuclei-size distribution in water.

5 Characteristics of Bubble Occurrence

In Fig. 6, incipient and desinent cavitation numbers are

Table 2 Details of cavitation-number data; $\bar{\sigma}_i$, $\bar{\sigma}_d$, $\hat{\sigma}_i$, $\hat{\sigma}_d$ = averaged values and standard deviations of incipient and desinent cavitation numbers, respectively

d mm	$\bar{\sigma}_i$	$\hat{\sigma}_i$	$\bar{\sigma}_d$	$\hat{\sigma}_d$
0.07	4.7	0.6	10.4	2.1
0.10	7.0	1.3	14.9	2.0
0.14	7.8	1.5	27.2	5.8
0.19	1.1	0.1	1.1	0.1
0.28	1.2	0.1	1.3	0.2
0.54	1.5	0.1	1.6	0.1
0.70	1.6	0.1	1.5	0.1

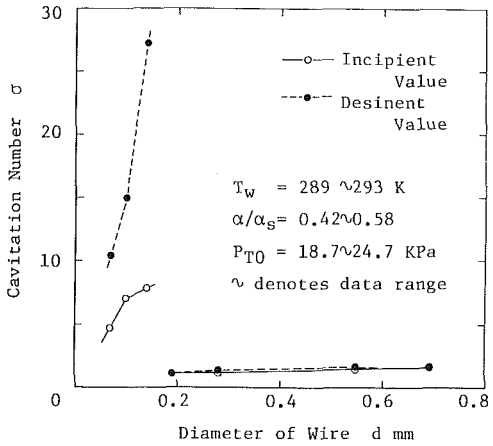

Fig. 6 Averaged incipient and desinent cavitation numbers for various wire-diameters (measurement uncertainty in wire diameter = see Table 1, in cavitation number = ±2 percent, scatters in incipient and desinent values of cavitation number = see Table 2)

plotted against wire diameters. The tendency of them varies discontinuously around the diameter from 0.14 to 0.19 mm. Table 2 shows the averaged values and the standard deviations of the cavitation-number data in Fig. 6. Figure 7 demonstrates the inception and desinence data under the condition of constant velocity. It is confirmed that the results in Fig. 6 under the condition of variable velocity approximately agree with those under constant velocity.

5.1 The Case of Wire Diameter From 0.07 to 0.14 mm. This case corresponds to the wire diameters for occurrence of streamer-type bubbles. Figure 6 shows that the incipient and the desinent cavitation numbers for the wire diameters of $d \leqq 0.14$ mm are relatively high and quite different from each other. This behavior is consistent with that of well-known gaseous cavitation (Holl, 1960). In Fig. 8, the limited values of free-stream velocity at bubble occurrence are plotted against the wire diameter. It shows that the limited velocity decreases with increasing the wire diameter.

5.2 The Case of Wire Diameter From 0.19 to 0.7 mm. Figure 6 and Table 2 show that the incipient and desinent cavitation numbers increase as the wire diameter increases. The value of incipient cavitation number from 1.1 to 1.6 suggests that the bubble occurrence can be closely related to vaporous growth because of the base pressure coefficient $C_{pb} \fallingdotseq -1$ in the present Reynolds number region (Unal and Rockwell, 1988). Figure 8 shows that the velocities at inception V_i and at desinence V_d slightly decrease with an increase in wire diameters. The deviation of the data is very small for $d \geqq 0.19$ mm.

6 Discussions

6.1 Streamer-Type Bubbles. It should be noted that the

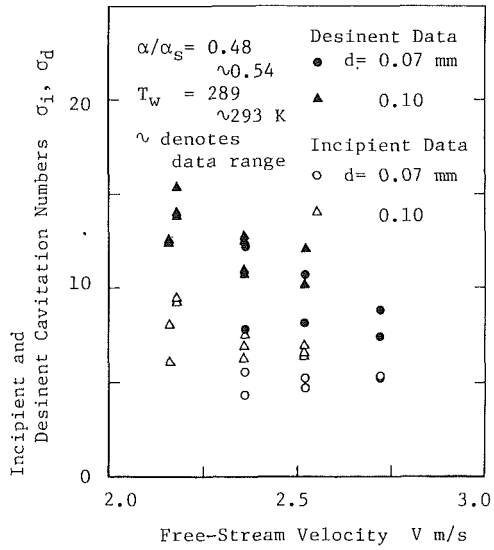

Fig. 7 Incipient and desinent cavitation numbers under constant free-stream velocity (measurement uncertainty in free-stream velocity = ±0.02 m/s, in cavitation number = ± 2 percent)

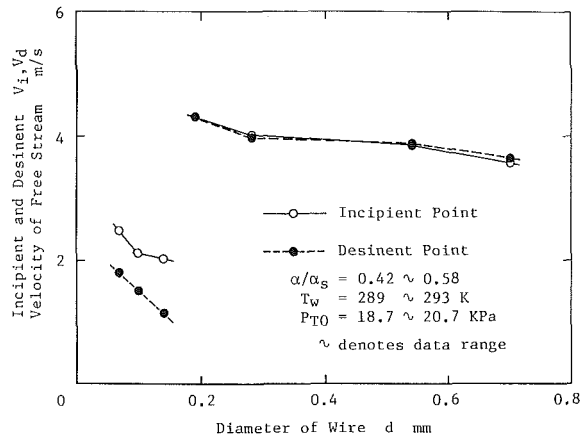

Fig. 8 Free-stream velocities at inception and desinence of bubbles; R_e = 120 ~ 260 for $d \leqq 0.14$ mm, R_e = 810 ~ 2420 for $d \geqq 0.19$ mm (measurement uncertainty in wire diameter = see Table 1, in incipient and desinent values of velocity = ±0.1 m/s)

streamer-type bubbles in the present work are similar to the clear finger-type bubbles on the hemispherical-nosed body (Kermeen, 1952) or the streamer bubbles in a Venturi tube (Ito and Oba, 1981). The separation zone in the present wires is very small and thin since the order is almost of the wire diameter. In addition, Reynolds number Re at bubble occurrence ranges from 120 to 260. The separated shear layer is estimated to be almost laminar for these thin wires (Bloor, 1964). These suggest that the presence of thin and laminar separation zone provides desirable circumstances for stable growth of bubbles.

As indicated previously (Fig. 3(*h*) and (*i*), the occurrence of streamer-type bubbles depends on the degree of air content in water. Therefore, streamer-type bubbles are suppressed from growing and replaced by small unspherical bubbles at low air content. For gaseous growth, the critical bubble diameter d_c can be calculated from the following well-known equilibrium equation of bubble (Strasberg, 1960), where rectified diffusion is neglected because of low pressure fluctuation at low Reynolds numbers.

$$d_c = 4S/P_b/(C/C_0 - 1), \quad (1)$$

where C_0 is the saturated concentration of gas in water at the static pressure of wake P_b and C is the actual concentration

of dissolved gas in water. In the present experimental condition, the critical diameter for $a/a_s = 0.3$ can be estimated to be about 20 μm with the aid of approximation $C/C_0 = (\alpha/\alpha_s)_B$ which is air content in terms of percent of saturation at the base pressure behind a wire. This critical diameter is almost two times as large as that for $\alpha/\alpha_s = 0.4$. Thus, in the case of low air content such as $\alpha/\alpha_s = 0.3$ the gaseous growth can be suppressed because of a small number of nuclei which decrease exponentially with an increase in the size. There are in general not many nuclei larger than 20μm.

In order to grow to streamer-type bubble, it is necessary for small bubbles or nuclei larger than the critical diameter to stay in separation zone for a period. It has been known (Parkin, 1981) that the laminar separation bubble provides suitable circumstances to stay there. Smaller bubbles or larger separation zones need longer residence for the growth. One mechanism to stay in the wake may be a three-dimensional structure of vortex motion (Gerrard, 1978). It was sometimes observed that small bubbles moved up and down within the separation zone just behind a wire. The typical example is shown in Fig. 5(*b*) for ventilated bubbles.

The process of two stages is needed in order to form the streamer-type bubbles. They are (i) to grow to the scale of the separation bubble within the wake and (ii) to grow to the streamer bubble beyond the separation bubble. The condition of (i) requires nuclei larger than the critical radius and the presence of laminar separation bubble. This condition can be also satisfied by an artificial injection of large bubbles or accidental large nuclei in water as shown in Fig. 5 or Fig. 3(*i*).

The next stage is for the condition (*ii*). It can be assumed that at the limited point of this stage the force due to the pressure difference ΔP between the outside and the inside of bubble is balanced by the surface tension S and the centrifugal force based on the curvature of separated free shear layer. Therefore, the following relation can be obtained at the limited point of the growth to streamer-type bubbles, provided that (*a*) the pressure within a bubble is almost equal to the base pressure of wire P_b, (*b*) the scale of vortex formation zone is almost equal to that of wire diameter, and (*c*) the pressure difference caused by the centrifugal force is in proportion to the dynamic pressure of flow. Thus,

$$W_c = A/(B + C_{pb}), \tag{2}$$

where the critical Weber number $W_c = \rho V_i^2 d/S$ is based on the free-stream velocity V_i at occurrence of streamer-type bubbles. The quantities A, B, and the base pressure coefficient C_{pb} can be roughly estimated to be almost constant in the Reynolds-number range of the present experiment (Unal and Rockwell, 1988) though they may exactly depend on the configuration of the vortex formation region and so on. Figure 9 shows the comparison between the curve with Weber number W_e = constant and the experimental results. The curve with Reynolds number $R_e = 300$ is also plotted. It is found that (i) the critical Weber number approximately remains constant irrespective of the variation of wire diameters and (ii) the curves with $W_e = 6$ and 8 intersect that with $R_e = 300$ around the wire diameter of $d \fallingdotseq 0.17$ mm which is in good agreement with the critical diameter from 0.14 to 0.19 mm between the streamer-type bubbles and the small unspherical bubbles in the present experiment.

6.2 Unspherical Small Bubbles. The present type of bubbles appears in the vortex region for wire diameters from 0.19 to 0.7 mm. The incipient and the desinent cavitation numbers can be expressed as follows.

$$\sigma_i \fallingdotseq \sigma_d = -C_{pb} + \Delta C_p, \tag{3}$$

where ΔC_p is a function of the wire diameter, Reynolds number, air content and so on. That is, it depends on the pressure reduction with the rotating motion of vortices and/or the turbulent pressure fluctuation, the possibility of encounters with nuclei and the affect of gas diffusion. The typical values of ΔC_p in the present experiments are as follows.

$$\left.\begin{aligned} \Delta C_p = \sigma_i (\fallingdotseq \sigma_d) + C_{pb} = 0.3 \text{ for } d = 0.19 \text{ mm and } \sigma_i = 1.1, \\ = 0.8 \text{ for } d = 0.7 \text{ mm and } \sigma_i = 1.6, \end{aligned}\right\} \tag{4}$$

Here, the base pressure coefficient for the circular wire is from the literature (Unal and Rockwell, 1988).

The incipient or the desinent cavitation number increases with an increase in the wire diameter. Larger diameter may bring about the increase of available nuclei and the fluctuation of pressure with an increase in Reynolds number. These results confirm the presence of the scale effect in vortex cavitation behind a circular cylinder. The present result is consistent with higher values of σ_i and σ_d in other results for higher Reynolds numbers. According to the literature, for example, Oba et al. (1980) presented the value of desinent cavitation number $\sigma_d = 2.5$ in high Reynolds number of $R_e = 1.9 \times 10^5$ where $\alpha/\alpha_s = 1.02 \sim 1.07$.

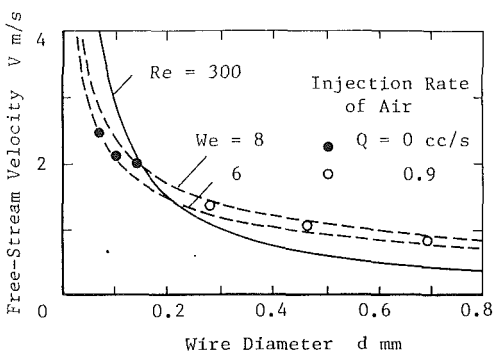

Fig. 9 Limits of occurrence for streamer-type bubbles; T_w = 289 ~ 293 K and α/α_s = 0.4 ~ 0.6 (measurement uncertainty in wire diameter = see Table 1, in velocity = ± 0.1 m/s), where the curves with R_e = 300 and W_e = 6, 8 are calculated as T_w = 293 K

7 Summary and Conclusion

The occurrence of bubbles for thin wires was investigated for various diameters from 0.07 to 0.7 mm under low Reynolds numbers and low tunnel pressure in the condition of air contents from 0.4 to 0.6. As a result, two kinds of bubbles were observed with changing the wire diameter.

For a smaller-wire group of diameters from 0.07 to 0.14 mm, clear streamer-type bubbles appear in regular spatial intervals behind the wire. The occurrence of bubbles is due to gaseous growth and can be affected greatly by air content in water. The presence of thin and laminar separation zone provides desirable circumstances for stable growth of bubbles. The Weber number at occurrence of bubbles remains almost constant within the scope of the present investigation and can be counted among the most important parameters as well as the Reynolds number with respect to the occurrence of streamer-type bubbles.

For a larger-wire group of diameters from 0.19 to 0.7 mm, on the other hand, small unspherical bubbles occur near the location of vortex roll-up in the vortex formation region. The bubbles are closely related to pressure reduction due to vortices. The size of bubbles increases with that of wires.

The incipient and desinent cavitation numbers also vary discontinuously around the wire diameter from 0.14 to 0.19 mm. The inception points for the smaller-wire group are much larger than those for the larger-wire group. There is a large hysteresis effect between the inception and the desinence for the smaller-wire group, but no effect for the larger wire group. It is found in both groups that the limited values of cavitation

number at occurrence of bubbles increase with the wire diameter.

The observations indicate that (i) an increase in the number of bubbles can be also caused by splitting of existing bubbles, (ii) streamer-type bubbles behind a thin wire have a regular spatial arrangement, and (iii) small bubbles can move within the wake along a wire axis.

As future investigations, it is recommended to find out the exact relation between the bubble growth and the vortex motion within the vortex formation region. The various patterns of bubble growth caused hydrodynamically should be also examined about their mechanisms and their mutual relations.

Acknowledgments

The author wishes to acknowledge to the staff and students of Department of Mechanical Engineering in Kanazawa Institute of Technology for their considerable assistance with experiments and useful advices. He is also grateful to Dr. K. Ravindra in Parks College of St. Louis University for helpful discussions and suggestions.

References

Arakeri, V. H., and Acosta, A. J., 1973, "Viscous Effects in the Inception of Cavitation on Axisymmetric Bodies," ASME JOURNAL OF FLUIDS ENGINEERING, Vol. 95, pp. 519–527.

Arakeri, V. H., Carroll, J. A. and Holl, J. W., 1981, "A Note on the Effect of Short and Long Laminar Separation Bubbles on Desinent Cavitation," ASME JOURNAL OF FLUIDS ENGINEERING, Vol. 103, pp. 28–32.

Arakeri, V. H., and Ramarajan, V., 1981, "Inception of Cavitation from a Backward Facing Step," ASME JOURNAL OF FLUIDS ENGINEERING, Vol. 103, pp. 288–293.

Arndt, R. E. A., 1981, "Cavitation in Fluid Machinery and Hydraulic Structures," *Ann. Rev. Fluid Mech.*, Vol. 13, pp. 273–328.

Bloor, M. S., 1964, "The Transition to Turbulence in the Wake of a Circular Cylinder," *Journal of Fluid Mechanics*, Vol. 19, pp. 290–304.

Bogard, D. G., and Gan, C. L., 1987, "An Evaluation of the Accuracy of an LDV Counter," ASME Third Int. Symp. on Laser Anemometry, Boston, pp. 23–30.

Gerrard, J. H., 1978, "The Wakes of Cylindrical Bluff Bodies at Low Reynolds Number," *Phil. Trans. Roy. Soc.* London, Vol. A-288, pp. 351–382.

Hammitt, F. G., 1972, "Effects of Gas Content Upon Cavitation Inception, Performance, and Damage," *Journal of Hydraulic Research*, Vol. 10, pp. 259–290.

Holl, J. W., 1960, "An Effect of Air Content on the Occurrence of Cavitation," ASME *Journal of Basic Engineering*, Vol. 82, pp. 941–946.

Holl, J. W., 1969, "Limited Cavitation," *Cavitation State of Knowledge*, American Society of Mechanical Engineers, New York.

Ito, Y., and Oba, R., 1981, "Several Types of Cavitation Bubbles, Especially Streamer-Bubbles," *ASME Cavitation and Polyphase Flow Forum - 1981*, pp. 14–16.

Ito, Y., and Oba, R., 1982, "A Limit in Separation-Bubble Role on Cavitation-Inception," *ASME Cavitation and Polyphase Flow Forum - 1982*, p. 9–11.

Kermeen, R. W., 1952, "Some Observations of Cavitation on Hemispherical Head Models," Report No. E-35.1, California Institute of Technology, Hydrodynamics Laboratory.

Oba, R., Ikohagi, T., and Yasu, S., 1980, "Supercavitating Cavity Observations by Means of Laser Velocimeter," ASME JOURNAL OF FLUIDS ENGINEERING, Vol. 102, pp. 433–440.

Parkin, B. R., 1981, "The Initiation of Gaseous Microbubble Growth in Laminar Separation Bubbles," ASME JOURNAL OF FLUIDS ENGINEERING, Vol. 103, pp. 543–550.

Peterson, F. B., 1972, "Hydrodynamic Cavitation and Some Considerations of the Influence of Free Gas Content," *Proc. 9th Symp. on Naval Hydrodynamics*, Paris, Vol. 2, pp. 1131–1186.

Strasberg, M., 1960, "Rectified Diffusion: Comments on a Paper of Hsieh and Plesset," *The Physics of Fluids*, Vol. 3, p. 359.

Unal, M. F., and Rockwell, D., 1988, "On Vortex Formation from a Cylinder. Part 1. The Initial Instability," *Journal of Fluid Mechanics*, Vol. 190, pp. 491–512.

Simultaneous Cavitation Susceptibility Meter and Holographic Measurements of Nuclei in Liquids

Luca d'Agostino[1]

S. I. Green[2]

California Institute of Technology,
Pasadena, California 91125

Cavitation Susceptibility Meter (CSM) and holographic measurements of cavitation nuclei distributions are compared in this paper. The CSM optically detects cavitation in water samples flowing through a venturi and relates the unstable nuclei concentration to the applied tension in the fluid. A ruby laser holographic system measures the nuclei size distribution directly. Microbubbles have been used as the dominant nuclei source. The data from the two detection schemes are correlated by accounting for the dynamic response of the cavities in the venturi throat. The active nuclei distributions predicted by the holographic data compare favorably with those measured by the CSM. Both detection methods show that the nuclei concentration rises approximately exponentially as the applied tension is increased and then, with further reduction in the pressure, tends to a nearly constant maximum due to the shortage of remaining cavitatable nuclei. The CSM consistently underestimates the concentration of active cavitation nuclei, due to limited electro-optical resolution and mutual interference effects between cavities in the venturi. The good qualitative agreement of the two techniques supports the validity of the data correlation model and clearly indicates that any practical interpretation of measured nuclei size distributions for cavitation predictions is highly dependent on the specific flow conditions. Attempts to cavitate saturated water of the California Institute of Technology Low Turbulence Water Tunnel in the CSM were unsuccessful even at the lowest attainable CSM throat pressures (about $-40kPa$). This is thought to be due to insufficient throat tension and, at least partially, to the short time available for cavity growth in the CSM.

1 Introduction

Cavitation nuclei strongly affect both the onset and extent of cavitation in liquid flows. Consequently, knowledge of the concentration of unstable nuclei as a function of the applied tension is essential to understanding cavitation. Billet (1985, 1986) has reviewed some of the nuclei detection methods, which include: Coulter Counters, acoustical attenuation, acoustical and optical scattering, photography, and holography. The shortcoming common to all these techniques is that the applied tension is never measured directly, but rather must be inferred from equilibrium bubble radii. Solid particles in the flow may be counted and sized, but information concerning their susceptibility to applied tension is lacking.

The Cavitation Susceptibility Meter (CSM) was proposed by Oldenziel (1982a, 1982b; Oldenziel et al., 1982) to overcome this difficulty. In his concept the CSM consists of a glass venturi where cavitation bubbles generated at the throat are detected optically. The CSM later developed by Neyretec in France uses a stainless-steel venturi where cavitation bubbles are monitored by recording the noise generated by their collapse in the diffuser section downstream of the throat (Le Goff and Lecoffre, 1983; Shen et al., 1984; Gowing et al., 1988). The flow in this venturi is turbulent owing to the high inlet Reynolds number. The present CSM concept uses a glass venturi where the flow possesses a laminar potential core throughout the throat, cavitation is detected optically, and the throat pressure is determined from the direct optical measurement of the throat flow velocity. This arrangement bypasses some of the uncertainties of earlier CSM designs in the measurement of the cavitating nuclei concentration and the throat pressure (d'Agostino, 1987; d'Agostino and Acosta, 1991; d'Agostino and Acosta, 1991b). In all these CSM concepts the concentration of unstable nuclei is found by dividing the average cavitation rate by the volumetric flux, and the mean throat pressure is derived from the flow velocity and upstream pressure using the continuity and energy equations, with proper corrections for viscous effects when necessary.

Several problems adversely affect CSM's, namely: sheet cav-

[1]Presently, Dipartimento di Ingegneria Aerospaziale, Università degli Studi di Pisa, Pisa, Italy.

[2]Presently, Mechanical Engineering Department, University of British Columbia, Vancouver, Canada.

Contributed by the Fluids Engineering Division for publication in the JOURNAL OF FLUIDS ENGINEERING. Manuscript received by the Fluids Engineering Division December 21, 1990. Associate Technical Editor: M. L. Billet.

itation in the throat section, cavitation-separation flow in the diffuser, choking of the flow and mutual interference effects between cavitation nuclei (d'Agostino, 1987; d'Agostino and Acosta, 1990; d'Agostino and Acosta, 1991c). However, CSM's also have several advantages over other nuclei detection techniques: they directly measure the active nuclei concentration as a function of applied tension, they are not limited in the size of nuclei they can detect (if it cavitates it can be detected), and CSM measurements are quickly carried out. This paper is part of our comparative research on cavitation nuclei detection methods (O'Hern et al., 1988; d'Agostino et al., 1989). It represents the natural extension our earlier work on this subject (d'Agostino et al., 1989) and compares the cavitation nuclei concentration measurements simultaneously recorded on the same water sample by holographic observation and by the CSM developed at Caltech.

2 Experimental Apparatus and Procedure

The CSM used in this experiment has been described previously (d'Agostino and Acosta, 1991a; d'Agostino and Acosta, 1991b; d'Agostino et al., 1989; d'Agostino, 1987), therefore only its main features are outlined here. A water sample passes through the throat section of the blown glass venturi tube (VT) of Fig. 1, where it cavitates. The intensity and the extent of cavitation are determined by the flow conditions, in particular by the throat pressure, nuclei concentration and susceptibility. Since the pressure gradient in the venturi throat is ideally zero, it can be shown that the slip velocity between the cavities and the liquid quickly approaches zero in the throat section regardless of the initial conditions. Cavitating bubbles themselves are therefore used by a back-scattering Laser Doppler Velocimeter (LDV) to measure the throat velocity, while the upstream pressure is obtained from an absolute pressure transducer. In all operating conditions the core flow in the venturi throat is potential, with a laminar boundary layer not exceeding about 10 percent of the local radius. The core throat pressure is taken as the nominal cavitation inception pressure and is calculated from Bernoulli's equation assuming ideal, incompressible, steady, fully-wetted flow. The direct measurement of the core throat velocity eliminates the uncertainties associated with the estimate of boundary layer blockage (d'Agostino, 1987; d'Agostino and Acosta, 1991a; d'Agostino and Acosta, 1991b). The throat pressure is controlled by adjusting the exhaust pressure. The dependence of the active nuclei concentration on throat pressure is measured by repeating the procedure at different exhaust pressures.

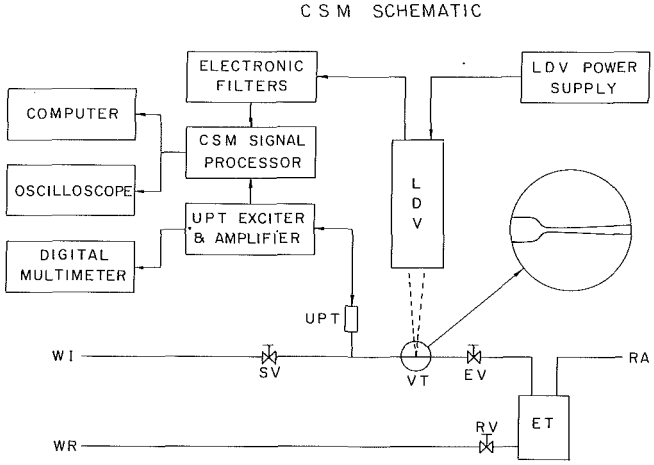

Fig. 1 Schematic of the various components of the CSM experimental apparatus: water inlet (WI), sampling valve (SV), upstream pressure transducer (UPT), venturi tube (VT), exhaust valve (EV), exhaust tank (ET), regulated air pressure line (RA), return valve (RV), water return (WR), laser Doppler velocimeter (LDV)

Locating the LDV focal volume 3 mm from the beginning of the throat section was found to give the best results. Since the LDV focal volume covers the entire tube cross-section, the CSM detects bubbles both in the potential core and in the laminar boundary layer. When necessary, the spurious readings in the boundary layer are eliminated by statistical filtering in the data reduction. The CSM Signal Processor compares the LDV signal to adjustable electronic thresholds in order to reject the electronic noise. These threshold settings essentially determine the number of LDV events registered as "cavitation" and therefore introduce an offset uncertainty in the measurement of cavitating nuclei concentration. Proper choice of these thresholds is dependent on the establishment of a general criterion for identifying unstable cavitating nuclei in dynamic conditions and on the correlation of the scatterer size to its LDV signature. In principle, the latter point could be addressed by measuring the LDV response to bubbles of known sizes, but in practice this is quite difficult even for slightly nonspherical bubbles. The former point, on the other hand, is essentially equivalent to the definition of cavitation inception conditions, a still open problem in modern cavitation research. Until these problems are solved, the selection of suitable CSM thresholds is arbitrary. For this work the thresholds were ad-

Nomenclature

A_t = CSM venturi throat cross-sectional area
D_t = CSM venturi throat diameter
L_f = bubble detection length
L_t = CSM venturi length
n = cavitating nuclei concentration
N = holographic bubble count
p_b = liquid pressure at the bubble interface
p_e = CSM venturi exhaust pressure
p_g = bubble internal gas pressure
p_o = bubble equilibrium far field pressure
p_t = CSM venturi throat pressure
p_v = liquid vapor pressure
r = radial coordinate from the bubble center
R = bubble radius
$\dot{R}, \ddot{R}$ = bubble radius Lagrangian time derivatives
R', R'' = bubble radius spatial derivatives
R_f = bubble detection radius
R_o = bubble equilibrium radius
S = bubble surface tension
t = time
T = liquid temperature
u_b, u_b' = bubble velocity and velocity perturbation
u_t, u_t' = CSM throat velocity and velocity perturbation
w' = velocity perturbation relative to the bubble center
x = CSM venturi axial coordinate
x_b = axial coordinate of the bubble center
α = dissolved air content in the liquid
γ = bubble gas specific heat ratio
ρ = liquid density

Subscripts

b = bubble
e = CSM venturi tube exit
g = bubble noncondensable gas
o = reference equilibrium conditions
t = venturi tube throat
v = vapor

Acronyms

CSM = Cavitation Susceptibility Meter
LDV = Laser Doppler Velocimeter

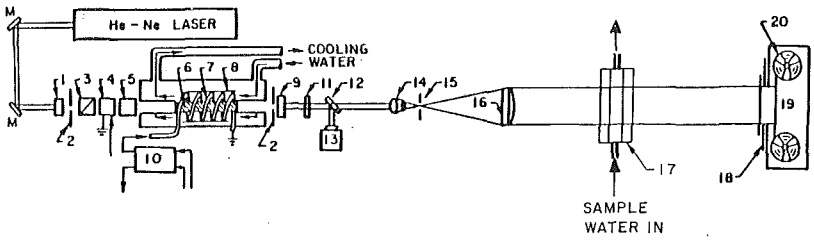

1. BACK MIRROR
2. IRIS APERTURE
3. POLARIZER
4. POCKEL S CELL
5. POLARIZER
6. RUBY ROD
7. XENON FLASH LAMP
8. REFLECTOR
9. FRONT MIRROR-SAPPHIRE ETALON
10. TRIGGER TRANSFORMER
11. NEUTRAL DENSITY FILTER
12. BEAM SPLITTER (4% REFLECTIVITY)
13. PIN DIODE
M. MIRROR
14. MICROSCOPE OBJECTIVE
15. SPATIAL FILTER-10μ PIN HOLE
16. COLLIMATING LENS
17. FLOW THROUGH SAMPLER
18. SHUTTER
19. AUTOMATIC FILM DRIVE
20. HOLOGRAPHIC FILM

Fig. 2 Schematic of the holographic experimental apparatus

justed to optimize the electric response and ensure the applicability of one set of thresholds to all operating conditions.

Figure 2 is a schematic of the holographic recording system. The holocamera itself has been described in previous publications (O'Hern et al., 1986; Katz et al., 1984), hence only a brief functional description is given here for clarity. A pulsed ruby laser produces a coherent, collimated light beam (components 1–16 in Fig. 2). Some of the light is diffracted by bubbles and particles in the sample volume, though the majority passes through undiffracted. Interference between the diffracted and undiffracted light is recorded on film as a hologram. The three-dimensional real image of the sample volume, reconstructed by passing collimated He-Ne laser light through the hologram, is then highly magnified and displaced on a video monitor. The number and dimensions of objects in the holographic volume are measured directly from the video images. Bubbles are distinguished from (the rare) particulates based on their circularity and brightness.

One of the problems affecting the earlier stage of this experiment (d'Agostino et al., 1989) was the accumulation of large bubbles in the feed line between the water source and the CSM. These bubbles, which caused multiple spurious readings and large fluctuations in the venturi flow, have been eliminated by running the sample water through a "bubble filter." The filter operates by flowing the water sample downwards slowly through a broad tube. The ratio of the buoyancy to drag of large bubbles exceeds that of smaller bubbles and hence the large bubbles preferentially rise through the water to the free surface. After leaving the bubble filter, the water inlet line branched in a horizontal T. Approximately equal lengths of upwards sloping line joined one T outlet to the CSM venturi and the other to the holographic sample cell (refer to Fig. 3), permitting CSM and holography data to be recorded simultaneously from the same water sample.

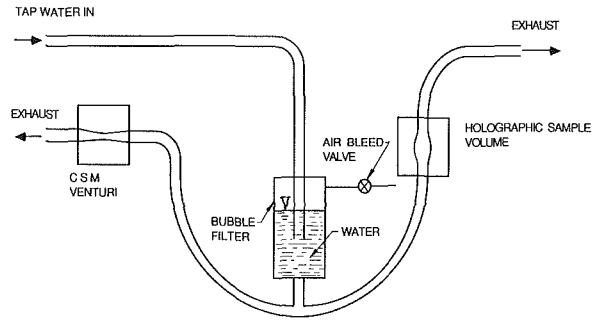

Fig. 3 Schematic of the combined CSM/holography system

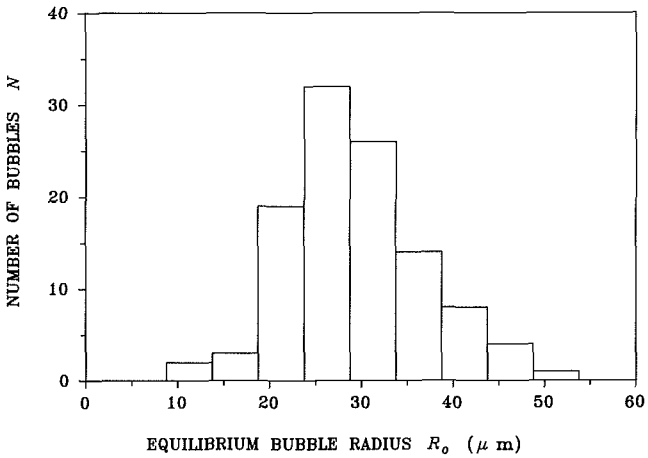

Fig. 4 Holographic nuclei size distribution measured in a 1.05 cm^3 tap water sample with temperature $T = 18°C$, pressure $p_o = 96.2$ kPa ca., and air content $\alpha = 18.5$ ppm

3 Experimental Results and Discussion

Tap water samples with a dominant population of suspended microbubbles were tested in order to eliminate the uncertainties associated with the dynamic behavior of other types of cavitation nuclei and with the finite optical resolution of the holographic system. Besides, this choice also bypassed the limitations of the CSM discussed later in this section. The nuclei concentrations in the tap water samples were two to three orders of magnitude larger than those typically measured in ocean water.

Holographic nuclei number distributions from three water samples are presented in Figs. 4, 5, and 6, and can be converted in a straightforward fashion into the cumulative distributions $n(R_o)$, where $n(R_o)$ is the concentration of bubbles with equilibrium radius not smaller than R_o. To compare holographic $n(R_o)$ data with the cavitating nuclei concentration data $n(p_t)$ measured by the CSM, the relation between the fully wetted inception throat pressure p_t in the CSM venturi and the bubble equilibrium radius R_o is required. The specific conditions of the flow must be considered, because the inception pressure of a cavity in dynamic conditions can be greatly different from its critical pressure in static equilibrium (see Fig. 7). Following the same general approach used in a previous paper (d'Agostino et al., 1989), we therefore consider the dynamic response of an isolated bubble in the CSM venturi throat. It is assumed that only bubbles larger than a certain detectable size at the LDV focal point are recognized by the CSM. Then the bubble dynamic response determines the minimum unperturbed throat pressure p_t necessary to grow a bubble of initial equilibrium size R_o and far field pressure p_o to a final detectable radius R_f over a prescribed distance L_f from the beginning of the venturi throat.

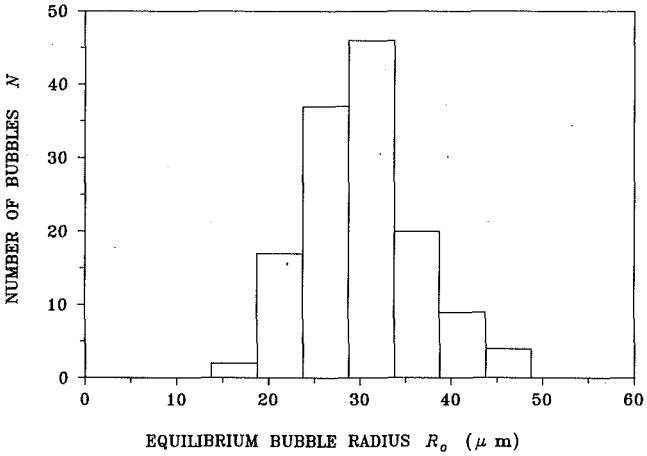

Fig. 5 Holographic nuclei size distribution measured in a 1.38 cm³ tap water sample with temperature $T = 18°C$, pressure $p_o = 91.4$ kPa ca., and air content $\alpha = 18.9$ ppm

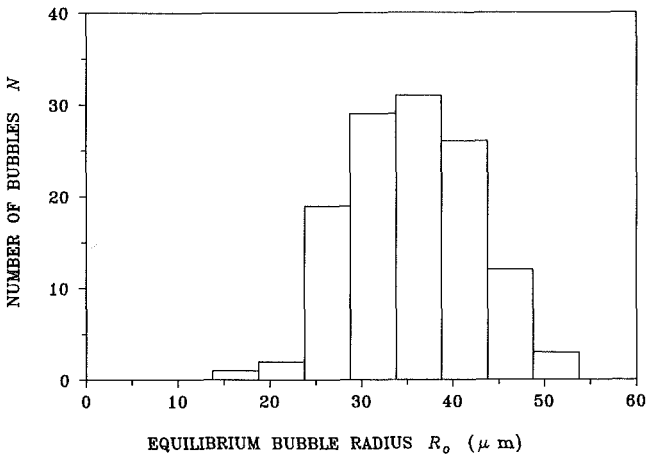

Fig. 6 Holographic nuclei size distribution measured in a 1.28 cm³ tap water sample with temperature $T = 19°C$, pressure $p_o = 92.6$ kPa ca., and air content $\alpha = 18.4$ ppm

The CSM venturi tube is modeled as a cylindrical duct of length L_t and constant radius R_t, connecting an infinite reservoir of ideal, incompressible liquid at pressure p_o to an atmospheric exhaust at constant pressure $p_e = p_t$. The bubble, moving along the centerline of the duct with instantaneous position $x_b(t)$ and zero slip velocity with respect to the liquid, remains essentially spherical with radius $R(t)$. The latter assumption is consistent with optical observations of cavitation in the CSM throat even for bubbles of size comparable to the venturi diameter (d'Agostino, 1987; d'Agostino and Acosta, 1991b). As mentioned earlier, the further assumption of zero slip velocity is acceptable in the absence of pressure gradients throughout the duct. If u_b' is the bubble perturbation velocity (equal, in the absence of the interphase slip, to the velocity perturbation at the center of the bubble) and w' is the source-like perturbation velocity relative to the bubble center due to the bubble response, then the overall perturbation velocity of the liquid at any location in the duct is: $u_t' = u_b' + w'$. To a first approximation it is assumed that w' is spherical in the bubble near field and cylindrically uniform in the bubble far field:

$$w' = \begin{cases} \dfrac{R^2\dot{R}}{r^2}; & R \le r \le r^* \\ \dfrac{2R^2\dot{R}}{R_t^2}; & r > r^* \end{cases}$$

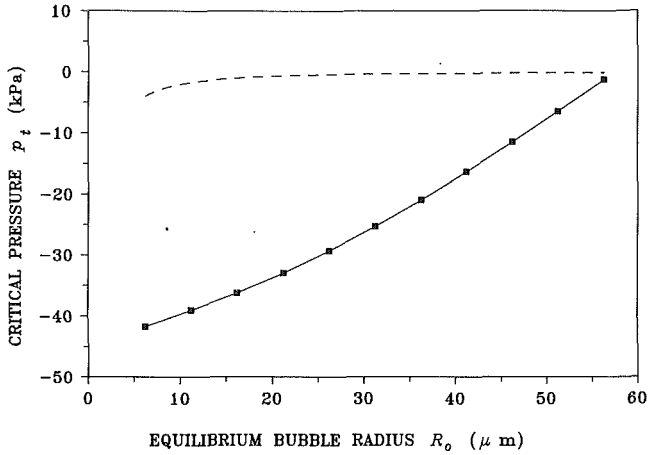

Fig. 7 Critical pressure of a gas bubble in water as a function of the equilibrium radius R_o under static (dashed line) and dynamic conditions (squares and solid line). Here: $p_o = 91.4$ kPa (equilibrium pressure), $p_v = 0$ kPa (vapor tension), $\gamma = 1.4$ (adiabatic exponent), $S = 0.0728$ N/m (surface tension), $R_t = 140$ μm (final radius), $R_t = 0.5$ mm (duct radius), $L_t = 2.65$ mm (detection distance), $L_t = 50$ mm (duct length).

with transition at a distance r from the bubble center equal to $r^* = R_t/\sqrt{2}$, obtained by equating the above two expressions of the perturbation velocity w'. Here $\dot{R}$ indicates the Lagrangian time derivative of the bubble radius. The bubble perturbation velocity u_b' and the exit perturbation velocity u_e' can be computed from the inlet and exit continuity equations:

$$A_t u_b' - A_o u_o' - 2\pi R^2 \dot{R} = 0$$
$$A_t u_e' - A_t u_b' - 2\pi R^2 \dot{R} = 0$$

assuming that the flow originates from an unperturbed velocity field ($u_o' = 0$). The duct velocity $u_t' = \nabla\phi'$ and its potential ϕ' are now completely specified in terms of the bubble response. The Bernoulli's equation along the duct centerline from the bubble interface to the exit section may be written as:

$$\left.\frac{\partial\phi'}{\partial t}\right|_{x=x_b+R} + \frac{p_b}{\rho} + \frac{1}{2}(u_t + u_b' + \dot{R})^2 = \left.\frac{\partial\phi'}{\partial t}\right|_{x=L_t} + \frac{p_t}{\rho} + \frac{1}{2}(u_t + u_e')^2$$

where p_t and u_t are the unperturbed pressure and velocity in the duct, ρ is the liquid density and x is the axial coordinate along the duct centerline. Neglecting thermal and diffusive effects, the liquid pressure p_b at the bubble interface is:

$$p_b = p_g \frac{R_o^{3\gamma}}{R^{3\gamma}} + p_v - \frac{2S}{R}$$

where the vapor pressure p_v and the noncondensable gas pressure p_g are constant, S is the surface tension, and γ is the specific heat ratio of the gas in the bubble, assumed to behave isoentropically. Finally, linearizing the above equations for small changes of the duct flow velocity and transforming the steady material time derivatives of the bubble radius in the corresponding convective spatial derivatives ($\dot{R} \simeq u_t R'$), the following second order differential equation for the bubble radius $R(x)$ is obtained:

$$(R^2R'' + 2RR'^2)\left(\frac{4(L_t - x_b) - 2(r^* + R)}{R_t^2} + \frac{1}{R} - \frac{1}{r^*}\right) + \left(\left(\frac{2R^2}{R_t^2} - 1\right)R' + \frac{1}{2(p_o - p_t)}\left(p_t - p_g\frac{R_o^{3\gamma}}{R^{3\gamma}} - p_v + \frac{2S}{R}\right)\right) = 0$$

This analysis generalizes the approach of our previous paper (d'Agostino et al., 1989) by modifying the Rayleigh-Plesset equation to account for the effects of finite CSM tube length and larger bubble-to-duct size ratios. One clear limitation of

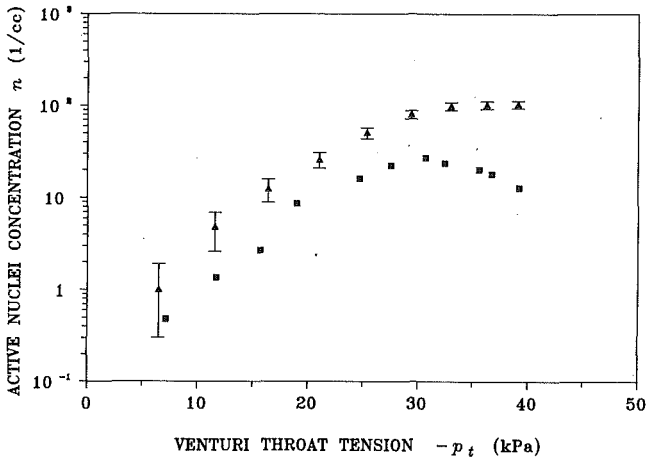

Fig. 8 Unstable nuclei concentration $n(p_t)$ measured by holographic observation (triangles) and by the CSM (squares) as a function of the venturi throat tension $-p_t$. The data refer to the first tap water sample of Fig. 4. The expected r.m.s. error of CSM data is about 3 percent for all data points.

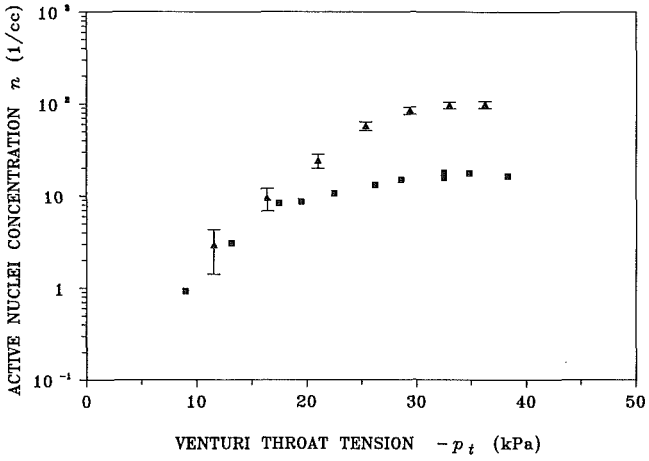

Fig. 9 Unstable nuclei concentration $n(p_t)$ measured by holographic observation (triangles) and by the CSM (squares) as a function of the venturi throat tension $-p_t$. The data refer to the second tap water sample of Fig. 5. The expected r.m.s. error of CSM data is about 3 percent for all data points.

our earlier approach is that the Rayleigh-Plesset equation, which governs the growth of spherical bubbles in an essentially uniform far field, was employed even when the final bubble radius was comparable to the tube radius. This limitation under-estimated the inception throat pressure and is eliminated in the present analysis, which applies to roughly spherical cavities of arbitrary size, as required for better correlation of CSM and holographic nuclei concentration data.

Throat pressures calculated by numerical integration of the above equation are shown in Fig. 7 as a function of the equilibrium bubble radius R_o. The critical pressure for static mechanical stability (Knapp et al., 1970):

$$p_t = p_v - \frac{4S}{3R_o}\left[3\left(1+\frac{p_o-p_v}{2S/R_o}\right)\right]^{-1/2}$$

is also shown in the same figure for comparison. Water and air properties at room conditions and realistic values of the CSM geometrical parameters have been used ($\gamma = 1.4$, $S = 0.0728$ N/m, $p_v = 0$, $R_t = 0.5$ mm, $L_t = 50$ cm, $p_o = 91.4$ kPa). The results are rather sensitive to the detection radius R_f and distance L_f, which in turn mainly determine the offset and slope of the curve. A representative value of L_f for the CSM flow can be estimated considering that, as mentioned earlier, the LDV focal point is located 3 mm from the beginning of

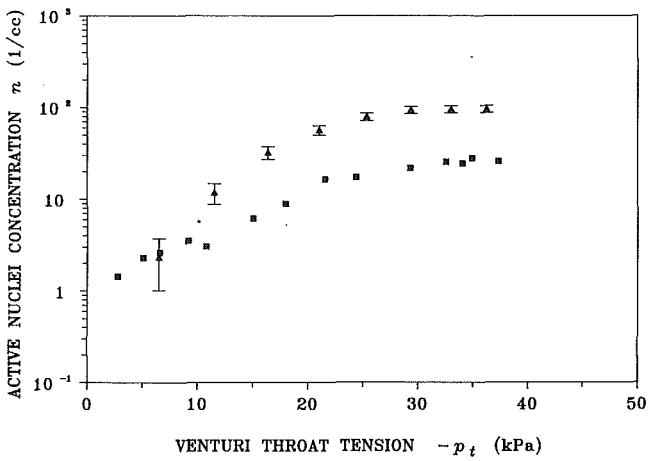

Fig. 10 Unstable nuclei concentration $n(p_t)$ measured by holographic observation (triangles) and by the CSM (squares) as a function of the venturi throat tension $-p_t$. The data refer to the third tap water sample of Fig. 6. The expected r.m.s. error of CSM data is about 3 percent for all data points.

the CSM throat section and that cavities will actually be detected ahead of this location depending on their scattering intensity through the LDV focal volume and the settings of the electronic thresholds. Here the detection length $L_f = 2.65$ mm has been chosen for the computations, implicitly assuming that cavities are typically recognized when they reach the location where the illuminating LDV intensity changes most rapidly (i.e., 0.35 mm ahead of the focal point). Unfortunately, since the LDV signature of the cavities cannot safely be related to their size, there is no reliable independent way to estimate the detection radius R_f and therefore the off-set of the curve in Fig. 7. Here it is assumed that the average size of the cavities recognized by the CSM is $R_f = 140$ μm. This choice provides good qualitative agreement between CSM and holographic data and is consistent with optical observations of cavitating bubbles in the CSM throat (d'Agostino, 1987; d'Agostino and Acosta, 1991b). Finally, note that not all tests were run at the nominal inlet pressure of 91.4 kPa, but the small variations from that value do not significantly affect the critical throat pressure p_t.

A comparison of the CSM results with the holographic data, reduced as described above, is displayed in Figs. 8, 9, and 10. Both data sets are repeatable within a factor of two. The r.m.s. relative error in estimating the nuclei concentrations from the number of counts N in each data group is of the order of $1/\sqrt{N}$. For the CSM data N is about 900 and therefore the expected error is quite small (about 3 percent), constant for all data points. For the holographic data N is the cumulative number of bubbles with radius not smaller than R_o, obtained from the observed nuclei number density distributions. The corresponding r.m.s. error is indicated in the figures. The throat pressures predicted from the holographic data are comparable to those measured by the CSM. The two techniques concur in finding that initial dependence of the concentration of unstable nuclei on the applied tension is approximately exponential, as observed by other investigators (Shen et al., 1984; Shen et al., 1986). Both techniques also consistently show that the cavitating nuclei concentration tends to level at higher tensions due to the shortage of remaining cavitatable nuclei. Reducing the throat pressure in this range (less than -30 kPa) makes growth and collapse of available nuclei more violent, which produces a parallel increase in the throat velocity unsteadiness (Fig. 11). For comparison, the fully wetted flow is essentially laminar, with negligible turbulence intensity.

When the CSM throat pressure is lowered and many nuclei simultaneously cavitate in the throat, the CSM response saturates and the minimum achievable pressure is drastically re-

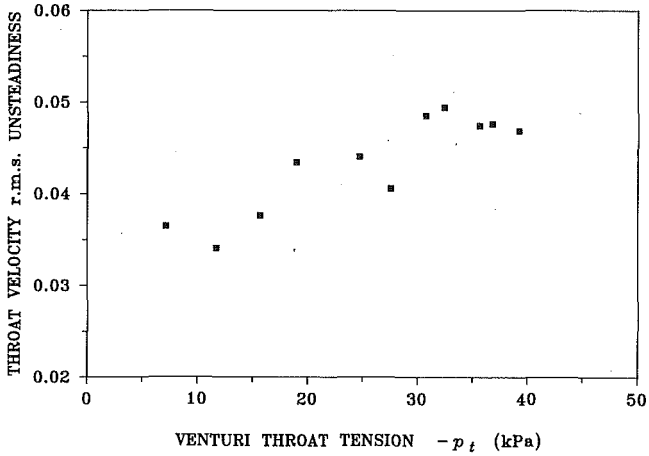

Fig. 11 Throat velocity r.m.s. unsteadiness measured by the CSM as a function of the venturi throat tension $-p_t$ for the tap water sample of Fig. 4

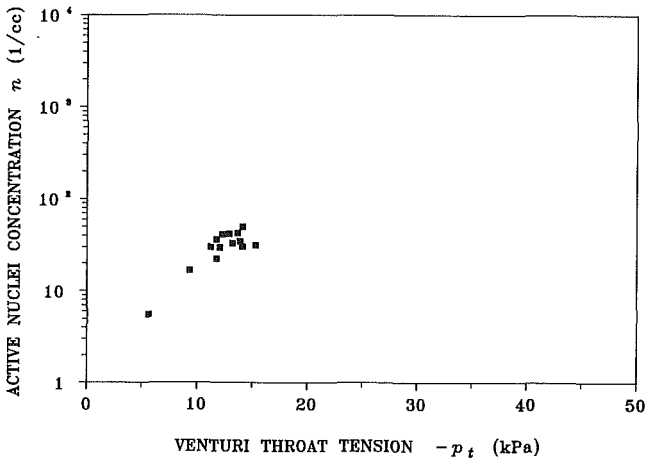

Fig. 12 Unstable nuclei concentration $n(p_t)$ measured by the CSM as a function of the venturi throat tension $-p_t$. The data refer to a tap water sample with temperature $T=35°C$, pressure $p_o=90.4$ kPa ca. and air content $\alpha=14.6$ ppm. The expected r.m.s. error of CSM data is about 3 percent for all data points.

duced. This phenomenon is illustrated in Fig. 12, which refers to a water sample with an active nuclei concentration approximately ten times larger than the previous ones. Under these conditions, about 4 nuclei are simultaneously present in the CSM throat volume at all times. The cluster of points at a throat pressure of -13 kPa was acquired with the exhaust pressure of the CSM varied by more than 10 kPa, while maintaining virtually constant the upstream pressure. These points represent therefore two phase choked flow in the venturi throat. Considerable unsteadiness is associated with choking of the flow (Fig. 11).

The concentration of unstable nuclei measured with the holocamera is consistently larger than that indicated by the CSM. This is not surprising, since the vast majority of the nuclei has intentionally been chosen larger than the resolution of the holographic system and therefore holography accounts for virtually all the nuclei, whereas the CSM electronic thresholds filters out many nuclei signals. The decreasing concentration of unstable nuclei measured by the CSM at higher tensions is clearly an artifact due to the flawed assumption of fully-wetted flow employed in the flow rate calculations. This assumption, essentially valid at low cavitation event rate, clearly becomes invalid when several cavities are continuously present in the venturi. Neglecting this two phase effect causes the liquid flow rate through the CSM to be overestimated, thus decreasing the measured concentration of unstable nuclei with respect to its actual value. A further possible cause of error is the reduction of cavity growth due to the mutual interference between cavitating nuclei. This effect increases at lower pressures, and contributes to reduce the CSM measured nuclei population.

The agreement of the cavitating nuclei concentration distributions measured by the two techniques is remarkable, at least in a qualitative sense, in view of their quite different nature. Admittedly this is due in part to the flexibility of the dynamic cavitation model used for data correlation, where the two parameters R_f and, to a much smaller extent, L_f are relatively uncertain and can be fitted to the data. Clearly these parameters need to be determined more accurately in future studies. For practical purposes, measurements of nuclei size distributions should ultimately lead to predictions of cavitation susceptibility in specific flows. The present results show that reasonable correlation of CSM and holographic data can indeed be achieved in a relatively simple case, and demonstrate the sensitivity of any practical interpretation of measured nuclei size distributions to the specific flow conditions. Despite their inherent limitations, the results of this study support the validity of the present approach and clearly indicate that the interactions between the cavity response and the driving flow will need to be included in the generalizations to more complex situations where many nuclei cavitate simultaneously.

Ultimately, any useful CSM must be able to measure the nuclei distribution of a far less bubbly liquid than that characterized in Figs. 8, 9, and 10. In this context, an attempt was made to measure the nuclei content of saturated water from the Caltech Low Turbulence Water Tunnel (LTWT). Bypassed tunnel water was driven through the bubble filter and into the CSM venturi. The transfer time of the water to the CSM was a few seconds. Even at the lowest CSM pressure attainable without laminar separation in the diffuser, the tunnel water simply did not cavitate appreciably. This is perhaps not surprising in light of the factor of 100 fewer cavitation nuclei in the tunnel water relative to tap water (Gates, 1977, measured about 3 nuclei per cc in the 20 to 50 μm size range in saturated LTWT water). Even if cavitation were to have occurred in the venturi, the time necessary to obtain sufficient CSM data for statistical purposes would have been a factor of 100 larger than for the bubbly tap water sample. With the present instrument this implies CSM runs of several hours, which is obviously completely impractical. Thus, a venturi more suitable to less susceptible waters should be designed with larger and longer throat volumes, in order to increase the probability of cavitation and to allow more time for cavity growth. At the same time such a venturi should also generate higher throat tensions by increasing the pressure recovery in the diffuser. However, this objective is quite difficult to achieve due to separation in the diffuser and surface nuclei effects on the flow boundaries, as discussed in detail in other publications (d'Agostino and Acosta, 1990; d'Agostino and Acosta, 1991c).

The results described herein differ somewhat from our earlier comparison (d'Agostino et al., 1989) between the two techniques. The differences, which are quantitative, not qualitative, may be attributed primarily to the different dynamic cavitation model used to correlate holographic nuclei size distributions to CSM cavitating nuclei distributions and to the addiction of the bubble filter for the removal of large bubbles. As mentioned earlier, the flow of these bubbles in the venturi causes several problems and is thought to have affected the previously reported results.

4 Conclusions

Holography and Cavitation Susceptibility Meter measurements of nuclei distributions in water samples with a dominant population of microbubbles have been compared. The CSM directly measured cavitating nuclei in a water sample, whereas cavitation behavior have been inferred from holographic meas-

urements of bubble size distributions using an appropriate cavitation model. The inception pressures predicted from holographic nuclei size distributions compare favorably with the throat pressures measured by the CSM. Both methods also show that the concentration of active cavitation nuclei increases almost exponentially with the applied tension, reaches a maximum and remains constant thereafter, when few nuclei are uncavitated. However, the holographic nuclei concentrations are generally about five times larger than those measured by the CSM. Two reasons account for these discrepancies: the finite CSM thresholds preclude measurement of smaller cavities and the simple assumptions made to model bubble dynamics in the CSM venturi do not allow for the multiplicity of bubbles occurring simultaneously in the throat at higher cavitation rate. The good qualitative agreement of the two techniques supports the validity of the cavitation model used in the correlation of the data and clearly indicates that the practical interpretation of measured nuclei size distributions for cavitation predictions is highly dependent on the specific flow conditions.

Acknowledgments

This research has been funded by the Office of Naval Research and by the Naval Sea Systems Command General Hydromechanics Research Program administered by the David W. Taylor Naval Ship Research and Development Center. The North Atlantic Treaty Organization—Consiglio Nazionale delle Ricerche, Italy, has also contributed to the support of this work through a 1982 and a 1983 Fellowship for Technological Research. Additional support has been provided by the Italian Ministero dell'Università e della Ricerca Scientifica e Tecnologica. The authors would especially like to thank Professor A. J. Acosta who suggested and encourage this research. Thanks are also owing to Dr. T. T. Huang of DTNSRDC, and to Mr. Joe Fontana, Mr. Rich Eastvedt, Mr. Leonard Montenegro, Mr. John Lee and other members of the Caltech support staff who aided us in this endeavor. Finally, Dr. Haskel Shapiro, Mr. Bob Kirkpatrick and their group are acknowledged for their role in the design and construction of the CSM electronics.

References

Billet, M., 1986, "The Importance and Measurement of Cavitation Nuclei," *Advancements in Aerodynamics, Fluid Mechanics and Hydraulics*, Minneapolis, Minn., pp. 967–989.

Billet, M., 1985, "Cavitation Nuclei Measurement—A Review," *ASME Cavitation and Multiphase Flow Forum*, Albuquerque, NM, pp. 31–38.

d'Agostino, L., 1987, "Experimental and Theoretical Study on Cavitation Inception and Bubble Flow Dynamics," Ph.D. thesis, Report No. Eng. 183.16, California Institute of Technology, Pasadena, Calif.

d'Agostino, L., and Acosta, A. J., 1983, "On the Design of Cavitation Susceptibility Meters," American Towing Tank Conference, Hoboken, NJ.

d'Agostino, L., and Acosta, A. J., 1990, "Separation and Surface Nuclei Effects in a Cavitation Susceptibility Meter," *Advances in Gas-Liquid Two-Phase Flows*, ASME Winter Annual Meeting, Dallas, Texas, pp. 179–186.

d'Agostino, L., and Acosta, A. J., 1991a, "A Cavitation Susceptibility Meter with Optical Cavitation Monitoring—Part One: Design Concepts," ASME JOURNAL OF FLUIDS ENGINEERING, Vol. 113, pp. 261–269.

d'Agostino, L., and Acosta, A. J., 1991b, "A Cavitation Susceptibility Meter with Optical Cavitation Monitoring—Part Two: Experimental Apparatus and Results," ASME JOURNAL OF FLUIDS ENGINEERING, Vol. 113, pp. 270–277.

d'Agostino, L., and Acosta, A. J., 1991c, "Separation and Surface Nuclei Effects in a Cavitation Susceptibility Meter," ASME JOURNAL OF FLUIDS ENGINEERING, Vol. 113, pp. 695–699.

d'Agostino, L., and Green, S. I., 1989, "Simultaneous Cavitation Susceptibility Meter and Holographic Measurement of Nuclei in Liquids," ASME *Cavitation and Multiphase Flow Forum*, San Diego, Calif.

d'Agostino, L., Thai Pham, and Green, S. I., 1989, "Comparison of a Cavitation Susceptibility Meter and Holographic Observation for Nuclei Detection in Liquids," ASME JOURNAL OF FLUIDS ENGINEERING, Vol. 111, No. 2, pp. 197–203.

Gates, E. M., 1977, "The Influence of Freestream Nuclei, Freestream Nuclei Populations and a Drag Reducing Polymer on Cavitation Inception on Two Axisymmetric Bodies," Ph.D. thesis, California Institute of Technology.

Gowing, S., Vikram, C. S., and Burton, S., 1988, "Comparison of Holographic, Light Scattering and Venturi Techniques for Bubble Measurements in a Water Tunnel," ASME *Cavitation and Multiphase Flow Forum*, pp. 25–28.

Katz, J., O'Hern, T. J., and Acosta, A. J., 1984, "An Underwater Holographic Camera System for Detection of Microparticulates," *ASME Cavitation and Multiphase Flow Forum*, pp. 22–25.

Knapp, R. T., Daily, J. W., and Hammitt, F. G., 1970, *Cavitation*, McGraw-Hill.

Le Goff, J. P., and Lecoffre, Y., 1983, "Nuclei and Cavitation," *14th Symposium on Naval Hydrodynamics*, National Academy Press, pp. 215–242.

Oldenziel, D. M., 1982a, "A New Instrument in Cavitation Research: the Cavitation Susceptibility Meter," ASME JOURNAL OF FLUIDS ENGINEERING, Vol. 104, pp. 136–142.

Oldenziel, D. M., 1982b, "Utility of Available Instruments during Cavitation Tests," *Proceedings of the IAHR Symposium on Operating Problems of Pump Stations and Power Plants*, Amsterdam.

Oldenziel, D. M., Jansen, R. H. J., Keller, A. P., Lecoffre, Y,, and van Renesse, R. L., 1982, "Comparison of Instruments for Detection of Particles and Bubbles in Water during Cavitation Studies," *Proceedings of the IAHR Symposium on Operating Problems of Pump Stations and Power Plants*, Amsterdam.

O'Hern, T. J., Green, S. I., and Morss, E. P., 1986, "Measurements of Oceanic Nuclei Distributions," ASME *Cavitation and Multiphase Flow Forum*, pp. 23–26.

O'Hern, T. J., d'Agostino, L., and Acosta, A. J., 1988, "Comparison of Holographic and Coulter Counter Measurements of Cavitation Nuclei in the Ocean," ASME JOURNAL OF FLUIDS ENGINEERING, Vol. 110, pp. 200–207.

Shen, Y. T., Gowing, S., and Pierce, R., 1984, "Cavitation Susceptibility Meters by a Venturi," ASME *International Symposium on Cavitation Inception*, pp. 9–18.

Shen, Y. T., Gowing, S., and Eckstein, B., 1986, "Cavitation Susceptibility Measurements of Ocean Lake and Laboratory Waters," Report DTNSRDC-86/D19, David W. Taylor Naval Ship Research and Development Center.

D. Fan
Research Fellow,
Department of Civil Engineering,
The University,
Dundee DD1 4HN
Scotland, U.K.

A. Tijsseling
Research Officer,
Department of Civil Engineering,
Delft University of Technology,
2600 GA Delft,
The Netherlands

Fluid-Structure Interaction With Cavitation in Transient Pipe Flows

The interactions between axial wave propagation and transient cavitation in a closed pipe are studied. Definitive experimental results of the phenomenon are produced in a novel apparatus. The apparatus is characterized by its simplicity and its capability of studying transient phenomena in a predictable sequence. The influence due to friction is small and the representations of the boundary conditions are straightforward. Measurements with different severity of cavitation are provided to enable other researchers in the area to compare with their theoretical models. A new cavitating fluid/structure interaction cavitation model is proposed. The measurements are compared with the column separation model of Tijsseling and Lavooij (1989) and the new model to validate the experimental results.

Introduction

Transient cavitation frequently occurs in liquid-filled pipelines in unsteady flow regions. It is a local phenomenon which develops wherever the fluid pressure drops to the vapor pressure. In fully-filled piping systems, transient cavitation is normally characterized by two flow regimes. In a distributed cavitation region, vapor bubbles are dispersed amongst the liquid. In a column separation region, the bubble population is sufficiently large to coalesce to form a vapor pocket within the pipe.

Most of the work on transient cavitation deals with pressure wave propagation in rigidly anchored pipelines. The flexibility effects of the pipewalls are taken into account by reducing the fluid wavespeed (Chaudhry, 1979). For distributed cavitation, authors such as Kranenburg (1974) and Martin et al. (1976) find that the Lax-Wendroff scheme is applicable for implicit treatment of shock waves. For cavitations which last longer than 1.5 seconds, Zielke et al. (1989) find that gas release effects should be taken into account. For vaporous cavitation, Provoost (1976) and Kot and Youngdahl (1978) find that the concentrated (discrete) cavity model is suitable for most applications. Fox and McGarry (1983) have developed a model which includes thermodynamic effects due to heat transfer between liquid and cavities. They found that the thermodynamic effects are important for liquids with large vapor pressure like propane or butane.

In practice, most pipelines are not rigidly anchored. In such cases. the flexibility of the pipewalls not only results in reduced fluid wavespeed but also in the presence of stress waves within the pipewalls. The dynamics of such a pipe system is therefore analogous to that of a structural frame coupled with the dynamics of the fluid. Wilkinson (1978), Wiggert et al. (1985, 1987) and Lavooij and Tijsseling (1989) have all proposed a variety of analytical and numerical methods to predict the coupled dynamic response of piping systems. In general, the dynamics of a pipework is influenced by four wave families: axial, flexural and torsional waves in the pipewall and pressure waves in the fluid. They coexist during transience and have different degrees of influence on transient cavitation.

Axial waves in the pipewall can induce negative fluid pressures upon reflection or transmission at geometrical discontinuities. In addition, radial expansion of the pipewall associated with compressive axial stress waves can also be sufficient to induce cavitation. If friction and cross-sectional flows are neglected, flexural and torsional waves cannot induce pressure changes at wavefronts. However, they can induce axial waves and hence cavitation when reflected at boundaries (e.g., at elbow and tee junctions). In most recent studies on fluid/structure interaction without cavitation, it is shown that the phenomenon can result in significant increases of peak pressures and significant reduction of natural frequencies of pipework (Tijsseling and Lavooij, 1990; Wiggert et al., 1987; and Wilkinson, 1978).

Although there is no lack of literature on fluid/structure interaction or transient cavitation, the work on both subjects is scarce. Schwirian (1982) developed a Finite Element technique which can model multidimensional fluid/structure interaction problems with cavitation. Tijsseling and Lavooij (1989) proposed a column separation—fluid/structure interaction model for piping systems. Their work is only applicable for column separation in a typical reservoir-pipe-valve system, and no validation results were given. In practice, distributed cavitation frequently accompanies column separation in low pressure regions during transience. This results in regions of reduced fluid wavespeed rather than a separated cavity as in the case of column separation. The additional effects due to the reduction of fluid wavespeed therefore must be taken into account in a comprehensive analysis.

Experimental Method

Accurate experimental measurements of transient cavitation in a closed tube are obtained. The apparatus consists of a slightly pressurized steel tube suspended by two long thin steel wires. Transients in the pipe are produced by impacting a solid steel rod onto one end of the pipe (Fig. 1). This method of

Contributed by the Fluids Engineering Division for publication in the JOURNAL OF FLUIDS ENGINEERING. Manuscript received by the Fluids Engineering Division September 13, 1990. Associate Technical Editor: E. Michaelides.

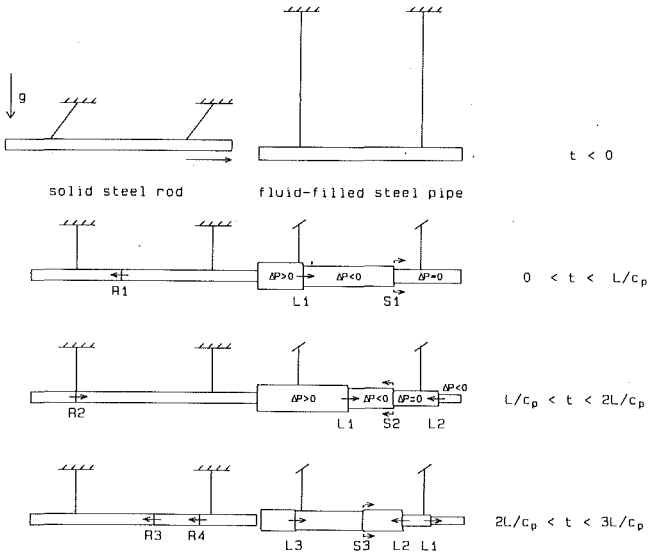

Fig. 1 Sequence of events in the apparatus

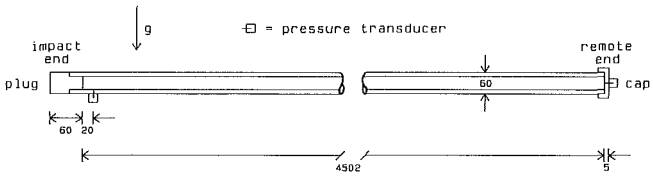

Fig. 2 End pieces

generating fluid transients by structural impact was developed by Vardy and Fan (1986, 1987) to study fluid/structure interactions in noncavitating flows. The method has the advantages of minimizing complications due to steady state-pressure gradients associated with friction and gravity. The boundary conditions can be modeled accurately, thus allowing the particular effect (and in this case the interactions between axial waves and vapor cavities) to be studied with confidence. Flexural and torsional effects are not introduced for the present application.

Sequence of Events. When the experiments commence, the rod is released from the raised position. It accelerates under the influence of gravity until it reaches its lowest position. At the instant of impact, two sets of wavefronts are generated in the pipe which travel along the fluid and the pipewall. In cases without cavitation, the wavespeed in the pipewall is about 3.4 times faster than in the fluids. Interactions exist between the pipewall and the fluid at the wavefronts due to Poisson ratio effects (Poisson coupling). At the stress wavefront S1, this produces a slight drop in the fluid pressure which is followed by an increase in pressure due to the pressure wavefront L1 (Fig. 1).

As the stress wavefront S1 reaches the remote end of the pipe, it pushes the closed end away from the fluid. This induces a large rarefraction wavefront L2. In cases without cavitation, the magnitude of L2 can be double that of the initial pressure rise due to L1. During the first $2L/c_p (\approx 2$ ms) after impact, the rod remains in contact with the pipe. The rod is deliberately chosen to be longer than the pipe such that the reflected wavefront in the rod (R2) cannot reach the impact end before S2 does. At $t = 2L/c_p$, the tensile stress wavefront S2 reaches the impact end and separates the rod from the pipe. The impact end becomes free and no multiple impact occurs. Therefore, the rod can be regarded as semi-infinite in the calculations. By varying the amount of initial pressure in the pipe, cavitation can be initiated either at the remote end (column separation) or at the stress wavefront S1 due to Poisson coupling effects (distributed cavitation). The time-scale of the experiments is in milliseconds and so the relatively slow effects due to gas release are insignificant (Zielke et al., 1989).

Cavitation Severity Index. A numerical index has been pro-

Table 1 Properties of the apparatus

Item	Method of measurement	Instrument Standard Accuracy	Deviation	Value	Unit
PIPE					
Young's modulus	Uniaxial compression test on a 200 mm long specimen			168±5	GN/m^2
Poisson's ratio	Uniaxial compression test on a 200 mm long specimen			0.29±0.01	
Steel mass density	Micrometer, and weight a 200 mm long specimen	2.0	5.0	7985±7	kg/m^3
Internal diameter	Direct measurement : micrometer	0.03	0.1	52.02±0.13	mm
External diameter	Direct measurement : micrometer	0.003	0.020	59.91±0.02	mm
Internal length	Direct measurement : tape measure	0.5	0.5	4502±1	mm
ROD					
Young's modulus	Uniaxial compression test on a 200 mm long section			200±6	GN/m^2
Mass density	Micrometer and weight a 200 mm long section	4.0	0.0	7848±4	kg/m^3
Diameter	Direct measurement : micrometer	0.01	0.04	50.74±0.05	mm
Length	Tape measure : include curvature at the impact end	0.5	0.5	5006±1	mm
END PIECES					
Mass of end plug	Direct = electronic scale			1.2866	kg
Mass of end cap	Direct = electronic scale			0.2925	kg
FLUID (assumed values)					
Water mass density				999	kg/m^3
Water bulk modulus				2.14	GN/m^2
Darcy-Weisbach friction factor				0.01	
Vapour pressure				0.02	bar

Nomenclature

A = cross-sectional area
c = wavespeed, defined in Wiggert et al. (1985)
f = Darcy-Weisbach friction factor
g = gravitational acceleration
G_f, G_p = Poisson coupling factors, defined in Wiggert et al. (1985)
L1–3 = liquid wavefronts
L = internal length
p = fluid pressure
R1–4 = axial stress wavefronts in the rod
R_H = hydraulic radius
S1–3 = axial stress wavefronts in the pipewall
S = cavitation severity index
t = time
T_c = duration of the first column separation at the remote end
U = axial velocity
w = self weight terms, defined in Vardy and Fan (1987)
ρ = mass density
σ = axial stress in pipewall
τ = shearing stress in fluid = $f\rho_f(U_f - U_p)|U_f - U_p|/2$
$\forall$ = cavity volume

Subscripts

f = fluid
p = pipewall
r = rod

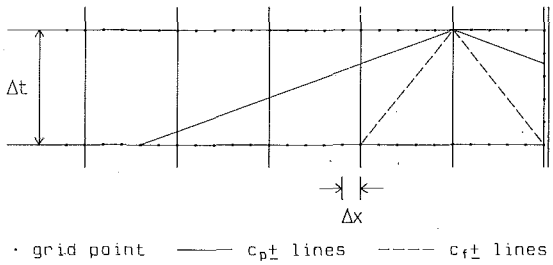

Fig. 3 Numerical grid

posed by Martin (1983) to classify the severity of cavitation in rigidly anchored pipelines. It is proportional to the fluid wavespeed and the duration of column separation. In cavitating fluid/structure interaction flows, the phenomenon is dominated by stress wave propagation in the pipewall. A similar severity index, which is based on the axial stress wavespeed, is chosen for the present study:

$$S=\frac{T_c}{(2L/c_p)} \tag{1}$$

where T_c is the duration of the first vapor cavity at the remote end. In the present apparatus, for cases where $S<1.5$, the situation is classified as slight. For cases where $S>2.5$, the situation is classified as severe. The intermediate cases are classified as moderate.

Details of the Apparatus. The pipe is 4.5 m long (316L stainless steel 2 in. NB 40s) and it is sealed by two end pieces (Fig. 2). Prior to the test runs, the pipe is filled with ordinary tap water and inclined to a vertical position. A mallet is used to tap the pipe to encourage the air bubbles attached on the pipewall to rise. A screw valve is located at the top of the pipe to bleed the air into the atmosphere. This process is repeated several times until there is negligible amount of air pocket left in the pipe. The fluid is then pressurized to the desired initial pressure by using a hand pump and a calibrated manometer.

The apparatus is extensively instrumented with pressure transducers (Kistler 7031), strain gauges, accelerometers (PCB 305A05), a laser Doppler vibrometer and a high speed video camera (Kodak Ektapro 1000). All instruments are connected to a high speed data acquisition system which has sixteen channels, each capable of taking 125,000 samples per second. Fluid pressure, structural displacement, velocity, acceleration and strain of the pipe and the rod have been measured. In this paper only a few of the measured results are selected for concise presentation. The laser and the video camera measurements are used to determine the rod impact velocity. The pressure measurements are used to study the interactions between axial wave propagations and vapor cavities.

The physical and material properties of the apparatus are presented in Table 1. All important parameters are measured, such that the theoretical and the experimental results can be assessed independently. The only parameter that needs to be inferred from the measurements is the initial pressure within the pipe. This is due to the thermal expansion of the fluid and the pipewall. As the apparatus is a closed tube, the volumetric changes associated with temperature changes can significantly influence the initial water pressure within the tube. The pressure change due to a typical daily temperature variation of 8°C can be as much as 1 MPa. The apparatus therefore behaves rather like a thermometer. In the theoretical simulations, the value of the initial pressure (measured by a manometer) is slightly adjusted such that the measured and the calculated cavitation levels at the remote end of the pipe are equal.

Repeatability of the Experiments. Five cases of results are presented, ranging from no cavitation ($S=0$) to Poisson coupling induced cavitation ($S=2.8$). There are three runs of experiments per test case, and the typical elapse time between each run is less than five minutes. The repeatability of the test cases is shown in Fig. 4. Two results from each test case are chosen randomly for inspection. In the case where there is no cavitation ($S=0$), the measurements are almost identical between different runs. In all cases the magnitude and the timing of the main pressure peaks are highly repeatable. As the severity of cavitation increases, only the smaller high frequency peaks become less repeatable. The level of repeatability is sufficient for our purpose. The present method of inducing cavitation produced sharper and more uniform excitations across the pipe cross section than those produced by valve closure.

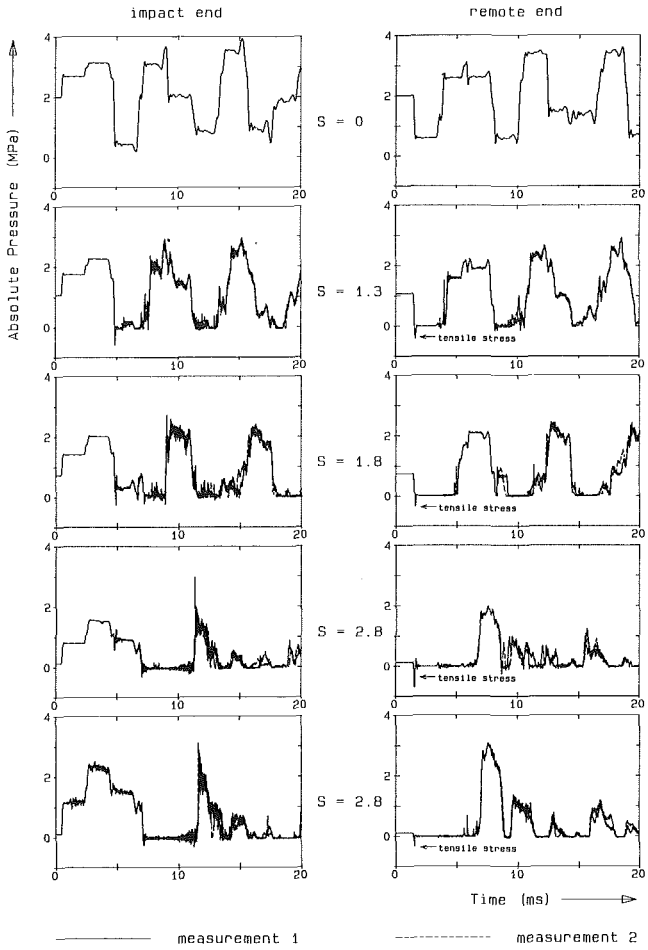

Fig. 4 Typical repeatability of pressure measurements in the apparatus

Theory

In the following analysis the theory assumes elastic pipewall material and straight thin-walled pipe geometry. Radial inertia of the pipewall is neglected so the phenomenon is nondispersive in the absence of cavitation. The free gas content in the liquid is assumed to be zero and no gas release or thermodynamic effects are included.

Governing Equations. A detailed discussion of the constitutive equations of axial wave propagations in transient pipe flows has been presented by Vardy and Fan (1987). The equations have been derived by considering the continuity, momentum and material relationship of the fluid and the pipewall. Similar expressions have also been found by Schwarz (1978) and Wiggert et al. (1985). The equations can be transformed by the Method of Characteristics to yield the following four compatibility equations which are valid along the characteristic directions:

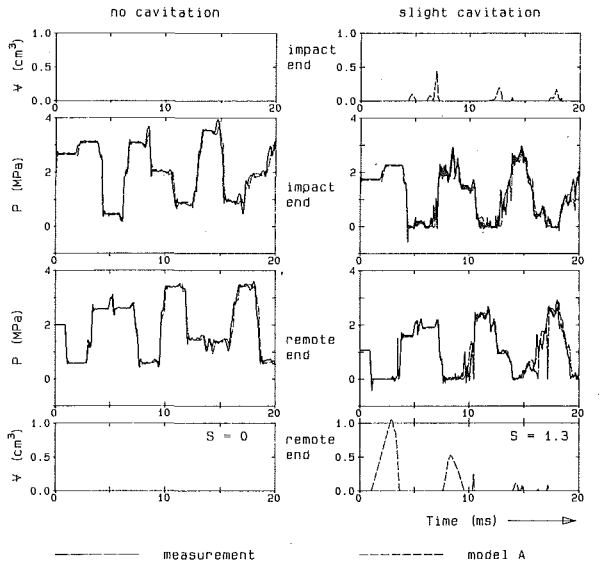

Fig. 5 None and slight cavitation: model A

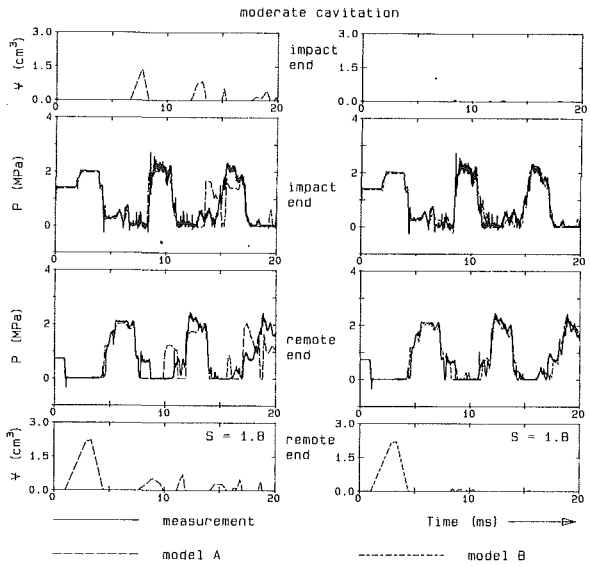

Fig. 6 Moderate cavitation: model A and model B

Fluid (along $dx/dt = \pm c_f$):

$$\frac{dp}{dt} \pm \rho_f c_f \frac{dU_f}{dt} - G_f\left(\frac{d\sigma_x}{dt} \mp \rho_p c_f \frac{dU_p}{dt}\right) = \mp c_f\left\{\left(\frac{\tau}{R_H} + w_f\right) - G_f\left(\frac{\tau}{R_H}\frac{A_f}{A_p} + w_p\right)\right\} \quad (2)$$

Pipe (along $dx/dt = \pm c_p$):

$$\frac{d\sigma_x}{dt} \mp \rho_p c_p \frac{dU_p}{dt} - \frac{1}{G_p}\left(\frac{dp}{dt} \pm \rho_f c_p \frac{dU_f}{dt}\right) = \mp c_p\left\{\left(+\frac{\tau}{R_H}\frac{A_f}{A_p} + w_p\right) - \frac{1}{G_p}\left(\frac{\tau}{R_H} + w_f\right)\right\} \quad (3)$$

The equations relate four unknowns, namely, the axial stress σ, pipe velocity U_p, pressure p, and fluid velocity U_f. The first two terms in the equations constitute the decoupled compatibility equations for axial waves in both media. The last two terms include Poisson ratio effects due to radial flexibility of the pipewall. The full expressions of the wavespeeds (c_f, c_p) and the Poisson coupling factors (G_f, G_p) are given by Wiggert et al. (1985). The solutions of the equations have been validated against experimental data as well as other methods of solving the constitutive equations (e.g., Lavooij and Tijsseling, 1989 and Wiggert et al., 1985).

In the cavitation regions, the concentrated cavity model by Streeter (1969) and Provoost (1976) is adopted for the present application. This model is preferred above others because of its ability to predict most vaporous cavitation situations. The model is also simple to implement and gives sufficiently accurate results. In the present application, the numerical oscillations reported by Provoost (1976) and Wylie (1984) have not been found. Therefore free gas pockets, like those used by the above authors to suppress numerical pressure spikes, are not necessary in the present model. The model concentrates the presence of vapor cavities at numerical grid points and thus allows the fluid wavespeed to remain constant in the intervening spaces. When an overpressure wave transverses a cavity, first it has to cause the cavity to collapse. The delay action associated with this behavior emulates the reduction of fluid wavespeed and its dependency on the void fraction. If a vapor cavity exists, the pipe axial stress and velocity are assumed to be the same across the cavity. In addition, the pressure in the cavity is assumed to stay constant at the vapor pressure level (Table 1).

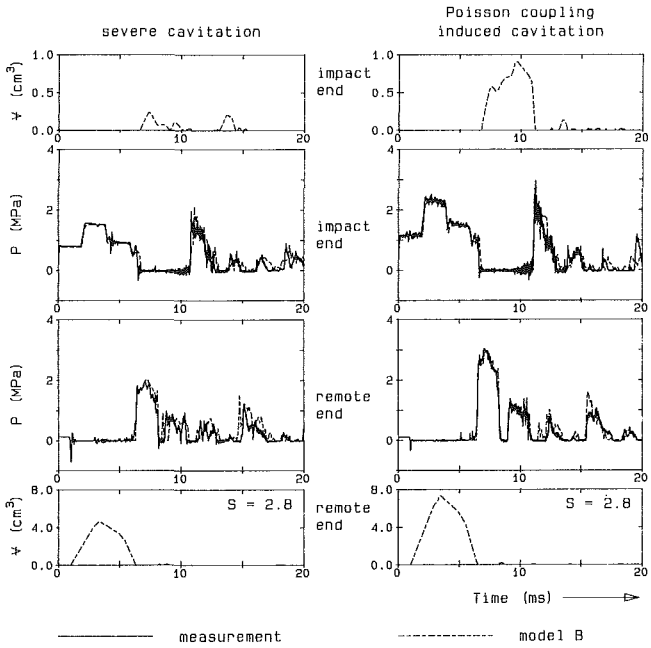

Fig. 7 Severe and Poisson coupling induced cavitation: model B

Solution Procedure. The numerical grid proposed by Tijsseling and Lavooij (1989) is adopted for the present application (Fig. 3). In their analysis, the characteristic lines are allowed to span several grid lengths and the wavespeeds are slightly adjusted such that interpolations are necessary only at the points near a boundary. In the absence of cavitation, Eqs. (2) and (3) are used to obtain the values of the four unknowns at the new time level. In cases where the pressure falls below the vapor pressure, Eqs. (2) and (3) are solved simultaneously with the vapor pressure to obtain the solution. The solution of these equations yields the fluid velocities on both sides of a vapor cavity at the grid point. These values are used to obtain the new cavity volume using the following relationship:

$$\forall_{\text{NEW}} = \forall_{\text{OLD}} + A_f(U_{fR} - U_{fL})\Delta t \quad (4)$$

where U_{fL} and U_{fR} are the fluid velocities on the left and the right hand side of the cavity respectively. A similar approach is also used for the transitory case of a collapsing cavity by solving Eqs. (2)~(5) simultaneously:

$$\forall_{NEW} = 0 \tag{5}$$

Boundary Conditions. At a boundary, only two characteristic lines are available and two boundary conditions must be used to obtain all the equations required.

(*a*) Impact end: For $0 \le t \le 2L/c_p$, the equilibrium and continuity relationships are:

$$\sigma A_p - pA_f = \sigma_r A_r$$
$$U_p = U_f = U_r$$
$$\sigma_r = \rho_r c_r (U_r - U_{ro}) \tag{6}$$

where U_{ro} is the initial velocity of the rod before impact and the subscript r denotes quantities related to the rod. The rod axis is in the same direction as the pipe axis. Note that the rod is simulated as a semi-infinite boundary because $2L_r/c_r$ is greater than $2L/c_p$.

(*b*) Remote (free) end: In the absence of a vapor cavity, the equilibrium and continuity equations are:

$$pA_f - \sigma A_p = 0$$
$$U_f = U_p \tag{7}$$

With column separation, the equilibrium relationship is still valid but the continuity equation is replaced by Eq. (8):

$$\forall_{NEW} = \forall_{OLD} + A_f(U_p - U_f)\Delta t \tag{8}$$

where $\forall_{OLD}$ and $\forall_{NEW}$ denote the cavity volume on the old and new time level respectively. This procedure is also used for the impact end in the presence of cavitation.

Results

The measurements from five different sets of experiments with increasing severity of cavitation are presented. The first two sets of measurements are compared with the column separation—fluid/structure interaction model (designated model A) by Tijsseling and Lavooij. Column separations at both ends of the pipe are modeled and no distributed cavitation effects are included. In the last two sets of experiments, the measurements are compared with the proposed cavitating fluid/structure interaction model (designated model B). In the intermediate case, the measurements are compared with both models. The rod impact velocity is 0.739 m/s in the first four cases, and is increased to 1.122 m/s in the last case.

In Figs. 5–7, the upper and lower graphs depict the calculated cavity volumes at the impact and the remote end of the pipe respectively. The duration of the first cavity formed at the remote end is used to calculate the cavitation severity parameter. In each figure, the continuous lines depict the measurements and the broken lines depict the numerical results from either model A or model B. In all simulations, the number of grid lengths in the pipe is 150. The $c_f \pm$ characteristic lines span five grid lengths, and the $c_p \pm$ characteristic lines span seventeen grid lengths (Fig. 3). This implies the time step is 0.11 milliseconds.

No Cavitation. In the absence of cavitation the minimum transient pressure in the pipe is about 1.8 MPa below the initial pressure (Fig. 5). The initial pressure in the pipe in this case is about 2 MPa. This pressure is sufficiently high to prevent cavitation and allow the experiment to be used as a control. It should be noted the pressure pattern of the present apparatus is very different from that of water hammer in a rigid pipeline (e.g., a reservoir-pipe-valve case: Chaudhry, 1979). The repetitive pressure pattern every $4L/c_f$ no longer exists. This is due to the presence of axial stress wavefronts which generate pressure changes at the wavefronts (Poisson coupling) and additional pressure waves when reflected at the boundaries. This phenomenon is not restricted to the present apparatus and it exists to some degree in all nonrigidly anchored pipelines. A related point of interest is that the initial pressure rise at the impact end is about 0.6 MPa. When the stress wavefront S1 (Fig. 1) reflects at the remote end, the magnitude of the rarefaction wave (L2) produced is about 1.4 MPa—more than double the initial pressure rise. Models A and B both predict identical results in this case and the comparisons with the measurements are almost exact. The results are consistent with the previous work on the apparatus (Vardy and Fan, 1989).

Slight Cavitation. In the second set of experiments, the initial pressure is lowered to about 1.07 MPa. At the impact and the remote ends, it is no longer possible to reduce the pressure by -1.8 MPa and -1.4 MPa, respectively (Fig. 5). Cavitation first occurs at the remote end due to S1 and later, at about 4 millisecond, at the impact end due to L2. The cavities exist only when the pressure at the corresponding location drops to the vapor pressure, hence confirming the validity of the results. One particular interesting observation is that the occurrence of the vapor bubbles mainly alternates between the pipe ends. This effect is more apparent as the severity of cavitation increases (Fig. 7). The fluid therefore behaves like an elastic column slopping between the end cavities. Model A predicts the events with good accuracy. Thus it can be inferred that the phenomenon is column separation dominant.

At the impact end, extremely high frequencies exist in the pressure measurements. This is thought to be due to the location of the pressure transducer relative to the vapor cavity. The transducer is located at about 20 mm from the inner surface of the end plug (Fig. 2). It is a recognized phenomenon (Safwat, 1972) that a small amount of distributed cavitation normally exists in the vicinity of a column separation region. It is therefore conceivable that the random collapse of the small bubbles within the distributed cavitation region can cause the high frequency signals in the measurements. This seems to be a local effect and the signals cannot be observed further along the pipe. At the remote end, the same effect cannot occur because the transducer is mounted on the inner surface of the end cap. In order to filter out the oscillations at the sampling frequency (125 kHz), a Shuman numerical procedure (Vliegenthart, 1970) is used for the pressure measurements at the impact end in all cases.

Moderate Cavitation. In Fig. 6, the initial pressure in the pipe is about 0.73 MPa. Cavitation is also initiated at the remote end by reflection of the stress wavefront S1 (Fig. 1). On the left hand side, the measurements are compared with model A. It predicts the first pressure peak due to cavity collapse at both ends of the pipe with a high degree of accuracy. The agreement between experiment and theory then begins to deteriorate with time. By using model B, distributed cavitation is modeled, and the subsequent pressure peaks are now accurately predicted. It can be deduced that distributed cavities are present and they interact significantly with pressure wave propagation. The calculated results indicate that model A overestimates the first cavity volume at the impact end. It is probably due to the model attempts to lump the distributed cavities towards the impact end. It is worthwhile noting that the results resemble that of cavitation in a reservoir-pipe-valve case (Martin, 1983), with additional secondary pressure peaks between the major ones.

Severe Cavitation. In Fig. 7, two cases of results with different rod impact velocity are presented. The initial pressure in the pipe is atmospheric in both cases. On the left hand side (low velocity), the pressure pattern changes significantly from the previous case. The duration of the cavity at the remote end is 50 percent longer than in the previous case but the magnitude of the first pressure peak is about the same. The most noticeable difference is the subsequent pressure peaks become less significant compared with the first one. Other measurements up to 5 seconds have shown that the pressure rapidly diminished to zero after 20 milliseconds. The reduction

of pressure and stress levels in the pipe is therefore highly significant. Most of the wavefront energy is converted to the kinetic energy used for moving the pipe away from the impact end. Model B is capable of predicting the amplitude and the timing of the events very well. The discrepancies at time greater than 14 millisecond correspond to the decrease in repeatability of the measurements (Fig. 4).

Poisson Coupling Induced Cavitation. In this set of experiments, the rod impact velocity is increased in order to generate cavitation associated with radial expansion of the pipewall due to the compressive stress wave S1 (Fig. 1). This effect is illustrated by the pressure trace at the impact end. The pressure level no longer remains constant during the first 2 milliseconds ($2L/c_p$) as in all the previous cases. The variable pressure level is due to the growth and collapse of the bubbles associated with S1. After S1 transverses the pipe, the entire length of the pipe is dispersed with bubbles. The overpressure wave L1 has first to cause all the bubbles to disappear before it can transverse the pipe. When S1 reaches the remote end, the cavity formed exists for about the same duration as in the previous case, even though the impact velocity is higher. However, the peak pressure is about 1 MPa higher and the relative magnitude of the subsequent pressure peaks is lower. Therefore, the rate of convertion of wavefront energy to kinetic energy is higher than the previous case. The ability of model B to predict these events is excellent, even in the presence of cavitation caused by radial expansion of the pipewall.

Tensile Strength of Water. At a short time after impact, the compressive stress wavefront S1 (Fig. 1) reaches the remote end and pushes the end cap away from the water. The water can be seen to sustain tensile stresses of between 0.35 to 0.7 MPa up to 0.15 millisecond before column separation occurs (Fig. 4). No direct correlation between the initial pressure, the duration and the magnitude of the tensile stresses seems to exist. Other work in this area has shown that water can sustain tensions up to much higher magnitudes in steel tubes. Plesset (1969) and Trevena (1984) gave informative reviews on theoretical and experimental aspects of the subject respectively. Davies et al. (1955) have also used a similar apparatus and found that water has a maximum dynamic tensile strength of about 1 MPa on clean steel surface.

The present apparatus is not specially designed for measuring the transient tensile strength of water. Indeed, only ordinary tap water has been used with a standard industrial steel pipe. Therefore, the abundance of nuclei in water must have encouraged the vapor cavities to grow. It is envisaged that higher transient tensile stresses can be measured if the water is purified and if the pipe interior is smooth.

Further Work

In the present theoretical model distributed bubbles in the fluid are lumped at the grid points to form localized vapor cavities. Whenever a pressure wave intersects a localized cavity, the magnitude of the pressure wave is modified by the presence of the cavity. However, an axial stress wave does not change in magnitude when it passes through a localized cavity (Fig. 3). This procedure is exact if Poisson coupling is absent between the fluid and the pipewall. If Poisson coupling effects are significant, the secondary pressure waves associated with axial stress waves must be modified by the vapor cavities. For the cases considered the interactions between the secondary pressure (precursor) waves and the localized vapor cavities is small enough to allow reasonably accurate predicted results. A more rigorous and general approach would be to allow the $c_p \pm$ lines to span one grid length and the $c_f \pm$ lines extend back several timesteps.

In principle, the experimental technique is not restricted to single pipe systems. Different piping configurations can be achieved by assembling elbow and tee junctions onto the remote end of the main pipe. In planar networks, additional effects due to flexural wave propagations in the pipewall must be taken into account. Work has already begun on the multipipe systems with and without cavitation.

Conclusions

1. Accurate experimental results of transient cavitation in a closed tube have been obtained. Significant interactions exist between the pipewall, the fluid and the vapor cavities.
2. Transient tensile stresses of water and Poisson coupling induced cavitation can be measured accurately in the present apparatus.
3. The numerical model proposed by Tijsseling and Lavooij (1989) is sufficiently accurate if the flow is column separation dominant.
4. The proposed concentrated cavity—fluid/structure interaction model predicts the phenomenon with sufficient accuracy for most practical purposes. It can even simulate transient cavitation induced by radial expansions of pipewalls.

Acknowledgment

Delft Hydraulics is thanked for financially supporting the cavitation experiments at the University of Dundee.

References

Chaudhry, M. H., 1979, *Applied Hydraulic Transients*, Van Nostrand Reinhold, New York, ISBN 0-442-21517-7, pp. 276–281.

Davies, R. M., Trevena, D. H., Rees, N. J. M., and Lewis, G. M., 1955, "The Tensile Strength of Liquids Under Dynamic Stressing," *Proc. NPL Symp. on Cavitation in Hydrodynamics*, Paper 5, H. M. Stationery Office, London, UK.

Fox, J. A., and McGarry, M., 1983, "Pressure Transients in Pipelines Transporting Volatile Liquids," *Proc. 4th Int. Conf. on Pressure Surges*, Bath, UK: 21–23 Sept., BHRA, Cranfield, UK, pp. 39–57.

Kot, C. A., and Youngdahl, C. K., 1978, "Transient Cavitation Effects in Fluid Piping Systems," *Nuclear Engineering and Design*, Vol. 45, pp. 93–100.

Kranenburg, C., 1974, "Gas Release During Transient Cavitation in Pipes," *Proc. ASCE, J. Hyd. Div.*, Vol. 100, HY10, pp. 1383–1398.

Lavooij, C. S. W., and Tijsseling, A. S., 1989, "Fluid-Structure Interaction in Compliant Piping Systems," *Proc. 6th Int. Conf. on Pressure Surges*, Cambridge, UK: 4–6 Oct., BHRA, Cranfield, UK, pp. 85–100.

Martin, C. S., Padmanabhan, M., and Wiggert, D. C., 1976, "Pressure Wave Propagation in Two-Phase Bubbly Air-Water Mixtures," *Proc. 2nd Intl. Conf. on Pressure Surges*, London, UK: 22–24 Sept., BHRA, Cranfield, UK, paper C1.

Martin, C. S., 1983, "Experimental Investigation of Column Separation With Rapid Closure of Downstream Valve," *Proc. 4th Intl. Conf. on Pressure Surges*, Bath, UK: 21–23 Sept., BHRA, Cranfield, UK, Paper B3.

Plesset, M. S., 1969, "The Tensile Strength of Liquids," Fluids Engrg. and Appl. Mech. Conf., *Cavitation State of Knowledge*, Evanston, Ill.: 16–18 June, ASME, pp. 15–25.

Provoost, G. A., 1976, "Investigation Into Cavitation in a Prototype Pipeline Caused by Water Hammer," *Proc. 2nd Intl. Conf. on Pressure Surges*, London, UK: 22–24 Sept., BHRA, Cranfield, UK, Paper D2.

Safwat, H. H., 1972, "Photographic Study of Water Column Separation," *Proc. ASCE, J. Hyd. Div.*, Vol. 98, HY4, pp. 739–746.

Schwarz, W., 1978, "Druckstossberechnung unter Berucksichtigung der Radial-und Langsverschiebungen der Rohrwandung," Institut fur Wasserbau der Universitat Stuttgart, Mitteilungsheft 43, Stuttgart, Germany, ISBN 3-921694-43-4.

Schwirian, R. E., 1982, "Methods for Simulating Fluid-Structure Interaction and Cavitation With Existing Finite Element Formulations," Pressure Vessel and Piping Conf., *Fluid Transients and Fluid-Structure Interaction*, Orlando, Fla., 27 June–2 July, ASME, PVP-64, pp. 261–285.

Streeter, V. L., 1969, "Water Hammer Analysis," *Proc. ASCE, J. Hyd. Div.*, Vol. 95, HY6, pp. 1959–1972.

Tijsseling, A. S., and Lavooij, C. S. W., 1989, "Fluid-Structure Interaction and Column Separation in a Straight Elastic Pipe," *Proc. 6th Intl. Conf. on Pressure Surges*, Cambridge, UK: 4–6 Oct., BHRA, Cranfield, UK, pp. 27–41.

Tijsseling, A. S., and Lavooij, C. S. W., 1990, "Water Hammer With Fluid-Structure Interaction," *Applied Scientific Research*, Vol. 47, pp. 273–285.

Trevena, D. H., 1984, "Cavitation and the Generation of Tension in Liquids," *J. Physics D: Applied Physics*, Vol. 17, pp. 2139–2164.

Vardy, A. E., and Fan, D., 1986, "Water Hammer in a Closed Tube," *Proc. 5th Intl. Conf. on Pressure Surges*, Hannover, F. R. Germany: Sept. 22–24, BHRA, Cranfield, UK, Paper E3, pp. 123–137.

Vardy, A. E., and Fan, D., 1987, "Constitutive Factors in Transient Internal Flows," *Proc. NUMETA '87 Conf.*, Vol. 2, Swansea University, UK, Martinus Nijhoff, Netherlands, Paper T37.

Vardy, A. E., and Fan, D., 1989, "Flexural Waves in a Closed Tube," *Proc. 6th Intl. Conf. on Pressure Surges*, Cambridge, UK: 4–6 Oct., BHRA, Cranfield, UK, pp. 43–57.

Vliegenthart, A. C., 1970, "The Shuman Filtering Operator and the Numerical Computation of Shock Waves," *J. Engrg. Math.*, Vol. 4, No. 4, pp. 341–348.

Wiggert, D. C., Otwell, R. S., and Hatfield, F. J., 1985, "The Effect of Elbow Restraint on Pressure Transients," ASME JOURNAL OF FLUIDS ENGINEERING, Vol. 107, No. 3, pp. 402–406.

Wiggert, D. C., Lesmez, M. L., and Hatfield, F. J., 1987, "Modal Analysis of Fluid Vibrations in Liquid-Filled Piping Systems," *Symp. on Fluid Transients in Fluid-Structure Interaction*, Boston, MA, Dec. 13–18, ASME Winter Annual Meeting, ASME FED-56, pp. 107–113.

Wilkinson, D. H., 1978, "Acoustic and Mechanical Vibrations in Liquid Filled Pipework Systems," *Proc. BNES Conf. on Vibrations in Nuclear Plant*, Keswick, UK.

Wylie, E. B., 1984, "Simulation of Vaporous and Gaseous Cavitation," ASME JOURNAL OF FLUIDS ENGINEERING, Vol. 106, pp. 307–311.

Zielke, W., Perko, H-D., and Keller, A., 1989, "Gas Release in Transient Pipe Flow," *Proc. 6th Intl. Conf. on Pressure Surges*, Cambridge, UK: 4–6 Oct., BHRA, Cranfield, UK, pp. 3–13.